Biomarkers, Martian Analogues and Raman Spectroscopy

Rory Porteous

B.Sc (Hons) University of Dundee

Submitted in fulfilment of the requirements for the Degree of Doctor of Philosophy

School of Geographical and Earth Sciences

College of Science and Engineering

University of Glasgow

October 2018

Declaration

The work in this thesis is a summation of 4 years of work at the University of Glasgow for the completion of a PhD. This work was carried out and written by myself under the supervision of Professor Jaime Toney and Dr Vernon Phoenix.

- Rory Porteous

I Abstract

In the search for signs or traces of extraterrestrial life we are confined to our understanding of how life arose on Earth, processes that are intrinsically tied to our understanding of both the biotic and abiotic process that formed many of the features on this planet. Understanding how life arose on Mars, and where any such signs of life could persist, requires an understanding of the same processes that took place on Earth, in addition to how those signs could have persisted over the timescale in which Mars would have been considered a 'lifeless' planet. Exploration of Mars is highly dependent on prioritization of sample sites that maximise the potential for discoveries that justify the expense and difficulty of exploring a planet that is not our own.

This study sought to determine whether a possible origin of life environment could provide data sufficient to encourage targeting such a location for future Mars missions. Hydrothermal vents where heated waters from a volcanically active zone could provide the necessary mineral surfaces, thermal gradient and possible sources of organic molecules from the earth's crust to form the first proto-cells. Both terrestrial and particularly aquatic hydrothermal vents are the source of energy for many bacteria. In aquatic settings a hydrothermal vent is often the sole source of energy for any potential community. The silica sinters analysed in this thesis returned 3 potential sources of biosignatures; actively viable bacteria that were able to be cultured; visual evidence of microbial encrustation in the form of filamentous or coccal bacteria; and organic biomarkers in the form of n-alkanes, fatty acids and other organic compounds.

It was also established that the Chilean Altiplano could be considered a Martian analogue due to its similar environmental characteristics (temperature, humidity, increased UV, low biomass) and a diurnal soil cycle matching that on Mars with regards to cold atmospheric

temperatures and surface heating of soils leading to a fluctuating temperature and soil humidity profile.

Contents

II Table of Figures

III Acknowledgements

I couldn't possibly have completed this PhD without the support of my dear old mother. I'm not sure what she thought she was getting into when she told me I could live with her whilst I worked out what I'd do with my life after 4 years of living away from home during my undergraduate degree. She has gone 5 years of putting up with my nonsense, be that forgetting to put plates in the dishwasher or sneaking gin and tonic into her lunch bag for work, and has done so with (almost) no complaint. I certainly wouldn't have been able to fund my way through this project without her support and I will be forever grateful as a result.

I'd also be remiss not to thank Dave Botham, who has done a tremendous job supporting me at every opportunity, always making sure that I was getting on well as the project continued.

I'd like to thank my pair of supervisors Jaime Toney and Vernon Phoenix, who have guided me through each half of the project. Their expertise and the back and forth that came from our conversations were a great help in answering the questions the project raised.

I'd like to thank Peter Chung who operates the Imaging Spectroscopy and Analysis Centre (ISAAC) here at the University of Glasgow. Peter's support has gone beyond what I could possibly have expected from anyone, and has had a profound impact on who I am as a person. Peter's encouragement and his patience for me distracting him in his office has seen me through four very difficult years and I would be significantly worse off without his support.

My officemates have been crucial to helping me survive 4 years of building works, broken equipment and mental fatigue. I'm not the most outgoing person but I always tried to make

an effort for all of you. Love and hugs to Caroline Miller, Áine O'Brien, Ellen Macdonald, Aimee Smith, Heather Baxter, Alyssa Bell, Phillipe Nauny, Charlotte Slaymark, Cameron Floyd, Charlotte Young, Chris Holdsworth, Crystal Smiley, Sammy Griffin, Eilidh Milne, Mike Zwick, Anca Amarei and Jennifer Mallon.

I'd be remiss not to thank all the friends that have supported me through the last 4 years, always asking about the project and offering encouragement when I needed. I'd like to thank Farhad Javed, James Howland, Emma Black, Chris McRandle, Andrew Holmes, Joe Holmes, Sarah Hardy, Briony Johnstone, Fiona Cullen, Ken Babarinsa, Paul Morton, Scot and Declan McInnes, Hamish Dobbie, David Hodson, Ryan Davidson, David Reid, Pamela Craig, Craig MacWilliams and more.

4 Mars and Martian Analogues

In March 2007 the Mars Exploration Rover Spirit uncovered amorphous silica deposits of 91% purity at Home Plate in Gusev crater on Mars which has been interpreted to be a former hydrothermal site. (Squyres, et al., 2008) In concentrations this high, silica will either have been precipitated out of silica-saturated water in an alkaline environment where water evaporates to leave behind a silica sinter, or is the by-product of the leaching away of other minerals in an acidic environment. In an acidic environment (which the Spirit site is thought to be) more insoluble minerals will be left behind such as silica. Evidence of the Spirit site being formed in an acidic environment is due to similar enrichment of insoluble Titanium and Chromium compared to typical Martian soil as these provide evidence of a decrease in element concentration with increasing atomic number. (Fig 1.) Evidence of acid-sulfate processes in Gusev crater also points towards origins in an acidic environment.

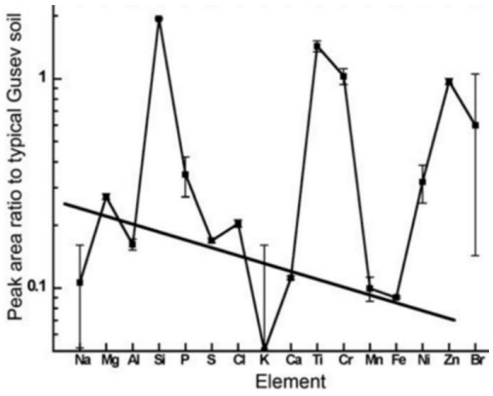

Figure 4.1 Composition of Kenosha Comets deposit showing a trend towards a decrease in element concentration with increased atomic number. This provides evidence of formation in an acidic environment as heavier elements are leached away. (Adapted from Squyres, et al., (2008))

The presence of volcanic materials in the Home Plate area strongly supports the hydrothermal theory of origin of these silica deposits. Home Plate is a volcanic deposit composed of fine-grained volcanic deposits and volcanic glass (Squyres, et al., 2008). The presence of bomb sag (ejecta from an explosive event) also suggests an explosive volcanic origin. Whilst an impact event could produce a similar composition the presence of more volatile elements such as nickel and germanium contradicts the impact theory. Hydrothermal sites are one geological environment in which Germanium is often found to be enriched in sulfide and zinc mineralizations. (Squyres, et al., 2008)

As a whole, the silica found at Gusev Crater is important evidence of former hydrothermal activity, and given the abundance of life often found around both terrestrial (geyser field) (Renaut & Jones, 2011; Cowan, et al., 2012; Takai & Sako, 1999; Reysenbach & Cady, 2001; Hou, et al., 2013) and aquatic (deep-sea hydrothermal vents, Black smokers) (Reysenbach & Cady, 2001; Antranikian, et al., 2017; Bell, et al., 2017; Djurhuus, et al., 2017; Beatty, et al., 2005; Gugliandolo, et al., 2010), high silica sites such as these could be important locations for future research into the history of water on Mars, as well as possible locations for sample-return missions in the future.

4.1 The Historical understanding of Water on Mars

The history of Mars exploration has often focused on the question of whether Mars had a watery past and with it extraterrestrial life.

It was initially thought that the red-orange of Mars was a feature granted by its atmosphere which would have had to be strongly absorbing at shorter wavelengths. This was famously disputed in 1894 by William Wallace Campbell (Campbell, 1894) who asserted that

observations of Mars showed that the planet was reddest near the centre where the atmosphere was thinnest. If the atmosphere was the cause of the planet's red-tint then it would be expected to be reddest at the edges where the atmosphere is thickest to the viewer. Campbell also asserted that it is reasonable to expect based on observations of the known planets in the solar system at the time that the mass of a planet's atmosphere is proportional to the mass of the planet itself. Mars had been (accurately) estimated to have a mass of around 0.11 Earths and so it was estimated that proportionally in line with the reduced surface area of Mars the atmosphere above a square mile would equate to around 39% of Earth's. In turn the reduced gravity of Mars would impact the density of the atmosphere at the surface level. Campbell estimated that the atmosphere at the surface would only be around 15% of that at sea level on Earth. Correspondingly, the reduced gravity would also cause the Martian atmosphere to be taller than that of Earth. (Campbell, 1894)

At the time it was assumed that the white polar caps of Mars were composed of water and thus the atmosphere must contain aqueous vapor but Campbell's findings contradicted this. He proposed that the lack of cloud data in the polar regions during the melting season contradicted the suggestion that the poles are composed of liquid water. When the poles retreat water vapour would be expected to form clouds. The lack of cloud evidence extended to the rest of the planet as well; no cloud evidence had been found in more equatorial regions of the planet so the evidence was against the theory that Mars contained water in it's atmosphere. Campbell goes on to discuss the theory that not only are the poles made up of frozen Carbon dioxide (he discusses it in the form of Carbonic acid) but that carbon dioxide could be the principal component of the atmosphere of Mars. Campbell surmised that a Carbonic acid theory would solve many of the problems astronomers at the time were encountering trying to rationalise the lack of evidence for atmospheric water whilst at the same time it would solve the problems associated with Mars climate by

assuming that Mars was far colder than Earth, whereas at the time it was expected to be similarly mild. Campbell doesn't commit to this theory, instead suggesting that it is one of many possible interpretations. However history would show that this theory was correct,

In 1926 Walter S, Adams would publish his own findings on the presence of water on Mars, showing that Martian water vapour was detected at trace levels, confirming that Campbell's findings had been correct (Adams, 1926). In addition, findings related to the temperature of Mars confirmed that it was a much colder planet than Earth. Edison Pettit and Seth B. Nicholson utilised thermocouples alongside a 100-inch telescope to measure the radiometric magnitude of Mars and subsequently interpret temperature data from it. (Pettit, 1924) Their observations showed that the centre of the Martian disk was a little above freezing temperatures (280K) whilst the pole caps were as low as 205K. It was clear by this point that Mars was not as wet a planet as first thought.

40 years later as part of their Mars exploration program the Mariner 4 flyby would send back the first images of Mars, showing a heavily cratered planet with no evidence of liquid water and no evidence of life. Mariner 4 would also perform its radio occultation experiment to provide the first precise data on the properties of the Martian atmosphere and the temperature of the planet. Mars was found to possess a Carbon Dioxide based atmosphere that was far less dense than that of Earths (~0.8%). Atmospheric density at the martian surface correlates to around 34km above sea level on Earth (mid-stratosphere) (Fjeldbo, et al., 1966) resulting in an Atmospheric pressure that varies from 400 to 870 Pa at the equator (Williams, 2018). Atmospheric pressure is similarly reduced but the low density atmosphere is more sensitive to changes by local atmospheric activity, varying by ~80Pa on average per day (Harri, et al., 2014), with recorded fluctuations of up to 3.6 Pa due to dust devil activity (Ellehoj, et al., 2010). The low pressure of the Martian

atmosphere is well below the Armstrong limit, the point at which water will boil at 37°C. Sublimation of water off of the Martian surface has been observable, most commonly around recurring slope lineae; brine flows that occasionally leak onto the surface when surface temperatures increase past the melting point (Ojha, et al., 2015).

Since Mariner 4 there have been in total 5 successful flyby missions and 10 successful orbiter missions, resulting in Mars being the most well understood extraterrestrial body aside from the Earth and moon. Mariner 9, the final mission in the program that visited Mars, would provide the first close to complete map of the planet, providing evidence of past aqueous activity from lakebeds and river activity. One of the most notable regions of the planet where past water activity can be seen is the Kasei Valles outflow channels that feed into the Chryse Planitia basin.

4.2 Kasei Valles and Martian Outflow Channels

The Kasei Valles provides some of the most conclusive evidence of water playing a role in shaping the Martian surface. Kasei Valles is a canyon region bordering Chryse Planitia and is one of the largest outflow channels on the planet. Within the outflow channel streamlined erosion features and dry waterfalls can be seen. In large Martian outflow channels the water flow has eroded the surface in such a way that teardrop shaped islands have formed in the middle of the channel. The size of these islands will have been influenced by the speed of the water flow around them and therefor the effects of drag. In several cases the head of the island is defined by a crater, Rongxar crater in the Kasei Valles is one such example, where the water flow cannot erode the hard rock from the crater impact and instead erodes around it, resulting in the teardrop feature forming behind (Komar, 1983). The tail of these islands can be elongated as a result of sediment deposition, as the flow velocity will reduce in these areas. Studies have shown that there is

an optimal length/width ratio for the formation of these islands of between 3:1 and 4:1. This represents the point at which the drag coefficient is at its lowest (Komar, 1983). It has previously been suggested that these island formations could be as a result of lava flows however, the evidence for the streamlined shape as well as the turbulent wake at the tail of the islands point to a water-based origin (Komar, 1983). From observations after the Viking missions, it was thought that these islands were either lava deposits that were unearthed during one of the great flood events (suggested by the coarse texture on the surface of the islands) and were more able to resist erosion, or that they consist of more strongly cemented rock as a result of past meteoric bombardment (Tanaka & Chapman, 1992).

Other features that can be observed in the Kasei Valles include channel lineations that mark the flow of water. These markings in the channel bed line up with the islands spread around Kasei Valles. These channel lineations are often found at differing altitudes when located in the same areas. This is due to different flooding events throughout the late Hesperian originating from the Tharsis region to the south-west (Tanaka & Chapman, 1992). The youngest originate from Echus Chasma some 1200km south near the Martian equator. Echus Chasma has been found to contain clay which confirms that water played a role in its formation.

These mass flooding events are estimated to have taken place during the Late Hesperian when Mars was transitioning from a warm and wet state to the present dry and cold state of the modern day. The planet was still volcanically and tectonically active and this tectonic activity is likely what resulted in the megafloods that formed the Kasei Valles .

4.3 Mars' Ancient Climate

The Valley networks and outflow channels that scar the Martian surface from low to middle latitudes provide evidence of a wetter past for Mars than in the current day (Hynek, et al., 2010; Mangold, et al., 2004; Carr, 1996) but this has left questions over the ancient climate of Mars and how it could impact the chances of life taking hold on the planet and in particular atmospheric composition and whether water at the surface was transient or persistent.

The geology of Earth has provided some of the most substantial evidence for past climate as the geological makeup can inform us of conditions of formation on early Earth. The same is true for paleoclimate studies of Mars. The stratigraphic record is capable of providing mineralogical, textural and geochemical signatures that are capable of characterizing changes in Mars ancient and global climate. Analysis of hydrous minerals present at the Martian surface has led to the hypothesis that Mars experienced a warm and wet period that led to increased clay formation.

Martian clays have provided evidence of the water and atmospheric conditions at the time of their formation across several studies with differing conclusions that have included; *subsurface* phyllosilicate formation in cold and arid conditions with subsurface hydrothermal water circulation (Ehlmann, et al., 2011; Bibring, et al., 2006), or *surface* formation of phyllosilicates which could occur in a warmer, wetter climate with a dense atmosphere (Bibring, et al., 2006). Phyllosilicate formation is dependent on alkaline conditions (Le Deit, et al., 2012) which dates their formation to the Noachian period (4.1Gya>3.7Gya) when the fluvial valley networks and the Tharsis bulge volcanic plateau are estimated to have formed.

In the deeper sub-surface scenario, phyllosilicate formation would require a water source deeper within the subsurface (Bibring, et al., 2006).. This can include hydrothermal water sources of which there is considerable evidence towards the presence of water in the Martian subsurface (Ehlmann, et al., 2011; Mitrofanov, et al., 2003; Boynton, et al., 2002; Carr, 1986; Labza, et al., 2010), as well as evidence supporting interactions between volcanism and water/ground ice (Squyres, et al., 1987; Head III & Wilson, 2007; Chapman & Tanaka, 2002; Allen, 1979). Hydrothermal processes could also lead to terrestrial hydrothermal mineral depositions that would be favourable to habitability (Bibring, et al., 2006).

Cratering could also act as a potential water source with impact events forming melt sheets below the surface that fracture and allow water to move upwards as steam, creating a hydrothermal vent. The water table below an impact will depress and move deeper into the crust whilst steam escapes through fractures in the melt sheet formed after crystallization (Newsom, 1980). Water movement to the surface would be in the form of steam with minimal liquid water movement upwards through the ice sheet. Water movement below the melt sheet resupplies water lost through steam venting and it is this water that would contribute to phyllosilicate formation (Newsom, 1980; Bibring, et al., 2006).

Near or at the surface there would not require high-temperature conditions for formation of phyllosilicate clay minerals as their formation would imply a persistent wet episode during the Noachian (Bibring, et al., 2006).

Le Deit *et al* proposed a timeline for phyllosilicate formation and burial in their paper covering pedogenic alteration of phyllosolicates around Valles Marineris (Le Deit, et al.,

2012). Phyllosilicate formation via pedogenesis would have occurred during the Noachian period would have experienced episodes of aqueous activity during a temperate-subarid climate in an alkaline environment. The subarid climate would continue into the Hesperian period whilst phyllosilicates formed during the Noachian would have been buried beneath the extensive lava flows of the Hesperian. Buried phyllosilicates were exhumed in the transition between the Hesperian and Amazonian periods by wind and fluvial erosion. Phyllosilicate formation could continue up to this stage via pedogenesis and exposure to water runoff at the surface.

Sulfates represent another example of how we can date and hypothesize conditions at the time of formation. Mars Express has observed large and diverse sulfate minerals in the region of the Valles Marineris that are most likely tied to volcanic processes. Sulfate mineral formation is dependent on large volumes of water to result in the broad array of minerals observed by the Mars Express orbiter, and evaporative processes which imply formation at or near the surface (Bibring, et al., 2006). It can therefore be inferred that these sulfate minerals would have formed in the late Noachian to the Hesperian, after phyllosilicate formation. Deposit size and spread would require high quantities of sulfur that most likely would originate from volcanic activity, which would also act as a source of volatiles and water (Bibring, et al., 2006).

4.4 The present state of water on Mars

The current understanding of water on Mars is predominantly based on subsurface permafrost that covers much of the planet at latitudes higher than 60º (Head, et al., 2003; Feldman, et al., 2004). This became one of the first major discoveries of the Phoenix lander in 2008 when upon drilling into the surface an ice layer was revealed that was confirmed to be water ice and not CO_2 ice, which would not have been stable at the surface

for the time that the ice was present. (Mellon, et al., 2009; Webster, et al., 2008). The triple point of water at which sublimation will occur is higher than that of CO_2 at an equivalent pressure. The average atmospheric pressure on Mars is ~0.6kPa and at deeper points such as Hellas Planitia it can reach 1.16kPa. At these pressures the triple point of water is at approximately 273.16K, whilst at 100kPa the sublimation point of CO_2 is at 194.65K. Sublimation will occur far more rapidly for CO_2 ice at Martian pressures than H_2O ice.

The Phoenix lander findings provided the first lander-based evidence of subsurface H_2O ice beneath the surface of Mars at a higher latitude than any other landing site. The higher latitude site is within the margin that freezes during the northern winter and the landscape is patterned by the repeated freeze-thaw cycle. Phoenix also provided evidence of water clouds and precipitation of ice crystals during northern summer nights as temperatures decrease (Whiteway, et al., 2009).

Subsurface ice sheets are not unique to Mars having been found on Earth in multiple locations. Smaller examples of subsurface ice layers include near-surface permafrost in high-altitude mountains such as the Andes in South America (Schrott, 1991) whilst larger examples include millions of years old glacial ice that has been preserved beneath the surface (Sugden, et al., 1995). Preserved ice on Earth can act as a record for climate conditions at the time of formation, with air bubbles within the ice enabling high-resolution records of past atmospheric conditions (Fischer, et al., 1999). It is expected that similar high-resolution records could be obtained from Martian ice both at the Martian polar ice caps and from subsurface ice sheets (Head, et al., 2003). Ice sheets in the polar regions are have been considered as a habitable site (Jakosky, et al., 2003), and as will be discussed later in this chapter, subsurface permafrost ice has been considered as a potential habitable site.

4.4.1.1 Recurring Slope Lineae

The sublimation point of water is important to consider with regards to discoveries of recurring slope lineae (RSL) in recent years as RSL can only occur when sublimation is not possible. These RSL have so far been found solely in the southern hemisphere of Mars at latitudes between 48ºS and 32ºS during the southern summer (McEwen, et al., 2011).

Recent discoveries of liquid water flowing on Mars in the form of a brine were made in 2001 (Mellon & Philips, 2001), 2011 (McEwen, et al., 2011) and confirmed in 2015 (Ojha, et al., 2015). Whilst liquid water is unstable at the surface the boiling point for brine is much higher than that of water, increasing the chance of it persisting at the surface for some time. These brines are thought to originate (mainly but not solely) from permafrost ice that sits beneath the upper layer of the Martian surface, since these flows were seen on a seasonal basis, mainly during the southern summer when the planet is at perihelion. During the southern summer surface temperatures are capable of frequently going above 250K and often above 273K. Salts that allow the formation of brines can potentially lower the melting point of ice by up to 40 - 70K. (Ojha, et al., 2015) In 2009 Altheide *et al* demonstrated that under Martian conditions, brines evaporated at a rate significantly slower than that of pure water across a narrow range of temperatures between 273K and 261K (Altheide, et al., 2009).

Subsurface ice is not the sole theory on the source of the flows. Deliquescence of hygroscopic salts could potentially pull enough water vapour out of the atmosphere to produce flows down slopes but there are doubts as to the rate of deliquescence being enough to solely support the frequency of flow events. (McEwen, et al., 2011) During

sublimation water vapour from melted subsurface ice could deliquesce. (McEwen, et al., 2011) This varies from simple melting of subsurface ice as the water experiences a gaseous phase prior to becoming a liquid.

4.4.1.2 Polar Ice on Mars

Mars Polar caps are predominantly made up of water ice with CO_2 ice deposition during winter due to the freezing of the atmosphere. The North pole has a diameter of 1100km whilst the South is smaller, with a diameter of 400km. Both experience the same expansion due to CO_2 ice deposition in the winter, and this deposition removes as much as 30% of the atmosphere. Mars experiences seasonal changes similar to those on Earth due to axial tilt, and the polar regions are similarly subject to long-term darkness during winter periods which is what enables the freezing and deposition of the atmosphere into CO_2 ice slabs that last the winter. These slabs will eventually sublimate back into the atmosphere during the summer when the sun reaches the poles again. The Northern polar cap of Mars is estimated to hold a volume of $1.6x10^6$ km^3 of H_2O ice, which is a fraction of the volume that makes up the Greenland ice sheet.

Recent remote observations have shown that the northern pole of Mars houses a large body of subterranean liquid water, likely brines, 1.5km below the surface (Clery, 2018). The depth of this lake puts it beyond the reach of any sampling mission at present (By comparison, terrestrial oil wells are on average 1.1km below the surface of the Earth)

4.5 Habitability on Mars from a Microbial Point of View

It’s important to consider how we define the environments on Mars that studies take place in. Specifically it’s important to clarify what is meant by ‘habitable’ and ‘preservation potential’ in the context of the search for biosignatures.

Present conditions on Mars are not conducive to long-term habitability at the surface, and those same conditions are why we must consider how we rank particular biosignatures according to how likely they are to be preserved. The preservation potential is dependent on the biosignature itself as well as the substrate that biosignature is found in. As an example, chemical and physical or geological biosignatures will preserve differently under Martian conditions. A study by Dartness *et al* demonstrated that Raman biosignatures were degraded or completely erased after exposure to ionizing radiation (Dartnell, et al., 2012). While a study by Wadsworth & Cockell (2017) showed that even without interactions with ionizing radiation, the presence of perchlorate in the soil and the influence of UV radiation combines to form a highly oxidizing environment detrimental to bacterial viability.

The simplest interpretation of what defines a site as habitable requires the presence of raw materials, water, energy and favourable conditions. However the exact nature of these parameters will be dependent on the nature of the site in question as well the preservation record of these factors. As with all aspects of astrobiology, these factors are constrained to how we understand life on Earth, but the inability to detect one or all of these factors don’t constrain discussion of a site as a formerly habitable environment (Mustard, et al., 2013).

Hydrothermal vents provide an environment in which a multitude of metabolic reactions can occur through which early microbial life could establish. The acetyl-coenzme A pathway is thought to be amongst the most ancient chemical pathways for CO_2 fixation (Martin, et al., 2008) and is perhaps an evolution on simpler biochemistry that metabolism

evolved from. The acetyl coenzyme A pathway also provides ATP as a byproduct of the reduction of CO_2, whilst modern day acetogens (acetate producers) and methanogens (methane producers) utilize the acetyl conenzyme A pathway as a means of creating an ion gradient that facilitates the use of CO instead of CO_2 and H_2 (Martin, et al., 2008; Rother & Metcalf, 2004). CO_2 would be one of the most ubiquitous compounds emitted from hydrothermal vents (Resing, et al., 2004) and found in the early Earth atmosphere.

Other chemosynthetic processes found in modern day hydrothermal vents include Methanogenesis, Sulfate reduction, Iron reduction and oxidation, anaerobic and aerobic Methane oxidation, and respiration. However early biological processes would have been the most simple pathways for production of energy.

Studies of Martian analogue sites can increase our understanding of past environments on Earth, particularly studies of origin of life sites. Given the lack of evidence for life so far found on Mars, origin of life sites provide the best opportunity to study an area in which life could have arisen in the past. Some of these sites on Earth have also shown to have a high potential for preservation. It is important to consider what is meant when we discuss habitability however. Mars at present would not be deemed habitable due to the lack of reliable liquid water, and possessing conditions unfavourable to life. When habitability is discussed in astrobiology it is either in reference to the exploration and discovery of extant life, or discussions on past life.

Westall *et al* state that habitability should be defined as "conditions necessary for the origin of life, the proliferation of life, and the survival of life" (Westall, et al., 2013). This would exclude conditions that would support the beginnings of prebiotic chemistry and that those that would allow identification of extinct or hibernating life. They note that the

traditional view that water is the key ingredient to the emergence of life is misleading given the notion of what makes a habitable planet needs to be defined further. Life could emerge out of an equivalent primordial soup, be established within its own niche or in a survival/dormant mode equivalent but all three scenarios would have different chemical requirements.

To establish ideal sites for the origin of life on Mars, the requirements for life and their potential sources within an environment must be considered first.

4.5.1 Prebiotic Chemistry

Whilst excluding evidence of prebiotic chemistry as evidence of habitability is an appropriate rule for how we define habitability, the natural difficulties associated with the extraterrestrial search for life or evidence of past life requires a broader search that does include evidence of prebiotic chemistry as a barometer for the likelihood of detecting biosignatures. Evidence of the biotic potential of selected sites of scientific interest on extraterrestrial bodies can provide insight into the likelihood of finding possible biosignatures in sites showing evidence of prebiotic chemistry. For the purposes of astrobiology, prebiotic chemistry can be defined as the initial building blocks that are capable of self-assembly into complex polymers that form the building blocks of primitive cellular life.

These initial building blocks can consist of monomeric nucleobases and racemic amino acids such as those found in some comets and meteorites Engel & Macko, 1997; Bada, et al., 2007; Martins, et al., 2008; Altwegg, et al., 2016; Elsila, et al., 2009; Engel & Macko, 1997; Bada, et al., 2007). Polycyclic aromatic hydrocarbons (PAHs) have also been

suggested as a component of prebiotic chemistry as they have been found to be ubiquitous throughout the cosmos. PAHs have been found in comets and meteorites, nebulae and surrounding a star. It has been shown that PAHs can be converted to more complex organics through hydrogenation, oxygenation and hydroxylation reactions to form amino acids and nucleotides (Shock & Schulte, 1990).

In a prebiotic environment the prebiotic ingredients necessary for the formation of primitive cell would need to be present within a natural reaction chamber that provided the environmental conditions necessary for formation. One location on Earth which is thought to be a likely location for the formation of a primitive cell is in seafloor hydrothermal vents. These vents double as a source of organic molecules necessary for life and as a reaction chamber capable of providing a reducing mineral surface that aids the restructuring of macromolecules.

Hydrothermal vents provide a convergence point for hydrothermal fluids and colder seawater that allows the establishment of a thermal gradient between the pores that provide reactive mineral surfaces (Westall, et al., 2013). Littoral swash environments have also been considered as an area capable of providing the necessary surface area for mineral attachment sites in addition to a continual resupply of reactants into the system via tidal movements (Westall, et al., 2013).

Reactive mineral surfaces are capable of providing a catalytic effect to initiate organic reactions that could be the starting point for the geochemical origins of life (Westall, et al., 2013). These adsorptive surfaces are capable of facilitating:

- Mineral-catalyzed organic synthesis including:

- Synthesis of amino acids from CO or CO_2,NH3 and H_2O and sulphides (Huber & Wachtershauser, 1997; Nakajima, et al., 1975; Cody, et al., 2001; Cody, 2004).

- Molecular Adsorption and Stabilization
  - Surface adsorption can aid the polymerization of amino acids on oxide and surface minerals (Lambert, 2008). Polymerization is aided by adsorption on a mineral surface but requires a drying period post-adsorption.
    - Adenine and Guanine have been shown to polymerize into structures on graphite and molybdenite (Sowerby, et al., 1998).
    - Tidal swash zones would allow for wetting and drying cycles as the tide ascends and descends the shoreline.
  - Adsorption characteristics are reliant upon environmental parameters such as pH, temperature, ionic strength and surface area (Hazen & Sverjensky, 2010).
- Chiral Molecular Adsorption
  - Life as we know it requires homochirality of its constituent parts (Engel & Macko, 1997).
    - Detection of a trend in the chirality of organics could provide evidence of the beginnings of the biogeochemical origins of life on an extraterrestrial body (Vandendriessche, et al., 2012; Meierhenrich, 2008; Bonner, 1991).
    - Deviations in the ratio of chirality between *L*- and *D*- entantiomers from a racemic mixture could provide evidence of surface adsorption and polymerization selecting for a particular chiral orientation.

    - Early Earth would have provided a multitude of surfaces capable of impacting chiral organisation in such a way that could result in a "self-replicating homochiral entity" (Hazen & Sverjensky, 2010).
- Mineral-induced Polymerization
    - Many macromolecules essential for life on Earth are long chain polymers built from individual monomer units. These monomer units include amino-acids, sugars and the nucleic acids which polymerize to form proteins, carbohydrates and DNA respectively (Hazen & Sverjensky, 2010).
    - Surface adsorption allows for the concentration and assembly of these polymers (Lahav, et al., 1978; Sowerby, et al., 1998).

It's generally agreed that any origin of life scenario would contain autocatalytic sets that allowed for the proliferation of more complex molecules that catalysed their own reaction. Similar reactions can be seen in life in the modern day, DNA being the most prominent example of a self-replicating system producing the compounds that can catalyse its own reactions, whilst RNA has been shown to be capable of self-sustaining replication in the absence of proteins (Lincoln & Joyce, 2009).

4.5.2 Carbon Sources

Extraterrestrial sources of Carbon from meteorites and comets are one theorised source of complex Carbon molecules. Studies of current comets and asteroids are capable of providing insight into the chemistry of the early solar system as the chemical make-up of these orbital bodies will remain unchanged since their creation (Mumma & Charnley, 2011; Fray, et al., 2016). They can also provide a way of determining the temperature and radiation environment of the early solar system. Those that brought lighter volatiles to

planets are theorised to have played a role in the formation of planetary atmospheres and oceans (Dello Russo, et al., 2006).

We know from recent studies of comets and asteroids that complex organic molecules are capable of originating independent of life. Notably the stardust mission in 1999, a sample return mission to the comet Wild 2 which captured particles from the coma of the comet as it passed around the sun. These samples were obtained by capturing them in aerogel before returning them to Earth. Analysis of the aerogel and embedded particles revealed the presence of amines and amino acids, most notably glycine (Elsila, et al., 2009). GC-MS and IRMS analysis revealed that the $\delta^{13}C$ for Glycine differed between the return sample and a terrestrial glycine standard, indicating that the sample was likely of extraterrestrial origin. By comparison, high concentrations of ε-amino-caproic acid (EACA) in the return sample were found to be of terrestrial origin as a result of contamination. This was already proposed by Elsila *et al* as EACA was found on both the comet-exposed and not-comet-exposed side of the foil. This was the first confirmation of the presence of amino acids in the cloud of a comet.

Whilst the discovery of cometary amino acids has been limited to the close encounter missions Stardust (Elsila, et al., 2009) and Rosetta/Philae (Altwegg, et al., 2016), spectroscopic analysis of comets has revealed a broad range of volatiles. A comprehensive review of cometary volatiles was published in 2011 by Mumma and Charnley covered the abundance of different volatiles across the collected surveys of more than 100 comets (Mumma & Charnley, 2011). Production of free radicals occurs within the cometary coma by photolysis or photoionization, chemical reactions between gases that make up the coma or destruction of refractory organics on dust grains. More than 20 primary species were found across the survey of comets, with varying abundances in comparison to H_2O content.

Several species included in the survey were only detected from comet Halle-Bopp, demonstrating that whilst comets may come from the same source their evolution can differ.

4.6 Martian analogues

Our understanding of potential habitable or formerly habitable sites on Mars is limited to our knowledge and experience of similar sites on Earth, and so in order to understand the current or former capacity for habitability on Mars we need to impose that knowledge onto these sites. Studies of Martian analogues provide an opportunity to study Mars-like environments with some limitations. The most notable limitation to Martian analogues on Earth is that the radiation environment here on Earth is substantially different to that on Mars. Mars is subject to extremes of galactic and solar ionizing radiation which sterilizes the Martian surface environment (Wadsworth & Cockell, 2017; Dartnell, et al., 2012) and contributes to the creation of the dusty Martian soil which covers the planet and often blows up into duststorms. This radiation environment is due to the lack of a strong enough magnetic field such as that which surrounds the Earth and repels radiation from the surface of the planet. Mars also lacks a significant atmosphere and ozone layer that results in radiation from the ultraviolet spectrum reaching the surface.

As mentioned above, Mars also has a tenuous atmosphere, too thin to allow liquid water to exist at the surface (Jakosky & Farmer, 1982). Whilst no ground environment on Earth experiences a similarly thin atmosphere, high-altitude locations can simulate the cool temperatures and solar heating of the surface that is normally observed in these locations. These high-altitude locations can match the dryness and low temperatures associated with

the Martian atmosphere, as geographical constraints on atmospheric humidity often cause these locations to resemble cold dry deserts such as the Chilean/Bolivian Altiplano.

Whether looking at past or present Mars conditions, a Mars analogue site can provide insight into the limiting factors that life experiences in a location such as available nutrition and food web complexity as well as the limits on the forms of life capable of finding its' niche there. If life did appear on Mars during a previous period in time it is expected that it would be confined to microorganisms, and so larger 'macroorganisms' are either surviving due to reliance on a wider habitat than what makes up the Mars analogue site, or the Martian analogue site may not be sufficiently fulfilling the requirements of a Martian analogue site. Even the most extreme of Martian analogue sites are likely to have microorganisms present and can demonstrate how life is able to survive in harsh conditions (Chicote, et al., 2005; Ordonez, et al., 2009).

When studying potential analogue sites on Earth, conditions such as this need to be taken into account when making comparisons to Mars, and often Martian analogue sites best represent how Mars could have been during the Noachian-Hesperian period over 3Gya ago.

The following sections will detail potential Martian analogue environments, and provide a case study relating to each of an example of an environment or novel organisms that have adapted to that environment.

4.6.1 Subterranean Martian analogues

For surface level exploration of Mars to have any success finding molecular signatures of life or past life it is necessary to consider where organic molecules would have the best chance of preservation. Due to the highly destructive radiation environment on Mars there are few easily accessed areas that could be considered for exploration. One of the most promising sites being considered currently is subterranean cave and lava-tube systems where any organic compounds could be protected from surface radiation for a long period of time (Léveillé & Datta, 2010).

On Earth it can be difficult to find a cave ecosystem that is sufficiently isolated from the surface environment that it is self-sustaining. To be considered self-sufficient a cave system must contain its own primary producers and not rely on carbon input originating from primary producers at the surface. For the purposes of Mars exploration it is important to consider self-sufficient cave ecosystems as thus far we have no evidence of surface life on Mars that could contribute to a cave ecosystem. Since we are limited to our own understanding of the forms and traces of life on Earth it is important to consider the traces such an ecosystem leaves and how we can distinguish between, as Boston *et al* puts it; "Differentiating abiotic imposters from biosignatures" (Boston, et al., 2001).

Whilst the chances of finding extant life on Mars are near zero, as the environment has been so inhospitable for so long, these subterranean habitats are an important consideration with regards to hypothesizing sites of scientific interest. Prioritising areas that could have once held life and at the same time are capable of preserving possible biosignatures from the Martian environment would maximise our chances of a positive discovery on a planet with a surface area of 144.8×10^6 Km^2.

4.6.1.1 Movile Cave

Movile cave in eastern Romania is one such location, within a few kilometers of the black sea near Mangalia and closed to the public to preserve its state of isolation. Movile cave was discovered in 1986 during a geological investigation of the area that broke into the cave. Since then the cave has been studied extensively as an example of an ecosystem sustained entirely by chemoautotrophic primary production, with both micro- and macroorganisms. (Kumaresan, et al., 2014) The Movile cave ecosystem has also been compared to deep-sea hydrothermal vent ecosystems that can also possess ecosystems driven by chemoautotrophs. (Chen, et al., 2009) The cave structure is notable for having distinct rooms that do not share an atmosphere but do share the water source. At least two air bells are found in the submerged level of the cave. (Rohwerder, et al., 2003; Kumaresan, et al., 2014)

Primary production in Movile cave is driven by predominantly aerobic sulfur oxidising bacteria that obtain their energy through the oxidation of hydrogen sulphide, which is found in high concentrations in the atmosphere and hydrothermal waters of the cave. (Chen, et al., 2009; Kumaresan, et al., 2014; Sarbu, et al., 1996) Microbiological activity is predominantly found in floating biofilms in the 'lake room' on the order of 1210 μW/g of calorimetric activity, compared to 43 ±20 μW/g in partially submerged rocks and 3.0 ±2.6 μW/g on rock surfaces 2 meters from the lake. (Rohwerder, et al., 2003) Anaerobic activity is also present in the cave at varying levels compared to the aerobic activity. In the surface biofilm anaerobic activity equates to 1% of the aerobic activity, whilst on the rocks 2 meters from the lake anaerobic activity equates 80% of the aerobic activity. (Rohwerder, et al., 2003)

The sulphur cycle within the cave is fed by hydrothermal waters that carry an influx of Hydrogen sulphide (0.2-0.3 mM) (as well as methane (0.02 mM) and ammonium(0.2-0.3 mM)) into the cave. Hydrogen sulphide is limited to the water/air interface and is not found in the upper levels of the cave. (Kumaresan, et al., 2014)

Whilst aerobic sulphur oxidation makes use of Oxygen as the electron acceptor, anaerobic oxidation makes use of other acceptors. In the case of Movile cave nitrate has the highest affinity as an electron acceptor after Oxygen. *Sulfuricurvum* spp. was detected in the 16S RNA clone library of a study published in 2009 by Chen *et al*. *Sulfuricurvum* is a facultatively anaerobic and microaerobic sulfur oxidiser that utilises nitrate as an electron acceptor. (Chen, et al., 2009; Kodama & Watanabe, 2004)

The airbells found in the submerged levels of the cave are notable for their differing atmospheric composition from the rest of the cave and the presence of microbial mats on the water surface. (Serban & Popa, 1992) In the lake room where the submerged level begins Oxygen makes up 19.763% of the composition of the atmosphere while CO_2 only makes up 0.516%.Composition changes slightly in Airbell one, with a 3x increase in CO_2 (O: 18.951%, CO_2: 1.743%). There's a dramatic change in composition in Airbell three, likely due to the presence of microbial mats on the surface of the water. (O: 10.321%, CO_2: 2.798%).

Notably, Methane is not present in either the lake room or airbell one, but makes up 1% of the composition of airbell three. Air bubbles in the water of the Air bells contains up to 13.5% methane which helps keep the microbial mats on the surface afloat. (Hutchens, et al., 2004)

4.6.2 Surface-level Martian analogues

For a site to be useful for the purpose of simulating a Martian environment it needs to meet several criteria in order to be deemed a suitable analogue. The most notable features of the Martian environment is that it is cold, dry (Martin-Torres, et al., 2015) and subject to extremes of radiation. The atmosphere of Mars is very thin and low in pressure and contributes to each of the parameters listed. (Seiff & Kirk, 1977) The surface is consistently well below freezing temperatures aside from short peak events in the Martian summer when temperatures on the surface are capable of peaking just above freezing (Musselwhite, et al., 2001). The atmospheric pressure at the surface of Mars is very close to the triple point of water, where water at the correct temperature will sublimate from a solid to gaseous phase without entering the liquid phase. Due to the thin atmosphere and the lack of an active core to provide a magnetic field the surface of Mars is subject to extremes of both ionizing radiation and ultraviolet radiation.

Surface level Martian analogues on Earth are limited to areas of the planet that see extremes of cold temperatures, thin atmosphere and dryness. There are a few locations on Earth that can satisfy all criteria but not to the same extent as Mars. In Antarctica the McMurdo Dry Valleys have been identified as a Martian analogue due to low temperatures, low humidity and low nutrient availability resulting in minimal-to-no life across much of the valleys (Goordial, et al., 2016).

By comparison, the Atacama Desert is in many ways the opposite of the McMurdo dry valleys. The Atacama is one of the hottest locations on Earth and its' higher altitude and low latitude result in higher doses of ultraviolet radiation to reach the surface. The Atacama Desert is the driest location on Earth but is still host to some life in certain areas

(Navarro-Gonzalez, et al., 2003). Notably after very rare rainfall events associated with El Nino the Atacama Desert can bloom with plant life which quickly dies off when the rain recedes (Dillion & Rundel, 1990; Orlando, et al., 2010).

A more recent Mars analogue has been higher up in the Andes of South America in the Altiplano that stretches from Peru down to the borders of Chile, Bolivia and Argentina. The Altiplano averages 3750m above sea level and in its' higher regions ultraviolet radiation levels are some of the highest in the world (Cabrol, et al., 2014). Like the Atacama and the Dry Valleys the Altiplano is one of the driest locations in the world with limited nutrient availability. There is evidence of bacteria near the surface of the soil and non-microbial life is limited to sparse lichens and small plants. Degradation rates at the surface due to ultraviolet radiation are too high for non-extremophiles.

4.6.2.1 The McMurdo Dry Valleys

The McMurdo dry valleys are located in Victoria Land by the Ross Sea. The Dry valleys are notable for their low humidity, comparable to desert conditions. These desert conditions are influenced by dry, dense air from the Trans-Atlantic Mountains falling into the valleys by the force of gravity, resulting in high strength, low humidity winds capable of desiccating the subsurface (Fountain, et al., 1999; Cameron, et al., 1970). These are the katabatic winds that are most often found at polar ice sheets. The Dry Valleys make up the largest ice free region of Antarctica, covering approximately 4800km^2, largely due to the Trans-Atlantic Mountains obstructing the Antarctic ice sheet. The Dry Valleys also receive a higher UV-B dosage compared to more tropical locations (Cary, et al., 2010).

The Dry valleys have been considered a Martian analogue site for several decades and continue to be used as an example of an environment that ranges from no biological activity to very little biological activity (Cameron, et al., 1970). Dry Valley soil and weathering of the soil surface has been identified as closely resembling that of Mars (Gibson, et al., 1983).

Average air temperatures at McMurdo station range between -14.8ºC to -30.0ºC depending on the time of year and location within the Dry Valleys area (Doran, et al., 2002). Temperatures at different sites within the area can vary by up to 30ºC depending on factors such as time of year, wind direction and wind speed. There is a great deal of variation in solar flux at the surface of the valleys due to topographical boundaries (Dana, et al., 1998). The McMurdo dry valleys are orientated East-to-West, with the most common winds coming from a westerly direction. Data on solar flux is partly constrained by the position of monitoring stations at their respective sites. Topographical constrains can similarly limit wind exposure depending on the direction, with nonsummer katabatic wind events being responsible for large changes in air temperature as they descend into the valleys, ignoring topographical restraints (Doran, et al., 2002; Nylen & Fountain, 2004). A strong correlation exists between distance from the coast and increases in temperature in-shore that result from winds warming as they progress up the valleys.

The majority of atmospheric water vapour in the Antarctic air comes from winds blowing from the southern oceans. Precipitation in Antarctica is almost always in a solid form and so quantification of precipitation is made difficult due to interactions with the wind affecting snow gauges (Bull, 1971). Instead measurements of snowfall are done via accumulation within the Dry Valleys, as minimal ablation occurs within. Snowfall is

variable but not infrequent, whilst rarer rainfall events have been recorded on coastal regions of Antarctica (Keys, 1980).

Water chemistry in the McMurdo Dry Valleys has been likened to that of Martian soil from the presence of perchlorate in interstitial brines beneath ice covering Antarctic lakes (Kounaves, et al., 2010; Kenig, et al., 2016; Navarro-González, et al., 2010). Reactions with perchlorate in Martian soils as a result of analysis by GC-MS equipped on Martian landers have obfuscated data collection due to its high potential for oxidization (Wadsworth & Cockell, 2017). Detection of chloromethane and dichloromethane by the Viking landers was revealed to be a miss-result due to reactions between Martian perchlorate and soil organics during GC-MS analyses (Navarro-González, et al., 2010; Pacheco, 2012) and prompted research into alternative methods for chloromethane formation (Pacheco, 2012).

Lake Vida is located in the northernmost valley of the McMurdo Dry Valleys and appears to be completely frozen at the surface. Beneath the surface of the ice are interstitial cryogenic anoxic brines that support an active ecosystem (Cawley, et al., 2016; Murray, et al., 2012), analogous to the brines observed on Mars in recurring slope lineae (Kenig, et al., 2016; Murray, et al., 2012; Mellon & Philips, 2001; McEwen, et al., 2011; Toner & Catling, 2016; Forte, et al., 2016). Brine was recorded as being -13.4ºC with a pH of 6.2 (Murray, et al., 2012). Thirty-two unique sequences associated with 8 bacterial phyla were revealed including *Proteobacteria, Lentisphaera, Firmicutes, Spirochaeta, Bacteroidetesm Verrucomicrobia,* TM7, and *Actinobacteria* (Murray, et al., 2012). Bacterial assemblages were found to be distinct from bacteria in other saline lakes in the Dry Valley's area. The closest similarities were found in the brine of the Blood Falls Glacial outflow ~38km from Lake Vida (Murray, et al., 2012). High volumes of electron acceptors such as NO_3^- prevent

depletion of organic reserves that would otherwise lead to redox reactions of sulfate reduction and methanogenesis (Murray, et al., 2012). Lake Vida brines were found to be seven times the salinity of seawater in addition to high concentrations of dissolved organic matter (Cawley, et al., 2016). The discovery of this ecosystem was notable for being an example of an ecosystem isolated for a millennial scale time period (Murray, et al., 2012).

Pyrolysis of samples containing perchlorate compounds leads to oxidation and oxychlorination of organic matter which can obfuscate experimental results and result in an incomplete result set (Millan, et al., 2016; Sephton, et al., 2014). High carbon concentrations (48.2±9.7 $mmol.L^{-1}$) in the Antarctic brines (Cawley, et al., 2016) contribute to a reduction in artefacts during GC-MS analysis due to higher Carbon/Oxychlorine ratios (Kenig, et al., 2016). Similarly on Mars the artefacts observed by the Viking landers could be mitigated by introduction of reduced carbon to artificially raise the Carbon/Oxychlorine ratios for pyrolysis analyses (Kenig, et al., 2016).

The soil biology of the McMurdo Dry Valleys has been studied extensively due to the low levels of biological activity that have been found. Early studies were limited to cultivation and microscopy and reported differences in the extent of bacterial colonization in different soil samples (Boyd & Boyd, 1962; Flint & Stout, 1960; Siebert & Hirsch, 1988). Thanks to developments in molecular microbial ecology later studies have been able to more accurately study the differences in colonization between different Antarctic sample sites (Arenz & Blanchette, 2011; Cary, et al., 2010) as well as studies on native invertebrates (Wharon & Brown, 1989; Nkem, et al., 2006; Freckman & Virginia, 1998). Prokaryotic life found in Dry Valley soils often fell into a so-called “unculturable” class of prokaryotes that would not show up in earlier culture-based experiments (Cary, et al., 2010; Lipson & Schmidt, 2004).

Recent studies of Dry Valley soils have shown a surprising diversity of microorganisms given the extreme niche that these microorganisms fill, but are still of low diversity according to calculated diversity indices (Smith, et al., 2006). Identified microbial taxa possess traits associated with desiccation resistance, halotolerance and can be psychrophilic or psychrotolerant (Cary, et al., 2010). This is in contrast with microbial communities nearer to the Antarctic coast which feature a greater microbial diversity and colonization of plants owing to a warmer and wetter environment due to the influencing factors of the ocean (Cary, et al., 2010).

Low organic concentrations within the soil (0.01-0.5mg $C/g/soil^{-1}$) reflect the low abundance of life present (Burkins, et al., 2001). The low volume of activity results in low Carbon fixation rates that have been estimated at 1g C m^2/yr (Friedmann, et al., 1993). Matsumoto *et al* estimated that the majority is *"probably derived from the erosion of the Beacon Supergroup and biological debris in the past containing vascular plant waxes as well as wind-transported cyanobacterial mats, rather than from living organisms."*(Matsumoto, et al., 1990).

In the role of a Martian analogue, the sparse distribution of life within the soils of the Dry Valleys demonstrates the potential for survival within dry, cold and nutrient poor soils.

4.6.3 The Atacama Desert and the South American Altiplano

The Atacama Desert has been considered a Martian analogue for several years, with the first studies using the barren landscape to test and compare results from Mars lander missions such as Viking (Navarro-Gonzalez, et al., 2003). The most notable finding from

that initial study was that if Viking had landed in the Atacama Desert it would have similarly found no signs of life. The Atacama Desert is a uniquely barren location on Earth, located in the Chilean Andes it is estimated to cover 105,000 km^2 and is recorded as the driest location on Earth, receiving on average 15mm of rainfall across a full year. During the austral winter rainfall drops to 1mm or less with the majority of rainfall coming in the austral summer. Total rainfall is influenced by the El Nino oscillations that occur periodically in the Southern Pacific Ocean. During El Nino years rainfall increases enough to cause floral blooms in the Atacama Desert.

Figure 4.2: The Atacama Desert in May 2015. Dried out and cracked mud can be seen from rainfall two months prior, in which a record volume of rain fell in a single day.

There are several geographical influences that are responsible for the conditions in the Atacama. The first of these is that it is located on what is known as the 'horse latitudes', where the atmosphere is dominated by the sinking air of the Hadley cell. Hadley cell function is based on hot air rising from the equator, cooling in higher altitudes and becoming drier before descending back to ground level in the direction of the poles at 30º

latitude. As a result this dry air brings no rain to the area that it descends on. (Houston & Hartley, 2003)

Secondly, the Amazon rainforest receives on average over 2000mm of rainfall every year and is separated from the Atacama by the Andes mountain range. The Andes act as a climate control, inhibiting the transport of water to the western edge of the South American continent. As the wet air from the Amazon moves west and rises up the Andes but with the increase in altitude it cools and begins to precipitate. As a result the air dries out and no moisture is carried over the range. In this way the Andes act as a rain shadow (Houston & Hartley, 2003). Finally the western coast of South America is affected by the Humboldt Current, which is a cold current that cools the air above, sapping it of moisture. Increased westward airflow throughout the air column will suppress eastward flow of moist air from the Amazon (Vuille, 1999).

So the climate of the Atacama is primarily affected by three influences that collectively prevent moisture from reaching the Atacama and thus causing its desert conditions. Air from both east and west is cold and dry and it is located at the 30th parallel which is ideal for desert conditions. The climate disruption associated with the El Nino phenomenon will nullify the effects of the Humboldt Current, resulting in warmer waters that don't dry out the surrounding air, thus allowing warm wet air to reach the Atacama. (Australian Government, 2005)

In addition to being Dry, the Atacama is subject to greater extremes of UV radiation. This is influenced by several factors, one of which is the high altitude that the Atacama is located at. A study in the region charting the differences in the solar spectrum at various altitudes found there was up to a 20% increase in UV irradiance from sea level up to

5100m (Cordero, et al., 2016). In addition, irradiance at visible wavelengths was increased by 6% and in the infrared range by 27%. Lack of water vapour in the air column above, and a low cloud volume results in a low cloud albedo effect which contributes to the higher than average UV (Cordero, et al., 2016). Ozone is also reduced in the region, and the highest UV values recorded on Earth have been recorded in the Altiplano surrounding the Atacama (Cabrol, et al., 2014).

The Altiplano and Atacama are also subject to dust storms that play an important role in soil development, transport of important elements and alterations to radiative balance which can impact on precipitation (Gaiero, et al., 2013). In the past 20 years it's been found that dust loading of the atmosphere will also reduce the likelihood of precipitation by reducing the potential for water drop coalescence (Rosenfield, et al., 2001) whilst it was previously thought that the opposite was the case.

Mass flooding events are rare but not unheard of in the Atacama and can be responsible for a high volume of erosion and sediment transport. In such a dry locale the ground surface can have a lower permeability than a location that is more frequently inundated, and the low permeability prevents water absorption in to the ground instead causing it to run off the surface, eventually forming a flood. Whilst these floods can be detrimental to the local populace, they can cause a bloom of plant life in the Atacama Desert. This is a phenomenon specific to the Atacama Desert, where dormant seeds and bulbs are germinated by the influx of water (Vidiella, et al., 1999) , causing the environment to resemble a more temperate one. These blooms provide evidence of species specifically adapted to survival in a hyper-arid environment by entering a dormant stage until the presence of water to initiate germination. Despite the presence of dormant plant life,

sampling of soils in the Atacama still returns only trace levels of organic material, and decomposition of material via inorganic processes (Navarro-Gonzalez, et al., 2003).

Figure 4.3: Cracked mud from rainfall 2 months prior. (May 2015)

Above the Atacama Desert, in the heights of the Sairecabur volcanic chain, conditions are similar to those of the Atacama but at even greater extremes. Compared to the Atacama (2400m), Sairecabur itself is 2000m higher at its base and reaches an altitude of 5971m at its peak. The reduction in atmospheric density associated with the rise in Altitude results in increased UV radiation, an expanded thermal gradient from surface to subsurface, and a greater variation in soil humidity from the surface down.

Air temperature can be close to zero with increasing altitude but superheating of the soil surface can leave it hot to the touch, and uncovering this soil will rapidly heat the surface. Temperature decreases quickly with depth as the heat from the sun struggles to penetrate the upper layers of soil. At the highest elevation there is a permafrost layer as deep as 7cm (Porteous, 2018). This permafrost layer moves in a diurnal cycle that brings the permafrost layer closer to the surface at night, demonstrating that heat from the sun still determines the temperature of the subsurface. Exploration of Mars over the past decade has revealed a similar soil/permafrost boundary to those in the Altiplano, and with similar diurnal cycles

(Mellon, et al., 2009; Paige, 1992). This opens up high-altitude Altiplano sites as possible Martian analogues for studying life at the ice/water boundary layer, which has been cited as an area of interest to astrobiology for future Mars missions (de Silva, et al., 2013; Phoenix, 2014). Intense solar irradiation of the surface during the day followed by freezing overnight leads to an unstable water/ice boundary that provides transient liquid water below the surface on a diurnal cycle each day that is capable of sublimating into the atmosphere (Bryson, et al., 2008) or possibly as a source that produces recurring slope lineae (McEwen, et al., 2011). It has been hypothesized that the ice-water interface in these soils could be capable of being a habitable niche for life.

4.6.4 Hydrothermal Martian Analogues

One of the most favoured sites for origin of life studies is in oceanic hydrothermal vents. Hydrothermal vents can serve as a mixing chamber for simple organics that would polymerize and react to form primitive simple cell units by providing a large surface area for reactive mineral surfaces (Hazen & Sverjensky, 2010), as well as means of hosting a thermal gradient. Hydrothermal vents are also capable of providing a source of rare earth minerals that are vacated from deep aquifers (German, et al., 1990), and could provide deeper insight into crustal composition.

Due to the innate fossilization processes in and around hydrothermal vents, they provide an opportunity to detect different forms of biosignatures. In their paper "Fossilization processes in siliceous thermal springs: trends in preservation along thermal gradients", submitted for Ciba Foundation Symposium 202, SL Cady *et al* discuss the three main categories of microbial biosignatures; Chemical biomarkers, microfossils and microbially influenced sedimentary structures (Cady, et al., 2003).

On Earth microfossil identification can be performed under optical microscopes or electron microscopy which is capable of highlighting the encrustation of cells covered in silica colloids. Cell sheath and contents can be preserved within the silica encrustation and distinguished through electron microscopy (Phoenix, et al., 2006). Fossilized microbial filaments can also be identified as part of the silica matrix that makes up silica sinter that has precipitated around these filaments (Berelson, et al., 2011).

Stromatolites are sedimentary structures that form in the presence of bacteria and are considered to be a biomarker. Archean stromatolites have been dated on Earth from 3.7Gya from the Isua Supracrustal Belt (ISB) in southwest Greenland (Nutman, et al., 2016). The ISB stromatolites represent the earliest fossil evidence of life. Analysis of the stromatolite revealed that the microbes within were likely capable of CO_2 sequestration to compensate for the reduced output of the dimmer young Sun and evidence of formation in a shallow marine environment demonstrates that stromatolite identification is a means of assessing past climate and environment as well as the presence of life (Nutman, et al., 2016).

Chemical biomarkers are some of the most commonly used biomarkers for the purposes of identification and past climate analysis on Earth. Thus far the lack of fossil or morphological biomarkers has limited research into any possible biological history on Mars to the presence of chemical signatures but analysis of chemical signatures has brought about a greater understanding of the geological and climate history on Mars.

4.6.4.1 Deep-sea hydrothermal vents

Problems exist with submarine hydrothermal sites, notably that the vent effluent can reach temperatures that limit hydrolytic stability. Temperatures in excess of 250ºC are capable of causing the decomposition of chemical bonds via hydrolysis reactions, causing the breakdown of essential chemical constituents including RNA, DNA and essential amino acids (Miller & Bada, 1988; White, 1984).

Despite this, it has been demonstrated that thermophilic bacteria are capable of survival and growth at these temperatures. In 1983 Baross and Deming (Baross & Deming, 1983) sampled a pair of microbial organisms from the vent plume of a black smoker hydrothermal vent. The vent effluent was recorded at 306ºC. These bacteria were then cultured at 250ºC in a growth chamber, demonstrating that bacteria could grow in the presence of a hot hydrothermal plume. It was also deemed likely that the chemistry of a vent flume could be influenced by the presence of bacteria. However, a year later these results were in debate. Trent, Chastain & Yayanos (Trent, et al., 1984) asserted that the results recorded by Baross and Deming were more likely to be as a result of contamination and/or artefacts in the sample medium. They repeated the study, without the sample bacteria, in order to demonstrate that the results recorded by Baross and Deming could have been identified as artefacts had they performed a full control experiment alongside the primary experiment. From their 'control' experiment Trent, Chastain & Yayanos observed similar results in protein assays that aligned with the results for Baross and Deming. However, in the same issue, Baross and Deming replied that the bacteria observed in the growth at 250ºC would have reappeared in the growth at 300ºC sample if it were a media contaminant (Baross & Deming, 1983).

In the three decades since, research on submarine hydrothermal ecosystems has expanded as they have been identified as an ideal site for origin of life studies, and black smokers have been identified as a source of rare earth elements that could possibly be 'mined' as a natural resource. Microbial life in these ecosystems is an example of a self-sustaining ecosystem, and novel organisms have arisen there with consequences for astrobiology and origin of life research.

One notable example was discovered in 2005 by Beatty *et al*. (Beatty, et al., 2005) of an obligately photosynthetic organism found in the vent plume of a deep-sea black smoker in the East Pacific Rise. The bacterium sampled was identified as an anaerobic green sulfur bacteria that oxidised sulfur compounds to reduce CO_2, and in addition was capable of photosynthesis at low light intensity. The photosynthetic light source was determined to be geothermal in origin as the hydrothermal vent is too deep in the ocean for the suns light to penetrate.

Novel organisms like this are a reminder that life will likely not materialize in the form that may be expected if it were to be discovered on a foreign body. Beatty *et al* noted that the green sulfur bacteria was unlikely to have descended from a line of photosynthetic organisms as subsurface geothermal vents such as these geothermal vents are short-lived on a geological timescale. This expands on potential sources of energy for life in energy-poor environments by including the possibility of photosynthetic-like reactions in unilluminated environments.

4.6.4.2 Terrestrial hydrothermal analogues

Whilst submarine hydrothermal sites are a relatively new discovery, terrestrial hydrothermal sites and their ecology have been well studied for several centuries now (Jaggar, 1898; Tilden, 1897). Terrestrial hydrothermal sites differ from their submarine equivalents by being above water, and thus water evacuated from the hydrothermal vent is further from the heat source and is consequently cooler. At the point of evacuation water transitions from the high pressure system of the vent to atmospheric pressure of the ejection point. At certain high altitude hydrothermal sites such as El Tatio in the Andes this causes water at temperatures lower than 100ºC to boil and evaporate.

Terrestrial sites allow for a closer representation of the dormant hydrothermal sites that exist on Mars. Hydrothermal sites are constantly in a state of flux, with old geysers drying out as new geysers form. This is most commonly seen in regions that make use of geothermal power as an energy source. Sites such as the Rotorua geothermal field in New Zealand have previously experienced drops in water output of up to 50% due to geothermal boreholes (Cody & Lumb, 1992). Following the closing of boreholes in the region, activity returned to the region, with one geyser re-erupting after a 34 year dormant period (Scott, et al., 2016).

El Tatio is a geothermal field located at 4320m in the Chilean Andes, causing it to be subject to some of the same environmental parameters that analogue sites such as Sairecabur experience. Water source varies across the field with the majority being chloride waters, along with some chloride-bicarbonate and sulphate-bicarbonate sources (Cortecci, et al., 2005). Due to lower air pressure, most hot springs in the area eject water close to the local atmospheric boiling point of 86ºC. Lower air pressure, low air humidity

and low-latitude result in greater incidence of UV at the surface. This leads to greater surface degradation rates than those at sea level.

Increased UV at the surface at El Tatio makes it a preferable Martian analogue to other hydrothermal sites on Earth. El Tatio provides an opportunity to study the differences in microbial community as a result of increased UV radiation, with particular respect to studying the UV attenuating effects of silica sinter, of which most of the geysers present at El Tatio consist of. Silica sinter is capable of attenuating UV at wafer-thin thicknesses. Phoenix *et al* (Phoenix, et al., 2006) recorded UV absorbance's of 21.2% (±8.7%) of UV-A, 29% (10.8%) of UV-B and 66.3% (11%) of UV-C from a 2μm thickness wafer, demonstrating that silica sinter is a potent attenuator of UV. Photosynthetically active radiation was subject to only a 13.3% (5.2%) absorbance, making silica sinter a viable protection from UV for photosynthetic life. The silicification process is abiotic, but the bacterial filaments and cells act as focal points for silica precipitation, which leads to the encrustation of bacteria within the silica. As a result, evidence of the presence of microbes can be seen in silica sinters via SEM.

Scattered around the El Tatio geothermal field are geysers with minimal activity. These geysers either emanate steam through the remnants of their vent (often collapsed in) or are dry and exhibit no activity at all. This brings these vents to be a closer analogue to the sites the Mars Exploration Rover Spirit reported in 2008 (Squyres, et al., 2008). As part of a currently active hydrothermal field, the content of these dry geysers can be directly compared to those that are still active, allowing an opportunity to compare recent and old microbial communities to observe differences that could have resulted from lack of geothermal waters and the minerals they bring, and a static supply of silica sinter. On

active geysers, continual precipitation of silica leads to continual growth of bacterial filaments upwards towards the light source.

Silicification provides the means to improve the preservation potential of any organic matter that becomes encrusted in silica, providing a means to entrap living organisms in a fossilization-like manner, as well as trapping organic material within the silica matrix and providing a means to preserve that content from exterior pressures. This fossilization process could provide another means of determining the presence of life from Martian samples. On Earth the fossilization process leaves visual evidence of the presence of microbes, without necessarily leaving direct evidence of the microbes themselves. As the silicification process is an encrustation process rather than a permineralization process the structure of silicified bacterial matrices is maintained as part of the makeup of the internal structure of the sinter (Phoenix, et al., 2000; Phoenix, et al., 2006; Konhauser, et al., 2003).

On Earth this is an entirely abiotic process, with the bacterial filaments acting only as a focusing point for the coalescence of silica colloids (Konhauser, et al., 2003). Cell surface ligands can adsorb silica from solution and reduce the activation energy for nucleation, which results in further coalescence of silica colloids making it an abiotic and autocatalytic process. Silicification occurs rapidly in hot-springs due to the high volume of silica in solution (often 100-400ppm with the saturation point increasing with temperature (White, et al., 1956)) and as noted by Phoenix et al (2003) surface ligands have only a minor effect on silicification, which in higher concentrations of silica becomes negligible.

These sinters often form nodular or digitate structures due to the influence of the bacteria acting as a focusing point for silica precipitation. If these structures are to be considered as potential biosignatures it would need to be established that they form as microstromatolites

due to the presence of bacteria rather than Aeolian erosion. Stromatolites are often considered to be a biosignature (Allwood, et al., 2006; Berelson, et al., 2011) .

Studies of sinters most often make use of X-Ray Diffraction (XRD) as a means of determining the composition and crystallinity of the sinter, with the majority of these studies only noting the presence of silicified bacteria as a side-note (Herdianita, et al., 2000). Studies focusing on the silicified bacteria that are located within and throughout some sinters have often attempted to characterize how the presence of bacteria relates to the process of silica precipitation and bacteria's influence as an aggregation point for further silica precipitation (Pepe-Ranney, et al., 2012; Yee, et al., 2003; Benning, et al., 2005; Phoenix , et al., 2003), with some additional studies that have focused on how silicification improves survivability in UV intense environments (Phoenix, et al., 2006; Phoenix, et al., 2001).

Some additional biomarker focused studies have been conducted on sinters as a means of determining the diversity of possible biomarkers within samples. A pair of preliminary studies performed by D. Carrizo, L. Sánchez-Garcia, V. Parro, S.L. Cady and N.A, Cabrol, and with a contribution from N.W. Hinman, with data shown at The Lunar and Planetary Science Conference 2018 and the European Planetary Science Congress 2017, have characterized biomarkers present in a set of three sinter samples taken from El Tatio (Carrizo, et al., 2018; Carrizo, et al., 2017). When comparing older and younger sinters, their findings indicated a greater volume of larger chain *n*-alkanes, with a majority of chain lengths between C11 and C33 in the oldest samples whilst the younger sinters contained *n*-alkanes between C11 and C30. A mix of *n*-carboxylic acids ranging between *n*-C6 and *n*-C30 were present in both samples however, shorter chained carboxylic acids were also present in the older sinter sample. Notably there was a large increase in the total weight of

the C16 and C18 carboxylic acids in the younger sample compared to the older sample (Carrizo, et al., 2017). They also reported differences between water-based, steam-based and dry sinters (Carrizo, et al., 2018). Unfortunately neither report provided further details of the samples used.

Pancost *et al* reported on the presence and diversity of lipids found within sinters taken from the Taupo Volcanic Zone, New Zealand (Pancost, et al., 2005). The sinter samples studied contained unidentifiable microbial remains, however, Pancost *et al* report on the presence of free fatty acids, 1,2-diacylglycerophospholipids, 1,2-di-O-alkylglycerols,glycerol dialkylglycerol tetraethers and 1-O-alkylglycerols. The presence of these fatty acids confirmed the presence of archaea and bacteria in the sinter samples analysed, thus identifying that identification of biomarkers through GC-MS is a viable method for confirmation of microbial presence despite the potential destruction of cell structure(s) due to the silicification process (Jones, et al., 1996).

4.7 Background to Raman Spectroscopy methodology

4.7.1 A General Overview of Raman Spectroscopy

Raman spectroscopy is a laser-based determinative method for non-destructive analyses of solid liquid and gaseous samples. Analysis using Raman is most often qualitative however, quantitative Raman spectroscopy is an available though little-used method due to decreased confidence in obtained results (Jawhari, et al., 1990).

The Raman scattering effect that forms the basis of Raman spectroscopy was discovered in 1928 by Sir Chandrasekhara Venkata Raman and Sir Kariamanickam Srinivasa Krishnan at the University of Calcutta (Raman & Krishnan, 1928; Raman, 1928). Raman scattering is best described as one of several secondary radiation given off by a sample illuminated by a known monochromatic radiation. Of the scattered secondary radiation there is Raleigh scattering that matches the frequency of the monochromatic laser source and is on the order of 10^{-8} weaker than the monochromatic source; and Raman scattering, a weaker radiation which is emitted in other frequencies approximately 10^{-3} weaker than the Raleigh scattering (Hendra & Stratton, 1969).

Raman spectra take the form of an *x*/*y* graph of the Raman shift (represented as a wavelength frequency) of scattered radiation vs the intensity of the scattered radiation. Raman shift represents the difference in energy between incident photons and scattered photons after excitation of target atoms. Raman shift is calculated as a function of the energy difference of the photons emitted from the laser and the photons that re-enter the detector. Loss or absorption of energy from the photon by the atoms present in the analysed molecule results in alteration of the scattered photon. The photon can either fail to excite or absorb energy from the target, excite the target (increase in energy in target atoms, scattered photon loses energy), or absorb energy from the target (atom loses energy,

scattered photon gains energy). These are termed Rayleigh scattering, Stokes scattering and anti-Stokes scattering respectively.

The baseline energy of the emitted photons establishes the background or baseline of a given Raman spectra. This is termed Rayleigh scattering, where the energy of the photon out is equal to the energy of the photon detected, as the emitted photon failed to cause any excitation of the component atoms of the molecule analysed. Rayleigh scattering is reflected on a Raman spectra at a Raman shift of $0cm^{-1}$, signifying no change in wavelength between emitted photons and scattered photons.

Stokes and anti-Stokes scattering is the result of changes to the energy level of the scattered photons (loss of energy and increase in energy respectively). The energy of the incident photons does not impact the Raman scattering that results from the Raman effect, but the absolute intensity of Raman peaks can be altered by increasing the quantity of photons over a target area. In practice this means that whilst laser parameters can be unchanged, the use of higher magnification optics will focus the incident beam of photons, in effect concentrating them on a smaller surface area. Raman scattering is a weak scattering phenomena and so increasing the concentration of photons will result in an increase in the frequency of occurrence of the Raman effect, thus increasing intensity.

Stokes radiation is reflected on a Raman spectra by a Raman shift $>0cm^{-1}$. Analysis of Raman spectra is most commonly an analysis of Stokes radiation. Anti-Stokes radiation is reflected by a Raman shift $<0cm^{-1}$. Anti-Stokes analysis can be performed through an alternative technique to Raman known as coherent anti-Stokes Raman spectroscopy which commonly utilises two separate laser sources and is capable of more coherent spectra than Stokes Raman spectroscopy (Tolles, et al., 1977).

For this reason Raman measurements are deemed to be consistent across a variety of laser wavelengths, the most common of which are 532nm, 785nm and 1064nm wavelength lasers. In general higher wavelength lasers will result in less efficient excitation and require

longer scan times than lower wavelength lasers, whilst also resulting in greater heat absorption on the sample with a reduction in fluorescence.

Fluorescence can obscure Raman spectra data as the fluorescence is a much stronger signal compared to that of Raman which is comparatively weak, particularly when multiple Raman signals are present in mineral samples such as those analysed in this chapter (Verkaaik, et al., 2015). Fluorescence arises from constant excitation of the target atoms through absorption of the incident light from the laser, and the emittance of photons of a greater energy level during de-excitation when the atoms relax to a lower energy level. The photons released during this process are related to a specific frequency different from the excitation frequency, which is why the appearance of fluorescence takes the form of a curve across the Raman spectra due to how Raman shift is calculated (see above).

Raman's use as a method for astrobiological investigations is relatively new, with the only two missions currently planned to utilize Raman as part of their science payload (Exomars & Mars 2020). Due to this it is important to understand the expected response from Raman spectroscopy to the sorts of substrates it would be expected to analyse on Mars and other potential sites of interest.

Peak data can be obscured by other peak data if particularly weak relative to surrounding peaks, sometimes reflected as a shoulder to a taller peak. Fluorescence is the most notable impairment to the recording of Raman spectra. Fluorescence is most commonly reflected as an upward or downward trend in the recorded spectra, often with no identifiable peaks. The fluorescence signal is significantly stronger than that of the Raman signal and peak data can be at best impaired and at worst completely obscured by the recorded fluorescence. Throughout the history of the use of Raman spectroscopy as an analytic tool, fluorescence has been the biggest obstacle to overcome for sample analysis.

All Raman analysis was performed using a Renishaw inVia Reflex Raman Spectrometer, equipped with 514nm and 785nm lasers. Sample preparation was dependent on the sample

form, with most samples being lightly polished, washed in deionised water and fixed to a mount after cutting to ensure a flat plain for analysis. Samples were analysed through a choice of x20, x50, x50 L (Long Working Distance) and x100 magnification lenses. Spot analyses of samples were performed with the x50 L and x100 lenses, whilst the x20 was used to produce maps of larger sample areas.

4.7.2 WiRE 4.2 setup, processing & methods of analysis

During the course of Raman experiments, Renishaw's WiRE 4.2 (Windows-based Raman Environment) software was used to control all sample acquisition and analysis. Software control of the spectrometer allowed for adjustments to the Raman range obtained, specific control over laser acquisition, timing control if multiple acquisitions were being utilised, some post-processing options for better peak identification and analysis options for post-sample acquisition.

Laser control allowed for detection on a fixed broad Raman spectrum that provided instantaneous spectra (dependent on the length laser exposure) determined by a fixed centre point of the Raman shift set by the user, with highest and lowest wavelengths set by the software. Alternatively an extended Raman shift could be set, however, this requires a minimum of 10 seconds of exposure to the laser, and the Raman shift is drawn in over a period of time rather than instantaneously. The benefit of an extended scan is that it allows for much wider Raman shift to be analysed in a single spectrum. The software controls the choice of grating and detector for the Raman signal depending on the choice of laser.

Raman spectra acquisitions were controlled through laser exposure times, power and total number of accumulations per spectra acquisition (accumulations are defined as the number of *repeat measurements* made to form a spectrum, whilst acquisitions are defined as the number of *spectra* obtained. A scan can be set up to perform 20 accumulations on the

sample, with 5 acquisitions total, resulting in 5 spectra composed of 20 scans (100 total accumulations)).

4.7.2.1 Scan Types Utilized

During the course of experimental work done, a multitude of scan types and analysis was utilised.

Most analysis was performed via a spot analysis on the sample, with the spot diameter determined by the lens used. Higher magnification lenses result in a smaller viewing area, and as such the laser passing through will cover a smaller area. A result of this is that lower magnification lenses are less suitable for Raman analyses than higher magnification lenses, as precision on a particular sample is important for minimizing signal noise and maximizing the production of measured Raman radiation. For wider sample analyses map, line and streamline scans can be performed. A map analysis will scan an area via set grid points, and on those grid points a spot scan will occur (with the same controls for each spot analysis as discussed in the previous paragraph). A map of the sample according to particular peaks on the Raman shift can be produced to show how particular peaks fluctuate across a sample. A line scan operates on the same principle but there is only one plane of coordinates to consider.

Streamline map scans will produce map data like a map scan, however, they utilize a laser focused as a line on the sample rather than multiple spot scans. This minimizes sample exposure to the laser, and minimizes the risk of sample damage as a result. It also operates much faster than that of a map scan since multiple points are scanned at once rather than individually, although spreading the laser over a greater surface area results in weaker Raman scattering.

Whilst Raman is a non-destructive process, samples can be burned by a combination of excessive laser exposure and intensity. Raman signals will be stronger with increased intensity of the Raman laser however, the samples studied in this thesis varied in their susceptibility to burning and so all samples used different laser configurations. This is not expected to affect the spectra obtained however, as most spectra obtained were obtainable under less intense conditions than the maximum a particular sample could sustain.

In addition to the number of acquisitions and accumulations that could be obtained, the software also allowed for control of the time between acquisitions as well as control over bleaching time for samples that experienced a lot of fluourescence and would benefit from bleaching. Unfortunately this option was of limited use for the samples analysed in this thesis.

After a sample had been obtained there were several post-processing options available to clean up data and/or make peak identification easier. Baseline subtraction was the main post-processing technique used. Most Raman spectra form with a curve or slant as the data is recorded, and depending on the laser the slant can be positive or negative on the produced graph. Baseline subtraction flattens the graph to a horizontal plane by calculating the curve or slant and determining that to be the ‘baseline’ from which Raman peaks originate.

Smoothing of data could clean up very rough spectra (typically from a weak Raman signal producing low count data) to produce a smoother spectra line. Care has to be taken that the smoothing factor is not so large that smaller peak data is smoothed out. Data can also be normalised for further analysis.

Cosmic ray interference can result in false peak data in a spectrum but they normally manifest as very tall, very slim peaks that stand out from the rest of the spectrum. These spikes can either be zapped individually or a cosmic-ray removal tool can be used to identify and isolate cosmic rays based on parameters for base width and peak height.

Analysis of Raman spectra can be both simple and more complex. Simple identification of peak data can be performed using a library search built into the WiRE software as well as a peak identification tool, however, the former is confined to a library dedicated to the identification of minerals and the latter occasionally misses peaks as they fall outside of the parameters for peak identification. Peaks can however, be identified individually using the same tool.

More complex analysis of spectra can be done via a component analysis (DCLS(Direct Component Least Squares analysis)) if a known spectrum is already available. DCLS analysis allows for a comparison between two or more spectra to determine differences in peak data via differences in pattern. DCLS data is output visually via a comparison based on percentage match between the sample data and the component data. DCLS is not influenced by the intensity of the compared spectra as data is normally normalized prior, however, differences in spectrum intensity can result in missing peak data.

If a map or line acquisition is used to collect data then multiple spectra are produced as part of an individual data file. The spectra that make up this dataset can be averaged to produce a single spectrum that represents the whole. Of course this is unlikely to result in a spectrum that is representative of the whole dataset as more intense spectra will be overemphasised relative to weaker spectra. This can be circumvented by normalizing a dataset prior to averaging so that the new spectrum is an average of the *shape* of the collected dataset rather than the intensity of that dataset. This had some interesting

applications when analysing weaker signals or highly fluorescent signals where data were less clear.

For some samples a lower intensity laser was used for acquisitions of data in an area off and to the side of the sample itself (by several μm). The collected data appeared on the initial collection to be nothing more than an interference signal (very low data counts, very rough line with no identifiable peaks). However by normalizing this dataset and averaging the collected dataset so that an average of the shape was obtained rather than an average based on the count values, a near-complete spectrum of a known spectrum was obtained despite what initially appeared to be rubbish data. Subtle differences in spectra shape reflected the spectra of the nearby sample. This technique was of limited use however, and was not always repeatable between different samples. It was also not always capable of producing a better signal than direct illumination of a sample, with fluorescence still a factor.

5 Terrestrial Hydrothermal Analogues and the Preservation Potential of Silica Sinter

5.1 Introduction

Silica sinters are a by-product of hydrothermal fields, sometimes referred to as geyserite when formed in water too hot for life and due to their prevalence around hot water vents such as cone geysers, fountain geysers and other hydrothermal water features (Campbell, et al., 2015). Silica sinter formations are most recognisable from their formation around cone geysers, producing tall columnar conduits through which water is ejected. These formations are the result of the accumulated precipitation of silica from vent fluid and, as noted by Guidry & Chafetz in their 2002 review (Guidry & Chafetz, 2002), precipitation is affected by a combination of abiotic factors such as evaporation (Hinman & Lindstrom, 1996; Orange, et al., 2013; Fournier, 1985; Jones & Renaut, 1997); cooling rates (Fournier, 1985; Jones & Renaut, 1997; Jones, et al., 1997); pH (Jones, et al., 1997; Tobler, et al., 2008; Andhika, et al., 2015; Jones & Renaut, 1997) and the presence of cations in vent effluent (Andhika, et al., 2015; Ichikuni, 1970), particularly in the presence of bacteria (Phoenix , et al., 2003).

Several studies have focused on how precipitation of silica sinter occurs mechanically, and how the influence on silica precipitation rates affects the formation of laminated sheets of silica (Hinman & Lindstrom, 1996; Jones & Renaut, 1997). Micro-columnar ‘digitate’ silica sinter (sometimes referred to as spicules) is composed of thinner laminae that have grown vertically through accumulation of domed laminations (Jones & Renaut, 1997). Jones and Renaut note that formation of digitate silica is primarily confined to a zone around the geyser pool where water spray on subaerial surfaces evaporates, and is thus

controlled by wind and ejection angle (Jones & Renaut, 1997) however, digitate sinter formation can also occur outside of the vicinity of the vent and direct interaction with vent fluid due to preferential precipitation, influenced by bacteria acting abiotically as a catalyst for silica precipitation (Jones & Renaut, 1997; Jones, et al., 1997; Phoenix, et al., 2000; Phoenix , et al., 2003). Formation of digitate silica structures on silica oncoids is initiated from a basal platform and growth can continue in three phases as detailed by Jones and Renaut (Jones & Renaut, 1997) and displayed in figure 5.1;

- Short term flooding of the platform on which 'spicules' grow and subsequent precipitation of silica on all submerged surfaces potentially resulting in spaces between 'spicules' being filled in and the formation of a new basal platform;
- Detached silica oncoids can be overturned by changes in vent water velocity resulting in 'spicule' development on the surface that was previously the undersurface
- Long-term submersion in vent fluid resulting in lamination of the oncoid on all surfaces.

Digitate sinter has also been identified as an indicator of aqueous activity on Mars due to the similarities between Martian observations and terrestrial sinter structures in hydrothermal locations such as El Tatio (Ruff & Farmer, 2016), New Zealand (Preston, et al., 2008) and Iceland (Preston, et al., 2008). In their 2016 paper, Ruff and Farmer determined that whilst there is no empirical evidence that biotic processes were involved in the production of digitate sinters on Mars, the production of comparable sinters on Earth and Mars "satisf[ies] an *a priori* definition of potential biosignatures" (Ruff & Farmer, 2016).

In addition to the work by Ruff and Farmer, Jones and Renaut suggest that the lack of evidence of microbes in sinter laminae is indicative of preservational biases in the fossil

record produced by silica sinters (Jones & Renaut, 1997) as microbial remains are disguised by the substrate. Biotic interactions could have a greater impact on silica precipitation in the geological record than is currently clear, which would increase the likelihood of the involvement of biotic interactions with the formation of Martian sinters.

The El Tatio Geothermal field is located at 4200m above sea level and is surrounded on all sides by volcanic peaks that are part of the Central Volcanic Zone (Fernandez-Turiel, et al., 2005), a region of the Andean Volcanic Belt that forms the western boundary of the Altiplano stretching from Peru to Northern Chile and Argentina (Stern, 2004).

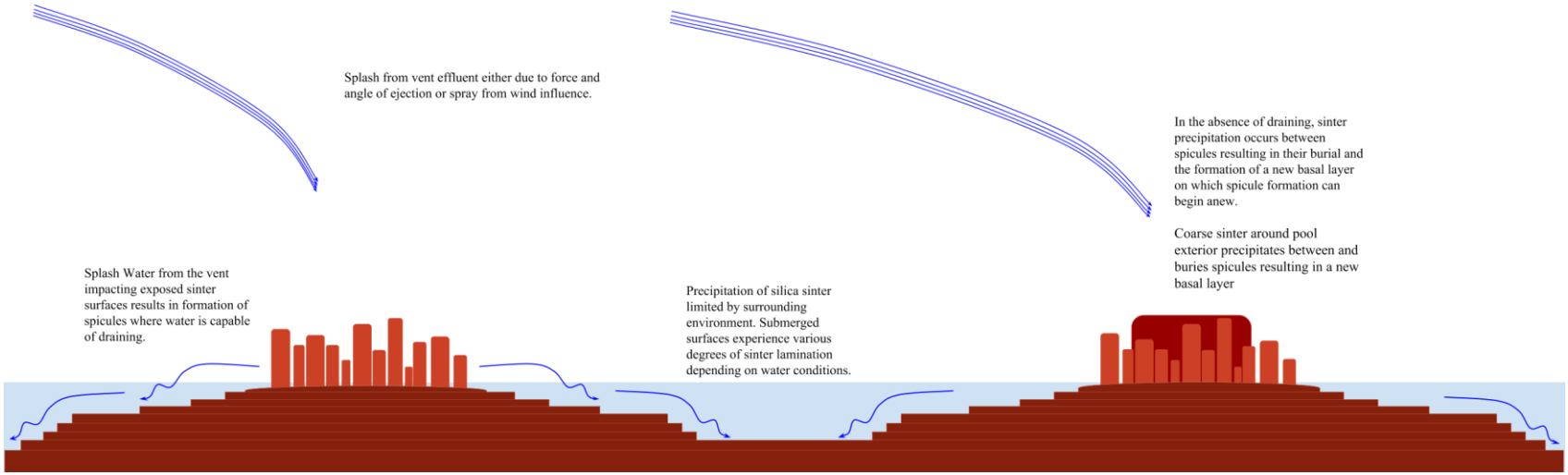

Figure 5.1. Diagram detailing the general sinter structure of pools in the splash zone of geothermal vents. Sinter surrounding geothermal vents can be separated into three common forms that arise due to conditions around the pool or vent. Submerged vents that form fountain geysers will cause a high degree of turbulence in the pool surrounding the vent itself which in turn inhibits the deposition of sinter below the waterline. Away from the vent where turbulence is reduced laminated sinter can form as distinct sheets such as those seen in **figure 2 C, D, H**, however, the formation of laminated sinter does not occur without submersion in water. At the edge of most fountain pools a more digitate sinter can be observed, where splashes off of eruption events result in the formation of short and thin columns of sinter (**Figure 2D, 5 & 7**). The outermost layer of sinter appears to be a much coarser formation that overlaps with any digitate sinter at the edge, most likely forming as a result of evaporation of silica concentrated water on the surface (**Figure 2D & 6**).

This chapter will catalogue the samples retrieved from the El Tatio geothermal field, as well as some additional samples collected from Whakarewarewa geothermal field in New Zealand. Some samples provided by colleagues from Krysuvik geothermal area and the in Iceland are also included as comparison sites representing lower altitudes and varying levels of local vegetation.

The Whakarewarewa geothermal field is a 0.15km^2 hydrothermal field in Rotorua on the north island of New Zealand. Like El Tatio the area contains a multitude of geyser types, both active and extinct, as well as active mud pools. It is also an active tourist site like El Tatio however the geothermal structures are far better protected from foot traffic by restricting the pubic to fenced footpaths. The key difference between the two zones is the volume of vegetation. Whakarewarewa is forested and the areas between individual geysers are covered in shrubbery. It is therefore expected that extra plant material will be incorporated into the silica matrix of geysers. Much of the geyser activity in Whakarewarewa has ceased or reduced as a result of local geothermal energy exploitation.

Iceland is a volcanically active island in the North Atlantic that has invested heavily in geothermal power. Iceland sits above a hotspot on the Mid-Atlantic Ridge (Bott, et al., 1983). Geothermal tourism is a popular activity in Iceland due to the number of hotspring sites scattered around the island. Samples in this study were collected from several sites rather than one site as in Chile and New Zealand. The Haukadalur Valley contains the most famous pairs of hot springs, Strokkur and Geysir, both of which samples were collected from. The Blue Lagoon is one of the most active tourism sites on the island, offering an opportunity for tourists to bathe in a man-made geothermal spring fed by the local geothermal power plant.

5.2 Method

Sample collection from **El Tatio** resulted in a collection of samples with similar morphological characteristics but varying composition. Samples were catalogued in order to keep track of their composition, as well as to show which samples were linked via the same water source in the geothermal field. Some samples were taken directly from a geyser itself; either from the vent exit where water is expelled, or from a dryer side where water had once passed over allowing deposition of sinter; or from the outflow channels that vent water flows into before leaving the geothermal field.

Samples from **New Zealand** were obtained from Whakarewarewa geothermal field that has experienced a similar reduction in geyser activity due to the harnessing of geothermal energy similar to El Tatio. At least 65 geyser vents exist in the Whakarewarewa geothermal field whilst only seven are currently active, most of which are on the formation known as Geyser Flat, the most notable of which is the Pohutu Geyser. Formerly active geysers are visible across the area, many of which are collapsed in on themselves, whilst some older vents off of the trails to the south are found on large sinter mounds not unlike the Geyser Flat. The area also contains several mudpools, most of which line the central path through the area from the west to the East.

Samples were collected from hydrothermal sites across **Iceland**, including the Blue Lagoon, Konunshver, Krysuvik, Gunnahver and Strokkur geysers. These samples were collected by a colleague conducting their own work in the area.

Samples were cut using CS10 Cutoff saw equipped with a diamond blade to expose the inner material. The saw utilises running water to prevent the blade and the sample overheating during the cutting process. This water is recycled throughout the cutting process. As a result the saw was thoroughly washed using a 1:3 decon mix and the saw rinsed in deionised water. The trough used to store water was drained and rinsed to

minimize contamination. Samples were cut from the top to the bottom of the sample to expose the interior from the most recently precipitated material to the oldest.

Following the cutting procedure, samples were polished down using new 150, 300, and 600 grade sandpaper and washed once more in deionised water before being left to dry under a fume hood. Samples were then stuck to microscope stage stubs.

All samples were cut in the presence of water, a result of which is the presence of salt on some surfaces that has been brought out of any pores in some samples. This is most notable in the sample in figure 5.21. Some samples were polished after being cut. Photographic images of samples in figures relating to SEM work were scanned prior to observations.

SEM work took place using a Carl Zeiss *Sigma VP* Field Emission-Scanning Electron Microscope (FE-SEM) and a Thermo Fisher Scientific *Quanta 200F* Scanning Electron Microscope.

5.3 Results

5.3.1 El Tatio

Due to El Tatio's significance as a tourism and culture site, it is possible that some anthropomorphic damage to vent structures may be observed, however, most of the significant vents are marked off to try and minimize the impact of foot traffic. The sampling covered in this chapter occurred at midday, several hours after the peak tourism times at 7AM - 9AM.

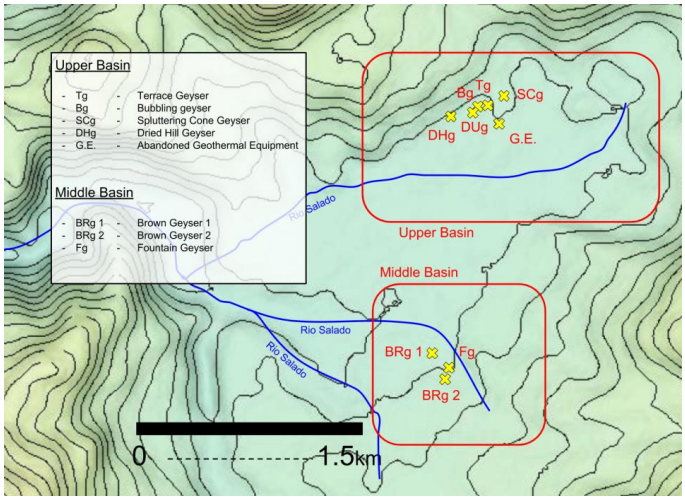

Figure 5.2. The El Tatio Geothermal Field with two of the three basins and sampled geysers marked.

Samples were collected from two different locations that feed into separate outflow channels that join at the boundary of the geothermal field. Most geysers in the North side of the geothermal field are not forceful enough to eject vent effluent out sufficiently to form an outflow channel although are still venting steam out. This is most likely as a result of past developments in attempting to harness geothermal energy at El Tatio. Previously the field was host to 67 geysers (Jones & Renaut, 1997) whilst at the time of sampling there were fewer than 20.

Comment [RP1]: Need scale bars for each image

Might be preferable to do south area collage first, then north area collage after.

Figure 5.3 Examples of different sinter structures observed in the El Tatio Geothermal field. A selection of vent and outflow channel structures are pictured. **A**. Backside of a large sinter mound that has formed around a geyser vent on the middle basin of the geothermal field. Inner surface of the sinter has been exposed in the centre by removing a piece (Figure 3). Darker colouration of the sinter is due to presence of carotenoids and successive encasement of microbial mats by precipitated sinter. **B**. Dry pool of sinter at the edge of a vent. Vent was active although not ejecting at the time of visiting. **C**. Bubbling pool in the upper basin of the geothermal field. Edges of laminated sheets of sinter can be seen clearly descending away from the vent. A taller build-up of laminated sheets can be seen immediately around the edge of the vent.. **D**. Pools surrounding bubbling pool seen in *G*. Clear distinction can be seen between laminated sheets below water level and digitate structures above the water level. **E**. Geyser vent that has formed from precipitated sinter building up around the edges of a vent. At the time of visiting the vent was spluttering just above its rim. **F**. Edge of what is known as the Terrace Geyser. The Vent is situated on an elevated terrace and pictured is the overhang where vent effluent flows. Very clear development of laminated sheets orientated almost vertically at the edge. **G**. Bubbling geyser in the

Comment [RP2]: Needs to be clearer in figure (arrows?)

Comment [RP3]: Confirm….

south side of the geothermal field. Notable differences in sinter structure around the edges of the pool as seen in *D*. Discolouration of sinter around the vent are due to the presence of biofilms. **H**. A closer image of the laminated sheets observed from the vent in *C*.

5.3.1.1 Samples from the Middle Basin

Sample sources in the middle basin of El Tatio came from four different sources, each displaying different sinter structures.

The two most prominent vents in this area are a pair of cone geysers 140m apart, but sharing similar physical characteristics. The mounds of silica sinter that make up each geyser are notable for their dark brown/red colouration which stands out against the dirty white of most sinter in El Tatio. Distinct colouration compared to regular sinter appearance can be clearly observed in Figure 3 and 4, whilst the sample in Figure 8 was taken from the runoff of the southernmost brown geyser. Sample in Figure 3 was taken from the rear of the vent, not exposed to vent effluent and thus additional precipitation. Outer layer of the sample is notably coarser than material within (Fig 3B) whilst the inner laminations of sinter running laterally through the sample are clearly observed along with pores (Fig 3B). These curved microlaminations are a feature of similar sinters, both of a silica origin (Campbell, et al., 2002) and of a calcareous origin (Freytet & Verrecchia, 1999).

These were also two of the most active geysers in the field, both with high volume outflow channels that feed into the Rio Salado that originates at El Tatio. Both cone geysers produced a strong smell of hydrogen sulphide and were the sole vents in the geothermal field to do so at the time of visiting.

Figure 5.4. A cut of the sample taken from the rear of the cone geyser pictured in Figure 2A. In **A** the sample is positioned with the inner surface facing upwards and the bottom of the sample orientated to the left. The lateral laminations from inside to out are pictured in **B**. Distinct colouration compared to regular sinter appearance can be clearly observed. Sample was taken from the rear of the vent, not exposed to vent effluent and thus additional precipitation. Outer layer of the sample is notably coarser than material within **(B)** whilst the inner laminations of sinter are clearly

observed along with pores **(A**). Despite size, sample is much lighter than it appears, a side effect of the high porosity. Dark streaks observed on the inner surface of **B** on the right are an artefact introduced during the cutting process.

The sample pictured in figure 5.4 was lifted off of the back of the northernmost brown geyser in the middle basin without any need to damage the sinter mound. As can be seen in figure 5.3 A, there is a distinct banding pattern where the block of sinter was removed (marked by a white arrow in the figure). Lateral microlaminations are visible in the thin band of whiter sinter indicating that growth took place vertically, however, in the thicker, darker bands that are located between the lighter bands there greater evidence of the growth of sinter is influenced to grow perpendicular to the sinter in the lighter bands. Similar banding patterns have been observed in other samples and on scales much smaller than those here (Figure 5.14 & 5.15).

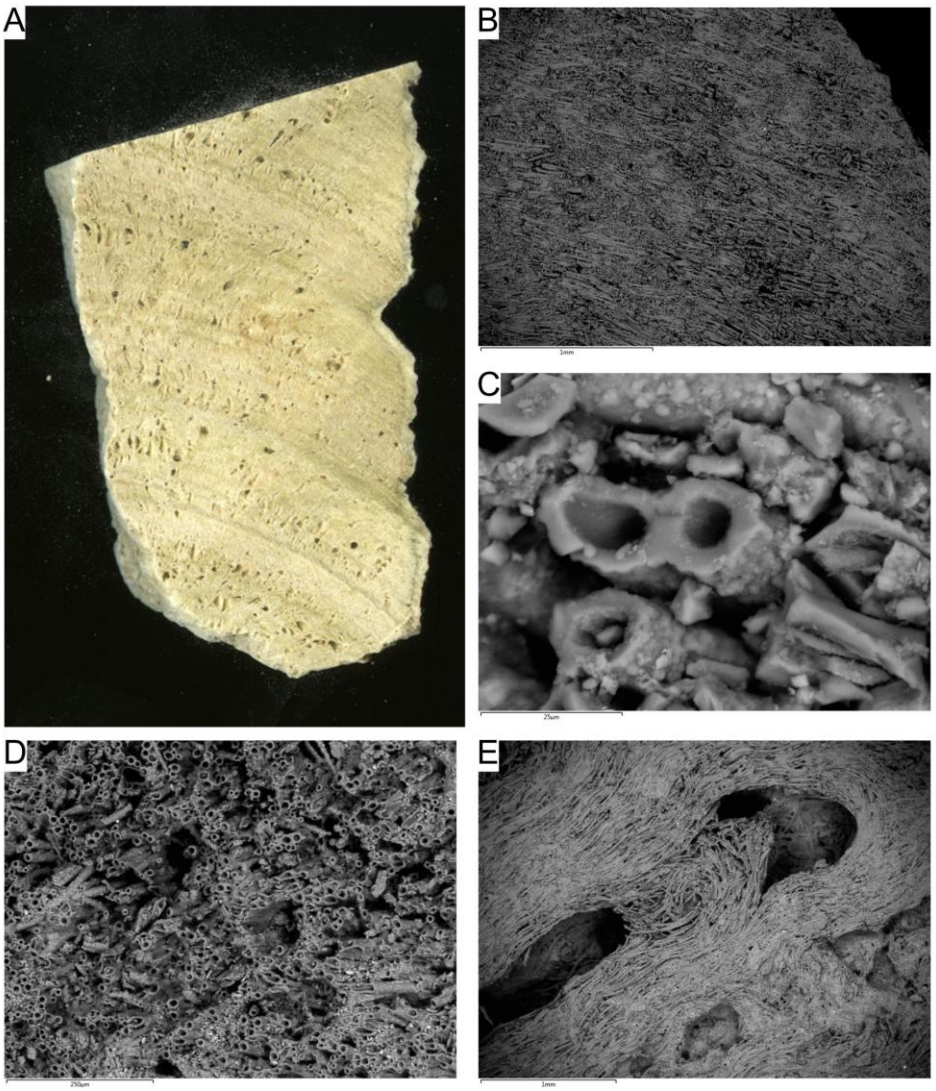

Figure 5.5. Surface images of the brown sinter sample obtained via SEM. A separate cut of the sample pictured in figure 4. The sample is almost entirely composed of silica tubules (B, C, D, E). In contrast to other samples, it was difficult to locate an area of the sample that did not possess evidence of biomarkers.

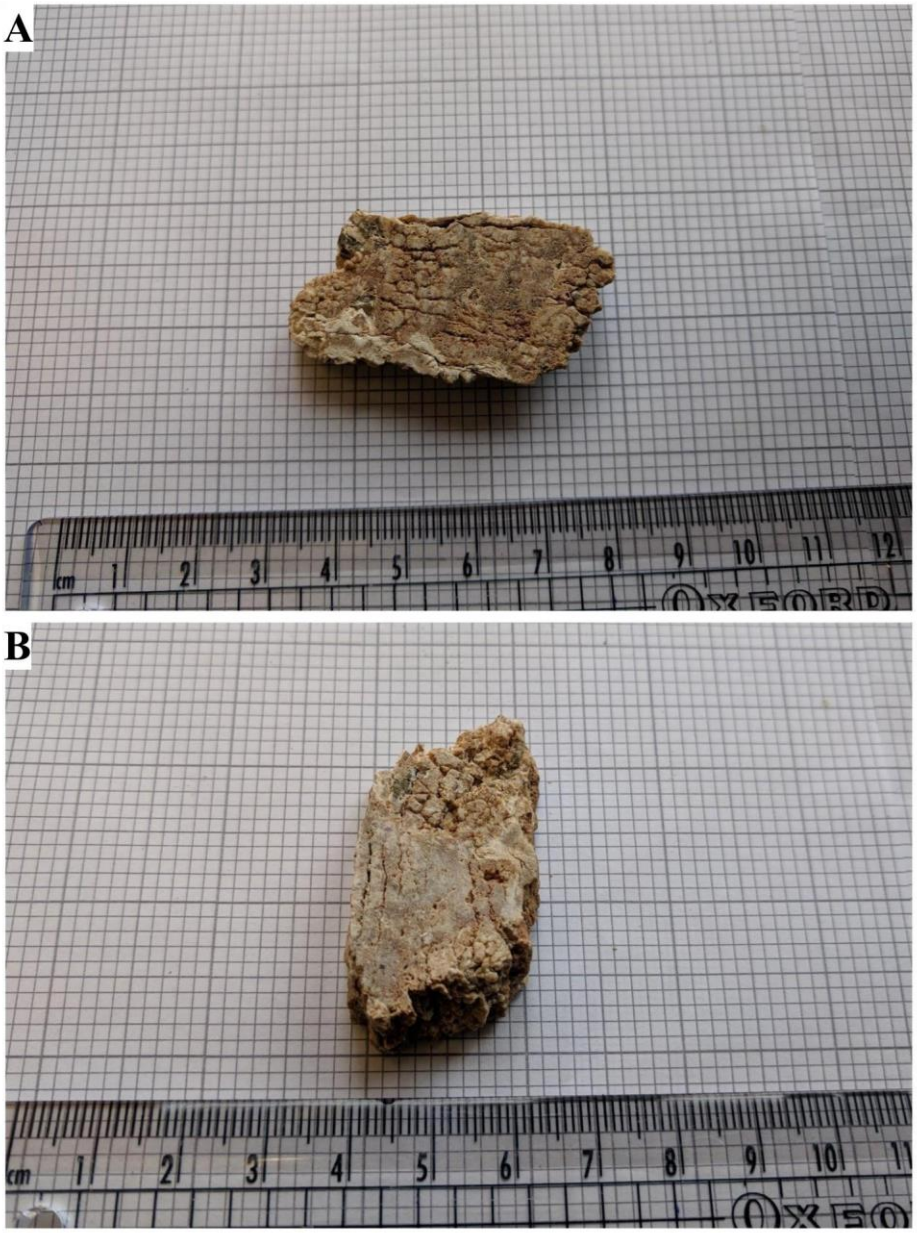

Figure 5.6. Sample cut taken from the rear cavity of the southernmost cone geyser with the brown sinter.

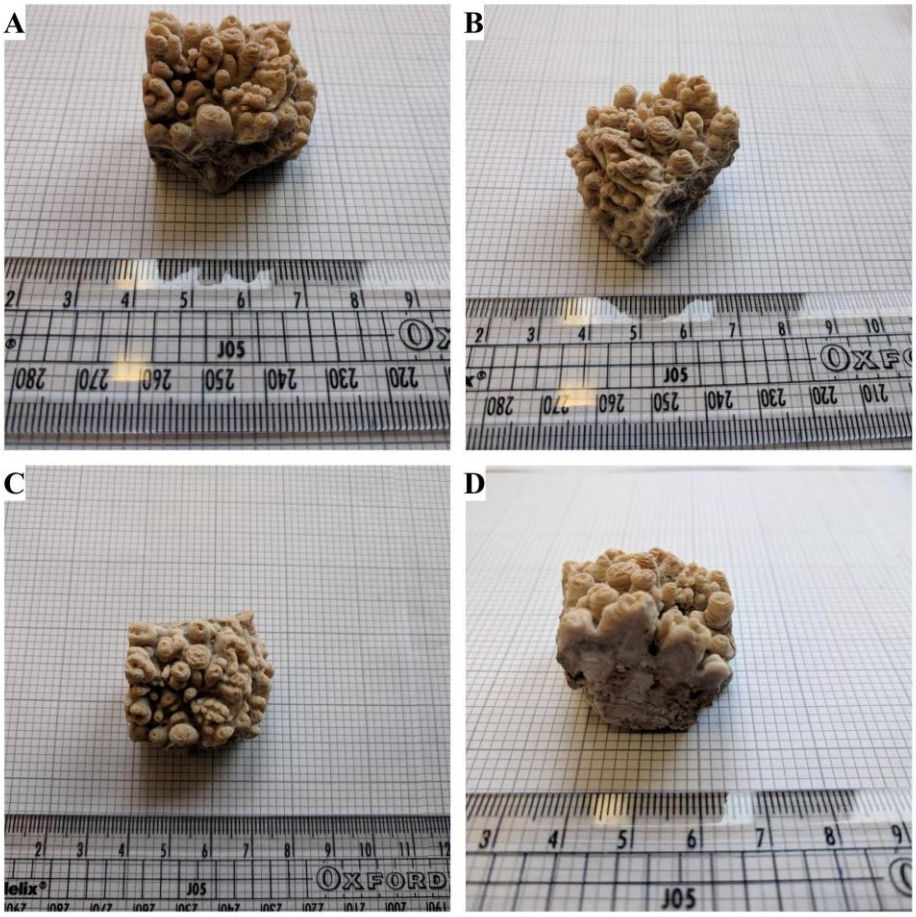

Figure 5.7. Digitate sinter sample obtained from the southernmost brown cone geyser. The sample was taken from a collapsed vent at the back of the geyser. As can be seen in **D** older columns of digitate sinter have been buried and covered by a new layer of digitate sinter with no direct continuation of previous growth structures. This sample is indicative of geyser pool structures being buried beneath newer sinter (**Figure 5.3d & Figure 5.7**).

SEM analysis of the sample in figure 5.7 can be observed in figures 5.8 and 5.9. The spicules that give the sample its digitate appearance take two forms. The core of the spicule (seen bisected in figure 5.8B,C) consists of solid silica sinter with no direct evidence of bacterial encrustation. However the tips of the spicules consist of disorganized bands of

laminated sinters with bacterial filaments between the main growth lines of each laminae (Figure 9).

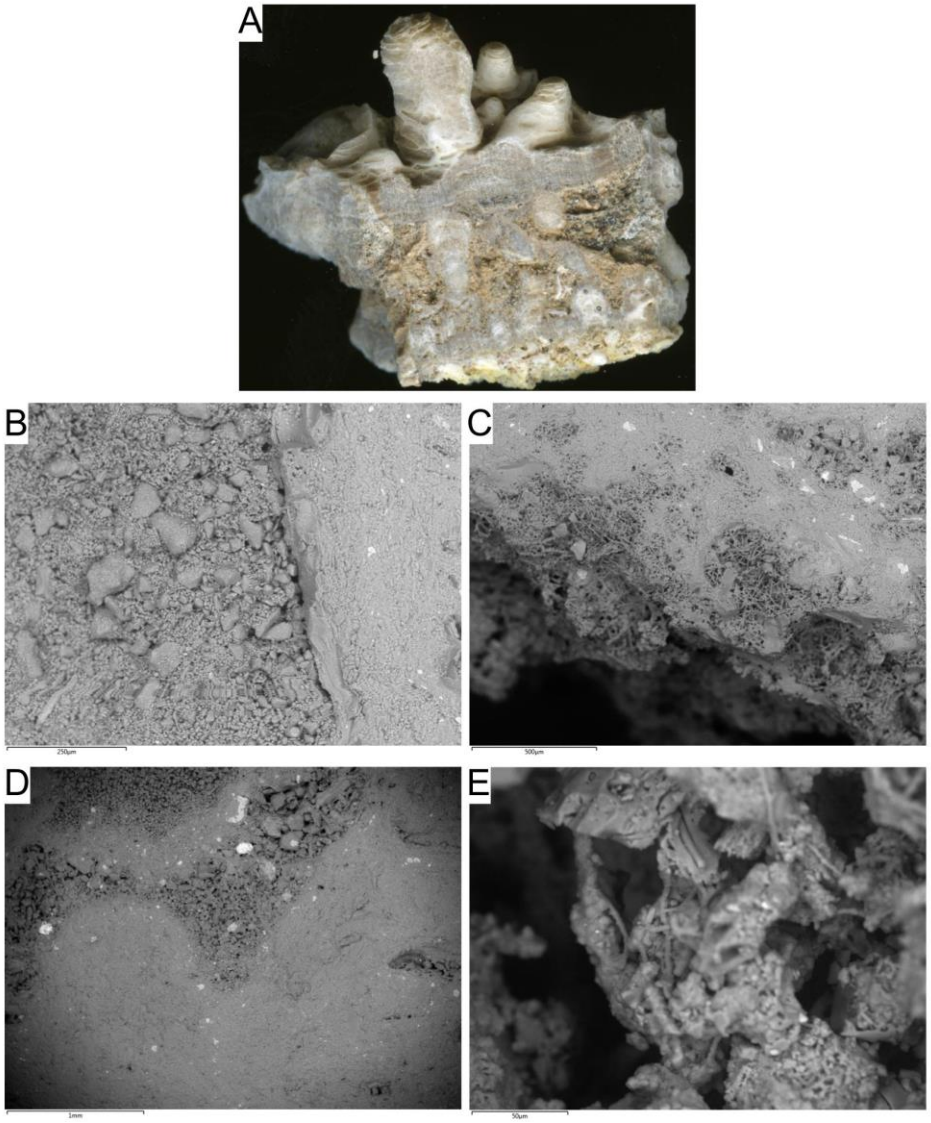

Figure 5.8. Surface SEM analysis of the sample pictured in Figure 7 depicting silica spicules that have grown on top of a basal layer covering pervious spicule growth. The sample pictured in A is the opposite cut of that pictured in Figure 7D. Evidence of biomarkers was more limited in this sample compared to that pictured in figure 5; however, silicified bacterial filaments could be observed at the bottom of the sample (C & E) and on the surface of the spicules themselves (Figure 9). Observations of the buried spicules and the surrounding material were also made (B & D). Lighter patches on SEM images are salt brought out during the cutting process.

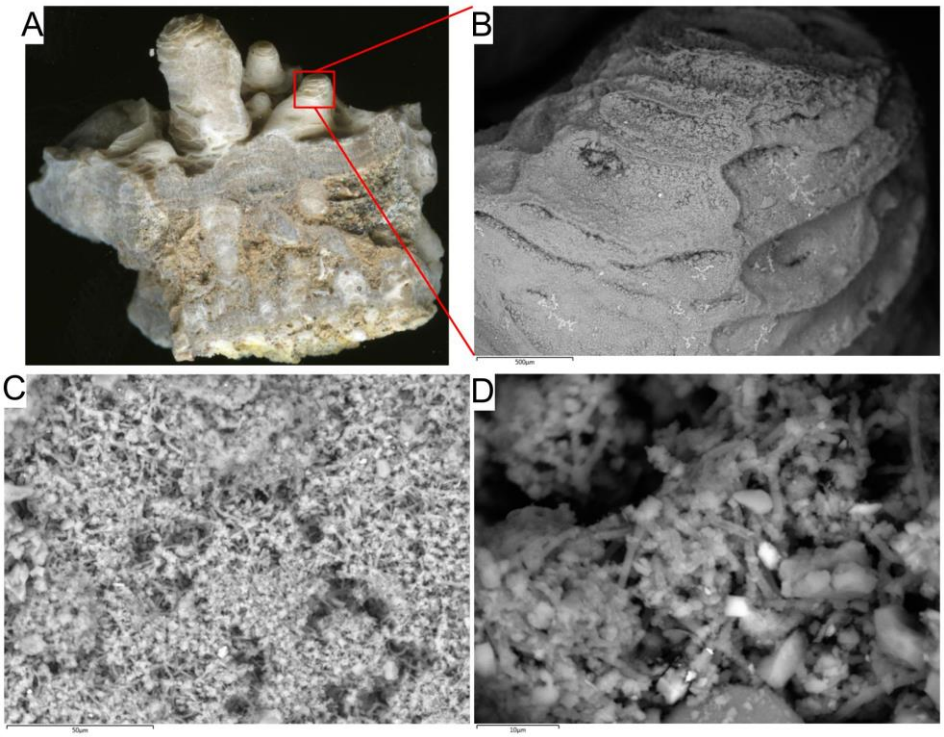

Figure 5.9. SEM imaging of a spicule revealing extensive bacterial filaments. Analysis of the tip of a spicule revealed thicker sinter bands (visible to the naked eye (A & B)) separating large patches of silicified bacterial filaments (C & D).

The middle basin also hosted a fountain geyser with a pool rim composed of highly disorganised laminated sheets submerged in vent water above the waterline of the main pool and a more digitate sinter structure surrounding these surrounding pools. Samples were taken

The sample pictured in figure 5.13 is a silica oncoid similar in texture to the coarser sinter that surrounds and separates the minor pools and spicule clusters. Close observation of the geyser pool rim showed that the coarser sinter has not precipitated as one continuous growth, but appears to occur in thicker laminations not unlike the internal sinter structure of most sinters detailed here (Figure 5.6). It is unknown whether or not this pattern extends further below the surface.

Figure 5.10. A magnified image of the surrounding sinter rim in figure 3G. Coarser sinter at the surface adjacent to the sinter pool on the left appears to be layered on top of previous coarse sinter in the form of a thick laminated layer (centre of image).

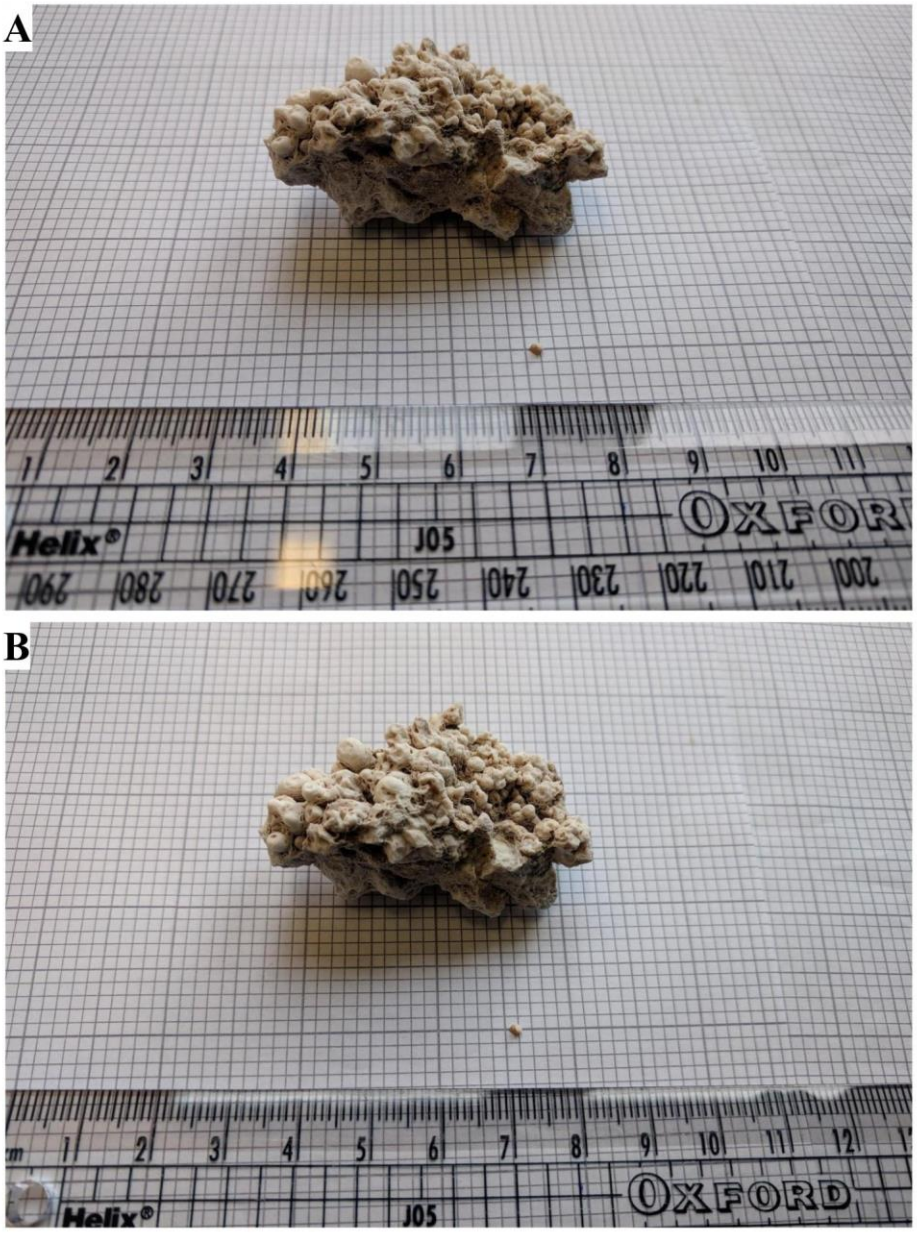

Figure 5.11. Digitate sinter taken from a fountain geyser in the middle basin. Sample was taken from the surface layers around the edge of the geyser pool **(Figure 3 D&G).**

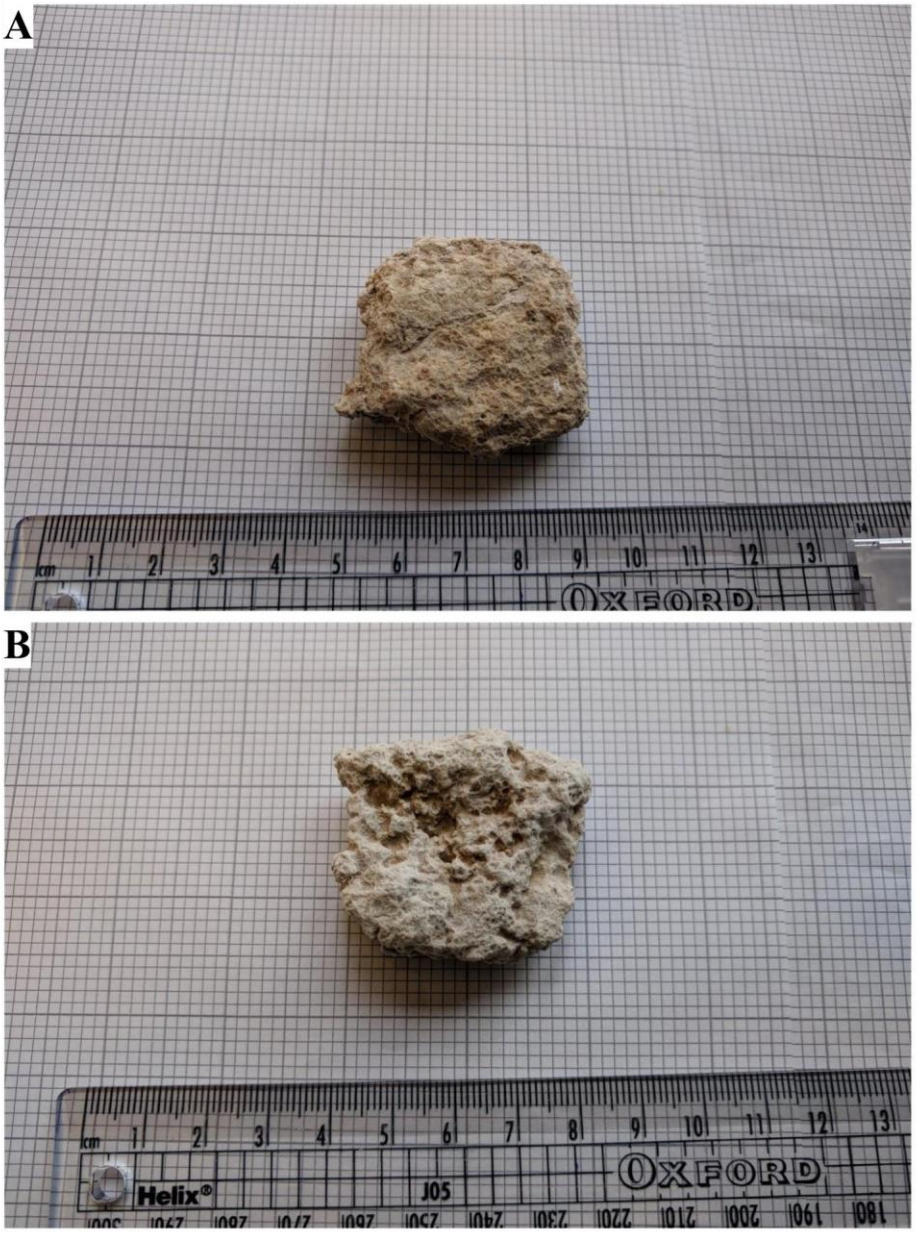

Figure 5.12. Coarse silica oncoid taken from the same fountain geyser as the sample in Figure 9. This coarser sinter sample was taken from the rougher edge of the pools of vent effluent seen in **Figure 5.3 D&G** where the rougher white sinter meets the digitate sinter at the border of pools (**Figure 5.7 & 5.8**).

Comment [RP4]: Confirm that notation matches final collage

Two samples were collected from the runoff streams of the northernmost brown cone geyser in the middle basin. These streams were notable for the presence of a red/brown biofilm on the rock and sinter surface, particularly below the waterline, and are most likely linked to the brown tint that characterises the cone geysers upstream. The two samples collected take two forms, one of which shows evidence of laminated sinter that has incorporated debris from the outflow stream (figure 5.14), the other of disorganised sinter that may incorporate rock from the stream base (figure 5.15). Both were covered in a light biofilm at the time of sampling, and both feature a similar discolouration of sinter as the brown geysers upstream.

Comment [RP5]: SEM to confirm

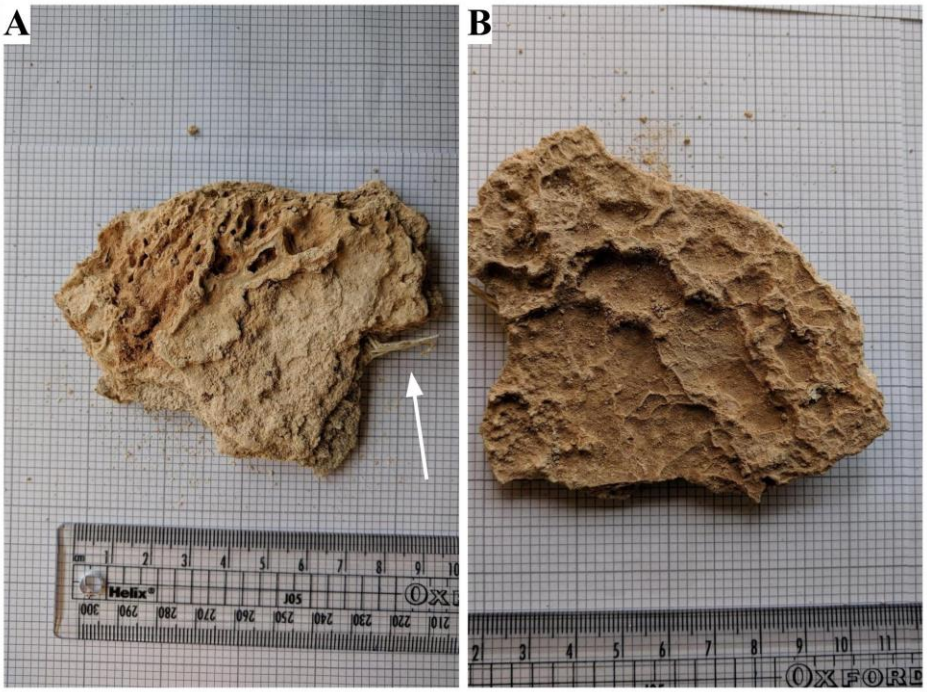

Figure 5.13. Laminated sinter from the edge of the base of the outflow stream. This sample is very brittle much like the samples in **Figure 3** however, the layers of the sample have much weaker connections between them compared to the highly interconnected layers that occur in the geyser structures. The top layer of the sample resembles the laminated sheets seen on the Terrace geyser surface in **Figure 2H** (*White arrow in **A** marks plant material protruding from the sample*).

Comment [RP6]: Figure needs redone because there should only be 2 images

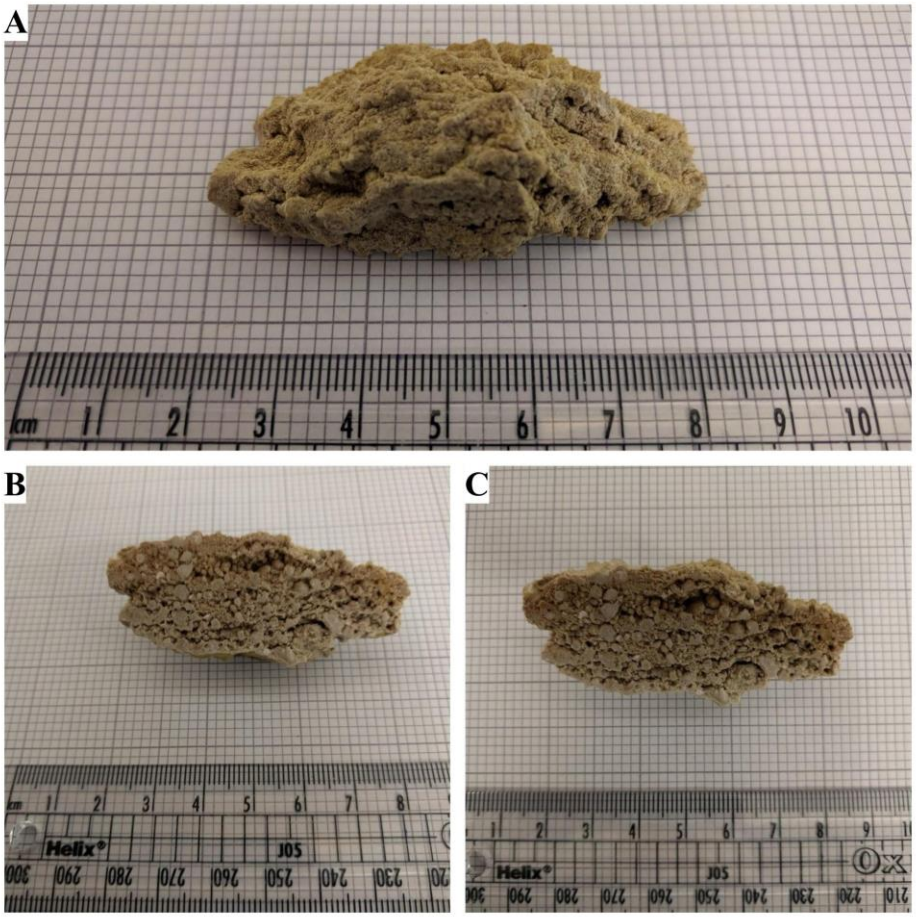

Figure 5.14. A highly disorganised sinter showing very little in the way of organised structure. The sample has been cut open to expose the interior (**A**&**B**). The sample was taken from the edge of the outflow channel where the sinter walls overhang next to the stream. Sample incorporates a lot of small pebble sized debris from the stream, with silica connecting in the gaps. The sample is diffuse with air pockets however, it does not share the same brittleness of the laminated sinter in **Figure 5.8**. The disorganised but diffuse mix of sinter and debris likely results in a more solid sinter piece than the laminated layered sinter taken from the outflow channel. Much like the laminated sinter, this piece incorporates the same red hue that can be seen in the brown cone geyser.

The disorganised but diffuse mix of sinter and debris in the sample in Figure 5.15 has resulted in a more solid sinter piece than the laminated layered sinter taken from the outflow channel (figure 5.14). Much like the laminated sinter, this piece incorporates the

same red hue that can be seen in the brown cone geyser. The silicification of other substrate material is visible to the eye, some of the material within the sample is not composed of silica, but has a silicified exterior. Connections of silica between pieces of substrate material are visible and strong enough to resist fracturing during the cutting process (Figure 5.16 F). Observations of the sample under SEM revealed a greater number of diatoms than in other samples (Figure 5.16 B & C) in addition to silicified microfilaments. Notably bacterial filaments were more deeply encased within the sinter material (Figure 5.16 D) than in samples such as those in Figures 5.5 & 5.9.

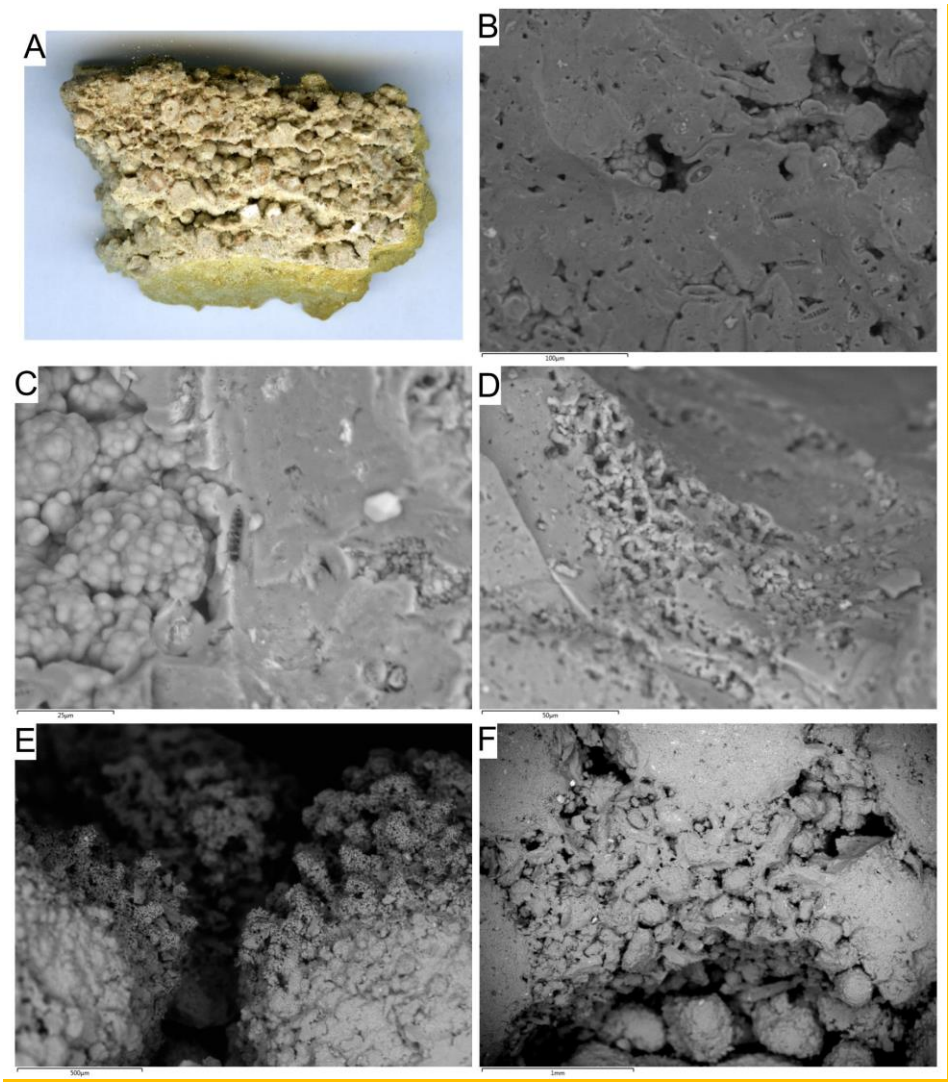

Figure 5.15. SEM imaging of the opposite cut of the sample in Figure 15. Sample contained high quantities of Diatoms (B & C) throughout with some evidence of silicified microfilaments (D). Surface sinter is rougher than that of the solid sinter that makes up the bulk of the sample interior (E). The majority of interstitial grains are coated with silica (F).

5.3.1.2 Samples from Upper basin

The upper basin contains most of the active vents at El Tatio geothermal field that were visited, but also contains most of the dormant or extinct vents. During the visit, many of the vents that were observed were active in that they were spouting some steam or there were some small ejections of water occurring, but flows of water into outflow channels were the exception rather than the norm. Several of these quieter vents were cone vents, indicating that they were at least in the past active enough to form significant sinter structures as a result of the vent effluent. Evidence of past efforts to extract geothermal energy from El Tatio for the purposes of power generation are present; most notably abandoned technical equipment in the North East of the area and piping running across the upper basin. The area also hosts active bubbling mud pools that were not present in the middle basin.

Some minor vents are still active on the slopes of the hills immediately off the road that marks the edge of the area. Most of these vents were observed venting steam, and their lack of sinter deposition suggests that steam venting is the sole activity at these vents. Past evidence of water movement could be observed from channels through the surface, though these channels consisted mainly of dry dirt at the time. Some sinter, as well as sinter-like structures, could be seen in the dry outflow channels around the hill vents but only a small portion was taken for sampling.

Comment [RP7]: Test dirt samples for silica content (Raman/SEM)

The majority of vents on the field itself were cone vents, albeit most had resulted in sinter deposition with a wide dispersion (Figure 2 C, H), rather than a tall one (Figure 2 E). An exception to this is known locally as the Terrace Geyser, which has dispersed widely but has a significant drop off on its eastern flank. The Terrace geyser has a significant outflow volume compared to other vents in the area, and the sinter laminations that have resulted are some of the best examples of layered precipitation in the area. Both the top of the geyser surrounding the vent and the overhang on the east flank feature prominent

Comment [RP8]: Reference

lamination of sinter (Figure 2 C, H, F). The overhang does not connect to the ground directly in some places, resulting in water flowing over the edge to drip off of the edge and an elongation of the sinter at these points (Figure 9). The entire area surrounding the Terrace Geyser, including the shelf that the main vent is situated on and the area surrounding the overhang is saturated with water.

Some of these samples also helped to reveal how the presence of microbial filaments influences the deposition of silica sinter, as well as how the sinter lamination process translates to a microscopic level after the initial deposition.

Figure 5.16. The southern edge of the Terrace Geyser platform. Both a wet edge (**A**) and a dry edge (**B**) are pictured. Brown colouration in **A** is a result of the biofilm coating the surface.

Comment [RP9]: Overhang similar in structure to microgours on waikite
Jones et al 2011, Life cycle of geyser discharge apron

Comment [RP10]: A good drawn diagram would help here

The terrace geyser is the largest platform of sinter in the El Tatio geothermal field, composed of a flat plain of sinter formed from water running downhill, before a drop off on its southern edge of approximately 1 meter in height. The edge of the sinter terrace is composed of sinter laminations, and overhangs the ground in some places (Figure 5.17 A).

Production of silica sinter is not confined to the platform itself, as water is capable of flowing around the edges of the platform that are not a vertical edge. The shallow gradient extends from the beginning of the edge of the platform, all the way to the steepest edge where the outflow begins, and wider sheets of laminated sinter are visible here. Much of the surface is coated in a slurry of dirt and sinter, and footprints from tourism at the site surround the main terrace. Several secondary vents are situated around the base of the terrace; however, none were active at the time of visiting. Steam emission shows that they are active in some form, although unlikely to be ejecting vent fluid due to the lack of sinter build-up around these vents.

The main vent in the centre of the terrace consists of a small mound of sinter that was spluttering water. Water movement away from the vent followed three routes at the time of visiting;

Centrally off of the platform edge

Around the edge of the terrace platform via the South-east or north-west.

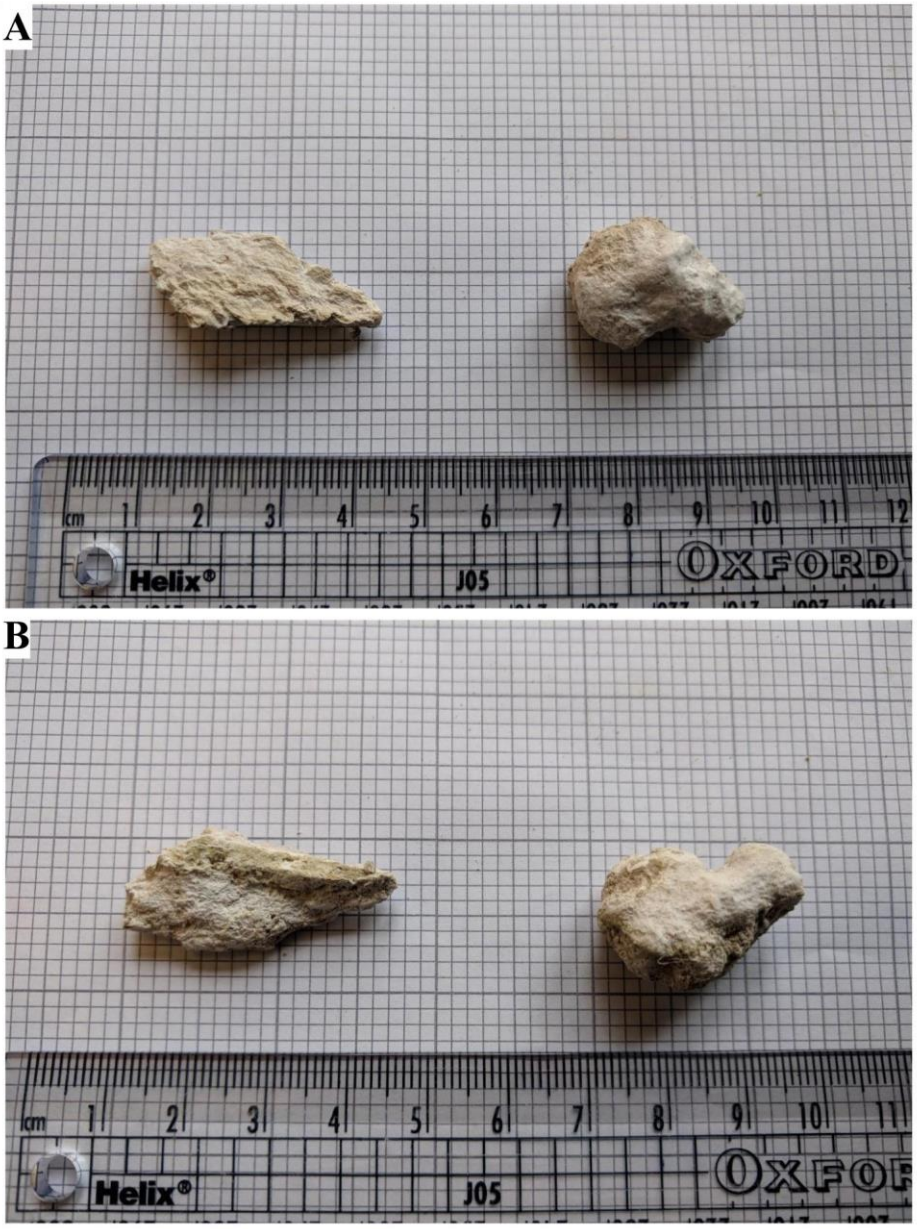

Figure 5.17. Terrace geyser fragments taken from the overhang of the Terrace geyser. These samples were taken from the lower lip of the overhang where water dripped into the runoff pools below.

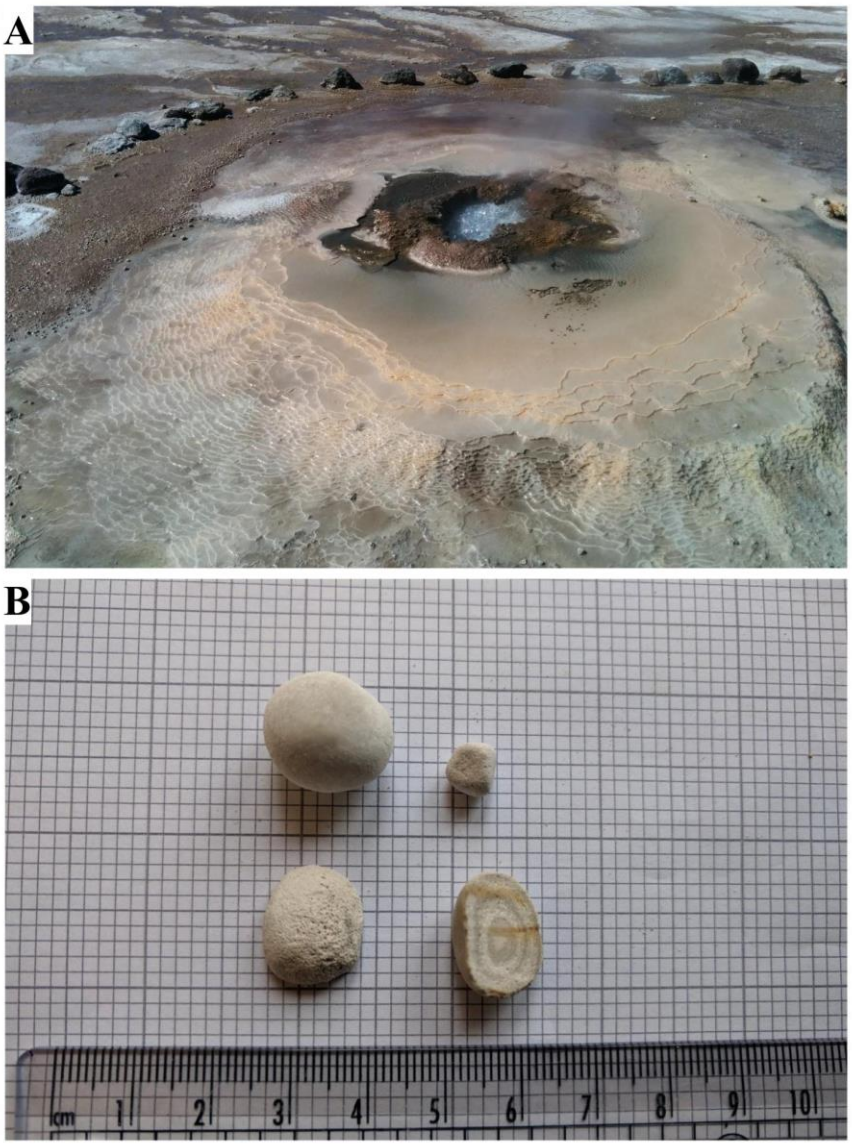

Figure 5.18. Balls of silica sinter that collected in a pocket in the uppermost layer of the Terrace Geyser. Contained within this pocket near the vent (**A**) were multiple balls of accumulated silica that had not been incorporated into the laminated sheets. The cause of this pocket and the balls of silica within are unknown, but it is suspected to be due to the mud that lines the interior of the pocket preventing agglutination of silica colloids to the surrounding laminated sheet. When dissected to reveal the inner structure, pattern of thin concentric laminae mixed with pockets of air are revealed, not dissimilar to the internal layering seen in **Figure 5.3A** and **Figure 5.13**. Discoloration on the open face of the sample in **B** is an artefact from the cutting process.

One of the more interesting samples collected from the Northern Basin was a sinter block from a cone geyser showing distinct lateral laminations that got progressively narrower from the top to bottom of the sample (Figure 5.20, 5.21, 5.22). This sample features laminations that appear to become tighter from the top of the sample to the bottom. It also has similar dark colouration to some of the samples in the middle basin although this dark colouration is confined to the bottom half of the sample. Like the samples in figure 4, 6 & 7 this colouration is most likely a result of pigmentation from the bacteria that were encased at the time of silicification. Porosity is also increased at the top of the sample.

Figure 5.19. Sinter cut taken from a cone geyser in the upper basin. One of the cone geysers in the upper basin had dried off leaving a crumbling sinter that could be easily prised away. The curious structure and colouration of the sinter can be attributed to the presence of filamentous bacteria, which upon investigation via SEM reveals a pattern of porous sinter laid on top of significantly less-porous sinter. This pattern this causes stands out upon visual observation, but the individual pores that are a partial cause of this are not visible to the naked eye. Other interesting features of the sample include the incorporation of a layer of mixed minerals that is presumed to be sediment, as well as changes in sinter structure from the topmost (and thus youngest) layers to the deepest (and thus oldest) layers.

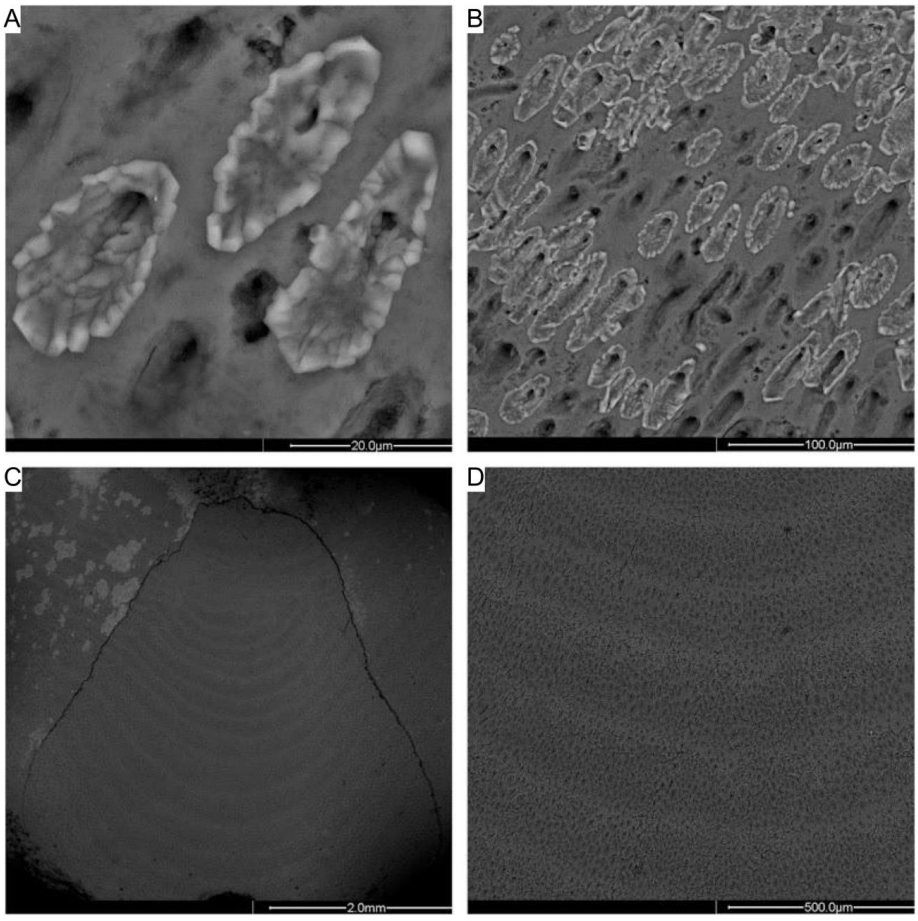

Comment [RP11]: Microlaminations at the bottom
-Ref: Freytet & Verrecchia 1999
-Calcitic radial palisadic fabric in freshwater stromatolites
- Calcite focused but principles the same

Non-porous laminae to finely porous laminae
Also Campbell et al 2002; an unusual modern silica-carbonate sinter from pavlova spring

Comment [RP12]: Obtain same top two images again, however, wash a sample deionised water and nailbrush to try and draw out some of the halite (salt)

Figure 5.20. SEM images of the sample pictured in Figure 5.20 showing how the ditribution of pores in the sinter affects the observed patterning in deeper layers. Pore distribution results in the dark/light bands of sinter in the lower layers of this sample (seen in colour in 5.20).

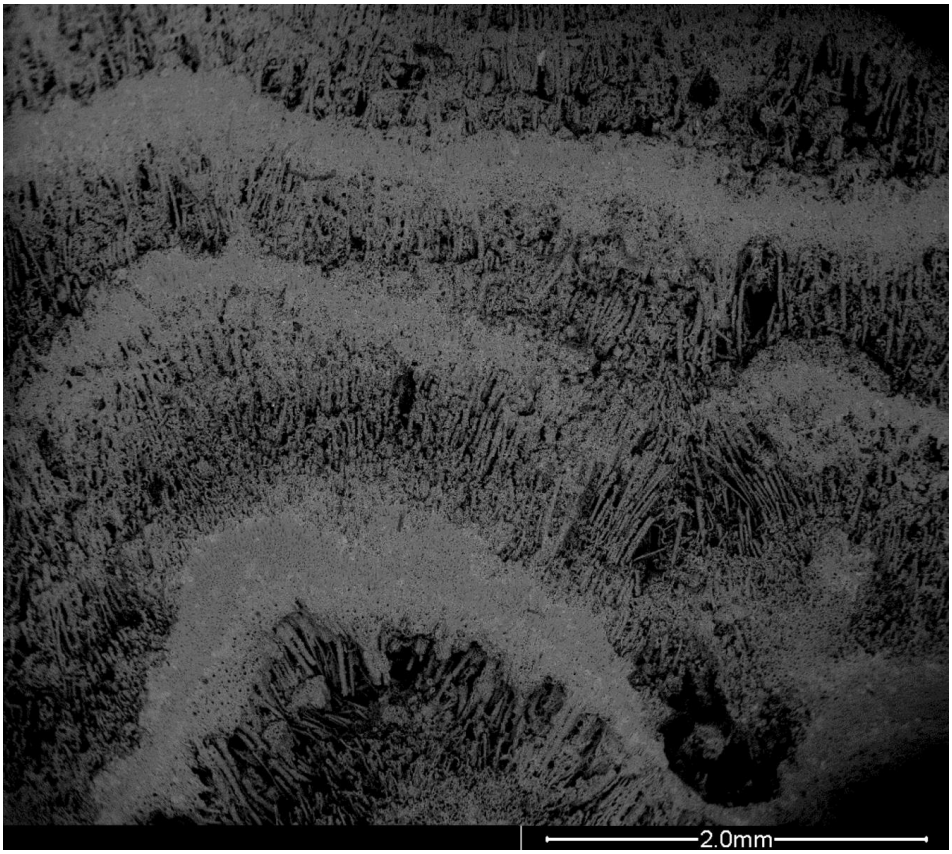

Figure 5.21. SEM image showing the influence of bacteria on sinter patterning in the upper (younger) layers of silica towards the top of the pictured in figure 5.20. As in figure 5.21, the morphology of the sinter influences the visual patterning of the material. In this instance full silicified fibres can be seen between thicker bands of silica sinter.

5.3.2 New Zealand

Comment [RP13]: Geyser activity discussion in Jones & Renaut 2003, Petrography and genesis of spicular and columnar geyserite from the Whakarewarewa and Orakeikorako geothermal areas, North Island, New Zealand

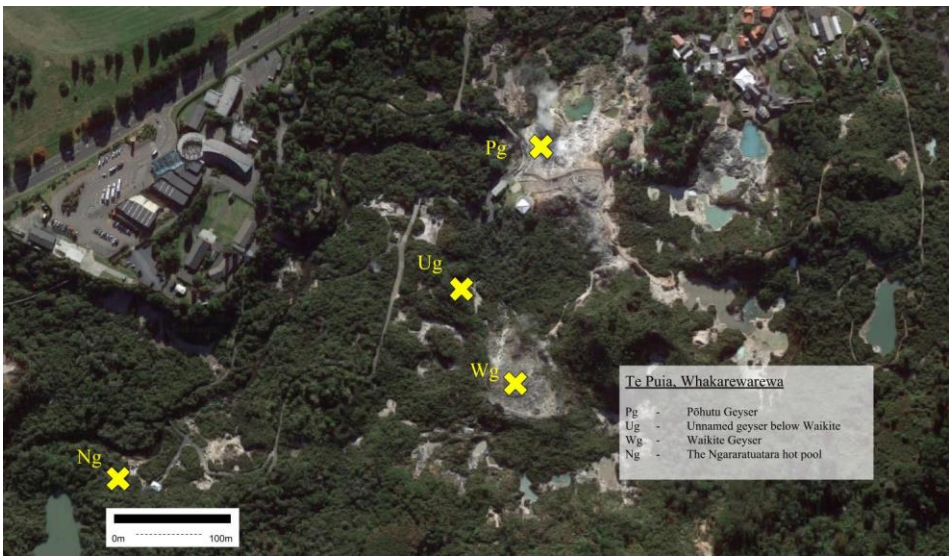

Figure 5.22. Map of sites sampled and discussed in the Whakarewarewa geothermal field, Te Puia.

Samples were obtained from several geysers, both active and inactive, across the area. However no permission was given to obtain samples from the most active sites at Geyser Flat due to its status as a cultural site. For the same reason only a few samples were obtained from the area in order to minimize impact.

The most noticeable difference between the New Zealand sample site and the Chilean and Icelandic sample sites is the volume of vegetation spread across the geothermal area. Whilst the Chilean and Icelandic sites were situated in cold desert environments, the Whakarewarewa geothermal field is more tropical. Of the three sites across the geothermal area where samples were collected, only the Waikite sample did not feature an overhang of vegetation.

The Ngararatuatara hot spring is a circular pool surrounded by bushes on all sides (Figure 5.24A). Its use as a cooking pool for the purposes of tourism also increases the chances of contamination for the purposes of organic chemistry, although the infrequency of its use in

this manner makes the risk of organic contamination likely to be negligible relative to the overall organic profile of samples taken from Ngararatuatara.

The Unnamed geysers at the foot of the Waikite discharge apron were situated adjacent to each other in a depression in the earth. This depression is surrounded by vegetation both around the overhang of earth above and in front of the open face of the depression. Whilst these two geysers are inactive and thus not currently precipitating silica and incorporating more material, they would have done so in the past.

Vent #130 near the top of the Waikite discharge apron was the most set apart from vegetation of any of the New Zealand samples, however, wind dispersion would result in plant material on or around material that make up the geyser.

5.3.2.1 Ngararatuatara

The most active pool geyser in the west of the area is the hot spring known locally as Ngararatuatara, which is used by the organization that runs the Whakarewarewa geothermal area as a cooking pool similarly to how the Maori people would have made use of it when the area was a gathering site for the Maori people. The pool consists of an approximately circular pool of boiling water that is depressed in the local surface (Figure 5.24A).

The surrounding ground around Ngararatuatara is composed of sinter which hangs over the edge of the pool. The vent is active at all times as a bubbling pool of water. Water splash reaches the edge of the rim but didn't appear to overlap the edge of the pool significantly. A white coating of sinter is visible around the outer edge of the pool rim, most likely depositing via evaporative precipitation from steam water that settles on the surface. Wicking of silica rich waters likely contributes to the build-up of sinter at the rim above the waterline.

Activity in the pool made it difficult to obtain clear images below the waterline.

Sample in figure 5.25 was obtained from the inside of the rim opposite the camera approximately 100mm above the waterline. As can be seen in both figure 25 A & B the sample is porous, particularly in the uppermost layers.

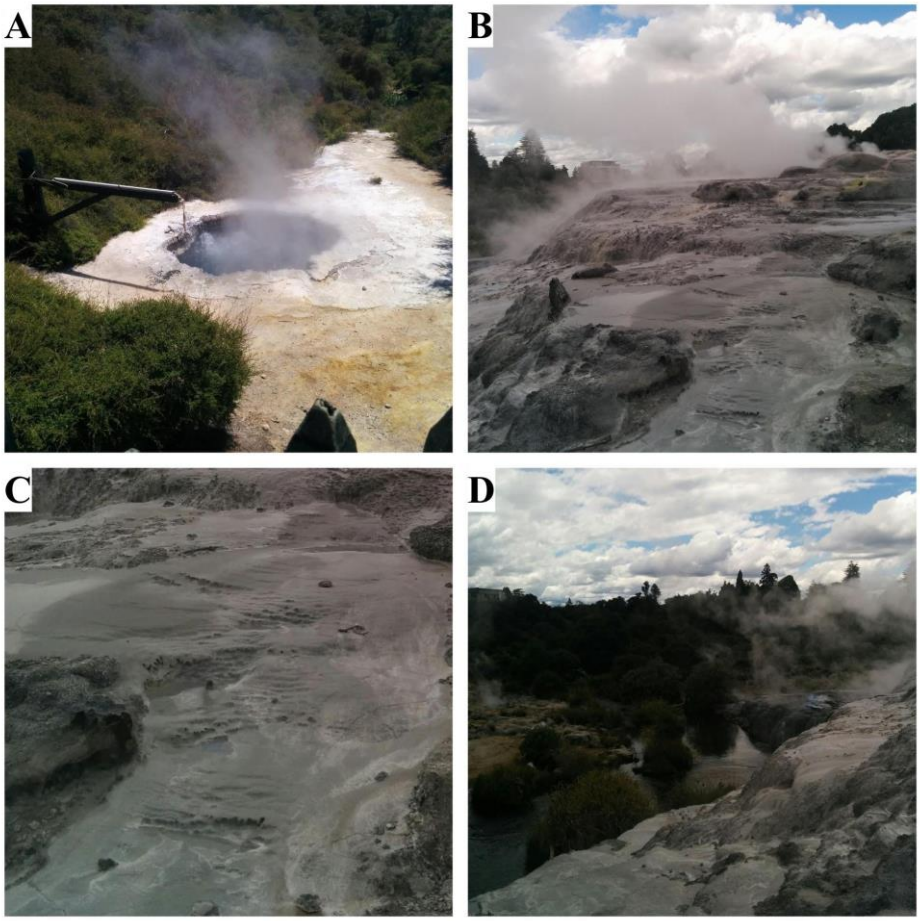

Figure 5.23. Images of the sinter formations of active vents around the Whakarewarewa geothermal area. The Ngararatuatara pool is pictured in **A**, recessed in the ground. The wooden arm on the left of the image is used for cooking purposes to lower food into the cauldron. The Pohutu geyser and the Geyser Flat is pictured in **B** whilst the overhanging ledge of the Geyser Flats is pictured in **D**. Pohutu Geyser erupts up to twenty times a day and can be seen as the main source of steam in **B** where most sinter buildup can be seen on the right of the image. Vent water is discharged across the Geyser flats and runs down the face into the valley below. Laminations can be seen in **C** but are covered by a slurry of material assumed to be streamer biofilm communities mixed with sinter.

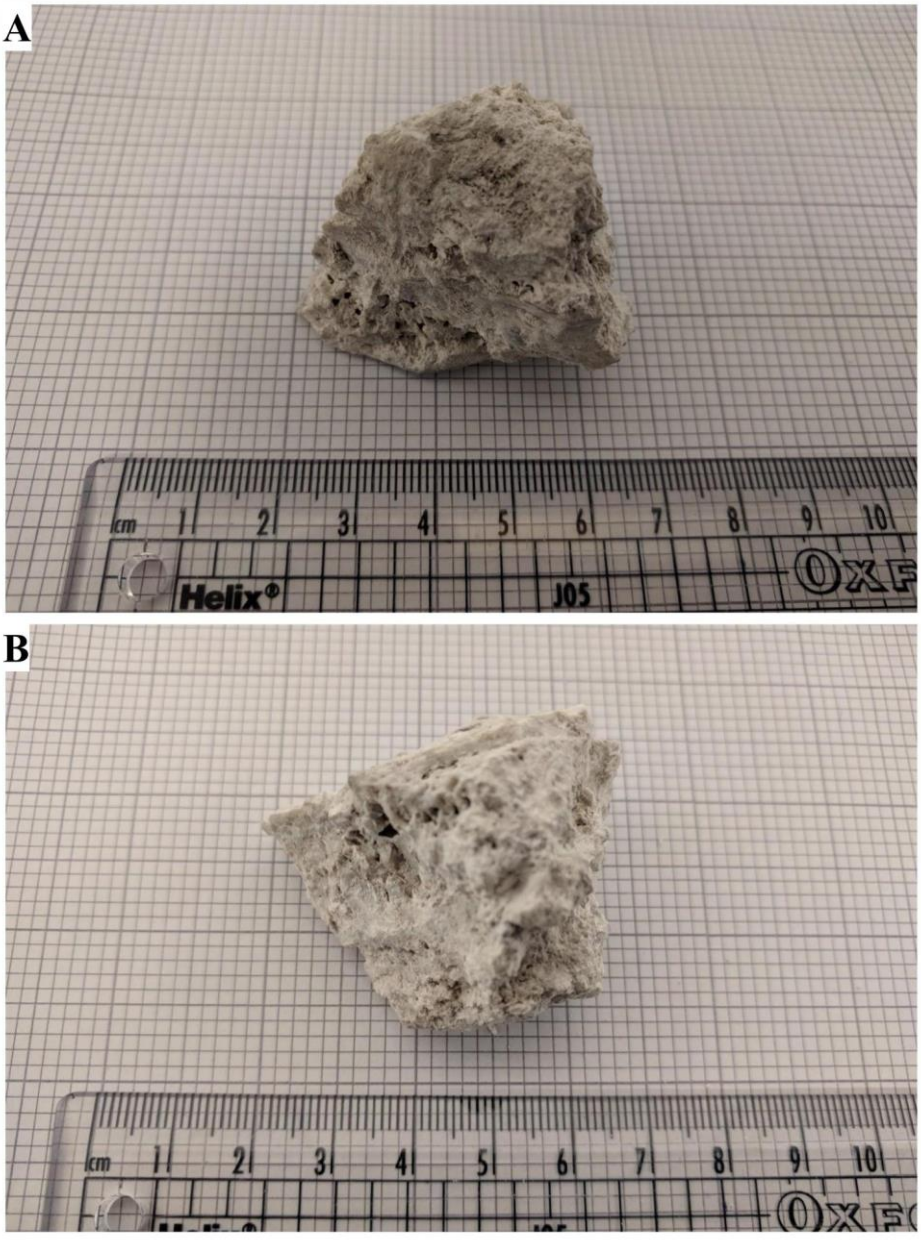

Figure 5.24. Sample taken from the rim of the Ngararatuatara vent. This sample was taken from a loose block of sinter on the inner rim of the cauldron vent approximately 50mm above the waterline. In **A** the sample has been photographed with the lower layers facing the camera and the uppermost layer resting on the paper, whilst in **B** the sample is orientated with the uppermost layers at the top of the image and the lower layers nearer the ruler.

Comment [RP14]: SEM

5.3.2.2 The Waikite Discharge apron

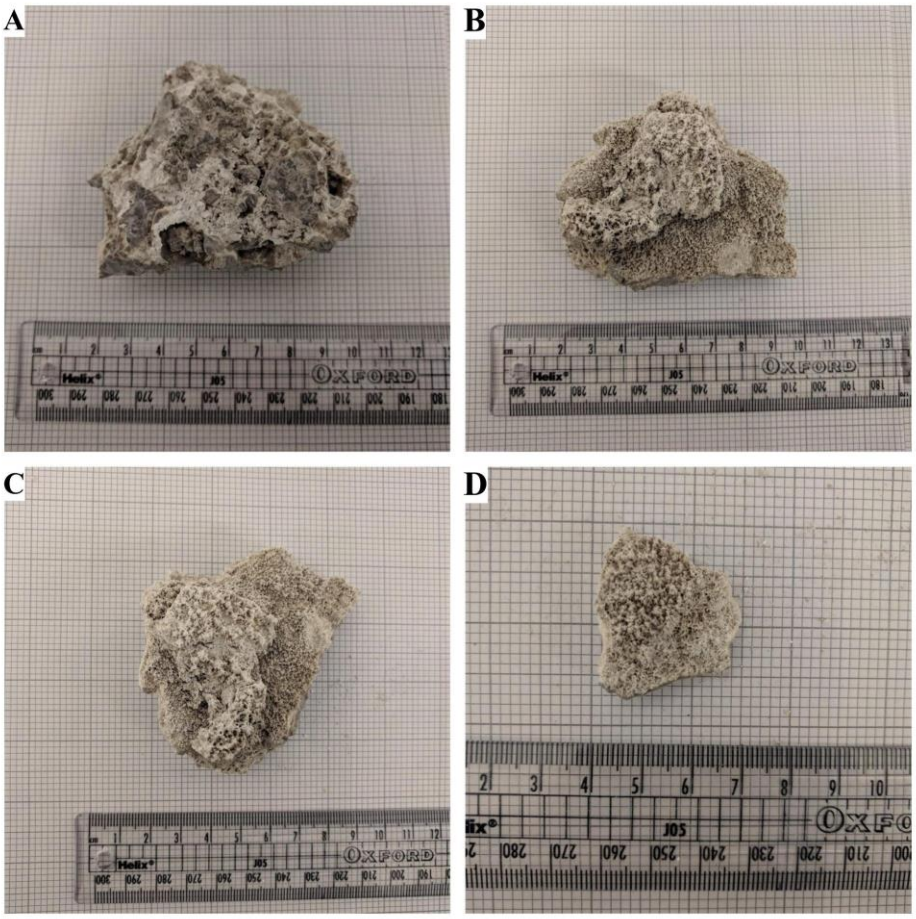

Figure 5.25. Sample taken from a collapsed vent of geyser #130 (designation taken from (Jones, et al., 2011) and (Lloyd, 1975)) on the waikite geyser apron in the Whakarewarewa hydrothermal zone. Whakarewarewa features many vents that are no longer active, some of which have collapsed in on themselves leaving fragments of sinter rubble.. As a result no confirmation of the original orientation of the sample in the field can be made, but the digitate patterning on one side of the sinter suggests that this is the top side (**B** & **D**). The sample appears to be laminated however, the layers are highly disorganised.

Comment [RP15]: March 1967 last recording of waikite

Comment [RP16]: SEM + xdif to determine patterning

Sample will need to be cut (fragile)

The sample pictured in figure 5.26 was obtained from a geyser situated on the eastern flank of the Waikite geyser apron. The only known identification of the geyser from which the

sample was obtained comes from a map produced in E.F. Lloyds 1975 book: *Geology of Whakarewarewa Hot Springs* (Lloyd, 1975) in which it is identified as geyser #130 and considered a part of the southern geyser apron (Jones, et al., 2011). The geyser is composed of three separate vents that have collapsed and are filled with sinter rubble, from which the sample in figure 22 was taken.

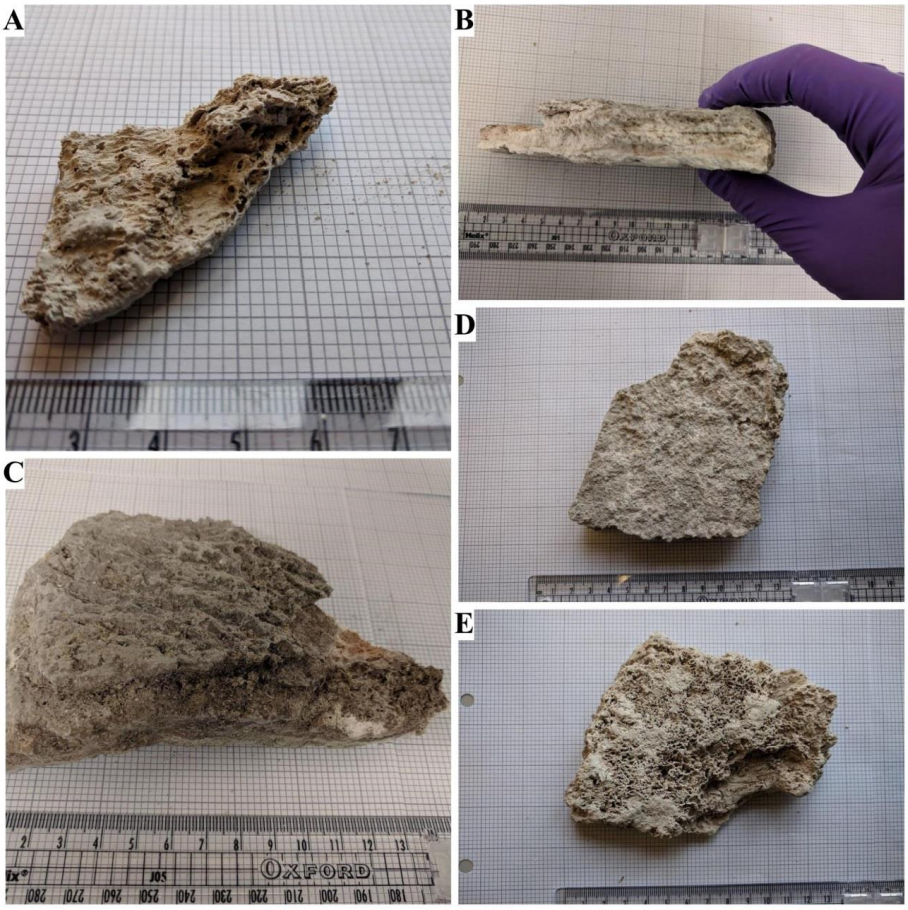

Figure 5.26. Samples taken from an inactive vent at the northernmost tip of the north apron of Wakite, between the Wairewarewa mudpools and the dormant Waikite vent. The sample pictured in **A** is a fragment from the sample pictured in **D** and **E** which was taken from the edges of the vent, whilst the sample pictured in **B** and **C** was taken from the centre of the collapsed pit.

5.3.3 Iceland

Comment [RP17]: Have map but put in last so figure #s don't mess up again

Figure 5.27. Site map for geyser and hot spring locations sampled in Iceland

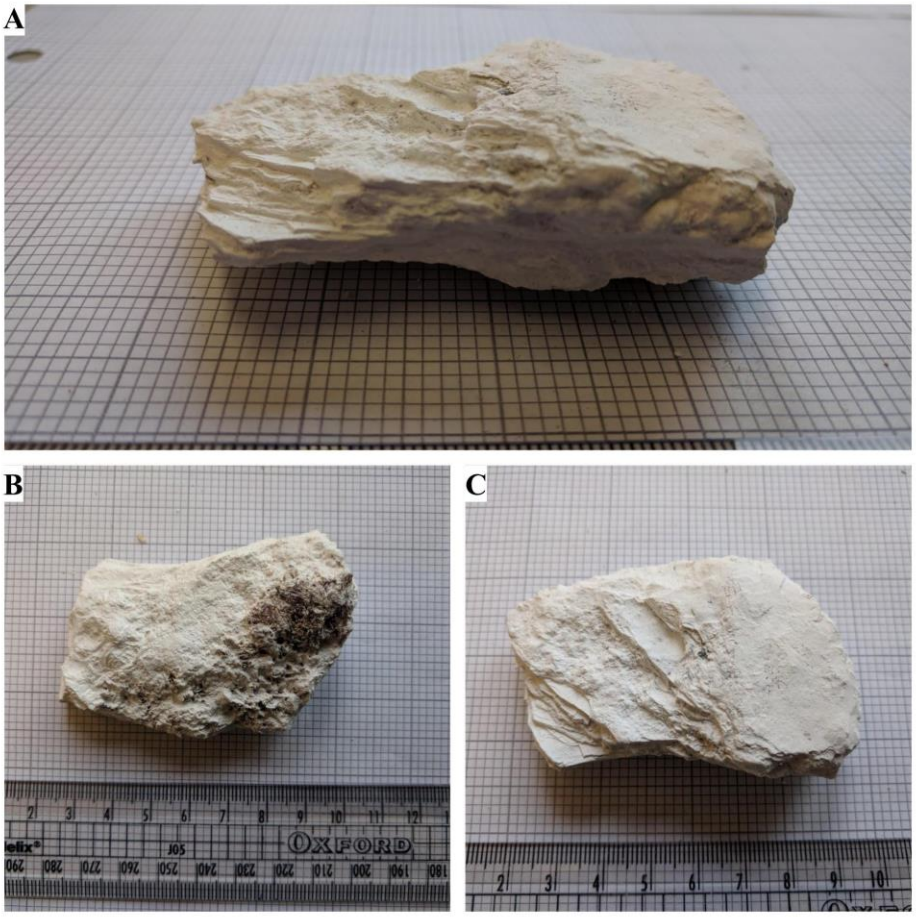

Figure 5.28. Sample taken from the Blue Lagoon geyser. This laminated sinter sample is composed of laminated layers of clean silica. As the cleanest sample in the collection it was assumed to have formed in the relative absence of pigmented bacteria.

Samples collected in Iceland took on more variation in form compared to those from Chile and New Zealand, although this is most likely to do with their collection from a much wider area in comparison to the previous locations. The sample taken from the Blue Lagoon geyser (Figure 5.29) stands out as a clean white sinter sample, with clear laminations and a similar alternating darker/lighter sinter banding pattern of laminations as those of the Brown geysers in Chile (Figure 5.4 & 5.16). Some darker discolouration on

the exterior of the sample is visible but does not extend significantly into the interior of the sample itself.

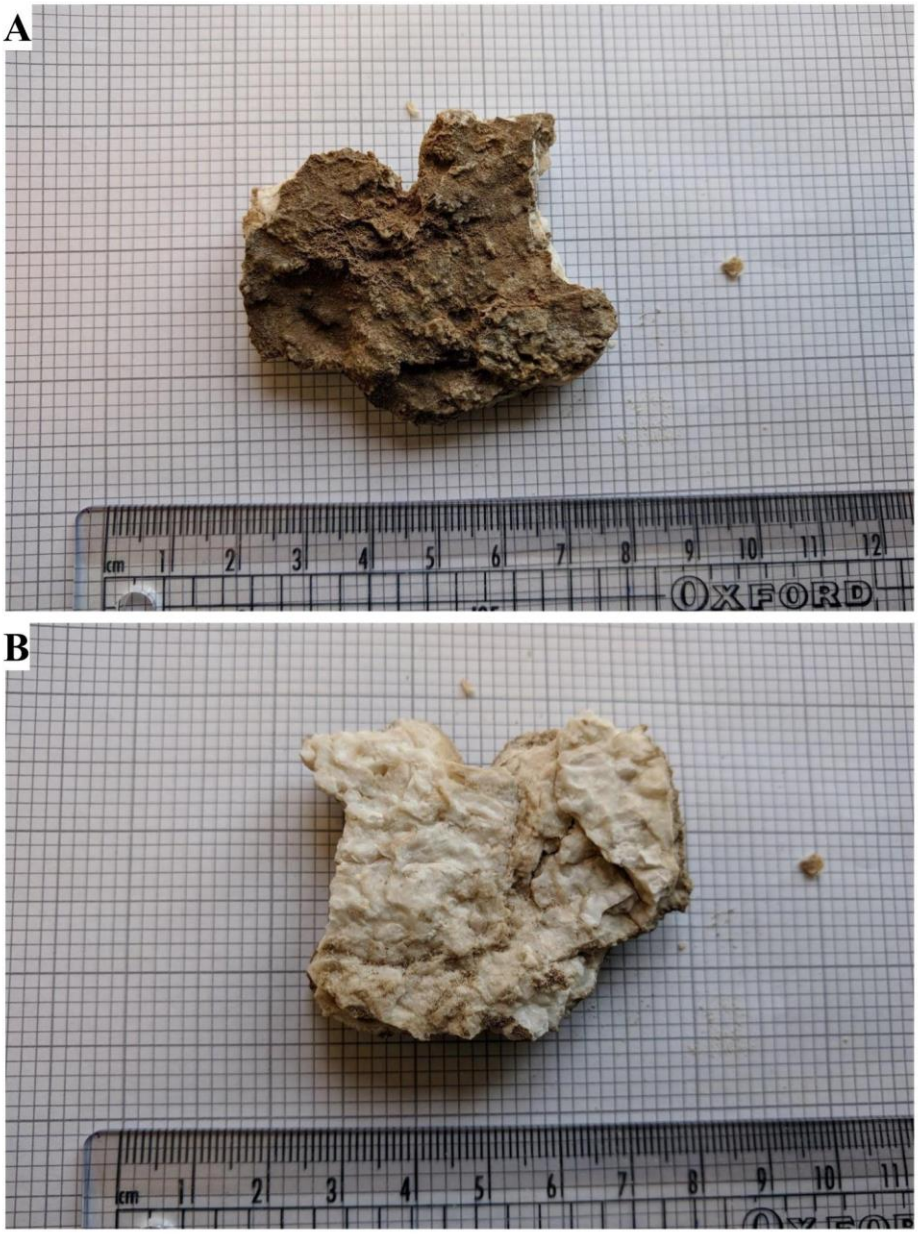

Figure 5.29. Sinter sample taken from the Strokkur geyser. The sample shows a lack of order to its precipitation whilst the dark upper layer shows signs of exposure and accumulation of dirt.

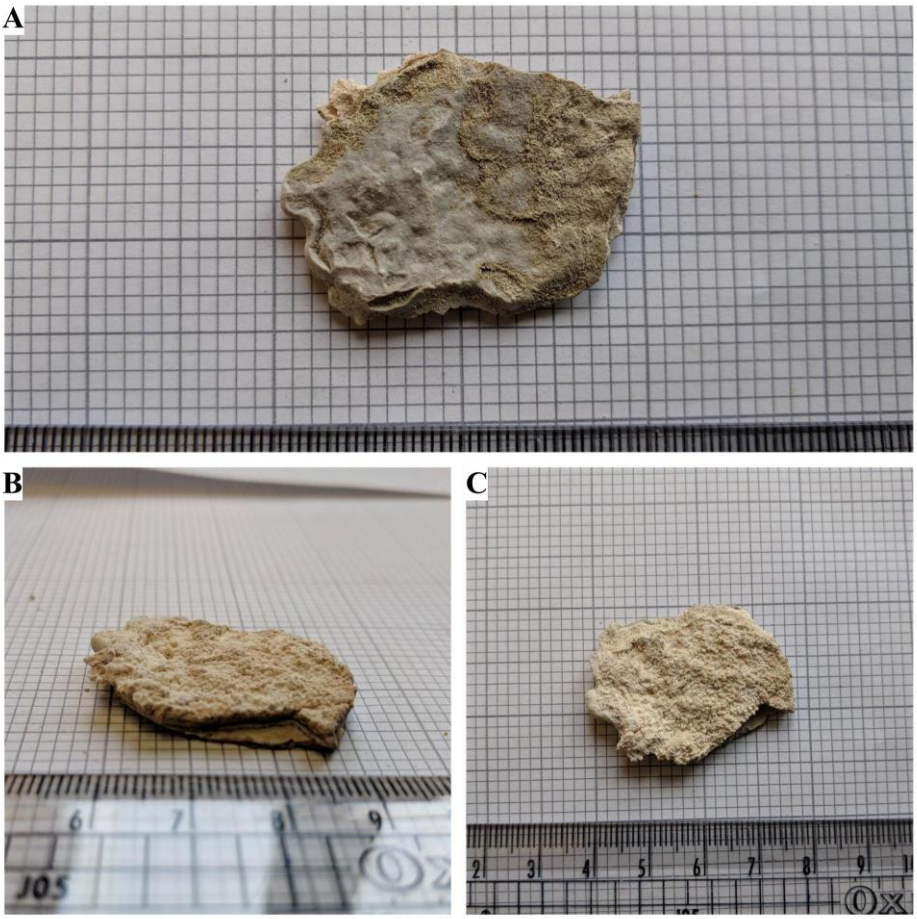

Figure 5.30. Sample taken downstream from the Geysir geyser. The sample is composed of several thick laminations, including a dark central band that can be seen when the edge of the sample has broken off. The upper layer is very coarse (C) whilst the underside of the sample appears to show two different laminations (A).

By contrast the samples from Strokkur (Figure 5.30) and Konungshver (Figure 5.32) more closely resemble some of the samples from Chile. The sample from Konungshver features similar light/brown banding as that of Figure 5.4 & 5.16 whilst the dark surface-facing exterior and lighter interior of the Strokkur sample in figure 5.30 is not dissimilar to that of the sample in figure 4. The underside of the sample in figure 5.30 shows no visible patterning for sinter structure, although if viewed laterally it may show laminations.

Laminations visible in the Strokkur sample in figure 5.30 resemble those of the laminated terrace in figure 5.3C&H.

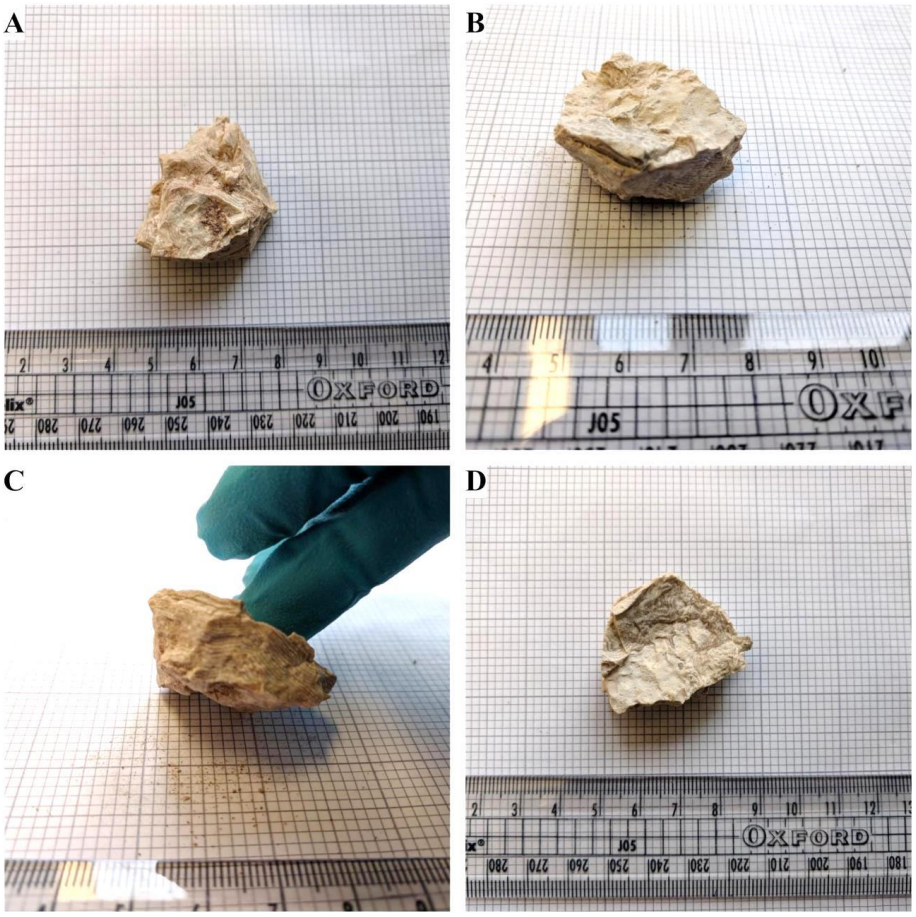

Figure 5.31. Sample taken from Konungshver hot spring. The sample shows some evidence of laminated layers of sinter.

5.4 Discussion

5.4.1 Chile

5.4.1.1 Samples from the Middle Basin

In some samples there is a notable difference in colour compared to other sinters in the area as a result of the presence of carotenoids (Fernandez-Turiel, et al., 2005). It has previously been reported that similar sinters in Yellowstone National Park, USA can be observed to change colour with the seasons as differences in light levels influence the ratio of carotenoids to chlorophyll (Brock, 1994). Those sinters that express a colour difference were located within the same location on the El Tatio geothermal field, and were only connected via the outflow channel. As a result it is assumed that they must share the same water source that results in the difference in appearance, although one other geyser between the two does not share this feature. These off-colour sinters are also simultaneously softer and more brittle than those found elsewhere on the field.

There is a high degree of variance in structure of vents and their local 'splash zone' across the geothermal field. The forcefulness of the output of a geyser will contribute to the morphological characteristics of the surrounding sinter (Jones, et al., 1997), with the most common distinctions being a built up mound of sinter with the vent at the top that result from vents that splutter water out known as a Cone geyser; or Fountain geysers that exist as part of a vent within a pool of water that has the potential to erupt periodically. In El Tatio some cone geysers exist as flatter but wider platforms that result from vents where water flows out over the edge of the vent but not significantly enough to result in significant build-up of sinter immediately around the vent, instead depositing it on a wider built-up platform around the vent that elevates it above the natural plane of the ground. However, it is important to consider that on the timescale in which the sinter structures around the vents in El Tatio formed the activity levels decreased over time, and as a result

the current activity level of vents will not be representative of the conditions in which many of the observed vent structures formed.

Structures in the outflow channels and in pools surrounding the vents are less likely to have been impacted by the disruption to vent activity. The two main features of sinter in the outflow channels and in pools are either small digitate sinter structures or laminated sheets of sinter (Figure 5.3 B, D, H.). A noticeable distinction between these two sinter structures is that they are segregated from each other as a result of the mechanics of their creation. The columnar sinter structures likely form as a result of splash activity from the vent, and notably do not occur below the water line either in the outflow channels or in the pools surrounding the vent.

By comparison, laminated sheets of sinter occur solely below the water line and form different patterns of deposition. Lamination is most likely to occur in water with minimal movement, which fits the samples observed and collected at El Tatio. In most runoff channels there was very little laminated sinter lining the channel bottom but it could occasionally be found in calmer corners of the stream. The segregation of these two forms of sinter occurs due to the inability for water splashes off of the main vent to influence sinter below the surface of the water, as a result the water level around the vent likely influences the manner in which sinter builds up, acting as a limiter for sinter growth in pockets that may be possible to observe in larger depth samples of the main body of larger, built up geysers. Additionally, laminated sinter likely forms unevenly across a geyser as the path of water movement is altered with successive precipitation of sinter.

Campbell *et al* and Hinman & Lindstrom describe the process of wicking as a means of sinter precipitation above the waterline via the movement of water upwards via capillary action (Campbell, et al., 2002; Hinman & Lindstrom, 1996). Silica-rich waters move upwards through microbial mats and precipitate at the surface of the mat due to evaporation, resulting in increased deposition of silica across the microbial mat. Mountain,

Benning and Boerema concluded that the wicking effect was also a cause of in-filling of sinter spicules (Mountain, et al., 2003).

Some sources of digitate sinter feature an additional form of coarse sinter that develops between digitate structures. This is likely occurring through evaporative precipitation of silica concentrated water that collects between the digitate structures (Jones & Renaut, 1997). There is also evidence elsewhere of production of silica residue through steam condensation (Rodgers, et al., 2011).

Vent water across the site feeds into outflow channels that form the source of the Rio Salado that crosses through the Antofagasta region of Northern Chile. These outflow channels were only investigated near the vents at El Tatio. In the middle basin the vents nearest the pair of brown cone geysers had a notably dark red biofilm growing on the surface of the sinter and rocks by the edges and below the waterline and are most likely the same cyanobacteria responsible for the colouration of the geysers they are downstream from. A high volume of water flowed through these outflow channels and dissolved minerals brought up from the deep source of vent water are a likely source of energy for bacterial respiration in addition to photosynthesis (Martin, et al., 2008).

Despite the size, the sample in figure 5.4 & 5.5 are much lighter than they appears, likely a side effect of the high porosity. This is also the most likely reason for the sample being so soft. This is a result of the high volume of bacterial filaments that are found in these sinters which influence the growth of the sinter. Close analysis of the pores via SEM reveal webs of bacterial filaments crossing over. These pores most likely exist due to either; trapped air bubbles created through the movement of turbulent water over the sinter as it formed or as a product of bacterial respiration/photosynthesis. Hinman and Lindstrom suggest that photosynthetic products become trapped by organic films that then silicify leaving pores in the silica matrix (Hinman & Lindstrom, 1996). This may account for the larger pores containing webs of silicified cyanobacteria in some of the samples observed in this chapter.

The latter is a possibility for the formation of the sample seen in figure 6. Like the sample in Figure 7, this sample was obtained from a cavity in the back of the sinter cone, away from the main vent plume and away from the path of vent effluent. A small secondary vent was present within a foot of the cavity that the sample was taken from, however, there were no indications that the secondary vent was erupting in a volume that could influence sinter growth in the cavity at present. Laminations can be clearly observed in all three images; however, images A&B demonstrate that lamination layers are not grown as consistent extensions of the layer, but rather the lamination layer comes together through the combination of separate clumps of precipitated silica binding together on a horizontal plain. By the time an additional layer is able to precipitate above the first, the first layer has hardened and so no binding occurs between layers.

As mentioned previously, there are two brown geysers in the middle basin, both of which feature large silica mounds around their vent with the distinct dark brown colouration. Observations of the large sinter block taken from the northernmost brown geyser reveal that the dark colouration is not shared on the interior of the sample. Whilst the sinter on the interior is not the dirty white of other sinters, it does not share the dark tone of the exterior (Figure 4). This is presumed to be due to weathering of the exterior altering the composition of the sinter material that was precipitated.

Analysis of the sinter in figure 4 via SEM revealed that it was composed almost entirely of silica tubules (Figure 5). The inner diameter of these tubules varied from approximately 5μm wide to 8.5μm wide. Energy Dispersive X-ray Analysis (EDX) showed that the sample was largely composed of Silicon (37.95±3.32 Wt%) and Oxygen (49.2±9.34 Wt%) which has been interpreted as Silica. Carbon was detected but at much lower concentrations (7.83±8.28 Wt%). EDX analysis transverse to the laminations showed a weak pattern of increasing and decreasing silica concentrations, possibly indicative of differences in silicification rate and concentration between laminae, however, this could

also be a result of the uneven and pocketed surface of the sinter resulting in a weaker signal.

The rear of the southernmost brown geyser featured a hollow in the sinter mound that appeared to have collapsed in on itself. This rear hollow was unexposed to vent effluent and at the time there was no evidence of interaction with steam coming off of the vent, however, photographs from other visitors to the area have shown that the entirety of the sinter mound can be obscured by steam at certain times. The hollow is situated near a secondary vent at the rear of the geyser, however, it seemed unlikely that the volume of water ejected at this vent would interact with the hollow, either through direct splashing or from wind-blown spray. Much of the sinter here were fragments of larger pieces, broken either through weathering or anthropogenic means (this geyser is well trafficked as part of tourism in the area).

Two samples which were taken from this hollow that highlighted two of the different sinter features that had been produced when sinter was still being precipitated on this part of the geyser. The samples in figures 5.6 and 5.7 were taken from the same rear hollow but feature different sinter layups. The sample in figure 5.6 features thick laminated sheets of sinter laid down on top of each other with some evidence of microlaminations. There is reduced structural integrity between layers compared to samples such as that of figure 5.4 and figure 5.13 which has required careful handling of the sample to prevent crumbling. By comparison the sample in figure 5.7 features digitate sinter productions laid on top of digitate sinter that has been buried in silica that has precipitated between spicules to form a new basal layer as described in Jones, Renaut & Rosen's 1997 paper on Vertical Zonation of Biota in Microstromatolites (Jones, et al., 1997) and Jones & Renaut's 1997 paper on the formation of silica oncoids at El Tatio (Jones & Renaut, 1997).

The middle basin also contained a hot spring with a pool rim that overhung the pool on the opposite side of the submerged hydrothermal vent, whilst the rim immediately surrounding

the vent rose up from water level with sinter structures on the exposed pool edge. Sinter within a meter the vent was a bright brown/red tint due to the presence of biofilms that coated the sinter surface, whilst the sinter that extended further out was a dark brown/grey within submerged pools and a bright white where exposed to the air (Figure 5.3G). The small pools that surrounded the vent were confined to the immediate area around the vent and were not seen on the sinter surface on the opposite rim. In addition, the white sinter that extended away from the vent gradually diminished in volume away from and around the edges of the hot spring. This is assumed to occur as a result of both the ejection of water being confined to the corner of the pool in which the vent is situated, whilst movement of water spray due to wind does not significantly extend over the pool itself.

The samples pictured in Figures 5.12 and 5.13, a digitate and coarse sinter sample respectively, were collected from one of the small pools near the vent. The digitate sinter sample in figure 5.12 is not unlike the sample taken from the southernmost brown geyser in figure 5.5, however, there's no visible evidence in figure 5.8 of previous sinter spicules that have been buried beneath precipitated sinter. These spicules are most likely to have originated from water splash off of the vent onto a surface which did not retain the water that made impact. Digitate columns of sinter form where silica enriched water from the vent effluent splashed onto the exposed surface leaving a residue of silica. Over time, subsequent splash events result in column growth of sinter through vertical build-up of laminae. Figure 5.3D demonstrates how these digitate structures can become buried over time and a new basal layer forms, resulting in growth of new digitate sinter on top.

It is notable that there is little evidence of spicules that are fully submerged on the sinter surface which lends evidence to the belief that such structures only develop sub-aerially (Jones & Renaut, 1997). Observations of the sinter surface in figure 5.3G & 5.11 show that digitate sinter is most prevalent at the edge of both the main pool and the small pools that have collected around the hot spring. Given Jones & Renaut's (Jones & Renaut, 1997)

work on the cycle of silica oncoids and how sinter spicules can become buried in successive precipitation of sinter due to the inability of splashed water to drain away, it is possible that broader clusters of sinter spicules can inhibit the movement of water away and thus cause precipitation of sinter between spicules similar to that seen in figure 5.3G and detailed in figure 5.2.

Observations via SEM of the digitate sinter sample containing buried spicules (Figure 5.8) shows solid sinter makes up the spicule itself (note the lack of evidence of any laminae), whilst the material buried between spicules is particulate and comes in various grain sizes (Figure 5.8 B & D). In comparison to the spicules at the top of the sample (Figure 5.9) there is no evidence of bacterial silicification around the buried spicule (Figure5. 8 B & D). There is however, evidence of bacterial silicification on the underside of the spicule base where the oldest growth would have occurred (Figure 5.8 C & E).

The patterning of the exposed spicule tips; thicker white sinter bands between large patches of pale sinter, is not unlike that of the surface of the inner pool of the fountain geyser pool in Figure 5.3D. It is possible that the 'disorganized' laminations in the pool share a similar composition to the spicule tips, with patches of silicified bacteria making up the bulk of the sinter surface; however, it is unknown what causes the formation of the thicker sinter bands, both in the context of the sinter spicules and the base of the pool. There is more extensive evidence of bacterial silicification in the spicule tips in these samples than those that Jones & Renaut observed where bacterial filaments were present but not pervasive (Jones & Renaut, 1997).

Jones & Renaut noted that precipitation of silica over time would eventually disguise any evidence of microbial filaments due to precipitation of amorphous silica within all pores in a silica oncoid. It's possible that the same is true for the spicules such as those in figures 5.8 and 5.9. Evidence of bacteria is clear in SEM images of the exterior of an exposed spicule (figure 9), however, the same cannot be said of the buried spicules or the surface

spicule that have been bisected here. There is no evidence of anything other than amorphous silica and some accessory minerals within the spicule, and so it is assumed that filaments become disguised by the progressive silicification that occurs during spicule growth.

Comment [RP18]: Thin section

The sample in figure 5.14 features a much more brittle example of laminated sinter. This is presumed to be due to the environmental differences between the geyser and stream structures, in particular the way that silica colloids are deposited on previous layers. Ideal conditions for lamination to occur are with minimal water movement. Whilst the sample location was calmer than the rest of the outflow stream, there was still enough turbulence to disrupt laminae formation. This turbulence likely also encouraged the incorporation of debris from the outflow channel to become embedded. The sample was coated in a thick biofilm in a similar colouration as the surrounding sinter.

5.4.1.2 Samples from the Upper Basin

The terrace geyser was the largest geyser formation in the El Tatio Geothermal field. As pictured in figure 5.17 the laminations are most obvious in B where the disorganised order of laminations is clearly shown towards the top of the platform edge. Some more digitate sinter structures can be observed sporadically across the face, whilst more widely spread laminations can be observed at the base of the structure, similar to those on the top near the vent itself (Figure 5.3 H). The wet edge pictured in A features similar laminations down the overhang, however, they are in some places more obscured due to the thick biofilm seen here as a brown coating. The constant flow of water has resulted in elongation of the points of sinter on the overhang where water adheres and drops. Very little order can be observed in the sinter that forms in the pool at the bottom, although some digitate sinter can be observed closer to the camera. Vent effluent that collects here flows down towards one of the tributaries into the beginning of the Rio Salado. Whilst the path of water away

from the geyser is easily seen, there is no outflow channel as such, partly due to disruption around the vent by foot traffic. A few metres around the outside of the geyser structure there are a pair of vents emitting steam.

Two fragments from the main Terrace Geyser drop-off are pictured in figure 13. The fragments of laminations taken from the edge of the terrace geyser overhang were notably thicker than the laminations taken from Figures 5.4, 5.5 & 5.11. Accumulation of water at the tip of a lamination likely leads to a more bulbous deposition of sinter where silica colloids accumulate. The presence of biofilms on the sinter surface as seen in Figure 5.17A will also contribute to increased deposition of silica due to the abiotic catalyst effects of bacteria on silica colloid agglutination.

The mystery upper sample in figure 5.20 is defined by the extensive laminations that can be seen throughout, in addition to how the laminations change from the top of the sample to the bottom of the sample. Lower laminations are defined by the presence of pores that extend through the sinter, visible through optical microscopy, with the most likely origin of these pores being from bacterial filaments that have since degraded. Silica sinter separates the pores, and what initially appear to be laminations due to successive layers of silica sinter was actually revealed through SEM to be changes in pore density rather than different laminations of sinter (Figure 5.21). The pattern observed in the lower layers is reflected in the upper layers (Figure 5.22), however, in the upper layers the lateral bands that define the sample are taller and broader than those in the lower layers. Broad bacterial filaments are visible in the upper layers aligned perpendicular to the bands of silica sinter that make up these laminations. The pores at the bottom of the sample are also aligned perpencicular to the laminations, however, this is only clear under optical microscopy. Assuming that continued sinter deposition results in the pattern of thicker silica laminations near the surface giving way to microlaminations in deeper layes, there is no conclusion on how these bands appear to contract so finely.

Comment [RP19]: Measure pore width vs filament width

Comment [RP20]: This will probably need to be confirmed as it is one of the most interesting parts
Discussed in next paragraph

One possibility for how this occurs is similar to the wicking process described by Hinman & Lindstrom (1996) and Campbell et al (2002). Whilst both groups discussed wicking in the context of water moving upwards through a substrate via capillary action, it is possible that the same action could be facilitated downwards through an otherwise impermeable substrate via the web of filaments that permeate the sinter. This would explain the loss of porosity in older (deeper) sinters as silica precipitation within pores such as those in younger sinters would cover evidence of bacterial filaments as described in Jones & Renaut (1997) (Jones & Renaut, 1997). However Jones and Renaut note that the loss of porosity "completely disguises" bacterial filaments in these older sinter laminations, but the presence of micropores in the deeper sinters (such as those in figure 5.21) that orientate in the same pattern as bacterial filaments between surface laminations (Figure 5.22) suggests this is not universally true. If micropores represent the remnants of bacterial filaments this would represent a possible visual biomarker.

The micropores present in this sample also contain high concentrations of NaCl in the form of halite crystals. The presence of halite around the opening of the micropores is not universal but has most likely been drawn out during the cutting process by the water that circulates with the cutting blade.

The lower layers of the sample in figure 5.21 are characterised by the high number of small pores approx. 2-4μm in diameter. The cutting process brought out NaCl in the form of Halite which can be seen as the whiter material surrounding some pores in images A and B, and can be seen as white/grey blots on the left of the image in C . Closer inspection of the structure of the banding seen most clearly in C and D reveals that the distinction between bands originates as a result of a reduction in pore density across the layer, and a corresponding increase in silica concentration around the pores.

In Contrast to the deeper layers of sinter and the tight banding as seen in Figure 14, the upper layers feature much broader bands of silica sinter and silicified bacterial filaments

but still retain the same sinter>filament>sinter>filament pattern. The image in figure 22 is at the same scale as that of Figure 5.21 C, demonstrating that sinter layers may be compressing and filling out over time as they transition from being the uppermost layers of sinter to a deeper layer as more sinter is deposited.

5.4.2 New Zealand

5.4.2.1 Waikite

Comment [RP21]: Geyser activity discussion in Jones & Renaut 2003, Petrography and genesis of spicular and columnar geyserite from the Whakarewarewa and Orakeikorako geothermal areas, North Island, New Zealand

Of the three samples taken from the Waikite discharge apron, the first two were from an inactive collapsed vent that was situated in a hollow in the ground near the base of the discharge apron. The Waikite discharge apron and all of the geysers situated on it have been dormant since the 1960's. Whilst no evidence of water was visible at the site at the time of sampling, it was assumed that the vent was likely a part of a fountain geyser due to the lack of evidence of run-off streams in the vicinity. Of the samples pictured in figure 5.27, B & C are notably denser than the sample in D and E, and are composed of thick laminated sheets of sinter and a very coarse surface. By comparison the sample in D and E is laminated however, these laminations are disorganized by comparison. The sample is also very porous on its upper surface (E) and is pocketed in places. The pit from which the samples were taken was surrounded on all sides by vegetation. The presence of this vegetation could be reflected in the biomarker composition of the samples as plant material both on a macro- and microscopic level would be incorporated during the precipitation of silica and the resulting encrustation (Jones & Renaut, 2011).

The third sample (Figure 5.26) was taken from near the top of the discharge apron on its flank and in contrast to the samples taken from the bottom was not in close proximity to any vegetation. Despite this it should be noted that the vegetation that covers the geothermal area is of a significantly higher biomass than the vegetated samples taken from Iceland, so even this 'non-vegetated' sample should be considered more exposed to plant

material than other more sparsely vegetated sites in Iceland and New Zealand. Like the samples taken from the foot of the discharge apron, the geyser was dormant and much of the sinter around the vent was cracked and broken.

5.4.2.2 Ngararatuatara

In contrast to the samples from Waikite, the Ngararatuatara geyser (figure 5.25) is an active fountain geyser. Geyser activity is confined to the rim of the pool, with little ejection of water outside of it. Most water leaving the confines of the pool is in the form of steam. The pool is situated in a depression in the ground, with the rim of the pool overhanging the surface of the water by approximately 20cm. The sample taken from Ngararatuatara is a heavy block of sinter that is porous on its upper surface. The block was situated within the inner lip of the rim of the pool where splash from the pool is the main source of silica for precipitation.

There are two potential sources of non-hydrothermal bacterial biosignatures in this geyser. The first is the surrounding vegetation around the geyser on all sides. The second is that Ngararatuatara is consistently used as a cooking pot by the local tourism industry. Water in Ngararatuatara is confined to the hotpot and thus has no method of escape, leaving it likely that any potential contamination brought into the system through tourism activities remains localised within the hotpot itself, and thus likely to be incorporated into the silica matrix at the edges on the inside of the pool. The frequency of the hotpot's use for cooking is not known, making calculating the extent to which contamination occurs not possible.

5.4.3 Iceland

Samples collected from Iceland were collected by a colleague during a taught course that visited each site. As a result the description of sample environment is limited.

The samples collected from Iceland are the most widely spread of any of the samples collected, spread across the southwestern quadrant of Iceland rather than confined to one geothermal area as with Chile and New Zealand. It would therefore be expected that GC-MS results in chapter 7.3 would show much greater variation in distribution of organic material.

5.4.3.1 Blue Lagoon

The Blue Lagoon sample (5.29) was collected from the tourist location of the same name. The Blue lagoon is a man-made geothermal spa with waters rich in silica and sulphur, supplied from the geothermal plant nearby. Its use as a tourist attraction introduces additional opportunities for contamination; however, like the Ngararatuatara geyser in New Zealand, the potential for contamination from human sources is still quite low due to the overall volume of water that makes up the pool.

The sample in question is the one of the cleanest examples of a silica-based sinter from any of the samples obtained from Chile, Iceland or New Zealand. It is pure white on its surface however; the interior of the sample is clearly consisted of laminated layers of sinter that form the oncoid. The sample was obtained from the bottom of the main pool that forms the lagoon where it would be vulnerable to direct human contact by those utilizing the geothermal pool. Being a geothermal pool, the high likelihood of sweating in hot waters introduces another potential source of contamination into the waters via the accumulation of fatty acids (Nunome, et al., 2010; Takemura, et al., 1989).

5.4.3.2 Geysir & Strokkur

Geysir (5.30) and Strokkur (5.31) come from the same hydrothermal field in the Huakadalur valley, a geothermal area that also incorporates mud pools and fumaroles. The area is sparsely vegetated by grasses and small trees species which could provide a source of vegetative contamination, though this would be expected to be a smaller contribution than is expected in the samples taken from Whakarewarewa, New Zealand.

Geysir is only periodically active, with most eruptions stimulated by the addition of surfactants by local tourists or scientists. In contrast to Geysir, Strokkur erupts on a regular schedule of approximately 6 minutes between eruptions, possibly allowing for a wider spread of precipitated material. By contrast the precipitated material from Geysir will be confined around the edges and floor of the pool. Pool geysers are unlikely to result in the sorts of precipitated deposits described by Jones & Renaut (1996) and displayed in Figure 5.1. The lack of these sorts of splash deposits could result in bacterial encrustation being more extensive due to the encrustation of surface biofilms. If this were the case then seasonal blooms of these biofilms could help explain the dark/light laminations seen in some samples as being a seasonal occurrence. This could also explain the variation in pore concentrations in the lower layers of the sample discussed in 5.4.1.2.

5.4.3.3 Konungshver

Konungshver (5.32) is a hot spring situated in the same Geysir field as Geysir and Strokkur, however, it is considered to be a dead geyer (Barth, 1947). Konungshver is fed from below by a shaft in the centre of the hot spring that is blocked by boulders; however it is not thought that Konungshver has ever fully erupted. The sample obtained from Konungshver was taken from the outer rim of the hot spring where the water met the edges.

5.5 Conclusions

The variety of sinter forms has been documented here, and the influence of their local environment on their formation has been discussed. Silica sinters have been shown to have varying degrees of microbial encrustation, and amongst these samples there are varying degrees of visual evidence. Samples such as that of the Brown Geyser in the middle basin

of El Tatio are so rife with bacterial filaments that the overall density of the sinter is significantly reduced, whilst samples like the digitate sinter taken from a small fountain geyser in the same area have very little direct visual evidence of microbial encrustation throughout the sample but do contain some surface indicators in the column tips.

Samples taken from New Zealand were mostly from inactive geysers and present a much drier, more fragile grey sinter than those from Iceland and Chile which are actively precipitating. Micro laminations in the New Zealand samples are less obvious but thicker laminations are still present. Comparisons between the older New Zealand samples and the samples from Chile and New Zealand will be discussed in Chapter 7.

The Icelandic samples are smaller than the samples taken from New Zealand and Chile though this is a result of sampling limitations. Perhaps of note is that the Icelandic samples will experience extremes of daylight and night depending on the time of year. It is possible that the prolonged periods in which photosynthesis is active and inactive could provide a seasonal biomarker in larger samples between lamination layers.

Visual identification has been shown to be a potential strong biosignature when the structure of material is preserved. However in the context of Mars it is unlikely that any visual preservation would remain fully intact. The loss of evidence can take multiple forms such as the pores in the Middle Basin sample in Chile or the full silicification of bacteria as described in the literature (Phoenix, et al., 2000; Phoenix, et al., 2001).

The potential incorporation of plant material has also been considered. Silica precipitation is non-specific to and will incorporate any material present, with varying degrees of preservation. This also counts for any plant waxes that might coat silicified surfaces and

become preserved in the silicified matrix. This will be tested for and discussed further in chapter 7.

6 Characterizing the diurnal cycle of high altitude soils of the Chilean Altiplano and their role as a Martian Analogue

6.1 Introduction

The Altiplano in western South America has been proposed for use as a site of astrobiological interest (Hock, et al., 2005; de Silva, et al., 2002; Hock, 2008; Pulschen, et al., 2015). For this study the volcano Sairecabur was chosen due to prior studies on the volcano's flank and road access to sampling sites up to 5971m . Sairecabur is part of the Sairecabur range which is divided by the Chilean-Bolivian border and includes the Escalante and Licancabur volcanoes (de Silva & Francis, 1991). Licancabur is notable for both being the site of the highest recorded UV radiation on Earth (Cabrol, et al., 2014), in addition to hosting one of the highest altitude lakes in the world in its crater (Cabrol, et al., 2014; Hock, et al., 2005). Sairecabur provides conditions that more closely approximate those of Mars than other potential Martian analogues, most notably the UV radiation environment (Cabrol, et al., 2014; Cockell, et al., 2000; Patel, et al., 2002), sub-zero atmospheric temperatures accompanied by solar heating of the surface (Fischer, et al., 2016), reduced precipitation at lower altitudes and the formation of a rain shadow in the Central Andean belt (Houston & Hartley, 2003; Rutllant & Ulriksen, 1979; Garreaud, et al., 2003), and reduced atmospheric density due to high altitude (4000-6000m above sea level). The region was classified as *BWk*, or a cold desert climate, under the Köppen climate classification (Kottek, et al., 2006). It is important that a Martian analogue satisfy some of these parameters, but the parameters it needs to match are dependent on the particular study being conducted.

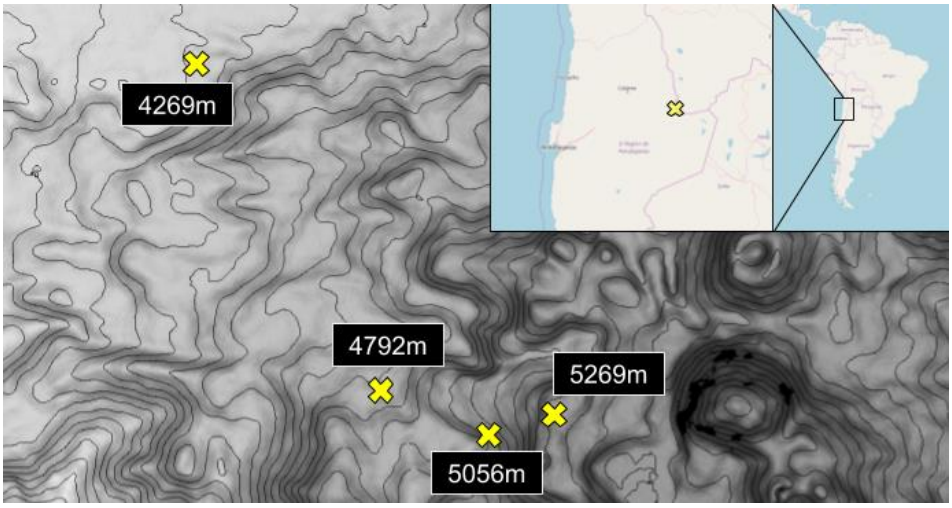

Figure 6.1. Sample locations on Sairecabur Volcano, Northern Chile. (Map insert © OpenStreetMap contributors)

Geological studies can ignore the present Martian environmental parameters that would restrict studies focusing on life and parameters that restrict life. As an example, it has been shown that certain geological deposits on Mars can closely resemble similar geological deposits on Earth. The inability to directly study Martian geological sites can be circumvented by studying the formation of similar sites on Earth. One such example is a study establishing the Tinto River in Southwestern Spain as a Martian analogue for the *Terra Meridiani* (Fernández-Remolar, et al., 2004). The Tinto River basin is an iron and sulfate rich environment influenced by iron biogeochemistry which features ancient iron formations which are seen as evidence of geological evolution towards a more hematite rich composition based on an aqueous origin. The low pressure atmosphere and radiation environment of Mars does not restrict geological studies in the same manner that biological or chemistry-based studies are restricted, as the parameters responsible for change on a geological time-scale are independent of many of the parameters that will restrict life on shorter time scales.

However within biologically focused studies the limiting factors on a Martian analogue are dependent on the environmental conditions of the analogue. Two of the most commonly cited Martian analogue sites are the Atacama Desert and the Dry Valleys of Antarctica. Each site shares low soil biomass controlled by abiotic factors (Navarro-Gonzalez, et al., 2003; Horowitz, et al., 1972; Paulino-Lima, et al., 2013), low humidity with little precipitation (Clarke, 2006; Tamppari, et al., 2012) and are subject to a higher UV dose than the global average (Cordero, et al., 2016; Cary, et al., 2010). However both of these sites feature drastically different temperature profiles both for the soil and the atmosphere, as well as different seasonal light levels. The Dry Valleys of Antarctica are cold year round, and due to seasonal axial tilting of the planet will move between 24 hour sunlight to 24 hour darkness depending on the season. By comparison the northern Atacama Desert has a much narrower range of daylight times, between 10.5 and 13.5 hours a day due to its lower latitude. The low latitude of the Atacama also results in stronger incident UV (Cockell, et al., 2008; Piacentini, et al., 2003; Paulino-Lima, et al., 2013), as well as higher temperatures, particularly at the surface due to direct solar heating (Rondanelli, et al., 2015).

The purpose of this study is to test the higher altitudes of the South American Altiplano as a new Martian analogue site to determine whether it provides a better fit to the necessary analogue parameters for studies on the Martian subsurface soils than McMurdo dry valleys or the Atacama Desert. The focus is to establish the nature of the diurnal temperature and water cycle just below the surface, to determine whether similar comparisons could be made to Mars. The initial decisions to undertake this study were based off of the initial discovery of water in the form of ice from the Phoenix lander in 2008 (Hecht, et al., 2009). Phoenix found lumps of ice after uncovering the subsurface, which was later confirmed to be water-ice due to the extended period of time it took to sublimate. In 2011 the Mars Reconnaissance Orbiter's High Resolution Imaging Science Experiment (HiRISE) would

observe dark downward streaks from rocky outcrops into small channels, forming in the late southern spring and summer at latitudes of 48ºS to 32ºS where surface temperatures are between 250-300ºK (McEwen, et al., 2011). Due to a lack of geothermal heating below the surface pure water would freeze almost instantaneously when part of a semi-pervious system based upon Martian environmental characteristics (Goldspiel & Squyres, 2010). Goldspiel and Squyres (2010) did not rule out the possibility of a pure groundwater emergence system, but acknowledge that the circumstances required for such a system to occur would be unusual in the context of Mars. Brine based liquids can suppress the freezing point of water enough that during the Martian summer water is capable of staying liquid beneath the surface, which could lead to the formation of recurring slope lineae (RSL). Ojha *et al.* found evidence of hydrated salts in 4 locations when RSL activity was most active (Ojha, et al., 2015). The presence of hydrated salts was consistent with the hypothesis that RSL occur as a result of subsurface brine activity.

The confirmation of water-ice near the surface of Mars, as well as the confirmation that the ice is capable of a phase-change from solid to liquid opened up a possible hypothesis for diurnal depth-dependent phase-change cycles beneath the surface. Whilst the atmospheric temperature on Mars is well below the freezing point of water, solar heating of the surface can go above 273 Kelvin at certain latitudes. Dependent on time of day, heating of the surface could result in the melting of the subsurface permafrost down to a certain depth, and the moving boundary of the ice/liquid layer could be capable of providing a possible niche for life if requirements for nutrition and radiation protection are met.

In order to establish the pattern of the diurnal cycle that in high altitude Altiplano soils, temperature and humidity changes below the soil surface were monitored across a depth gradient using dataloggers to establish this cycle over a period of days. iButton dataloggers and a pair of Campbell Scientific CR1000 dataloggers would be used to monitor the diurnal cycle on a short and longer term respectively.

6.2 Method

6.2.1 Effectiveness of dataloggers at sub-zero temperatures

This study had been attempted a year prior by members of the lab group utilizing a Campbell Scientific CR23X datalogger (Thomas, 2017), which either failed to record or failed to save the data obtained. It was thought that this was most likely due to the extreme cold of the site drained the on-board batteries faster than anticipated despite the unit itself being rated to operate at temperatures down to -25ºC in the normal operating range. To avoid a similar scenario occurring again it was decided that the Campbell Scientific CR1000 dataloggers would be powered by a 330Amp car battery each as the high capacity of the battery and the low power requirements of the datalogger would minimize the danger of data loss due to power loss.

The datalogger and battery setup was tested in laboratory conditions prior to the departure to monitor battery drain and data storage concerns from the previous year. A laboratory battery (Lead acid, 12V, 7Ah) was used as the control representing a smaller power source that would not be as resistant to temperature changes as the larger car battery. Tests were run continuously over an 18 day period alternating between two 4.5 day stints at room temperature and two 4.5 day stints in a freezer set to -18°C. Installation of the dataloggers in the Chile sites was intended to be for a similar timescale.

A sample container filled with sand and a small volume of water was used to test datalogger probes that would be utilised during the experiment (Table 1). A laboratory freezer maintaining temperatures ~-18ºC was used to house the dataloggers, battery and sample container for the duration of the cold test, whilst the unit was left on a laboratory bench to operate at room temperature (15ºC-20ºC) as a control. Temperature probes were planted in a sand bucket as a means of tracking temperature during the experiment. A CMP3 solar pyrometer was also included in the test as part of the planned datalogger setup

for Chile, as well as providing a means to correlate temperature movements with sun activity or the opening of the freezer. Whilst set up in the laboratory at room temperatures the experiment was situated near a South-East-facing obscure glass window. A laptop was used to monitor and obtain data from the dataloggers at regular intervals using Campbell Scientific's PC200W datalogger software. Testing was able to be performed uninterrupted except for transitions between batteries and location.

The potential for power loss was monitored by voltage measurements by the datalogger itself. An increase in charge-transfer resistance between the electrode of the battery and the liquid within is the primary cause of voltage loss in batteries in cold conditions. When a sufficient drop in voltage occurs it could cause a power loss to the datalogger resulting in loss of data like that observed the year prior. The datalogger (Campbell Scientific CR1000) voltage requirements lie between 9.6V and 16V whilst the battery operating voltage in regular conditions is approximately 12.6V. Batteries were not recharged in between test locations.

Table 6.1. Probes available for data monitoring in high altitude Chilean sites

Probe	Measured Parameters	Number
Campbell Scientific 107 Temperature Probe	Temperature (ºC)	8
Campbell CS655 Soil Humidity Probe	Volumetric Water Content (m^3/m^3)	2
	Electrical Conductivity (dS/M)	
	Temperature (ºC)	
	Permittivity (unitless)	
	Period Average (nSec)	
	Voltage Ratio (Unitless)	
Campbell CMP3 Pyranometer	Flux Density (kW/m^2)	1
	Total Flux (kJ/m^2)	
Decagon Dielectric Leaf Wetness Sensor	Voltage (mV)	3
	Minutes Dry (Minutes)	
	Minutes Wet or Contaminated (Minutes)	

	Minutes Wet (Minutes)	
Campbell CS215 Air Temperature and Humidity Probe (Fitted with Sunshield)	Temperature (ºC) Relative Humidity (%)	2

6.2.2 Monitoring the diurnal cycle in Altiplano soils

6.2.2.1 Sample Sites and On-Site Measurements

The volcano Sairecabur on the Chilean/Bolivian border (Figure 1) would be monitored from its base to the higher altitudes towards the peak. Due to previously severe weather the upper reaches of the volcano were unreachable due to ice on the road, the highest altitude accessible being ~5269m. The base of the volcano was situated at 4296m, while a lower site situated in the Atacama Desert (2462m) was used as a comparison. Two intermediate sites were also monitored at 4792m and 5052m.

Limitations on total volume of samples restricted sampling to four sites. Sites were selected based on ease of access, lack of evidence of human or animal contamination (tracks from feet, tyres, etc), proximity to plantlife where present, and a visual assessment of how the environment has changed with altitude (loss of biodiversity/volume, temperature). It was also necessary that selected sites were able to be sampled in the same manner both as part of soil sampling and hand-held temperature, air humidity, radiation measurements and thermal imaging (similar exposure to sunlight).

Sample sites were investigated on successive days over a 4 day period. At every site a small trench was excavated for sampling at different depths as well as measurements timed to between 1:30PM and 2:00PM at each site for all parameters in order to obtain comparable data. Soil moisture levels were measured using a Decagon EC-5 Soil Moisture

probe. Measurements were taken in 2cm intervals down to the lowest depth attainable which was site dependent based on the depth of the ice layer. Additional measurements of atmospheric temperature and relative humidity readings were taken on arrival at the site, as well as measurements of UV radiation in all 3 sub-ranges and measurements of photosynthetically active radiation at the surface. Care was taken to ensure that all measurements took place at approximately the same time of day at each site however, minor differences in weather between each sampling day will likely have affected some results. A FLIR-E49001 Thermal Imaging Camera was also used to exam surface solar heating rate by scraping away ~5cm of the top soil and comparing temperatures before and after exposure as a means of examining the influence of direct surface heating.

Soil was taken from the trench at predetermined depths in order to assess how the composition of organic content changed with depth. As a result extra care was taken to clean and sterilize excavating equipment with three washes in sterilizing alcohol to ensure that no contamination between layers took place. Prevention of sample contamination also extended to on-the-spot soil moisture readings, as the dry topsoil was at risk of collapsing into the hole which could obfuscate results, or the instant sun exposure that was capable of immediately causing evaporation of subsurface soils. To compensate for this care was taken to prevent the edges of the pit from collapsing in, as well as ensuring that soil moisture measurements occurred at each depth immediately after being unearthed and that all measurements with the exception of UV radiation measurements occurred in the shade.

At all sites hand held measurements were taken of atmospheric temperature, atmospheric relative humidity and UV and photosynthetically active radiation (PAR) irradiance. Visits to sites were timed so that measurements took place at approximately the same time of day, however, differences in weather between days will have offset these measurements from the expected differences due to the increase in altitude.

A thermal camera was used to determine surface heating rates, by exposing soil 5cm below the surface and capturing images of the soil immediately after excavation and after sixty seconds of exposure to direct sunlight.

Samples taken from the site at 5056m were sorted via sieving and weighed according to grain size in order to determine whether soils were homogenous or heterogeneous in nature (Table 2).

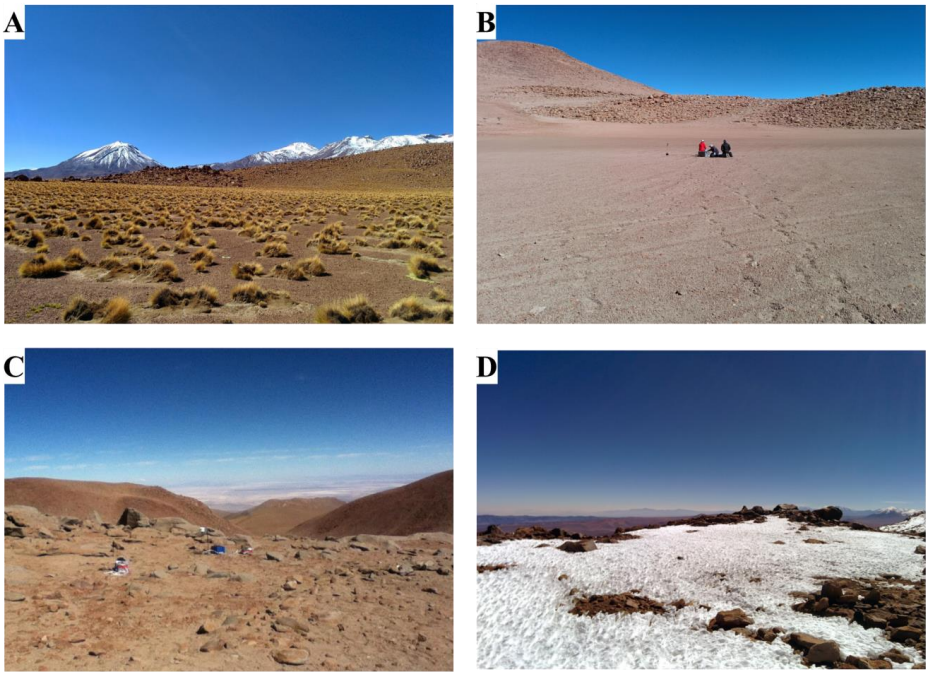

Figure 6.2. The local environments of data collections sites on Sairecabur volcano. [A] The lowest site situated at 4269m. *Jarava ichu* features as the predominant plant species, separating barren patches of top soil. Greater species diversity can be found amidst rocks clustered around the hillside, most notably lichen species that can resist the UV environment (Chollet-Krugler, et al., 2013) (not pictured). Majority of species are likely pioneer species. [B] The second lowest site at 4792m was characterised by a large flat plateau of largely undisturbed topsoil. The site of the sample trench was situated away from tyre tracks that were sporadic across the plateau. No soil plant life was observed in exposed areas but rocks on the hills featured lichens and sheltered smaller plants. [C] The second highest site at 5056m was selected as the datalogger installation site due to being the highest area of open soil that could safely be accessed. As with the site at 5269m vegetation was sparse with sporadic lichen growth. [D] The highest site at 5269m lacked any surface soil vegetation, with sporadic presence of lichen on rock surfaces. Recent weather events had resulted in the majority of the soil surface being covered in a layer of penitente ice. The presence of ice prevented the safe access of any higher site. Dataloggers were initially planned to be installed at the highest site accessed but due to the dangers posed by the ice they were installed at the second highest site.

6.2.2.1.1 The Atacama Desert (2462m)

The Atacama site was located in the Antofagasta region 60km away from the high altitude sampling sites, and an altitude of approximately 2462m. The site was covered in dead and desiccated plants are presumed to have bloomed during a previous wet spell of weather. There was no evidence of live plant life, but it did provide evidence that despite the harshness of the dry and hot weather in the Atacama, plants were able to remain dormant in the subsurface waiting to bloom. Evidence of water activity could be seen in the dry, cracked mud that could be found across much of the area, particularly on the downslope side of the road, whilst satellite imagery of the area showed evidence of past water movement. The sampling site was situated away from any plants and the road.

6.2.2.1.2 Sairecabur lower (4296m)

The site at the base of the volcano at 4296m was characterised by dry and dusty topsoil, with patches of shrubbery. Surface conditions were monitored both in an exposed area of topsoil and in the shadow of the shrubbery, but in both cases care was taken to ensure that the sample area did not occur in close proximity to plant-life due to sample collection work being done in the same location. Despite these precautions the sample pit was permeated with roots. Subsurface monitoring was performed overnight with iButtons from surface level down to 25cm in 5cm increments in order to obtain a more detailed profile of changes in temperature and soil humidity at depth.

6.2.2.1.3 Sairecabur plateau (4792m)

The site at 4792m was situated on a large plateau on the volcanoes' western flank exposed to the North and South. Little plant life was visible on the plateau itself, but small plants and lichen were present in the surrounding rocky outcrops. The sampling area itself was devoid of any plant life, and no evidence of plant life was found in the surface after excavation. The same depths were excavated as at the previous site, and monitored with the iButton Dataloggers overnight.

6.2.2.1.4 Sairecabur Upper (5056m) & Datalogger Installation

The site at 5056m was situated near the roadside and was one of the few locations above the 4792m site to have workable soil. However the ice layer that was expected to be found beneath the surface soil was found much closer to the surface than the previous sites. Due to the difficulties of digging at altitude, the depth of the ice layer would be the lowest depth used at the site. In addition to the iButton dataloggers, this site was used to install the CR1000 dataloggers. The datalogger probes were installed in the same manner as the iButton dataloggers at other sites. It was initially planned to install a pyrometer as part of the CR1000 datalogger probes but the pyrometer unfortunately did not remain intact during transit to Chile. The dataloggers and iButtons were installed at this site for a period of 3 days and nights to obtain a more complete picture of several diurnal cycles. The days following the insertion of the long-term dataloggers had temperatures below the average for the region and this is reflected in the data. However the expected pattern of diurnal cycles was not disrupted by the temperature changes.

6.2.2.1.4.1 Datalogger Probe Loadout

Two dataloggers were setup with the probes listed in table 6.1 split between them. All temperature probes and the leaf wetness sensors were equipped onto the same datalogger, whilst the CS655 Soil Humidity Probes were equipped on separate dataloggers. The CS215 air temperature and humidity probes were equipped on the second datalogger along with the pyranometer.

Leaf Wetness Sensors were installed on one of the dataloggers to determine the presence and state of water in the depth at which the sensor was installed. Leaf wetness sensors are normally used to monitor the dew point in plants and trees, but in an environment that is suitably dry, such as the Altiplano, leaf wetness sensors can also act as a soil moisture sensor. The sensors function by tracking the increase in conductivity on the surface caused

by increased water surface area on the face of the sensor. The Decagon Dielectric Leaf Wetness Sensor that was used during this experiment was also non-hygroscopic, ensuring that moisture pulled out of air would not disrupt the result, although air humidity is so low at the altitudes where testing occurred that this is unlikely to have been a problem. To distinguish between 'wet' and 'dry', the leaf wetness sensor has a set threshold at which the sensor is deemed to be wet, with an additional 'contaminated' result between dry and wet where conductivity is high enough to be deemed wet but contamination could possibly have caused the result. In the data gathered from the 5056m Altiplano site 'contaminated' results were the least seen of the three options, but still represented up to several hours of data. Contamination results occurred during the transition between wet and dry states and as such are interpreted here as the beginnings of moisture formation in the morning as ground ice melts, and from water movement back towards the surface after the sun sets and the corresponding formation of ice.

Temperature probe data gives a good indicator as to the water phase transition that is expected to be occurring in the soil at particular depths but the state of water at each depth can only be inferred. The addition of the Leaf Wetness Sensor data clarifies whether liquid water is present at the probe surface as a result of the soil becoming oversaturated, in conjunction with the soil humidity probes which indicate the extent to which the soil has become saturated. Leaf Wetness Sensor probes were inserted 0-5cm from the surface, 10cm from the surface, and 25cm from the surface. Sensor readings <274mV are classed as a Dry result, whilst readings >=284 are considered wet. Contaminated results are considered wet but their inclusion is at the user's discretion according to the state of the probe upon inspection.

6.2.2.1.4.2 Datalogger Analysis

Datalogger data was analysed collectively to understand how the environment described during the trench digging process was reflected in the soil temperature and humidity data that was recorded. Due to abrupt change in datalogger probe conditions between being activated and being implanted in the soil at their set depth, and the disruption to the local temperature and humidity state due to the trench being refilled, data used for analysis discounted an initial 30minute period at the start of the data recording during which the environmental conditions returned to normal conditions.

Simple graphical representations of the data were created in Microsoft Excel to identify trends in the diurnal cycle and determine how local environmental conditions led to those trends.

The Pearson correlation coefficient was calculated between data lines to determine how temperature and humidity data correlated through the data recording period. The Pearson correlation coefficient determines the degree to which a bivariate dataset is in a linear relationship. The Pearson correlation coefficient ranges from -1.0 to 1.0. -1.0 would represent a perfectly inversely correlated pair of datasets, whilst a coefficient of 1.0 represents a perfectly positive correlation of datasets. A correlation coefficient of 0 would represent a pair of datasets with no correlation between them.

6.2.2.1.5 Sairecabur Top (5269m)

The final site inspected was located at 5269m and was iced over. Previous wet weather in the region was thought to have caused the large ice deposits in the higher altitudes, as well as contributing to the formation of dried mud and the dead plant blooms found at the lower Atacama site. On the day that measurements were took weather conditions had deteriorated from the previous days of measurements, which will likely have impacted atmospheric humidity and temperature measurements. When the trench for this site was excavated, ice

was struck at only 7cm below the surface layer, greatly limiting sample options compared to previous sites. Soil moisture, atmospheric readings and thermal camera data acquisition were still performed at the site. However as a result of the shallow ice layer and the dangers associated with accessing the site, it was decided not to insert any dataloggers.

6.3 Results

6.3.1 Effectiveness of dataloggers at sub-zero temperatures

The purpose of these laboratory tests was to ensure that under any load the dataloggers would be capable of operating in the extreme cold of the Altiplano by stress testing them in a freezer for a set period of time, whilst monitoring data storage and power draw from the battery. By monitoring battery draw the necessary battery requirements and equipment setup for monitoring the diurnal cycle in the Altiplano could be met in advance.

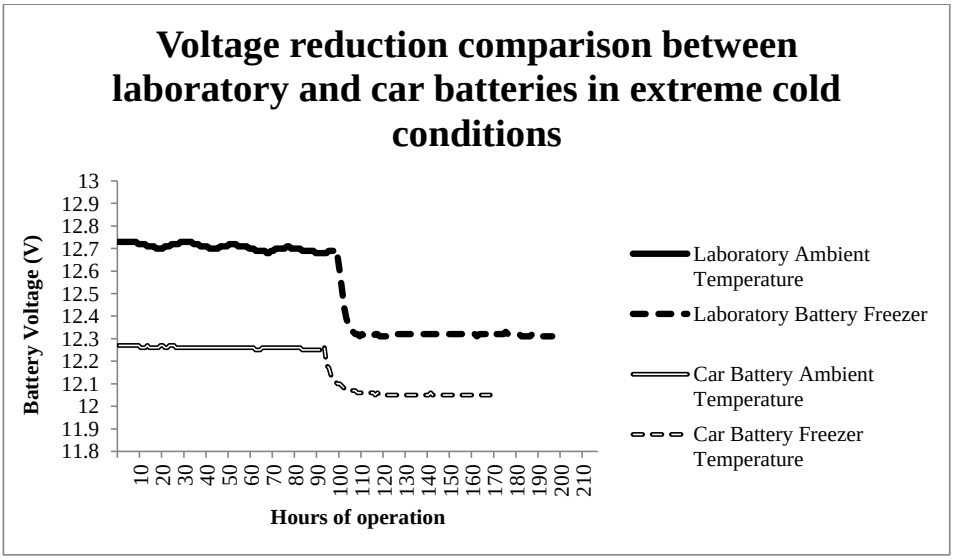

Figure 6.3. Comparison in reduction in voltage between a laboratory battery and car battery power supply due to freezing conditions. Working voltage for the CR1000 dataloggers is 9.6 -16Vdc, significantly below the supplied voltage from both the laboratory (~12.3V) and car batteries (~12.0V) during the cold test.

The laboratory test demonstrated that there should be no expected loss of power as a result of prolonged cold conditions affecting the battery, either on the laboratory battery or the car battery (Figure 3). Dataloggers remain functional under both setups, with no data loss occurring within any data fields. Temperature and solar flux data (figure 4) was collected as a means of determining whether data loss could occur in cold conditions even if no loss of battery power occurred.

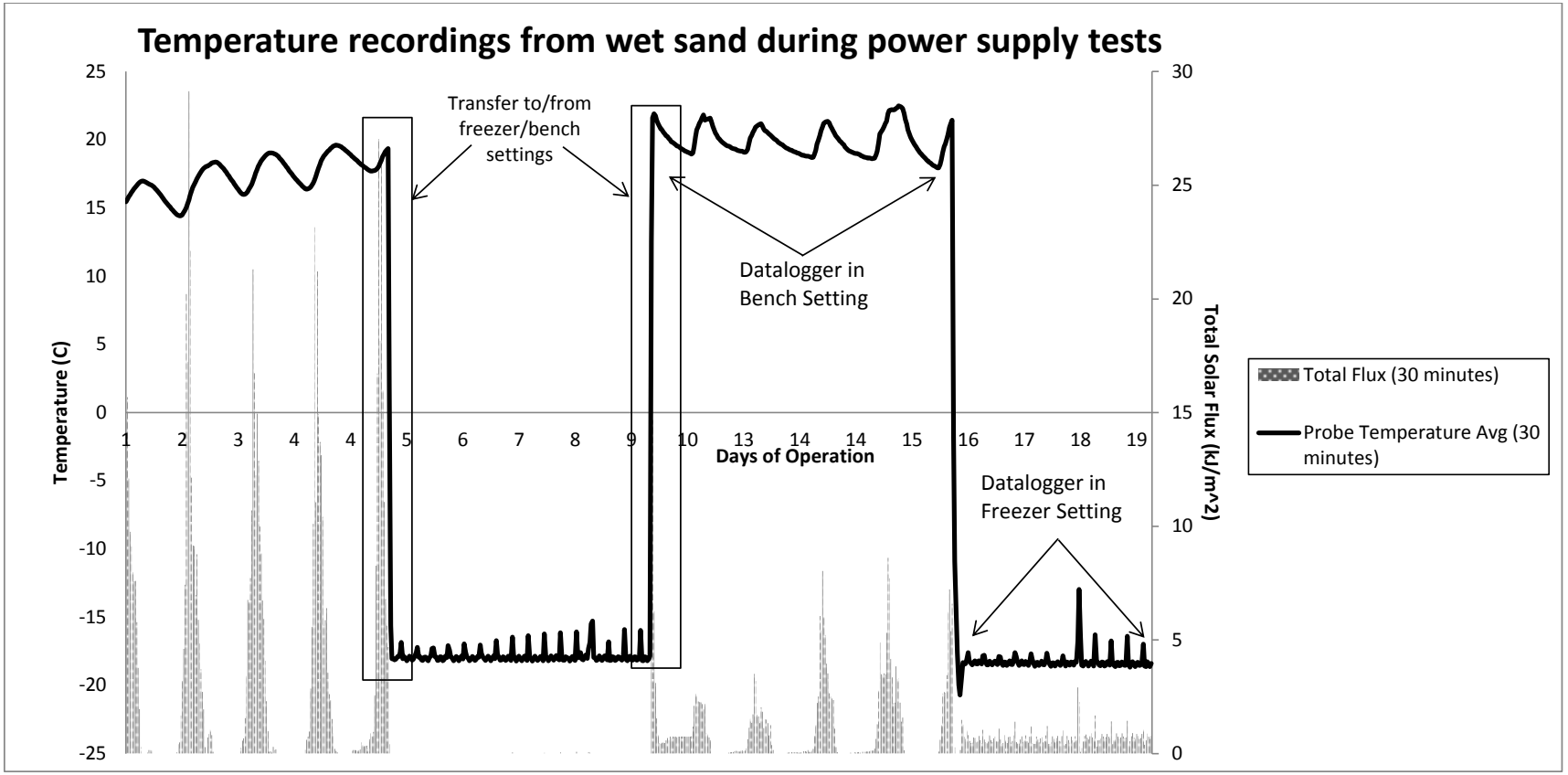

Figure 6.4. Temperature and solar flux data collected during battery freeze tests over 19 days of operation. Spikes on the total flux chart reflect daily sunlight movement during the room temperature period, whilst spikes in the cold period reflect the freezer being opened by other users. There was no pause in recording during transitions between settings.

6.3.2 Monitoring the diurnal cycle in Altiplano soils

The stated goal of the study, to establish an understanding of the diurnal temperature and water cycle of high altitude soils, was a success with all sites returning evidence of a diurnal cycle the effects of which are buffered by the soil above the tested depth. This is best reflected with temperature data at all four sites that had dataloggers inserted.

The diurnal cycle observed at the 5056m site can be seen in Figure 5. Of note is the significant difference in temperature readings between atmospheric temperature (measured from the CS215 probe) and the temperature of the -5cm, -10cm and -15cm measurements, most notable during day two when atmospheric temperature fails to rise above 0ºC.

The reduction in temperature associated with the reduction in atmospheric density between the low altitude and high altitude sites can be observed in Table 2.

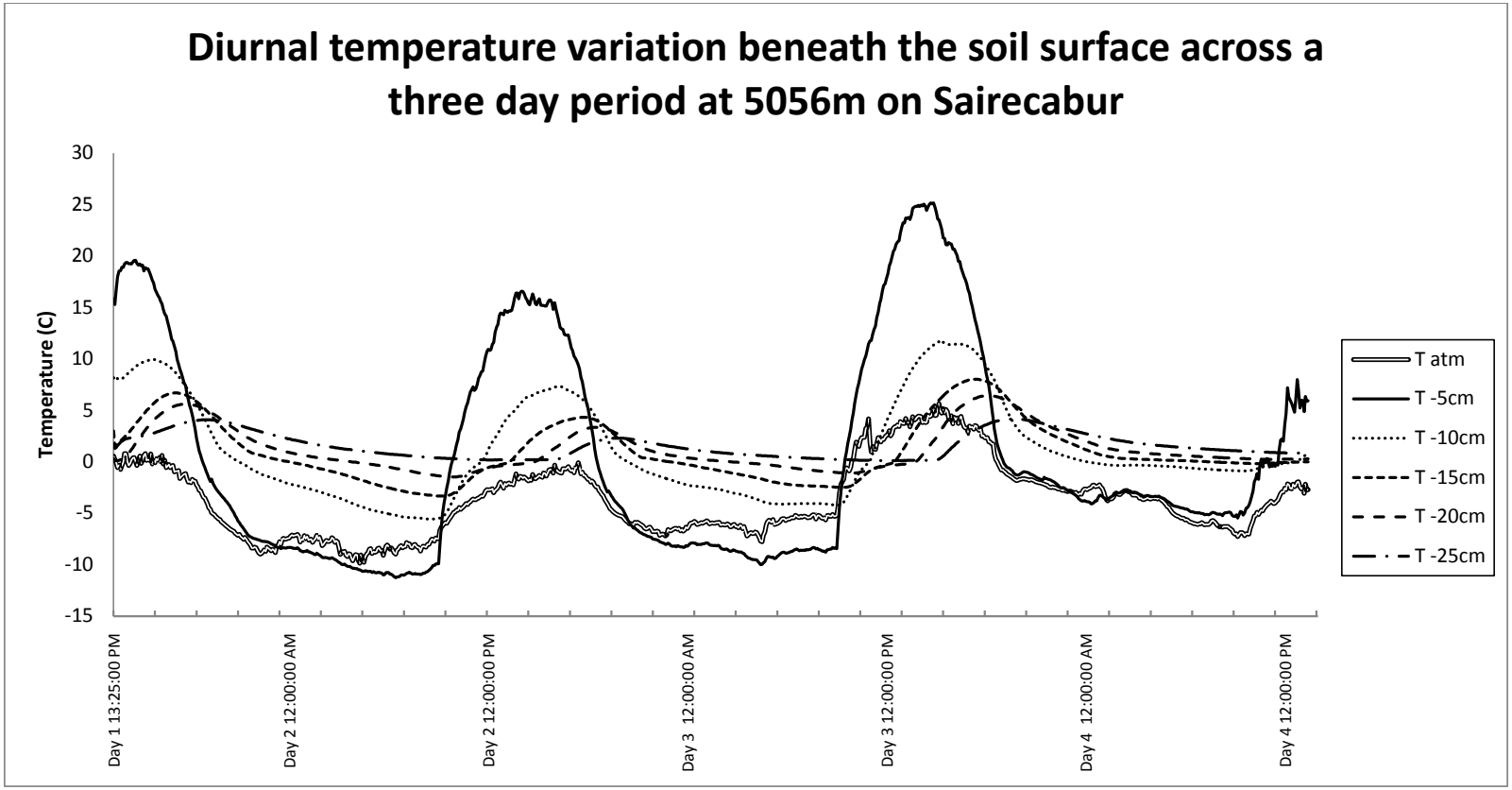

Figure 6.5. Diurnal temperature variation beneath the soil surface at 5056m across a period lasting three nights. Phase lag between different depths can be observed from the delay in peak temperature between each layer.

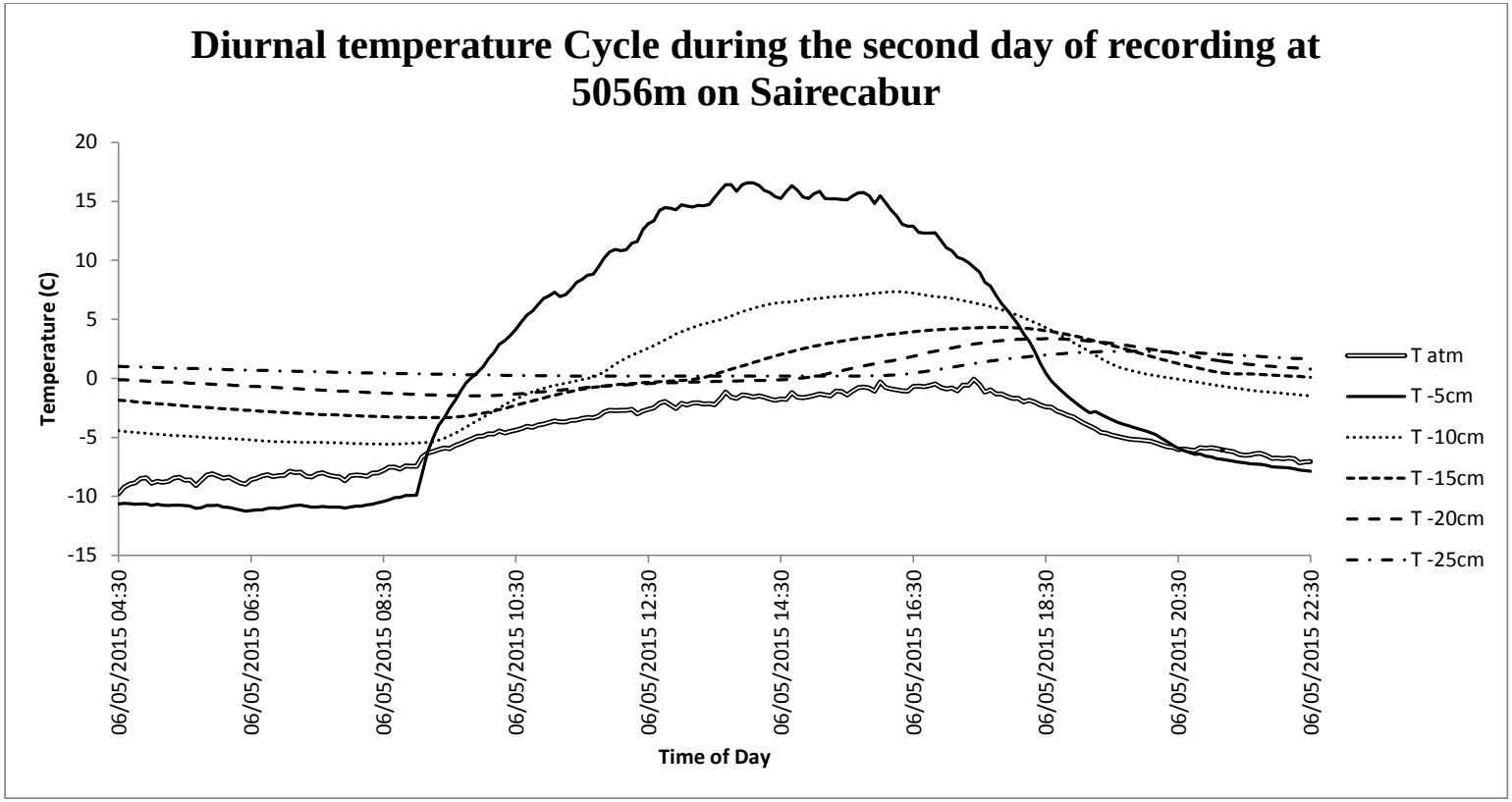

Figure 6.6. Graph depicting the diurnal cycle taking place during the second cycle from datalogger data. Delays in heating of the deeper layers can be identified by the timing of the upward growth of the temperature curve.

In figure 6 a more detailed view of the second day allows more specific details of the rate of atmospheric heating to be observed in the Altiplano soils at 5056m. Of note is the data from the probe located 25cm below the surface, where temperatures approach zero degrees while cooling but never reach it. A delay in the propagation of temperature increases can be observed, with the probe at -25cm not warming until 16:30, almost eight hours after the surface layer begins to heat and three hours after the surface reaches its peak temperature at 13:35.

Changes in soil temperature below the surface at the datalogger site are also reflected in measured volume of water content (VWC) from the same layer. Total VWC (measured at 15cm) in the near surface never amounts to more than 4% of soil mass during the peak of the day which is indicative of highly desiccated soil. Changes in VWC across the three day period correlate strongly (R=0.859) with the diurnal temperature cycle at the same layer despite the low water content of the soil. Leaf wetness sensor data suggested the presence and movement of water at all depths, however, at both the 10cm and 25cm depths there was not enough water to pass the wet threshold determined by the recording program prior to installation (Figure 9). The probe at 0-5cm experienced the most fluctuation due to its proximity to the surface and surface heating contributing to an exaggerated heat flux compared to the deeper sensors. Interestingly, the sensor experienced two peaks of liquid water during each diurnal cycle, one occurring up to two hours before noon each day, and the second occurring in the early-to-mid evening. The morning and evening peaks show an inverse pattern. There is also a moderate to strong correlation with the data obtained from the leaf wetness sensor at 10cm (R=0.6801) which never passed the threshold required to state that the soil layer was wet. However the leaf wetness sensor at 10cm also recorded the largest variance in measurement compared to the LWS at 5cm and 25cm despite not crossing the threshold. The probe located at 10cm returned data that indicated dry

conditions from the beginning of data recording to the end, however, large variances in voltage were observable in the data suggesting that some soil moisture was present. The probe at 25cm showed inverse data from that of the probe at 10cm. Data indicated wet soil for the duration of data recording with similar but smaller variations in voltage measured by the probe at 10cm.

The leaf wetness sensor data indicates that soil is not homogenous throughout the soil column, despite the approximate consistency of grain sizes throughout most of the soil column (Table 2)

Note that the peak observed each morning by the LWS at 5cm occurs several hours after sunrise whilst the evening peak occurs in tandem with sunrise. This is most likely a result of the local geography, with the peak of Sairecabur blocking direct sunlight for approximately fifty minutes after sunrise.

Table 2. Timed measurements from four analysed sites on Sairecabur.

Site:	4269m	4792m	5056m	5269m	Martian Equator (Cockell, et al., 2000)[a] (Harri, et al., 2014)[b]
Time of measurements:	1:40 PM	1:40 PM	1:40 PM	1:50 PM	N/A
UV-A (W/m2)	22.74	23.6	21.56	22.6	41.5 [a]
UV-B (W/m2)	3.78	3.72	3.29	3.5	
UV-C (W/m2)	0	0	0	0	13.2 [a]
PAR (μmol/m2/s)	1750	1750	1696	1622	111.965 [a]
Air Temp (C)	17	5	10	0.4	-75 [b]
Air RH (%)	11.6	26.4	18.2	21.44	50 [b]

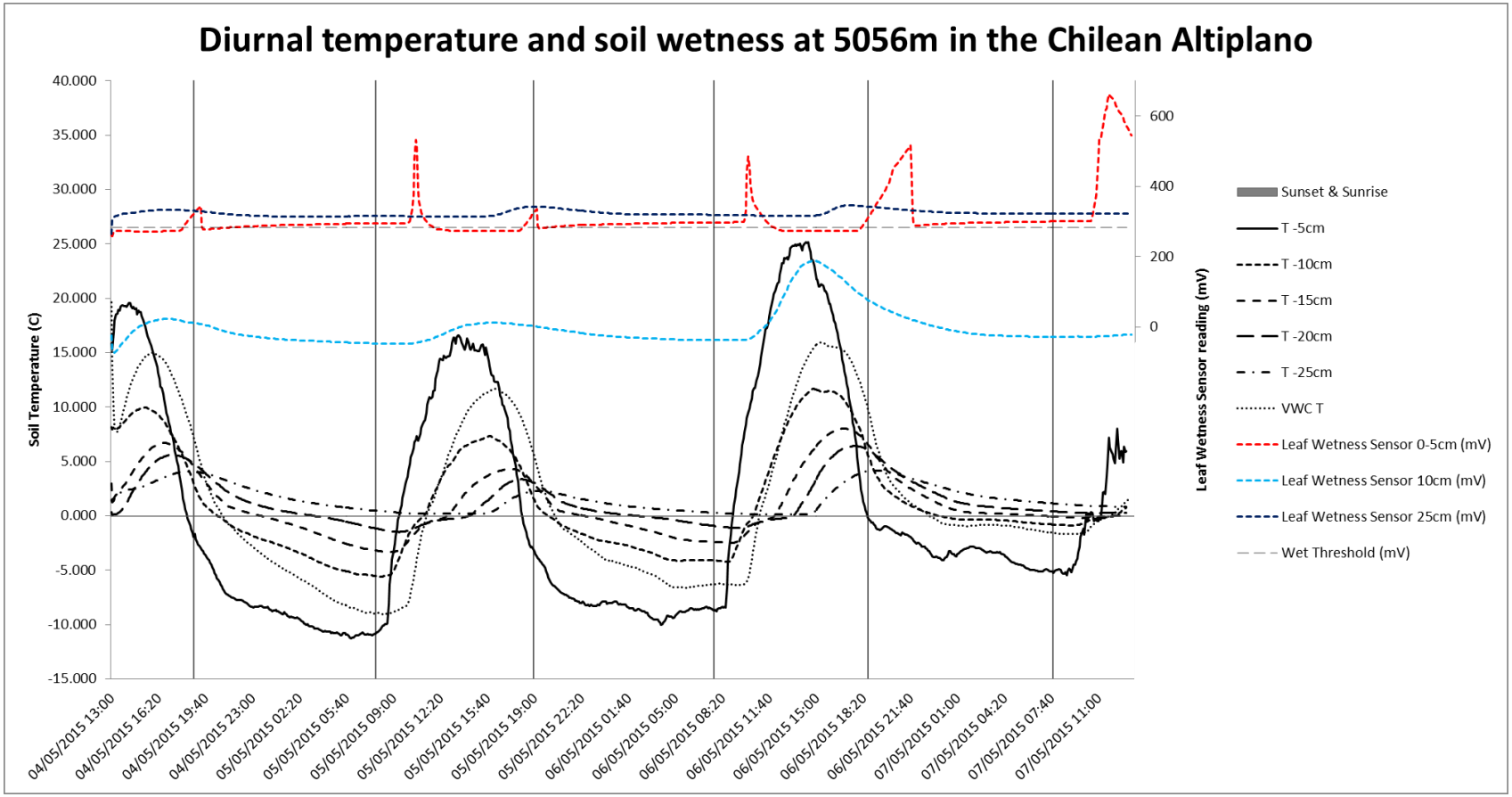

Figure 6.7. Graph depicting leaf wetness sensor data alongside temperature probe data.

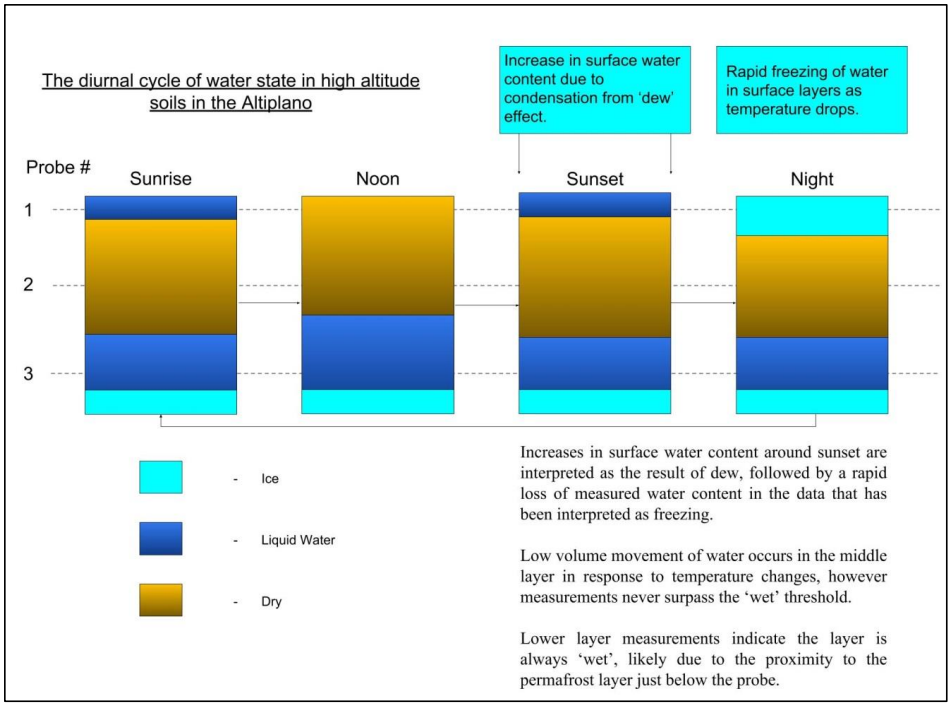

Figure 6.8. Diagram detailing the physical state of water during a diurnal cycle in high altitude soils in the Altiplano according to data from Figure 9. Probes one, two and three were located at depths of 0-5cm, 10cm and 25cm respectively to obtain a gradient of the state of water through the soil column that corresponded to temperature probes inserted at the same intervals. State changes occur only at the uppermost layer of the soil as temperature changes in the middle and lowest layer do not pass the threshold between solid and liquid. Phase changes in the uppermost layer occur most notably at sunrise and sunset where temperatures change rapidly due to the impact of surface heating. During daylight hours surface heating is responsible for the desiccation of the uppermost layer and from temperature data it can be inferred that a dry layer will exist at 10cm, although some variance in permittivity that correlates to temperature changes can be observed. When surface heating halts at sunset the uppermost layer returns to a wet state due to atmospheric condensation. The rapid loss of permittivity in the uppermost layer after the increases in water content is the result of the layer freezing. The lowermost layer is always measured as wet, likely due to its proximity to the permafrost layer beneath where the probe was inserted. Permittivity in the deeper layer correlates to changes in temperature, although there is no indication in the data that the layer ever freezes.

The only solar radiation data available from the study was from the UV and Photosynthetically Active Radiation (PAR) measurements taken on arrival at each site due to a fault developed in the pyranometer during transit. UV-A and UV-B measurements for all sites matched the expected data. It was expected that UV incidence would increase in all bands as altitude increased due to the increased density of air at lower altitudes (Table 2). Recordings at 5269m were affected by colder than average weather on the day of measurement and due to safety concerns accessing sites above 5056m it was not possible to obtain data in clearer weather. UV-C readings were all negative and reflect the UV attenuating effects of the atmosphere as would be expected on Earth (Table 2).

The timed testing of soil moisture at each depth with the EC-5 Soil Moisture probe provided results (Table 3) that matched the expected scenario for each site monitored; a clear inversion from a dry surface and near-surface where solar heating has desiccated the soil, to a wetter layer where the ice/water boundary layer occurs that is found at different depths according to the heat cycle of the soil as it changes with altitude (Table 2). At the two lowest sites (4269m & 4792m) the trench was not deep enough to discover an ice layer, however, the soil became visibly damp with increasing depth. Due to a shallow ice layer at the highest altitude (5300m) deeper data matching that of the 4269m and 4792m sites could not be obtained as the ice layer was too tough to break through by hand.

Table 3. EC-5 soil moisture probe data taken at various depths during excavation of the trench. Blank depths at the highest altitude are due to the impassable ice layer below 7cm, whilst the blank depths at the lowest altitude were due to sampling limitations.

Time	1:40 PM	1:40 PM	1:50 PM
EC-5 Soil Moisture Sensor Depth (cm)	Altitude 4269m	4792m	5269m
-1	-0.142	-0.149	-0.149
0	-0.122	-0.047	-0.019
1	-0.022	-0.013	0.035
3	0.004	-0.02	0.038
5	-0.009	-0.022	0.033
7	0.044	-0.007	-0.008
9	0.038	0.04	Solid Ice Layer
11	0.054	0.06	
13	0.076	0.087	
15	0.076	0.052	
17		0.083	
19		0.069	
21		0.016	
25		0.062	
33		0.018	
37	0.083	0.026	

Thermal camera data was used to determine the heating rate of the surface after being exposed to direct surface heating. Surface heating occurred rapidly at all sites confirming that direct exposure to sunlight was the primary driver of the thermal cycle in the soil. At each site uncovered soil was cold and wet relative to the surrounding topsoil immediately following excavation. Thermal imaging occurred immediately after exposure of the subsurface due to rapid evaporation and surface heating.

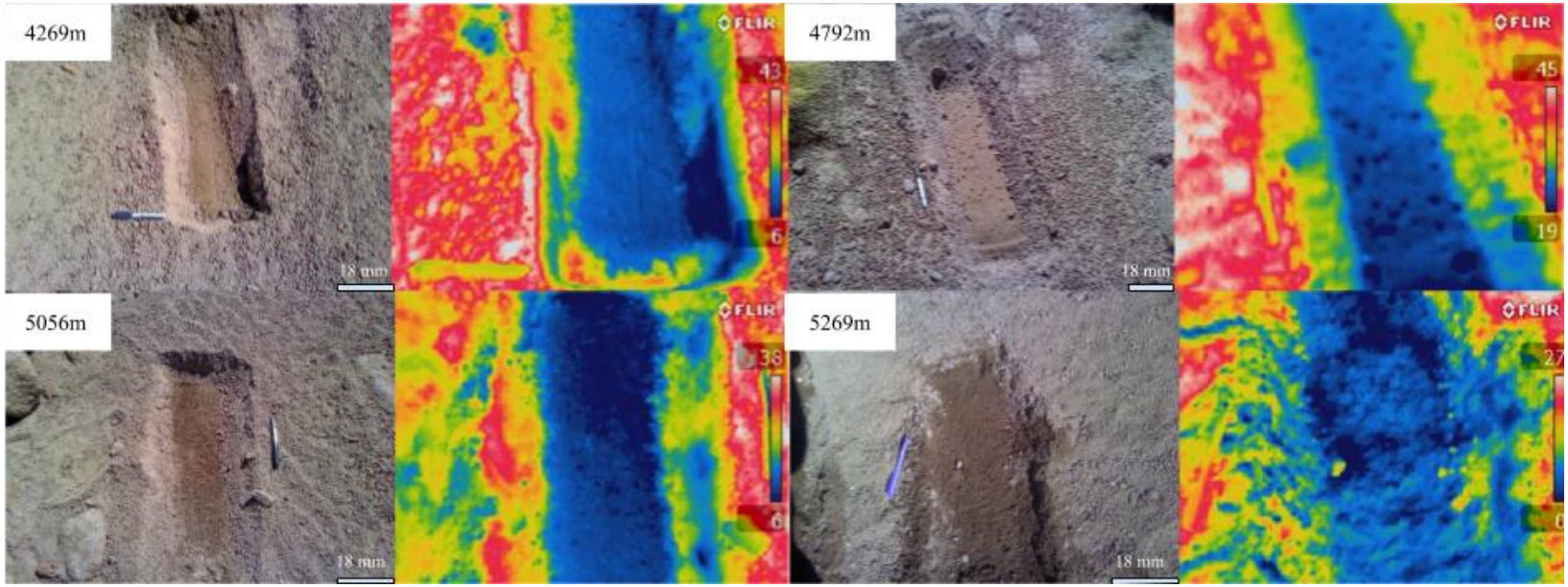

Figure 6.9. Thermal images of each sample site demonstrating that cold, wet soil could be found below the surface. In all sites thermal imaging needed to be taken immediately after the exposure of the wet layer due to rapid evaporation and surface heating. The pens in the figure are for scale purposes (18 mm)

Table 4. Divisions of grain size by wt% from the datalogger trench at the site located at 5056m on Sairecabur.

Depth (cm)	8–16mm	4–8mm	2–4mm	1–2mm	0.5–1mm	250–500µm	125–250µm	63–125µm	<63µm	Total
0	0.00%	7.90%	23.70%	17.40%	13.00%	13.30%	14.10%	8.50%	2.10%	100.00%
-1	0.00%	2.40%	10.60%	22.30%	11.90%	14.20%	21.50%	14.10%	3.10%	100.10%
-3	0.00%	3.90%	9.30%	17.50%	14.00%	16.00%	22.50%	14.10%	2.80%	100.10%
-5	0.00%	3.70%	17.00%	29.50%	16.90%	12.40%	12.40%	6.50%	1.50%	99.90%
-7	0.00%	0.00%	13.50%	22.70%	18.30%	16.40%	18.10%	8.90%	2.10%	100.00%
-9	0.00%	1.80%	7.40%	12.90%	16.40%	21.80%	27.90%	10.20%	1.50%	99.90%
-11	0.00%	0.00%	10.90%	27.00%	21.90%	17.40%	15.20%	6.20%	1.40%	100.00%
-13	0.00%	0.00%	8.20%	14.30%	11.90%	18.80%	29.50%	13.80%	3.40%	99.90%
-15	0.00%	0.00%	5.70%	10.20%	13.60%	20.60%	29.50%	14.80%	5.60%	100.00%
-17	0.00%	0.00%	2.80%	6.90%	12.80%	20.60%	25.40%	18.90%	12.60%	100.00%
-19	0.00%	0.00%	4.70%	8.20%	11.50%	18.70%	19.50%	18.30%	19.20%	100.10%
-21	0.00%	5.20%	11.60%	9.90%	10.50%	17.00%	18.40%	15.10%	12.30%	100.00%
Aggregated Depth (cm)	8–16mm	4–8mm	2–4mm	1–2mm	0.5–1mm	250–500µm	125–250µm	63–125µm	<63µm	Total
-1	0.00%	5.15%	17.15%	19.85%	12.45%	13.75%	17.80%	11.30%	2.60%	100.05%
-5	0.00%	2.53%	13.27%	23.23%	16.40%	14.93%	17.67%	9.83%	2.13%	100.00%
-10	0.00%	0.90%	9.15%	19.95%	19.15%	19.60%	21.55%	8.20%	1.45%	99.95%
-15	0.00%	0.00%	5.57%	10.47%	12.77%	20.00%	28.13%	15.83%	7.20%	99.97%
-20	0.00%	2.60%	8.15%	9.05%	11.00%	17.85%	18.95%	16.70%	15.75%	100.05%

6.4 Discussion

6.4.1 Effectiveness of dataloggers at sub-zero temperatures

In below freezing conditions a reduction in voltage occurs regardless of the battery; however, the car battery experienced a smaller reduction in voltage relative to the lab battery. Lab Battery reduction from room temperature to freezing temperatures was a reduction of ~2.76%, whilst voltage reduction between room and freezer temperatures for the car battery was ~1.87%, a 56.8% smaller decrease in voltage reduction reflecting the car battery's ability to withstand colder temperatures. Also of note is that the voltage reduction rate of the car battery in operation was approximately half that of the lab battery when operating at room temperature.

The timescales tested in the laboratory freezer (4.5 days *2) demonstrated that for short periods of time there are no temperature related issues that would have resulted in datalogger failure. The CR1000 datalogger only draws 16mA whilst the car battery is capable of supplying up to 330A. Assuming a linear reduction in battery charge and no further loss of voltage as charge decreases; the car battery would take a total of 8,100,000 hours to deplete.

This is determined by the equation:

$$C' = xT$$

Where:

C'	=	*Charge (Coulombs(C))*
		The car battery holds a full charge of 129600C
x	=	*Current (Amperes)*
		The datalogger draws a max current of 16mA
T	=	*Time (Hours)*

For the datalogger and car battery tested in the lab this resolves to:

$$129600 = 0.016 * T$$

$$\frac{129600}{0.016} = T$$

$$T = 8100000\ Hours\ of\ Operation$$

Charge depletion was unlikely to be the cause of any datalogger failure, but this data shows that low power monitoring electronics can be powered off of easily sourced power supplies and are unlikely to require any means of recharging during operation. This is particularly important for longer-term datalogger usage.

The temperature and solar flux data collection (Figure 3) allowed the monitoring of temperature within the freezer as well as a greater understanding of datalogger setup and programming for the portion of the experiment focused on datalogging in the Altiplano. The CR1000 datalogger is certified to operate at temperatures between -20°C and +50°C (Campbell Scientific, 2018) and results in the freezer test as well as lowest temperature results in Chile demonstrate that the CR1000 datalogger was suitable for use in both scenarios, as were both battery options.

6.4.2 Monitoring the diurnal cycle in Altiplano soils

6.4.2.1 Surface Heating and Atmospheric Temperatures

The disparity in temperature between the surface soil probe and that of the CS215 atmospheric temperature and relative humidity sensor is due to solar heating of the surface which exceeds the atmospheric temperature of the site, similar to Martian conditions where surface temperatures have been measured at up to 300 K despite an atmospheric temperature closer to 220 K (McEwen, et al., 2011). On the second day of datalogging adverse weather and increased cloud cover would have resulted in reduced solar heating due to the reduction in exposure to direct sunlight. The degree to which cloud cover impacted surface heating could not be determined due to a malfunctioning pyranometer. Whilst some pyranometer data was collected, it was not in a sufficient enough quantity of data (approximately 6 hours of data prior to sunrise on the third day) to draw any conclusions.

6.4.2.2 Layered heating of high altitude soils due to surface heating

One of the most notable observations that can be taken is that there is a notable phase lag between the peak temperatures reached by the upper layers of soil and the atmospheric temperature of the air above (figure 5). This indicates the effects of solar surface heating of the soil being the dominant driving force of the diurnal cycle beneath the soil rather than heat convection from the atmosphere. The CS215 atmospheric temperature recorded the maximum atmospheric temperature of -0.08ºC for this cycle 140 minutes after the peak `temperature of 16.57ºC for the probe located at -5cm and 100 minutes prior to the sun setting, although due to the local geography the site was likely in shade prior to sunset.

A similar pattern can be seen during all three diurnal cycles available (figure 5) and the difference in peak temperature between layers across the three cycles can be seen in figure 8. Heat dissipates into the soil from the surface and this dissipation is reflected in the reduced peak temperature in lower layers (Figures 5 & 8) and the reduced difference in peak temperatures between layers (Figure 7). The time difference between peak temperatures of surface and deeper layers is also of note. Peak temperatures at the deepest (-25cm) layer monitored took place four to six hours after peak temperatures at the surface layer (-5cm). Peak surface layer temperatures two o'clock each day depending on weather conditions at the time, whilst peak temperatures in the lower layers occurred in the region of seven o'clock.

Rate of heating was reduced in deeper layers due to the diffusion of heat energy across a greater volume of soil. During the third day the deepest layer at 25 cm experienced a heating rate of 0.014ºC per minute with a maximum heating rate of 0.029ºC per minute 40 minutes after temperatures in the layer began to rise. By contrast, the layer at 5cm experienced a greater heating rate of 0.09ºC per minute up to its peak temperature, with a peak heating rate of 0.44ºC per minute which occurred at 9AM shortly after surface heating commenced. The difference in heating rate between the uppermost layers of soil and the deeper layers results in a thermal gradient which will affect the state and presence of water in deeper layers if soil, eventually reaching a depth at which an equilibrium point is found where water is either stable as liquid or ice. In the case of the site on Sairecabur the data suggests that this site is likely to be stable as a water layer (although the depth and state could vary based on season) whereas on Mars the extreme dust storms that can engulf the entire planet will lead to oscillating depths at which any such equilibrium will be established. It would be generally expected that less surface heating would contribute to a shallower ice layer as heat loss becomes greater than surface heating itself. Although

recent evidence of a liquid brine layer beneath the Martian pole suggests that stable bodies of water could exist elsewhere at depth beneath the crust (Clery, 2018).

6.4.2.3 Delayed heating of deeper soil layers

Another notable feature of the dataset is that the deepest monitored layer (-25cm) never reaches freezing temperatures with a minimum temperature of 0.126ºC at 10:50AM on the third day. Whilst the surface layer at this time was reaching a temperature of 11.78ºC, the lowest layer would remain near its lowest temperature until 14:35 when it would begin to heat towards its peak temperature for the day. Thermal inertia in Altiplano soils could have been calculated had the pyranometer data been obtained, which could have allowed another method through which to compare this analogue site to estimated Martian conditions. Peak temperatures in deeper soil layers are influenced by the thermal capacity of the soil, thermal inertia through that soil and the solar heat flux at the soil surface. Ground heat flux on Mars has previously been estimated via measurements of net radiation, turbulent heat flux and latent heat flux (Wang, et al., 2010). Thermal inertia of the Martian surface has also been estimated previously (Kieffer, et al., 1977; Mellon, et al., 2000; Putzig & Mellon, 2007) by adjusting modelled temperature to observations based on albedo, thermal inertia and the influence of atmospheric dust in the Martian atmosphere (Pollack, et al., 1995; Pollack, et al., 1979). Establishing the ground heat flux of Altiplano soils would establish a maximum possible depth for an annual soil climate cycle capable of supporting life. It is likely that similar patterns could be seen between annual cycles of Altiplano soils and Martian soil due to the similar obliquity of Earth and Mars (25º and 23º respectively). With longer colder periods taking up half the year of each environment colder temperatures would be expected deeper in the soil due to the rebalancing of latent heat flux than ground heat flux towards a new equilibrium. The increased day length of

Mars must also be taken into consideration for the purpose of determining the extended timescale of increased ground heat flux during the day and latent heat flux at night.

6.4.2.4 Impact of soil conditions on delays in heating with increasing depth

The thermal conductivity of the soil is also influence by soil water content, with increasing water content in the soil translating to an increase in thermal conductivity over dry soils. Thermal diffusivity will peak in most soils at a moisture content of 8-20%, as higher water content will increase the heat capacity of the soil which will result in a smaller temperature change per fraction of the heat capacity. Soil moisture content is influenced by pore size, with smaller pores promoting higher moisture content in the soil, whilst increased surface area of a unit mass of the soil will result in increases in soil water content (Sellers, 1965).

Whilst the soils that were monitored in the Altiplano at all sites would be considered to be desiccated it is important to note that these soils are not dry solely due to the inability to maintain water, but that local climate in this region features a yearly average rainfall of less than 200mm a year (Minvielle & Garreaud, 2011), which falls mainly in the months of austral summer. This also results in the majority of rainfall occurring during the period at which temperatures are highest which are detrimental to the soil retaining water.

It is also important to consider whether the soil column should be deemed homogenous (thermal conductivity remains constant between soil depths) or heterogeneous (thermal conductivity varies with depth). If the soil profile is homogenous then the thermal diffusivity of the soil can be derived from a figure depicting changes in temperature with depth by observing whether the curvature of the graph is positive (heating) or negative (cooling) (Sellers, 1965). By contrast a heterogeneous soil becomes more difficult to determine the thermal diffusivity, as varying composition will impact the moisture content due to changes in soil components, which in turn will result in differing thermal capacity, thermal conductivity and thermal diffusivity.

It should be noted that during the repacking of the trench in which datalogger probes were planted that the soil profile will have been disrupted. To mitigate the impact of disruption to grain distribution through the soil, probes were inserted into the wall of the trench where the soil profile remained intact in order to minimize the possible effects of soil disruption. For this reason it is not believed that the soil profile has been significantly altered in such a way that the data collected is not representative of the site when undisturbed.

6.4.2.5 Grain size and soil heterogeneity

With regards to grain size, data obtained from the trench (Table 2) indicates that the soil profile remains relatively homogenous in the top 10cm. Some variation in grain size occurs, most notably the data skews towards increased presence of larger grains near the surface and smaller grains in the deeper layers. There is very little to distinguish between the data obtained from the layers located in the first 5cm compared to those in the next 5cm down to 10cm. There is a notable distribution of smaller particle sizes in the deeper layers from -15cm to -21cm.

However soil moisture distribution is not homogenous according to the data obtained from the leaf wetness sensors. LWS data showed a varying moisture content in the surface layers, likely related to a dew effect and subsequent freezing and drying of the upper layer, whilst the layers at 10cm were interpreted as dry at all times despite variances in permittivity in the layer that correlated with temperature changes at the same time. Finally the lowermost layer at 25cm was permanently wet with minor variances that linked to temperature and no indication of any changes in phase.

Sellers (1965) noted that thermal conductivity was dependent in part on the ratio between mineral and organic matter in the soil, as well as the moisture content of the soil. It was found that thermal conductivity of soils low in organic matter increased significantly with

increasing moisture content, whilst soils rich in organic content were less influenced by increasing water content.

Previous attempts have been made to estimate the diurnal temperature variations in the Martian subsurface based on understanding of Martian atmospheric and physical characteristics, combined with the understanding of the thermal properties of various soils. In a 1969 paper J.W. Ells estimated the diurnal cycle of Martian soil from the following equation:

$$T = T_m + T_0 \,.\, e^{-x\sqrt{\frac{\omega}{2\alpha}}} \,.\sin\left(t - x\sqrt{\frac{\omega}{2\alpha}}\right)$$

Where:

T = temperature (ºC)

T_m = mean temperature of the body

x = distance from the bounding surface

t = time (s)

α = diffusivity of the body = $\frac{k}{C\rho}$

Where k= thermal conductivity (cal sec^{-1} cm^{-1} $ºC^{-1}$), C= specific heat (calgm^{-1} °C) and ρ= density (gm cm^{-3})

ω = $\frac{2\pi}{\text{periodic time}}$ (sec^{-1})

ω=$\frac{2\pi}{24\times3600}$ for daily variation on Earth

ω=$\frac{2\pi}{24.62\times3600}$ for daily variation on Mars

$T_0 \,.\, e^{-x\sqrt{\frac{\omega}{2\alpha}}}$ = amplitude of variation at depth *x* (°C) = $\frac{1}{2}$ range of variation at depth *x* (°C)

Ells' equation has shown to be a good approximation for providing diurnal and annual predictions for the temperature cycle beneath the soil surface despite the equations reliance on a homogenous medium and natural soil not being perfectly homogeneous (Ellis, 1969).

Ellis was able to apply the equation to a Martian context by determining that the reduction in thermal conductivity due to lower atmospheric density and low-to-negligible water content would be cancelled out by the reduction in soil density, which would result in minimal reduction in thermal diffusivity for certain soils ($\frac{k}{C\rho}$). Thermal diffusivity of Martian soils could be estimated from known values of terrestrial soils as Martian soil composition would need to be considerably far from the norm to deviate from known diffusivity values. Ellis estimated a thermal diffusivity value of 0.0036 based on the assumption of a light sandy soil in around equatorial Mars and a lack of moisture, finding that for surface temperatures observed at an equatorial location with warmer temperatures than the Martian average that temperatures above 0°C only occur in the most shallow depths of the soil on a diurnal time scale.

This is corroborated by findings from the MSL Rover Curiosity, which tracked changes in surface temperatures of the Martian soil at the surface and calculated the diurnal subsurface thermal profile at -15cm from a simplified model that accounts for site-to-site variations in thermal inertia via a heat and mass-transfer model, with data inputs on an hourly basis (Martin-Torres, et al., 2015). Maximum temperatures recorded at the soil surface between late-winter (~130 Ls) and mid-summer (~315 Ls) in the Martian calendar were periodically above the 273K melting point for water, and regularly above 273K during the start of the Martian Spring period at 180 Ls. Minimum temperatures at the surface are significantly below the freezing point, and below the known metabolic thermal threshold for all known life on Earth. The same is true for the calculated average diurnal temperatures for soil monitored at 15cm below the surface which average approximately between 210°K and 235°K (Martin-Torres, et al., 2015). While the maximum temperature rises above the metabolic thermal threshold every day, and the threshold for replication on most days, any currently active lifeforms near the Martian surface would necessitate a daily state of torpor during which cell function ceases.

Soil conditions below 15cm on Mars were found to be capable of sustaining permanently hydrated perchlorates, indicative of the presence of wet brines. However the desiccated state of the upper soil layers, as well as thermal variation at those layers, results in a loss of soil humidity to the atmosphere through the upper soil layers throughout the Martian year. Increased temperatures during the daytime will result in the loss of water from the soil absorbed during night-time, resulting in very dry topsoil over the layers containing hydrated perchlorates. This was verified across the tract of Mars that MSL Curiosity travelled during its first Martian year through measurements from the Dynamic Albedo of Neutrons (DAN) instrument, revealing a dry upper regolith layer over a wetter regolith layer beneath according to water equivalent hydrogen beneath the surface (Martin-Torres, et al., 2015).

The lower sites in the Altiplano exhibited a similar stratigraphic profile. When the sample trench was excavated there was a notable transition from the dry topsoil layer covering the top 10cm of soil, to a wetter layer of soil from that point down. This was best reflected at the 4269m site, although the highest site at 5269m transitioned immediately from dry topsoil to a solid ice layer after 7cm, reflecting the change in the thermal profile of the soil at increased altitude. Notably at the boundary of the ice layer there is a thin wet layer. This wet layer has been hypothesized as one possible site for biological activity as the presence of water could be supportive of life. If the ice layer moves through the depth gradient of the soil according to how minimum temperatures move during the diurnal cycle as Figure 5 and Figure 6 detail then a moving habitable boundary of wet soil could be supportive of microbial life while remaining deep enough to avoid the degradative effects of the heightened radiation at the surface.

At present there is a limited understanding of the layering of Martian soil over greater depths that should become better understood when the ExoMars rover begins operation on the Martian surface. The ESA rover ExoMars will be equipped with a drill capable of

digging to 2m below the surface and could provide new insight into the Martian subsurface and better characterization of the thermal and water profile of Martian soils. This will in turn allow for greater specificity for soil composition requirements in Martian analogue sites as well as providing the opportunity to classify new Mars analogue sites based on their soil parameters. However any possible Martian analogue site would still be restricted by other known Martian parameters although analogue sites can be selected to reflect a specific experimental parameter.

6.4.2.6 Soil moisture

The leaf wetness sensor data (Figure 9) suggests that during the initial morning heating period, ice frozen overnight melts resulting in a spike in the sensor data which gradually comes back down during the day until the data indicates the soil is dry, likely due to evaporation from the top layers of soil. The second spike in the evening gradually rises up before a sharp drop-off in the data which has been interpreted as the water returning to the surface layers before freezing. Overnight the sensor reads as wet, likely due to ice, until the morning heating event restarts the cycle.

In addition to the leaf wetness sensor data in the top 5cm, thermal imaging data demonstrates that the upper soil layers are both wet and cold, even in the middle of the day. This aligns with the datalogger findings at the top sample site where the temperature probes implanted at 5 and 10 cm only begin to see significant heating at midday onwards as a result of the slow rate of heating through multiple layers of soil. The Thermal imaging data shows that surface heating at the 5050m site had, at the time of imaging, a thermal gradient from 38C at the surface to 6C where the soil was wet. This aligns with similar findings from the Phoenix lander on Mars where a short drilled hole in the surface exposed ice which subsequently sublimated (Mellon, et al., 2009).

By comparison, the leaf wetness sensors at 10cm and 25cm do not cross the threshold for a wet/dry reading. At 10cm there is a constant reading of dry whilst at 25cm there is a constant reading of wet. Sensors at both depths recorded fluctuations in the conductivity at the surface of the sensor, but the fluctuations never sufficient to cross the wet/dry threshold. The layer at 25cm is likely to contain liquid water at all times of the day as according to the temperature data it never goes below freezing, however, it also experienced the least variation in conductivity (Standard Deviation=8.538), similar to the temperature variation at the same depth. By contrast the layer at 10cm always read as dry with much higher variance than the deeper 25cm layer (Standard Deviation= 51.347). Due to the daily conductivity pattern of the 0-5cm and 10cm it appears that as the conductivity of the 10cm layer decreases the 0-5cm layer begins its second peak in the evening. Whilst the sensor at 10cm never records a conductivity that indicates the presence of liquid water, it still records a rise and fall in conductivity due to the fluctuating humidity of the soil itself. This would imply that while the layer at 10cm is never 'wet' during the recorded period by the definition of the sensor, it is also not completely dry. Low volume water movement from the deeper layers up towards to surface layer could result in the 'dry' layer seen here. This data is collected in figure 9 and reflected in figure 10 which depicts the phases that water goes through at the three measured depths throughout the day.

The combination of data points from the leaf wetness sensor at 10cm and the volumetric water sensor at the same depth is suggestive of slight water movement in the layer. The low volume of water attributed to water movement through the soil does not account for the significantly higher peaks of water near the surface (Figure 9) at sunset and sunrise unless it is interpreted as water movement downwards during the day. Measured VWC increases occur at midday at the 10cm sensor and meltwater from surface frost that fails to evaporate could account for this. The peak recorded by the LWS at 5cm at sunrise would therefore be interpreted as condensation due to evening dew.

Whereas dew is well studied as one of the primary sources of water in hot deserts (Jacobs, et al., 1999; Zangvil, 1996; del Prado & Sancho, 2007; Kidron, et al., 2002), there is less work in the literature on high altitude cold deserts such as the Altiplano. Dew confined to sunrise and sunset makes sense given the surrounding environmental conditions of low atmospheric humidity, high surface temperatures, and very cold atmospheric temperatures which would inhibit continual condensation at other times of the day. The pattern of data recorded by the LWS at 5cm also suggests a pattern of gradual condensation followed by freezing of water at the surface. Freezing of water results in a reduction in movement of ion molecules responsible for conductivity as ions are pushed out or locked into the ice matrix. Subsequently this results in a reduction in electrical conductivity. Sunrise leads to a rapid thaw and increase in conductivity as a result of a return to liquidity, and a gradual evaporation and movement of water out of the surface layers.

6.4.2.7 Hand-Held measurements

Past measurements in the region have revealed it to be an area with the greatest potential for UV irradiance as the highest recorded UV readings on Earth occurred on Sairecabur's neighbouring volcano Licancabur, where a UV-B dose equivalent of 43.3 on the UV index (UVI) was reported from late 2003 likely caused by Ozone destruction in the upper atmosphere by negative ozone anomalies or photochemical reactions, as well as the possible influence of a solar flare that took place in November 2003 (Cabrol, et al., 2014). A UVI of 11 is considered to be at the extremes of UV irradiance in countries that experience highs of UV, and is often exceeded throughout the year in geographical locations between 50º S and 40º N (Liley & McKenzie, 2006). This is still some way short of the daily index measured on Mars by Mars Science Laboratory (MSL) Curiosity, which frequently records a UVI of over 100 (Centro de Astrobiologia (Spain), 2017). Mars is

also subject to ionizing radiation that the Earth is not, representing another obstacle for astrobiological studies that cannot be replicated in Earth based analogue sites by natural means.

By referring to the diurnal temperature data from the CR1000 dataloggers it can be inferred that it is unlikely that the 7cm boundary unearthed at the 5056m site represented the lowest possible limit for an ice layer in these soils as the peak temperature in the soil layer at 10cm occurs between three and four o'clock each day at all sites, although the maximum possible depth for an ice layer would not be significantly deeper. Moisture content of soils will impact the thermal diffusivity of the soil, with the optimum rate of warming and cooling occurring at moderately low percentage of moisture content whilst increasingly higher moisture content will begin to inhibit thermal diffusivity due to the increasing thermal capacity of the soil (Sellers, 1965). Probe sampling at 5269m occurred at 1:50PM and in the time up to three o'clock it would be expected that the temperature could rise by as much as 3ºC in the soil at 10cm assuming heating rates reflected those at the datalogger site at 5056m.

6.4.2.8 Conclusions

In summary, the environmental parameters of the Altiplano, particularly the impact of higher altitude, create an ideal Martian analogue site for studies regarding diurnal soil temperature and moisture parameters. Martian analogue sites must fit a selection of parameters resembling Martian conditions that enable their use as a location to conduct Mars related experiments. In this regard, the high-altitude Altiplano experiences;

1. Higher than the global average dose of UV radiation at the surface, with some of the highest ever natural measurements previously recorded.
2. Very low atmospheric temperatures due to the high-altitude.

3. Low air and soil humidity due to the geographical location and influence of the local climate.
    a. However condensation when temperatures drop after sunset results in a measurable dew effect.
4. Surface heating due to solar radiation resulting in a diurnal soil heating pattern that influences the local climate of the soil column.
    a. This diurnal cycle is reflected in the movement and state of water at different soil depths.

These factors distinguish the high altitude Altiplano from other Martian analogue sites such as the Atacama Desert and the McMurdo Dry valleys, neither of which match the intensity of UV radiation at the soil surface, and both feature different climate profiles that correlate less closely to recorded Martian conditions.

The thermal properties of high-altitude Altiplano soils make it ideal for examining Martian-like soil conditions, particularly with regards to the state of water at particular depths, and how and if life is able to survive at the ice-water boundary where liquid water would be available. By monitoring sub-surface conditions over a period of three diurnal cycles, the diurnal temperature and soil moisture profile has been shown to resemble estimated Martian conditions, and resembles the conditions that would likely allow for the formation of ‘recurring slope lineae’ which form when temperatures are sufficient for brine flows at the surface. A longer term observation of the site and similar sites would further evaluate the degree to which the soil parameters imitate those of Martian soils.

7 Biomarker Analysis of Silica sinters from Chile, Iceland and New Zealand

7.1 Introduction

Silica sinter samples taken from hydrothermal zones in Chile, Iceland and New Zealand have been used to analyse biomarker presence and stability after exposure to polychromatic UV mimicking that of the Martian UV environment. Additionally a test utilizing a mix of standards as a control substance allowed for analysis of how biomarkers altered outside of the presence of the silica sinter. A 2017 study by Wadsworth and Cockell demonstrated that short term exposure (10s) to a polychromatic UV source could cut viability of a sample of *Bacillus subtilis* down to 3.13%, however, the addition of perchlorate to mimic Martian soil conditions would cut viability to 0.29% (Wadsworth & Cockell, 2017). Photolysis of the subject cells was listed as the main cause of cell death but it is unknown the degree to which alteration of organic compounds occurred that could also have resulted in a reduction in the detectable biosignature of the organism.

Organic compounds appear to be more common than originally thought. Analyses of Comets (Kissel & Krueger, 1987; Briggs, et al., 1992; Mumma, et al., 2001; Sandford, et al., 2006; Capaccioni, et al., 2015), meteorite fragments (Kvenvolden, et al., 1970; Kvenolden, et al., 1971; Cronin & Chang, 1993; Pizzarello, et al., 2001) and other planetary bodies in our solar system have expanded our understanding of how common organic compounds are, and with that expanded the necessary parameters for the creation of organic compounds. In particular, the presence of organic compounds on and around comets has raised questions over the susceptibility of these compounds to the harsh radiation environment of space. Curiously organic compounds often used as biomarkers such as low-weight hydrocarbon compounds or amino acids have been shown to

experience few detectable deleterious effects when exposed to protons at a fluence equivalent to solar energetic particles (SEPs) similar to those experienced on Earth's moon (Matthewman, et al., 2016).

Previous studies have shown alkane compounds to be highly stable in the presence of UV radiation unless other oxidative species are present. The C-H and C-C bonds that alkanes are composed of are some of the most stable in nature and thus acute degradation of alkanes is typically in the form of a substitution reaction with halogen free radicals. Haloalkanes arise from the substitution of a hydrogen atom and a halogen free radical in a process termed Halogenation. Highly oxidative species such as Chloride ions, Chlorates, Bromide ions, Fluoride ions, etc, are necessary before a UV photolytic reaction can occur to alkane chains.

By comparison, a study by Portugal *et al* determined the half-life of the amino acid Glycine (in the form of α-glycine) when subject to radiolysis by analogues for heavy cosmic ray utilizing $^{58}Ni^{11+}$ ions. Their results showed that in an interstellar medium the half-life of glycine would be in the region of $2.8x10^3$ to $7.8x10^3$ years depending on temperature, whilst in the solar system the half-life is significantly shortened at $8.4x10^2$ to $3.6x10^3$ years (Portugal, et al., 2014).

Given the timescales involved on Mars and other extraterrestrial bodies, and the approximate age of the bodies where these organics are being detected, the potential for damage to individual organic compounds, and the potential for the loss of structure beyond detectable limits is lower than first thought. Whilst more complex structures such as living cells are more susceptible to damage and loss of identity due to the increased complexity and size of the subject, individual smaller chain compounds are more durable in the radiation environment outside of Earth's boundaries. Additionally, the creation of simple organic compounds through photolytic interactions with radiation sources is well

documented (Throop & Bally, 2009; Bar-Nun & Hartman, 1978; Konig, 2017; Miller & Urey, 1959).

7.2 Methodology

7.2.1 Sample collection

Samples were collected from three countries around the world; Chile, New Zealand, and Iceland. Samples from New Zealand and Chile were collected from a single hydrothermal zone, whilst samples from Iceland were collected from several sites in the southwestern quadrant of the island. Care was taken to minimize contamination of collected samples through use of gloves and double bagging in Whirlpak sample bags.

The El Tatio hydrothermal field can be split into three different basins where hydrothermal activity is concentrated. The sample named 'Brown#1' was taken from the middle basin whilst the sample named 'Mystery Upper' is the top cut of a sinter sample taken from the upper basin. Brown #1 is largely composed of silicified microbial filaments and is of a noticeably lower density than any other sample collected. The Mystery Upper sample is taken from the upper layers of a sample taken from the upper basin. The sample in question has noticeable differences in structure and appearance from its upper (younger) layers to the deeper (older) layers at the bottom of the sample. Both the upper and lower layers were selected for organic extraction but only the upper layer had enough material to proceed to separation of organic fractions.

Icelandic samples came from multiple geothermal zones, most notably the Blue lagoon in the southwestern cape of Iceland, and the Haukadalur geothermal valley situated further inland. Two samples were collected from the Haukadalur geothermal valley for the purposes of biomarker analysis. The two most prominent geysers in this area are the Strokkur and Geysir fountain geysers. Strokkur is considered to be a very active geyser, with multiple eruptions per hour, whilst Geysir is less reliable and has been known to go

dormant for long periods of time although it can be provoked into an eruption through the addition of surfactants (Zakharova, 2010). The Geysir/Strokkur field site is well vegetated in comparison to other locations on the island.

Samples from New Zealand came from the Whakarewarewa geothermal area in Rotorua, on the north island of New Zealand. All four samples were collected from this zone. The Ngararatuatara geothermal feature is a geothermal hot pot used by the Maori locals as a pool for cooking as part of the tourism that the Whakarewarewa park brings in (Ngararatuatara translates to cooking pool). The three other samples, Unnamed Dry #1 and #2 and Waikite are found at the foot of and on the Waikite discharge apron respectively. The Waikite discharge apron is the largest in the area and previously the largest active geyser but has been inactive since 1968/69 due to local hydrothermal energy capture (Jones, et al., 2011).

Bacterial samples utilized as controls for cyanobacteria of hydrothermal origin (*Phormidium*) and a bacterium of non-hydrothermal origin representing a common soil bacterium (*Bacillus subtilis*) were cultured on BG-11 and Tryptic Soy Broth respectively. *Phormidium* was supplied by Vernon Phoenix and was obtained directly from biofilms in the El Tatio geyser field. *Phormidium* represents a common cyanobacterium found in hydrothermal vent ecosystems and thus represents the most complex form of life that could be found in an extraterrestrial context due to development of pigment compounds. *Bacillus subtilis* was sourced from frozen stock. A sterile inoculation loop was used to scrape some of the frozen stock off and a new culture prepared by streaking onto an LB agar plate. The plate was left to grow overnight after which a colony was taken from the agar plate and transferred into Tryptic Soy Broth (liquid media). *Bacillus subitilis* represents an example of a bacterium capable of enduring extremes of temperature and dessication.

Past studies focusing on the alkane profile of various cyanobacteria have shown that the growth medium does not result in any alterations to alkane production (Shakeel, et al., 2015).

7.2.2 Sample Preparation

Sample selection for biomarker analysis was based off of previous analyses of samples via Raman, Electron Microscopy and culture experiments.

In order to minimize potential sources of contamination, samples were broken down within the sample bag they were stored in, before being transferred to a mortar and pestle for breakdown into a powder. All equipment used to make contact with the sample were washed thoroughly with dichloromethane at the start of the preparation and between samples. Powdered samples were transferred to new whirlpak bags and weighed prior to freeze-drying.

Samples were frozen prior to freeze-drying and left in the freeze-drier for 3 nights to ensure complete loss of water. Bacteria being utilized as controls underwent the same freeze dry procedure as regular samples. Following freeze drying the bacteria were each mixed with combusted sand as a means of adding bulk to the sample and easier preparation of ASE cells. Bacteria were reduced to dry masses of aggregated material in the case of *Bacillus subtilis* or flakes of dry bacteria in the case of the *Phormidium*.

7.2.3 Extraction of Organic Compounds

All glassware utilised during the separation process was washed in 10% decon and furnaced for 8 hours at 450°C to prevent pre-contamination. All work was carried out under extraction hoods and glassware was covered when not in use. Care was taken to ensure no cross-contamination of samples took place both between samples and between

separations. Fresh solvent was utilized at each stage of the process to minimize the possibility of contamination from other lab users.

A Dionex accelerated solvent extractor (ASE) was used to separate the total lipid extract (TLE) from the powdered sample using a 9:1 *v/v* DCM:MeOH mixture. The ASE is capable of running up to 24 10ml cells, each capable of holding approximately 3g of sample, with the remaining volume filled with combusted sand as an inert packing material to minimize the volume of solvent required per extraction.

The TLE and all successive fractions of the TLE were dried under Nitrogen and the weight recorded. The weight of each fraction was recorded as fraction weight per gram of sample.

Top Fraction	Fraction	Solvent	Compound(s) of interest
Total Neutral Fraction	N1	Hexane	*n*-Alkanes Hopanes
	N2	Dichloromethane (DCM)	Alkenones Aldehydes PAHs
	N3	1:3 Ethyl Acetate:Hexane (Fraction requires further derivatization)	*n*-Alcohols Sterols Diols
	N4	Methanol	GDGTs
Total Acid Fraction	Hexane	Hexane	N/A
	DCM	Dichloromethane	Fatty Acid Methyl Esters (FAMEs)

Table 5. Sub-fractions of the Total Lipid Extract (TLE)

7.2.4 Separation of Organic compounds

The collected TLE was transferred into 8ml vials to be weighed then divided into acid (TAF) and neutral (TNF) fractions utilizing an LC-NH2 SPE column. A 1:1 *v/*v Dichloromethane:Isopropanol (DCM:ISO) solvent mixture was used to re-suspend the dried TLE and separate the neutral fraction from the TLE. Following this the acid fraction was eluted using a 4% acetic acid in ether solution through the same column.

The acidic fraction was then derivatized using Borontrifluoride-Methanol (BF3 derivatization) and separated into a Hexane and DCM fraction through a standard silica gel column. The DCM fraction contains fatty acid methyl esters (FAMEs) (Table 1) whilst the Hexane fraction was discarded after analysis of the DCM fraction.

The neutral fraction was separated into four neutral fractions without any prior derivatization through a 4-stage silica gel column using Hexane, DCM, 1:3 Ethyl Acetate:Hexane and a final methanol fraction. These fractions correspond to the compounds listed in Table 1.

7.2.5 Qualification and Quantification of Organic Compounds

Initial analysis and quantification of compounds in each fraction was performed using an Agilent 7890 GC-FID (Gas Chromatography-Flame Ionization Detector). Analysis time was 63minutes with a temperature program that started at 60°C for 2 minutes, then increased at a rate of 30°C/minute to 120°C, followed by a heating rate of 5°C until 330°C where the temperature was held for 15 minutes. A selection of alkanes from short through to long chain, as well as hopanes and a selection of other potential biomarkers were used as

an all-purpose standard for the construction of calibration curves. Hydrogen was utilized as the carrier gas for the GC-FID.

Additional characterisation of organic compounds was performed utilising GC-MS (Gas Chromatography-Mass Spectroscopy) to distinguish between saturated, unsaturated, aromatic and branched compounds. The same heating program was run for the GC-MS and the GC-FID, however, Helium was utilized as the carrier gas for GC-MS.

7.2.6 UV treatment experiments

Samples were selected for UV treatment based on the initial alkane profile of the untreated sinters. The alkane profile for the selected samples represented samples that were light in overall alkane content (Brown #1, Chile), a low-chain heavy sample (Mystery Upper, Chile), a long-chain heavy sample (Strokkur, Iceland), and a sample from New Zealand that represented a mid-chain heavy sample (Unnamed NZ1, New Zealand).

Samples were exposed to a L2273 150W xenon lamp (Hamamatsu Photonics) that produced radiation in the wavelengths 165nm to 2000nm. The lamp was housed in a purpose made cabinet that allowed for increases in flux from a baseline of 18.4W/m^2 in the UVB range (280-320nm). The lamp in question was utilised to better represent the Martian UV environment however, the set flux was significantly above the peak measurements made on Mars to date.

Phormidium and *Bacillus subtilis* were used as NON-UV controls and were not irradiated as part of the experiment.

Average sample size exposed to the lamp was 12cm^2 which corresponds to a total of 79.488 J of energy transmitted into each sample over the course of an hours exposure. This equates to approximately 1.39 hours, or 1hr 23min 24s, on Mars when the sun is at its zenith (Cockell, et al., 2000). Whilst Martian degradation conditions have lasted up to

2.5Gya the current conditions on Mars have been deemed detrimental to the viability of life on the order of minutes (Cockell, et al., 2000; Wadsworth & Cockell, 2017).

The exposed area of the sample was approximately the same for both the solid and powdered samples, however, it should be noted that the total exposure of the powdered samples will be higher per gram due to the increase in exposed surface area. Samples were irradiated separately on glass disks sterilized through a DCM wash and autoclaved.. The chamber was well vented and air circulation established to minimize build-up of ozone within the chamber. The UV chamber was housed inside a sterile fume hood to safely dispose of ozone and to minimize the risk of contamination into the chamber by circulating air.

7.3 Results

7.3.1 Calibration Linearity

Standards run to allow for quantification of samples of interest were plotted at known concentrations and a regression curve constructed to build a calibration curve to determine concentrations of samples. The n-alkane standards (Table 2) ranged from shorter- to long-chain. Standards were run at three different concentrations; 10µg/ml, 5µg/mg and 2.5µg/ml.

The correlation coefficient of the drawn regression (locked to a *y* intercept at 0) ranged from 0.9983 to 0.9998, indicating that the instrument readings and the established method was consistent at all chain lengths (Table 2). The chromatograms produced by the GC-FID have a minimum area quantification limit of 1. The lowest measurable concentration of each *n*-alkane chain length can be found in Table 2. Whilst chromatogram peaks with an area lower than 1 cannot be accurately quantified, they are still possible to identify according to the retention times of the peak.

Table 6. Calibration table for quantification of FC-FID data. The calibrated areas reflect the concentration measured by the GC-FID. The regression equation for the standards is included, along with the correlation coefficient for the plotted regression. The minimum detectable concentration of chain length is included for each alkane in the standard used for quantification.

n-alkane	Calibrated Area (10µg/ml)	Calibrated Area (5µg/mg)	Calibrated Area (2.5µg/ml)	Regression equation	Correlation coefficient *(r)*	Instrument quantification limit on area (area=1) (µg/ml)
C16	10.051	4.887	2.522	y= 15.223*x*	0.9995	0.066
C18	10.038	4.915	2.521	y= 15.830*x*	0.9997	0.063
C19	10.029	4.923	2.536	y= 12.025*x*	0.9997	0.083
C20	10.019	4.942	2.539	y= 7.3657*x*	0.9998	0.136
C25	10.014	4.935	2.574	y= 15.928*x*	0.9997	0.063
C30	10.053	4.885	2.515	y= 11.688*x*	0.9995	0.086
C32	10.112	4.824	2.406	y= 16.585*x*	0.9983	0.060

7.3.2 *n*-alkane content of sinters collected from Chile, Iceland and New Zealand

A spread of *n*-alkanes from 16 to 30 carbon atoms were found across analyzed samples, although total concentrations varied quite significantly between samples and between sites. Figure 1 displays the concentration of *n*-alkanes from nine samples; two from Chile, three from Iceland and four samples from three sites in New Zealand. Most alkane content was concentrated in chain lengths ranging from 16 to 25 carbon atoms (Table 3).

Shorter chain alkanes fit the expected alkane profile due to the presence of microbial activity in the water column and the incorporation of microbial biofilms into the sinters themselves. Longer chain alkanes are typically the result of terrestrial plant waxes and would be expected to make up a higher ratio of the total alkane profile where plant life was more abundant (Rencoret, et al., 2007). Of the samples analysed, only the samples

collected from New Zealand and the Geysir/Strokkur samples were surrounded by any sort of vegetation. The ratios of short:mid:long chain alkanes for each sample analysed can be observed at the bottom of Table 3. It can be clearly seen that there is a higher relative concentration of long chain alkanes in the Chilean samples than there is in the Icelandic or New Zealand samples.

The Chilean samples from El Tatio featured the lowest diversity of *n*-alkane content but the highest weight per gram of sample, with a maximum chain length of C31. The sample from the Brown geyser, selected for analyses due to the abundance of silicified microbial filaments that made up the sample, had the lowest diversity of alkane chains of the nine samples analysed, however, those alkane chains that were present were at higher concentrations than most other samples. In contrast the Mystery upper sample contained a more diverse set of alkanes dominated by short-chain alkanes in the region of 20 to 22 carbon atoms (eicosane, henicosane & docosane).

The Icelandic samples were the most diverse samples based on chain length distributions, with Strokkur returning the greatest diversity of organic material across all samples analysed. The Geysir and Strokkur geysers share the same water source, and the similarity of their alkane profile is unsurprising given this and their proximity (Figure 1). The Blue Lagoon sample displayed an alkane profile centred on C21, with chain lengths up to C29.

The samples from New Zealand are found in the same geothermal area but three of the four (Unnamed dry #1&2 & Waikite geyser #130) are a part of the same inactive discharge apron. These three samples share some similarity in their alkane profile although there is some variance in absolute concentration of alkanes (Figure 1). Proportionally, the sample taken from the top of the Waikite discharge apron features fewer long chains in proportion to mid and short chains than the two unnamed geysers situated at the bottom of the discharge apron.

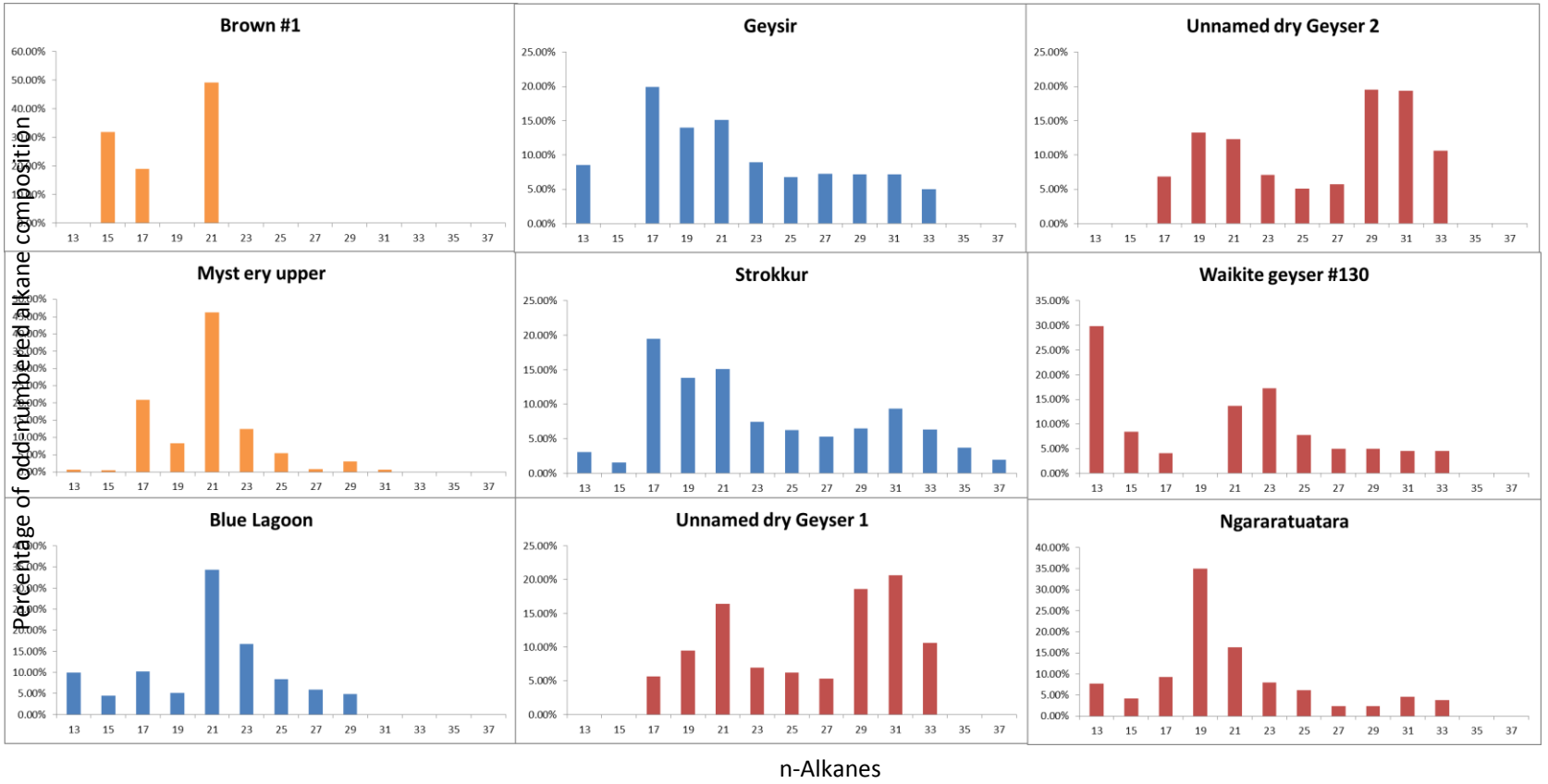

Figure 7.1. Charts depicting *n*-Alkane content found within select sinters collected from Chile (orange), Iceland (blue) and New Zealand (red). Sinters from Chile and New Zealand were collected from a single hydrothermal field, whilst samples from Iceland were collected from several areas across the south-western corner of the island.

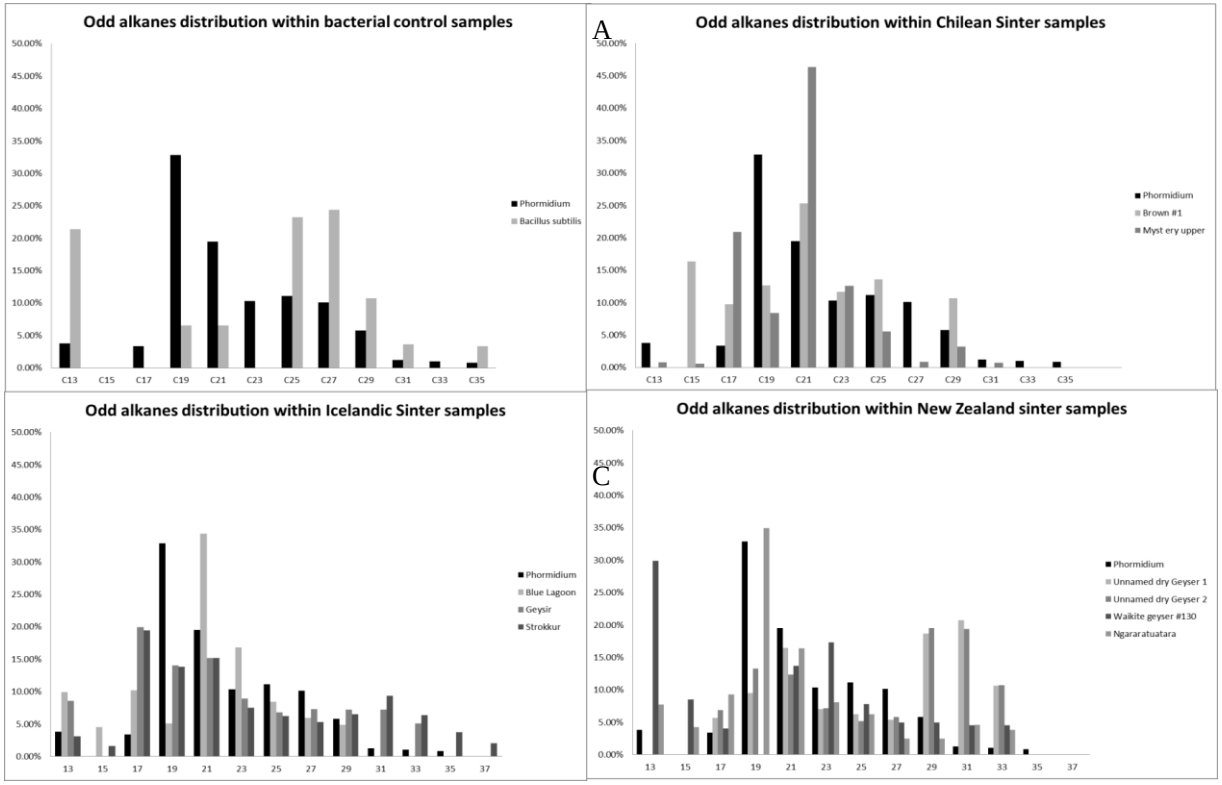

Figure 7.2. Odd alkane distributions from sinters taken from Chile, Iceland and New Zealand. **A** displays the alkane distribution within the bacterial control samples; *Phormidium* and *Bacillus subtilis.* **B** displays the alkane profile of samples taken from El Tatio and Chile; Brown geyser #1 & Mystery Geyser, **C** displays the Icelandic samples; Blue Lagoon, Geysir & Strokkur. D displays samples taken from New Zealand; Unnamed geyser #1, Unnamed geyser #2, Waikite geyser #130 & Ngararatuatara.

Sample		Brown #1	Myst ery upper	Blue Lagoon	Geysir	Strokkur	Unnamed dry Geyser #1	Unnamed dry Geyser #2	Waikite geyser #130	Ngararatuatara

Total Alkane content		(ng/g)	931.868	640.186	14375.336	333.528	2095.858	844.705	216.449	639.677	696.21
Total Short chain	≤C19		620.241	119.361	4969.196	143.528	863.857	145.375	13.365	172.656	260.897
Total mid chain	C20-C25		221.937	387.130	8900.311	120.289	736.994	374.477	121.554	203.325	307.085
Total long chain	≥C26		89.690	133.695	505.829	69.711	495.007	324.853	81.530	263.696	128.228
Ratio long:mid:short			**1:0.36:0.14**	**1:3.24:1.12**	**1:1.79:0.10**	**1:0.84:0.49**	**1:0.85:0.57**	**1:2.58:2.23**	**1:9.09:6.10**	**1:1.18:1.53**	**1:1.18:0.49**

Sample			Brown #1	Myst ery upper	Blue Lagoon	Geysir	Strokkur	Unnamed dry Geyser #1	Unnamed dry Geyser #2	Waikite geyser #130	Ngararatuatara
Total Alkane content		(ng/g)	981.851	14518.842	700.943	356.702	2159.377	844.700	639.742	305.984	763.371
Total Short chain	≤C19		670.279	4674.117	166.913	147.744	819.659	105.322	126.642	102.847	209.352
Total mid chain	C20-C25		221.893	9047.362	378.673	130.090	800.070	388.133	231.587	110.344	404.650
Total long chain	≥C26		89.679	797.362	155.357	78.868	539.648	351.245	281.513	92.794	149.369
Ratio long:mid:short			**1:0.33:0.13**	**1:1.94:0.17**	**1:2.27:0.93**	**1:0.88:0.53**	**1:0.98:0.66**	**1:3.69:3.33**	**1:1.83:2.22**	**1:1.07:0.90**	**1:1.93:0.71**

Table 4. Distributions of odd-numbered straight chain alkanes in the samples analysed from Chile, Iceland and New Zealand. The total weight of the odd chains is given and the distribution of alkane chains is given in the table as a percentage. Averages of alkane composition are given for each country of origin. Note that of the samples from Iceland only Geysir and Strokkur are taken from the same geothermal area. *Phormidium* and *Bacillus subtilis* control organisms are also included.

	Chile			Iceland				New Zealand						Bacterial Controls			UV Samples		
Sample	Brown #1	Myst ery upper	Chilean Sinter Average	Blue Lagoon	Geysir	Strokkur	Icelandic Sinter Average	Unnamed dry	Unnamed dry	Waikite geyser	Ngararatuatara	New Zealand Sinter Average	All Sinter Average	Phormidium	Bacillus subtilis	Sample	Brown	Mystery Upper	Unnamed NZ 1
Total Weight (ng/g sample)	64.61	3621.61		181.45	78.20	513.87		359.42	83.08	277.58	149.16			120034.93	7050.14	Total Weight (ng/g sample)	3919.82	4190.47	773.90
13	0.00%	0.80%	0.40%	9.92%	8.53%	3.09%	7.18%	0.00%	0.00%	29.84%	7.70%	9.38%	6.65%	3.82%	21.39%	13	1.84%	2.84%	5.28%
15	16.33%	0.58%	8.46%	4.53%	0.00%	1.58%	2.04%	0.00%	0.00%	8.47%	4.18%	3.16%	5.68%	0.00%	0.00%	15	6.63%	5.86%	6.02%
17	9.75%	20.93%	15.34%	10.19%	19.91%	19.45%	16.52%	5.67%	6.87%	4.03%	9.28%	6.46%	12.81%	3.34%	0.00%	17	24.15%	37.30%	15.04%
19	12.64%	8.39%	10.52%	5.10%	13.99%	13.83%	10.97%	9.46%	13.25%	0.00%	34.94%	14.41%	11.00%	32.85%	6.57%	19	21.94%	26.78%	18.85%
21	25.30%	46.34%	35.82%	34.31%	15.15%	15.14%	21.53%	16.43%	12.34%	13.70%	16.38%	14.71%	24.34%	19.48%	6.57%	21	14.83%	14.84%	14.37%
23	11.67%	12.56%	12.12%	16.77%	8.94%	7.47%	11.06%	6.96%	7.15%	17.28%	8.04%	9.86%	9.46%	10.34%	0.00%	23	8.50%	5.64%	11.08%
25	13.61%	5.58%	9.59%	8.39%	6.76%	6.22%	7.12%	6.23%	5.13%	7.80%	6.23%	6.35%	5.82%	11.15%	23.29%	25	6.99%	2.48%	8.41%
27	0.00%	0.90%	0.45%	5.90%	7.26%	5.31%	6.15%	5.34%	5.75%	4.93%	2.41%	4.61%	4.20%	10.14%	24.37%	27	5.48%	1.43%	5.79%
29	10.69%	3.18%	6.94%	4.89%	7.21%	6.52%	6.21%	18.61%	19.50%	4.93%	2.41%	11.36%	7.47%	5.77%	10.79%	29	4.46%	0.88%	
31	0.00%	0.73%	0.36%	0.00%	7.21%	9.34%	5.51%	20.67%	19.34%	4.51%	4.60%	12.28%	7.38%	1.24%	3.65%	31			
33	0.00%	0.00%	0.00%	0.00%	5.05%	6.36%	3.80%	10.63%	10.67%	4.51%	3.82%	7.41%	4.56%	1.04%	0.00%	33	4.48%	1.27%	9.23%
35	0.00%	0.00%	0.00%	0.00%	0.00%	3.72%	1.24%	0.00%	0.00%	0.00%	0.00%	0.00%	0.41%	0.84%	3.37%	35		0.68%	5.93%
37	0.00%	0.00%	0.00%	0.00%	0.00%	1.98%	0.66%	0.00%	0.00%	0.00%	0.00%	0.00%	0.22%	0.00%	0.00%	37	0.26%		

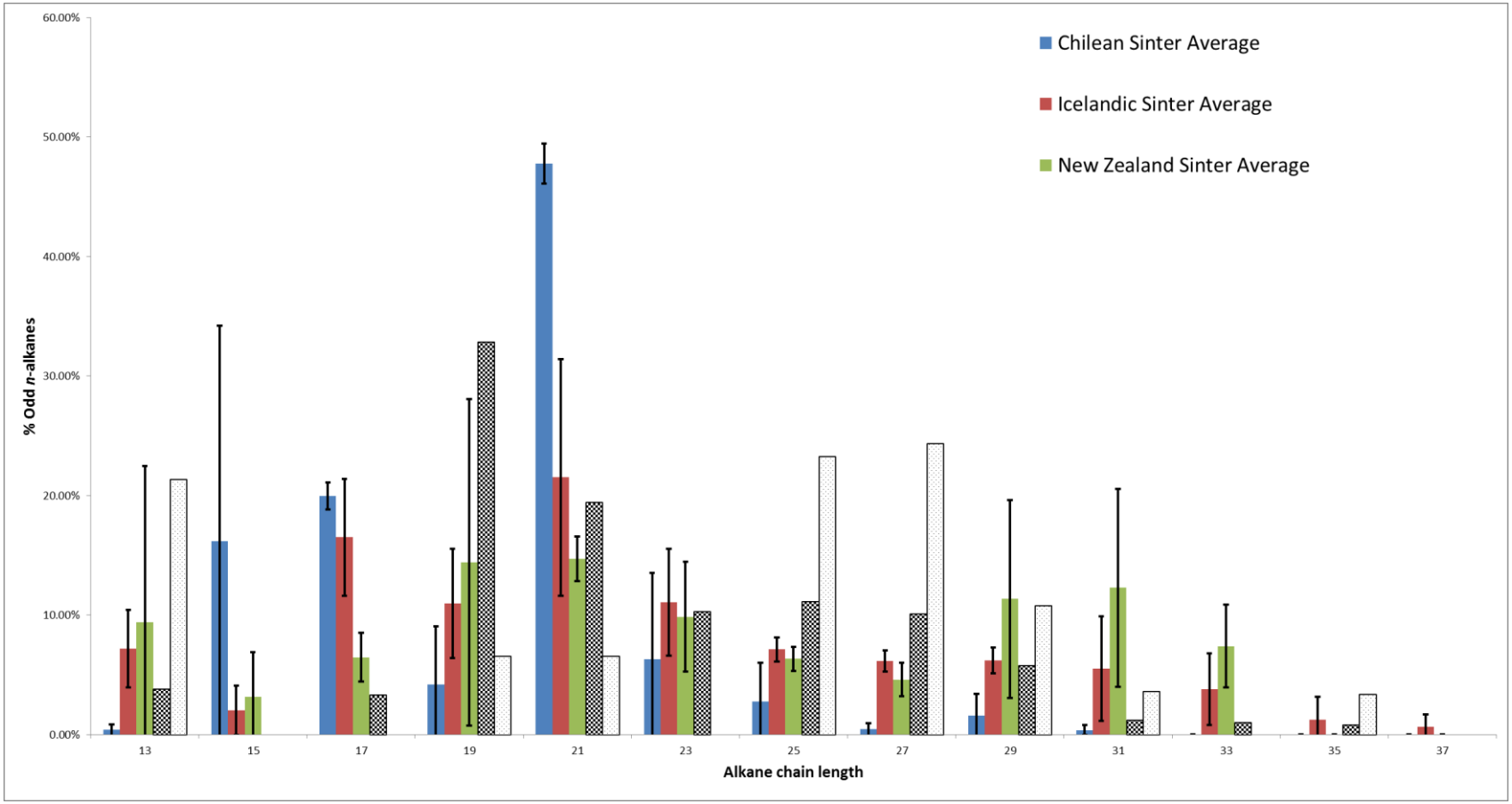

Figure 7.3. Graphic representation of average alkane data taken from Table 4. *Phormidium* and *Bacillus subtilis* data is provided as a means of comparison.

Table 7. Table of n-alkanes found during the course of this experiment. Bold retention times represent n-alkanes that are not a part of the standards mix.

Alkanes C(n)	Compound name	Retention Time based on Standards & **RT estimates**
16	n-hexadecane	16.004
17	n-heptadecane	**18.052**
18	n-octadecane	19.976
19	n-nonadecane	21.900
20	n-icosane	23.763
21	n-henicosane	**25.526**
22	n-docosane	**27.189**
23	n-tricosane	28.947
24	n-tetracosane	**30.665**
25	n-pentacosane	32.087
26	n-hexacosane	33.574
27	n-heptacosane	**35.332**
28	n-octacosane	36.391
29	n-nonacosane	**37.350**
30	n-triacontane	39.022
31	n-hentriacontane	40.425
32	n-dotriacontane	41.497
33	n-tritriacontane	**42.830**
34	n-tetratriacontane	**44.096**
35	n-pentatriacontane	**45.274**
36	n-hexatriacontane	**46.369**
37	n-heptatriacontane	47.137

7.3.3 Fatty Acid Methyl Esters (FAMEs) analysis

Fatty Acid content of the collected samples can be observed in Figure 2. There is a notable profile to the distribution of fatty acids within local sample sites (Both Chilean samples, Geysir & Strokkur, all four New Zealand samples) demonstrating that fatty acid profiles are conserved within local species. A contaminated peak can be identified in the Icelandic and New Zealand samples in the form of a 22 carbon chain acid. This point of

contamination has most likely arisen due to the sampling procedures that differed compared to those conducted in Chile.

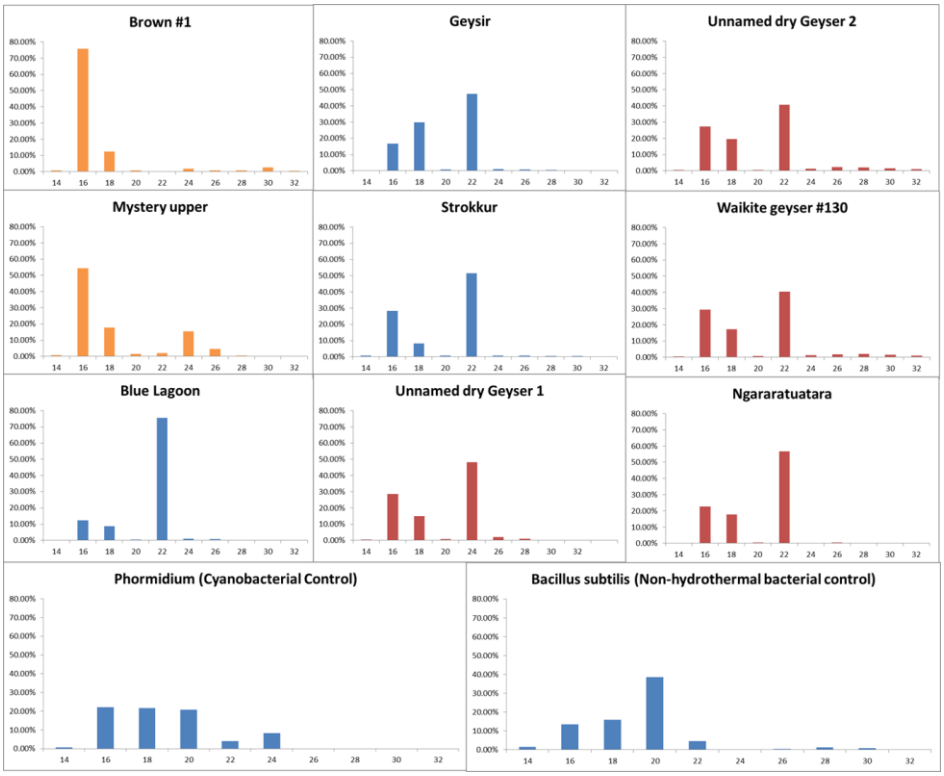

Figure 7.4. Charts depicting the percentage of saturated Fatty Acid Methyl Ester content of sinters collected from Chile (orange), Iceland (blue), and New Zealand (red). Sinters from Chile and New Zealand were collected from a single hydrothermal field, whilst samples from Iceland were collected from several areas across the south-western corner of the island. Bacterial samples included were lab grown.

Table 8. Distribution of fatty acxd methyl esters within samples taken from Chile, Iceland and New Zealand. The peak at C22 in the samples sourced from Iceland and New Zealand is the product of contamination whilst handling the sample during collection.

Sample	Chile		Chilean Sinter Average	Iceland			Icelandic Sinter Average	New Zealand				New Zealand Sinter Average	All Sinter Average	Bacterial Controls	
	Brown #1	Mystery		Blue Lagoon	Geysir	Strokkur		Unnamed dry	Unnamed dry	Waikite	Ngararatuatar			Phormidium	Bacillus
Total Weight (ug/g sample)	420.35	188.60		145.20	69.87	131.28		76.98	59.37	46.22	70.21			453.79	99.98
n-14	0.66%	0.73%	0.69%	0.15%	0.20%	0.72%	0.46%	0.38%	0.59%	0.43%	0.27%	0.35%	0.50%	0.67%	1.55%
n-16	75.83%	54.50%	65.17%	12.22%	16.72%	28.37%	22.54%	28.57%	29.42%	27.20%	22.65%	24.92%	37.55%	22.12%	13.62%
n-18	12.36%	17.84%	15.10%	8.60%	29.97%	8.15%	19.06%	14.84%	17.19%	19.53%	17.62%	18.57%	17.58%	21.66%	15.92%
n-20	0.75%	1.41%	1.08%	0.38%	0.77%	0.63%	0.70%	0.75%	0.60%	0.45%	0.38%	0.41%	0.73%	20.80%	38.51%
n-22		2.04%	2.04%	75.49%	47.49%	51.42%	49.46%	48.07%	40.45%	40.79%	56.69%	48.74%	33.41%	3.98%	4.68%
n-24	1.83%	15.52%	8.68%	1.09%	0.91%	0.74%	0.83%	2.06%	1.29%	1.33%	0.25%	0.79%	3.43%	8.26%	0.00%
n-26	0.74%	4.48%	2.61%	0.63%	0.80%	0.84%	0.82%	1.00%	1.84%	2.25%	0.37%	1.31%	1.58%	0.00%	0.30%
n-28	0.65%	0.37%	0.51%	0.22%	0.54%	0.56%	0.55%	0.24%	2.04%	1.95%	0.25%	1.10%	0.72%	0.00%	1.24%
n-30	2.46%	0.20%	1.33%	0.13%	0.30%	0.38%	0.34%	0.18%	1.52%	1.57%	0.30%	0.94%	0.87%	0.00%	0.90%
n-32	0.49%	0.06%	0.28%		0.11%	0.16%	0.14%		0.91%	0.97%		0.97%	0.46%	0.00%	0.00%

Table 9. Impact of Ultraviolet radiation on the alkane profile of sinter samples. Samples designated as NONUV represent the initial alkane profile of the sinter without UV treatment. Samples designated as UV were exposed to one hour of polychromatic UV radiation of an intensity of 18.4 W/m^2. Samples are split according to the state in which the UV treatment was conducted (powdered or solid). Coloured cells indicate the presence of alkanes that are not present in the corresponding control or treated sample. The Strokkur sample was not treated as a solid due to a limited amount of sample.

Sample	NON-UV Powder				UV Powder				NON-UV Solid				UV Solid			Bacterial Controls	
	Brown #1	Mystery Upper	Strokkur	Unnamed NZ1	Brown #1	Mystery Upper	Strokkur	Unnamed NZ1	Brown #1	Myst ery upper	Strokkur*	Unnamed NZ1	Brown #1	Mystery Upper	Unnamed NZ1	Phormidium	Bacillus subtilis
c-15	-	-	-	-	-	-	-	-	+	+	+	-	+	+	-	-	-
c-17	-	-	-	-	-	-	-	-	+	+	+	+	+	+	+	+	-
c-19	+	-	-	-	-	-	-	-	+	+	+	+	+	+	+	+	+
c-21	+	+	-	+	+	+	+	+	+	+	+	+	+	+	+	+	+
c-23	+	+	-	+	+	+	+	+	+	+	+	+	+	+	+	+	+
c-25	+	+	+	+	+	+	+	+	+	+	+	+	+	+	+	+	+
c-27	+	+	+	+	+	+	+	+	-	+	+	+	+	+	+	+	+
c-29	+	+	+	+	+	+	+	+	+	+	+	+	+	+	+	+	+
c-31	+	+	+	+	-	-	+	-	-	-	+	+	+	-	-	-	-
c-33	-	-	-	-	-	-	-	-	-	-	+	+	+	-	-	+	+
c-35	-	-	-	+	-	-	-	+	-	-	+	-	-	-	-	-	-
c-37	-	-	-	-	-	-	-	-	-	-	+	-	+	-	-	-	-

Analysis of the alkane fraction under different UV irradiation conditions resulted in some interesting data. The results can be seen in Table 5 where the two experiments have been split according to whether they were treated with UV as a solid or as a powder. The Strokkur sample was not given the UV-treatment as a solid sample due to a lack of sample.

Due to detection issues with the GC-FID samples were only able to be analysed qualitatively rather than quantitatively. As such table 5 displays those straight-chain alkanes that were present, rather than quantified data on their abundance. The presence of alkanes is relatively constant

across all samples, with little change in distribution outside of a few alkanes that could be the result of limits in detection from the device that prevented quantification of samples.

7.4 Discussion

7.4.1 Alkanes analysis

The alkane profile for all sinters is recorded in Tables 3&4 and reflected in Figure 3. Alkane distribution is predominantly centred on C17>C21 with some variation in particular sample locations. Chilean Samples are particularly weighted towards C15>C17 in comparison to sites in Iceland and New Zealand, While samples in New Zealand feature a greater proportion of long chain alkanes. Alkane concentrations were low in all samples relative to the average sample weight of other experiments run using this method, reflecting the low *w*/*w* of biomass/sample mass. Peaks present were above the detection limit for the GC-FID in most instances; however, some samples did not provide alkane content over the detection limit and were thus only able to undergo qualitative analysis.

The *Phormidium* control sample was run as an example of a hydrothermal bacterium to obtain an example of the expected alkane profile if only cyanobacteria were present. The *Phormidium* profile was very heavy in mid- and long-chain alkanes from C16>C21 and the profile extended out to C29, with traces from C31>C35. The non-hydrothermal origin control, *Bacillus subtilis*, displayed an alkane profile heavy in short- and long-chains but lighter in mid-chains. Both bacterial samples were noticeably richer in alkane content than any sinter samples analysed with the exception of the Mystery upper cut sample which is discussed below.

Previous studies of cyanobacteria have shown that their alkane profile is altered depending on whether the bacterium is of marine or freshwater origin (Shakeel, et al., 2015). As a result of this it can be determined whether the alkane profile of the sinter samples analysed resembles those of freshwater or marine bacteria. The study by Shakeel *et al* demonstrated that differences in alkane production between marine and freshwater strains manifests in the production of pentadecane, hexadecane and heptadecane. In freshwater strains heptadecane production is dominant with some pentadecane production, whilst in marine strains pentadecane is dominant with some production of heptadecane and trace production of hexadecane.

This pattern of production is reflected in both the cyanobacterial control sample. The *Phormidium* control sample exhibited a majority of short-chain alkane production in the form of heptadecane, with little to no production of pentadecane and hexadecane indicating that the bacterium is a freshwater origin species. By contrast the sinter samples analysed display an average heptadecane:hexadecane distribution of 1:0.425 (±0.21) and an average heptadecane:pentadecane distribution of 1:0.14 (±0.208). The outlier to this distribution comes from the sample that shows the most visual evidence of bacterial presence; the Brown geyser sample from Chile. This sample displays an inverse distribution of heptadecane:hexadecane at a ratio of 1:36.50 and heptadecane:pentadecane of 1:1.67.

Overall patterns in chain length vary according to sample (Tables 3, 4). On average the analysed sinters are mid-chain heavy although for some samples the total short-chain alkane content is approximately equal to the mid-chain component. Across the Chilean samples there is a shortage of long-chain alkanes compared to short- and mid-chains, likely due to the reduced vegetation in the area. The two Chilean samples that underwent gas chromatography were also the two samples with the greatest visual evidence of the presence of silicified bacterial filaments and it is

unsurprising that they returned the heaviest total alkane content (Table 3). Despite this the Chilean samples also possessed the lowest diversity of alkanes, even when just taking short-chain alkane content into account. The upper cut of the mystery sample was the richest sample analysed with odd-chain alkane content peaking at C21 and C17. The analysed area of this sample shows high quantities of thick silicified filamentous bacteria. By contrast the lowest layers of this sample display no direct evidence of silicified filaments and the total organic carbon was not high enough to attempt chromatography given the already low total organic content of all samples. The alkane distribution of the Mystery sample is not too dissimilar from that of the *Phormidium* control sample but is missing the high concentration of C19.

The Brown geyser sample shows similar evidence of filamentous bacteria throughout however, the sample is likely much older than that of the mystery sample. Whilst the mystery sample was taken from the vent of an active cone geyser and was actively being precipitated onto, the Brown geyser sample was taken from the back of the geyser in question. Precipitation was likely still occurring as a result of the thick steam that surrounded the geyser, but the rate of precipitation would be significantly reduced. As a result the Brown geyser sample is likely older and has experienced more degradation of organic content.

The alkane profile of the Brown sinter was similar in profile to that of the Mystery sample and the cyanobacterial control, however, some peaks in the chromatogram corresponding to longer chain alkanes did not elute during GC/FID.

Of the samples obtained from New Zealand, the two samples from the foot of the Waikite discharge apron share a similar short- and long-chain dominated profile peaking between C19&C23 and C29&C33. The abundance of long chains on these samples is most likely a product of the overhanging vegetation around the pit from which these samples were obtained.

Vegetation hung over the lip of the depression on its western flank whilst the opposite side was open in the direction of the peak of the geyser apron. Vegetation surrounded the paths and walkways towards the depression where easterly winds could blow material into the pit where the geyser was formerly active. Incorporation of any plant material could result in an increase in long-chain alkane concentrations which would be expected to be matched by the presence of long chain fatty acids associated with plant waxes.

A study by Bush & McInerney (2013) found that on average plant leaf wax alkanes were distributed around C23>C35, with the predominant alkane peaks occurring at C29 & C31 (Bush & McInerney, 2013). In temperate climates such as those of New Zealand (considered a wet maritime climate) the dominant peaks arise around C27>C31, however, there was a great deal of deviation in alkane content within the same plant species. The data gathered from the sinter samples collected in New Zealand is likely reflecting the high plant content of the sampling area. Whereas the Chilean and Icelandic samples were collected from locations nearly devoid of plant life, the New Zealand sample site was overgrown with vegetation. Of the collected dataset, the two unnamed geysers at the foot of the Waikite discharge apron both feature a greater percentage of C29 &C31 alkanes, possibly corresponding to plant material that has been incorporated into the samples during their precipitation.

In contrast to the unnamed geyser, the Ngaratuatara and Waikite samples both show a bias towards short- and mid-chains and only trace-evidence of long-chain alkanes. The Waikite geyser #130 sample was the furthest from any plant life of the New Zealand samples although it should be noted that there was still a greater volume of vegetation surrounding the Waikite geyser than any of the samples taken from Chile or Iceland (The Strokkur/Geysir area was vegetated but only lightly). Total alkane content of the Waikite sample was lower than that of the

unnamed geysers at the foot of the discharge apron and lower than the Ngararatuatara and this is most likely a consequence of the reduced proximity to plant life. Total short-chain alkane content is comparable to that of the two unnamed geysers, however, mid- and long-chain alkanes in the Waikite sample are half those of the unnamed samples. This suggests that the sinters that make up the Waikite discharge apron could have preserved the same alkane profile from the bacterial component whilst there is an unknown degree of incorporation of plant material during the period in which the geysers on the Waikite discharge apron have been dormant.

Local plant life around the Whakarewarewa area consists predominantly of various ferns and higher plants, with trees in the surrounding area. The Moss species *Sphagnum falcatulum* can be found across the sampling area, and was identified in the Bush & McInerney study as temperate plant heavier in C21>C25 than other temperate plants (Bush & McInerney, 2013), a possible explanation for the C21 > C25 heavy samples; Waikite #130 and Ngararatuatara.

The Ngararatuatara sample displays an alkane profile similar in distribution to the *Phormidium* control sample, peaking at C19 with declining chain length towards C33. The sample from Ngararatuatara possess higher concentrations of the long-chain alkanes that it shares with the *Phormidium* bacteria which, like the three samples on the Waikite discharge apron, is likely a consequence of its vegetated surroundings.

The low- and mid- chain heavy samples taken from Chile and Iceland are not as heavy in alkane chains corresponding to plant waxes, although the Strokkur and Geyser samples (both taken from the same sample area) are slightly heavier in longer chain alkanes but in even smaller quantities than the samples from New Zealand. Despite Iceland's barren landscape, the space around Geysir and Strokkur is vegetated. Most vegetation in the area is short grasses and small shrubs, although some deciduous trees surround the immediate area. In contrast to the Whakarewarewa

sampling site, Geysir and Strokkur are not as overgrown in the immediate vicinity, however, it's quite likely that some wind deposition occurs, leading to the longer chain alkanes that can be seen in these two samples. Graminoid grasses produce an alkane profile from C29-C33 (Bush & McInerney, 2013), not dissimilar to the long chain alkane data seen in the Geysir and Strokkur samples.

The Blue Lagoon sample was taken from the bottom of the same geothermal pool that is utilised as a tourist attraction. As a result the alkane and fatty acid profiles should be carefully considered as there is a much greater opportunity for contamination to occur, however, given the size of the pool and the total volume of the pool the data is assumed to be representative. The Blue Lagoon sample varies in alkane distribution compared to the Geysir and Strokkur samples with a profile more closely resembling that of the *Phormidium* control however, the depth of the geothermal pool likely makes the direct comparison to the cyanobacterium a poor one due to the bacterium's reliance on photosynthesis for energy production. It's possible that the profile could more closely resemble that of a chemoautotrophic bacterium but no such control bacterium was available for use.

7.4.2 Fatty Acid Methyl Esters

The lipid compositions of bacteria are well established as chemotaxonomic markers capable of distinguishing between different bacterial taxa (Shaw, 1974). It can also be utilised as a means of comparing similar environmental samples such as the sinters collected from Chile, Iceland and New Zealand as the varying lipid profile between different samples could give insight into how samples vary within the same area (differences that could be owed to shared/unique water sources, local vegetation presence, geyser type, etc) or between areas apart from each other.

The bacterial control samples produced similar alkane profiles however, concentrations varied between the *Phormidium* sample and the *Bacillus* subtilis sample. Saturated fatty acids from *Phormidium* and *B. subtilis* were concentrated between C18 and C20, making up 64.58% and 68.05% of total lipid content respectively. Distributions of acids within this region were approximately equal in the *Phormidium* sample, however, in the *Bacillus subtilis* sample there was an increase in fatty acid content with increasing chain length.

Unsaturated fatty acids are also present in both control samples. *Phormidium* most prominently features 7-hexadecanoic acid (C16:1), 9,12-octadecanoic (C18:2) and 9-octadecanoic acid(C18:1)

The fatty acid content of the sinters is given in Table 3 and Figure 4. Hexadecanoic (palmitic) and octadecanoic (stearic) saturated fatty acids are the predominant marker within the acidic fraction in all sinter samples which reflects their abundance in nature. The fatty acid profile of individual geysers (Figure 4) appears conserved over most of the samples analysed at chain lengths shorter than C22, with differentiation occurring at chain-lengths greater than C20. Whilst there are observable differences in total weight percentage of the longer chains in all samples, it should be noted that the total mass of fatty acids in these ranges is at trace amounts compared to the significant peaks at C16 & C18 in all samples. The sole exception to this is in the upper cut of the Mystery sample where the prominent peaks at C24 are on par with the C18 peak.

The greatest variation in long chain distribution is seen within the samples from Chile. The upper cut of the mystery sample exhibits larger peaks at C24 to C26, with traces of C28 to C32. The Brown geyser from the middle basin displays a more even distribution of acids from C24 to C32. Interesting to note is that whilst vegetation around the El Tatio geothermal field is scant, plant material was found to be incorporated into some sinters around the Brown geyser in the middle

basin. The sample in question was found within the runoff stream approximately 10 metres downstream from the vent itself. The material consists of disorganised laminated sinter with a strand of plant material stuck between two layers. There is no other evidence of plant material in any samples but the presence of this piece suggests that either windblown material makes it into the valley that houses El Tatio or that there was previously plantlife that grew in the vicinity of the runoff stream. Given the lack of visual evidence for any major plants around the geyser it is assumed that it is the product of windblown contamination. This does however, explain the trace evidence of some of the longer chain material present in the El Tatio samples. Long-chain alkanes are very low quantity compared to that of the short- and mid-chain material which would be expected in the case of wind-blown material.

The Mystery sample displays a particularly tall peak at C24 (Tetracosanoic/Lignoceric acid) which is a by-product of lignin production and also a known component of some coralline algal species (an organic polymer key to plant structures (Martone, et al., 2009)) (Rencoret, et al., 2007). Its presence here is unlikely to be a product of any algal species that incorporates lignin into its cell wall which is another suggestion towards wind blown material being brought into the El Tatio valley. SEM imaging of the sample shows no evidence of any large plant micro- or macrostructures similar to those found in the runoff of the Brown geyser. One theory towards how this material has appeared in this sample is that the cut of the sample was taken from it's upper layers. These upper layers are rough and not unlike the digitate sinters seen around the fountain geyser in the middle basin. The tight grouping of the sinter in these upper layers could result in trapped wind-blown material that becomes trapped within the pockets of the sinter that have not yet been filled in by further silicification of the upper layers. If this was the case then plant material would not necessarily be visually obvious, even under SEM. The large filaments

observable in the upper layers of the sample are unlikely to be plant material due to their uniformity and the lack of available nutrients for any plant that could have been incorporated into the sinter.

Of the Icelandic samples, the Geysir sample stands out from all other samples with respect to C16 and C18 fatty acids. Whilst in all other samples there is a preference for C16 over C18 this is inverted in the Geysir samples which exhibit a preference for C18. This is interesting given that the remaining acids profile for Geysir shows some correlation ($p=0.86$) to the sample from the nearby Strokkur geyser (similar profile of long chain alkanes C24>C32, variation in total weight% seen at C14). Like the Chile samples, long-chain alkanes are present in trace quantities, again likely a product of wind-blown contamination however, the Geysir/Strokkur geothermal field is lightly vegetated by short grasses and some tree-life. Long-chain fatty acids that are present as a result of contamination are presumably from a more local source than those present in the Chile samples.

The FAMEs profile in the Icelandic and New Zealand samples displays a notable peak at the retention time where C22 would be situated that is not shared by the Chile samples. This is a Phthalate peak resulting from contamination that has co-eluted with the peak for C22. It cannot be ascertained as to whether C22 is present for certain in these samples however, mass fragments associated with C22 are identifiable within the chromatogram peak.

7.4.3 Effects of UV-Treatment

The samples utilised in the UV-treatment experiment experienced an undiagnosed issue that resulted in some samples exhibiting peaks that were above the detection level but below the level needed for quantification. This is a GC-MS software issue relating to how peak integration is

calculated. Peaks are identifiable however, by their presence in the chromatogram at the expected retention times. As a result analysis of these samples has been done qualitatively rather than quantitatively (Table 4).

All samples underwent the same method as the untreated samples that were discussed above. Those samples that underwent UV treatment were treated at one of two stages; as a solid sample prior to being broken into a powder, or after being broken into a powder. The samples that were least able to be quantified were both powdered sets of samples, only half of which underwent the UV treatment.

Alkane distributions in the powdered samples displayed a broad spread of alkanes between C19 and C31 in the untreated datasets. There is some loss of long-chain alkanes in the UV-treated samples, with the spread of alkanes extending from C19-C29.

The samples that underwent UV treatment while solid did not experience the same problems associated with quantification and can thus be analysed both qualitatively and quantitatively.

The most immediately noticeable difference between the UV-treated solid samples and the untreated samples is the total mass of alkanes in each sample. The UV-Mystery upper and UV-Unnamed geyser samples both exhibited an increase of approximately 25% and 50% respectively, whilst the UV-Brown sample displayed a 15676% increase in total alkane mass.

In addition to the increases in alkane mass, all samples show an unique alkane profile from the samples that did not undergo UV treatment. The presence of long-chain alkanes is significantly decreased when interpreted as a percentage of the whole sample.

The data from the UV-Brown sample shows a similar set of alkanes present but the distribution in the UV-treated sample is weighted towards the shorter alkane chains. The UV-treated sample

also contains more long-chain alkanes. It is unlikely that the sample experienced simultaneous synthesis of longer chain alkanes and synthesis of shorter chain alkanes without a corresponding increase in mid-chain alkanes so it is presumed that the presence of long-chain alkanes in the UV-treated sample would have been mirrored in the untreated sample had those peaks eluted on the GC-FID. In the UV-treated sample alkanes were clustered around C17 to C29, decreasing in quantity with increasing chain length.

The UV-Mystery sample also experienced a change in alkane distribution towards shorter-chain alkanes. The alkane profile of the untreated sample was centred on C21 with 46% of the total odd-chain alkane content situated there. Whereas in the UV-treated sample most alkanes were spread from C17 to C21, decreasing in quantity with increasing chain length. There was an increase in short chain alkane content between C13 and C15 in the UV-treated sample compared to the untreated sample which could possibly have resulted from breaking of longer chain alkanes. Longer chains in excess of C25 experienced a drop in total mass, possibly a result of oxidation from reactions between other components of the silica sinter and the UV-treatment. The presence of chloroalkanes is unconfirmed from the mass spectra obtained. Compounds of a mass equal to that of different chloroalkanes are present in the data but not in any volume that would allow for quantification.

The final UV-treated solid sample was from the dried geyser at the foot of the Waikite discharge apron in New Zealand. Like the previous two samples, there was an increase in total alkane content and the distribution of alkanes has been altered although the total alkane content of the sample was significantly less than that of the UV-treated Brown and Mystery samples. Whilst the two previous samples peaked in concentration at C17 and saw a decrease in total content with increasing chain length, the unnamed sample peaked at C19 and possessed an alkane profile

more closely resembling a bell curve. In the Untreated sample alkane content peaked at C29 and C31 which are both absent from the UV-treated sample though C33 and C35 are both still present.

The significant increase in alkane content and the increase in longer-chain alkanes can be explained in several ways.

The first, and most likely, is that the discrepancies in alkane content in the UV solid samples, particularly Brown #1, are a result of differences in biomarker concentration within the samples themselves. Despite care taken to ensure that the before and after samples were taken from the same location of the larger sample, it's possible that they do not share an identical alkane profile.

The second possibility is that cleavage of the carboxylic acid group at the tail of fatty acids present in the sample resulted in an increase in alkane content. When the functional group is lost the remaining molecule is an alkane chain. Fatty acid weights (mg/g of sample) in these samples are three orders of magnitude larger than the alkane weights (n/g of sample) and could explain the significant increase in alkane content.

The third possibility is that it is the result of contamination, however, all samples underwent the same protocol and yet do not share the same differences in alkane content. For one sample to be as significantly contaminated as to exhibit a 15676% increase in total alkane mass would suggest a significant source of contamination that would not be confined to one sample.

The fourth possibility is an error during the separations phase when the total lipid extract was being divided into neutral and acidic fractions. Errors occurring in this phase would be more likely to result in a *lower* total alkane mass due to insufficient separation of the N1 fraction.

7.5 Conclusion

The work described has established that in comparison to other sources of organic carbon (lake sediment, soils, geologic deposits, etc) that are often considered to be prime locations for astrobiological studies, silica sinters are quite low in overall concentration even in higher-biomass environments such as geothermal fields, despite visible evidence of biomass formation on the surface of many of the sinters discussed and visual evidence of microbial encrustation in silica through optical and electron microscopy.

However identification of carbon compounds was still possible within these samples although care had to be taken through the extraction and chromatographic stage to ensure that all carbon was obtained. Sources of contamination should always be carefully managed, particularly with low mass samples such as these as seen in the Fatty acids data taken from samples from Iceland and New Zealand. The presence of biological signatures confirms that geothermal sinter samples are an ideal environment to target for further astrobiological interest. Additionally it has been shown that alteration of n-alkane profiles and the increase in shorter chain alkanes as a result of UV treatment is likely to be of detriment to detection of organics on Mars after an eon of exposure to Martian conditions.

Organic molecules can serve as a potential biomarker for astrobiological purposes; however, the deleterious effects of direct irradiation and oxidation of Martian surface components will significantly lower the chances of their detection, particularly over extreme timescales at the

Martian surface. Complexity alone is not sufficient for identification of organic material as being of a biotic or an abiotic origin. Organic material of a biotic origin is characterized by chiral preference (Stillinger, 2013), predominantly straight chain or cyclic forms and no decline in abundance with carbon number (i.e. A non-linear relationship between molecule size and abundance) (Sephton & Botta, 2005; Sephton, et al., 2018). Comparisons between organic material of an abiogenic origin and future data obtained from extraterrestrial studies are one of the first methods for identifying material origin. Studies of meteorite material represent examples of organic matter formed completely outside of the influence of both biogenic and abiogenic planetary processes. Extraterrestrial material obtained in future studies of other planetary bodies can be quickly identified as abiogenic if it matches the established pattern of abiogenic material.

Future Mars missions focusing on material from deeper layers of the soil such as with ExoMars will be better equipped to assess biomarker presence in Martian soils. Comparisons between soil surface and deeper soil layers should allow for a comparison in organic molecule complexity assuming such compounds are present in the deeper layers.

This study also relates to future missions focusing on the icy moons of Jupiter and Saturn. Bodies that are thought to exhibit active hydrothermal activity (Hsu, et al., 2015; Waite, et al., 2017) are some of the most promising locations for finding extant life and in turn could serve active producers of biomarkers. Current mission plans for the icy moons focus on analysis of plume ejecta to assess whether the presence of organic content within the plume could be indicative of a biogenic origin (Phillips & Pappalardo, 2014; Sephton, et al., 2018).

8 Evaluating the use of Raman Spectroscopy as a biomarker detection tool in precipitated silica substrates.

8.1 Introduction

8.1.1 Silica Sinters and Mars

In 2007 the Mars Exploration Rover Spirit uncovered a patch of highly concentrated silica beneath the surface regolith on Mars around Home Plate. Spirit rover had previously suffered a malfunction to its right front wheel that forced the rover to drive backwards from then on. Whilst travelling around the site Home Plate the broken wheel dragged up the surface regolith and uncovered a lighter layer beneath. Upon analysing this lighter patch it was revealed to be highly concentrated silica (90%). On Earth, silica is only known to be concentrated like this due to the presence of water which it precipitates from, in sites such as geothermal geyser fields. As a result, sites on Mars that are high in Silica are of interest to astrobiology as these areas on Earth are well colonised by life, and are also studied as possible origin of life sites.

One of limiting factors of the search for life on Mars is the hostile radiation environment which is not conducive to preserving traces of life. Mars' surface lacks the protection that the surface of the Earth does from its magnetosphere and Ozone layers, and as a result radiation levels are about significantly higher than the Annual Cosmic Radiation dose at sea level on Earth (Hassler, et al., 2014). However since Mars lost it's atmosphere sometime between the start and end of the Noachian era (3.7-4.0Gya) (Brain & Jakowsky, 1998; Webster, et al., 2013; Ehresmann, et al., 2011; Kahn, 1985) Long term exposure to an environment as detrimental to organic preservation as Mars' will significantly limit the number of viable environments in which to look for signs of

biosignatures. As a result, it makes sense to look for life in locations that would offer better protection from radiation. One of the most commonly suggested areas to look are in subterranean systems such as caves, where life could have settled prior to the loss of water and the thicker atmosphere, and would not be exposed to the radiation levels at the surface. However the technology required navigating and communicating to an unmanned vehicle exploring extraterrestrial cave systems will limit the viability of such projects until technology can match the ambitions of its explorers.

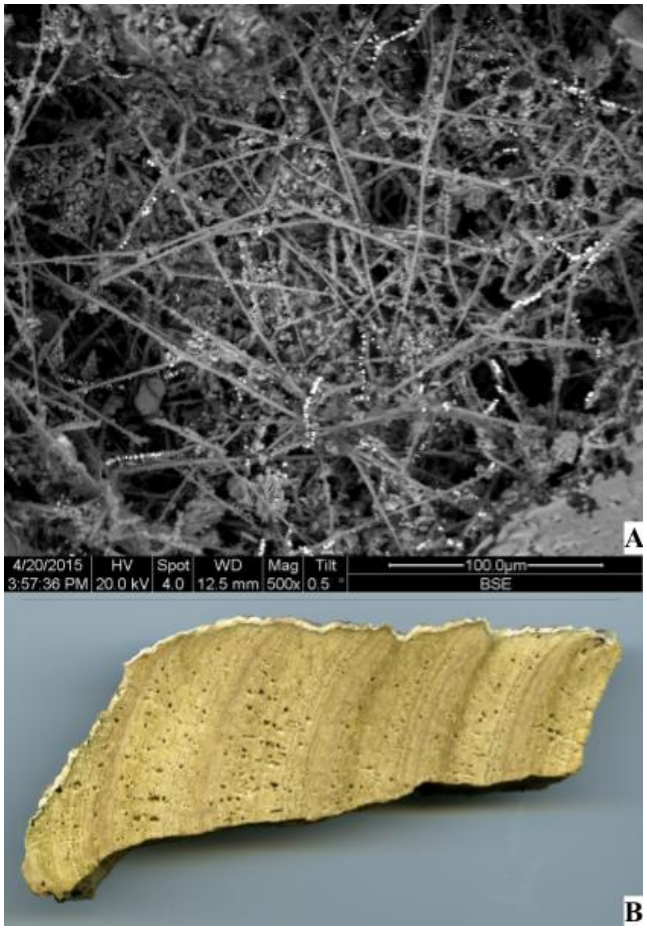

Figure 8.1. A) Bacterial filaments encased in Silica. B) Layers of Silica precipitated into a sinter.

An alternative area to search for life is in locations where preservation of biosignatures would be higher, such as old hydrothermal sites, where life could have formerly thrived much like it does in similar sites on Earth. Sites containing silica rich minerals have been found on Mars by both Mars Exploration Rover: Spirit (MER-A), and the Mars Science Laboratory (MSL/Curiosity) (Squyres, et al., 2008; Skok, et al., 2010; Morris, et al., 2016). Each has discovered highly concentrated silica in the Martian regolith, and in these high concentrations the primary

assumptions for a source could be from precipitation in an aqueous environment, such as a hydrothermal field; or as an authigenic sediment that 'forms' as a result of leaching of other minerals. In the paper by Squyres (2008) announcing the discovery of silica rich material beneath the top layer of soil on Mars, it was hypothesised that the presence of Silica was the result of passive and active enrichment similar to how silica precipitates out in hydrothermal settings on earth. However in the case of the Curiosity research site at Gale Crater the mineral phases associated with hydrothermal settings were not found (Frydenvang, et al., 2017).

Silica laid down as a sinter has other benefits to life, most relevantly that it is an attenuator of UV radiation. Whilst 4 billion years of irradiation could be too great to preserve any source of organic matter that is not being continuously replenished, any benefit from radiation protection could still increase the chance of detecting organics near the surface, in a location easily reached by unmanned vehicles. Silica sinter also has the advantage of preserving life within by 'fossilizing' it in layers of silica (Figure 1). Discussion of the viability of visual biomarker identification can be found in chapter 5.4.

In the absence of chemical signatures of life it is possible to identify life from geological signatures. Stromatolites are one such example of an organosedimentary structure that forms in the presence of bacteria and have for some time been considered a biomarker (Golubic, 1976; Reid, et al., 2000). It should be noted however, that stromatolites have been shown to develop in absence of any microbial influence. McLoughlin, Wilson and Brasier demonstrated in a 2008 paper that the formation of mini-columnar structures resembling stromatolites was possible in the absence of microbes via solely physicochemical processes (McLoughlin, et al., 2008). Whilst stromatolites can be a potential indicator of biological activity, they cannot act as the sole evidence of biological activity. This is reflected in samples taken from El Tatio in chapter 5.

Whilst there is a high volume of biological material woven through many of the samples taken from around geysers and the outflow channels, there are some samples where no biological material is present. The patterning observed by Mcloughlin, Wilson and Brasier from their synthetic stromatolites is reflected in both the bacteria present and bacteria absent samples that were analysed from El Tatio.

The European Space Agency is preparing to land the ExoMars rover on Mars by 2021, carrying with it a science payload containing two important pieces of equipment to Mars that will be the first of their kind. The first is a drill capable of extracting core samples from up to 2 metres below the surface. The second is a Raman spectrometer. Raman is a technique often used in geological studies, but also has applications in drug design applications.

8.1.2 Silica Sinter

Precipitated silica sinter originates at locations in the Earth's crust where superheating of sub-surface water carries silica and other minerals to the surface (German, et al., 1990) where it emerges in the form of a terrestrial geyser or oceanic hydrothermal vent. Hydrothermal vents have been identified as a possible origin of life location due to the presence of reactive mineral surfaces, the ability to maintain a temperature and chemical gradient and could function as a mixing chamber for simple through to complex prebiotic molecules (Westall, et al., 2013; Hazen & Sverjensky, 2010). The innate fossilization processes that occur in the presence of silica precipitation around hydrothermal vents make them an optimal location for studying past life in that location with potential for use as a site of astrobiological interest for studies on other planetary bodies. Fossilization within silica leaves structural fossils similar to stromatolite

formations even in the absence of biological material allowing for visual evaluation of silica sinter structures to determine any potential role they might have had in a biotic system.

Fossilization within silica is an abiotic process though bacterial reactive surfaces have been shown to act as a nucleating agent for silica polymerization in acidic solutions (Fortin & Beveridge, 1997). However hydrothermal systems are often near-neutral pH systems where silica precipitation occurs via formation of silica colloids which more rapidly reduce the concentration of soluble silica in solution (Iler, 1979; Yee, et al., 2003). For the purposes of preservation, the cell wall and sheath (if present) is analogous to the mineralized skeleton of an animal and are the most likely cell component to be preserved. The loss of internal cell structures is increased due to the decomposition of cells prior to permineralization as seen in Proterozoic microfossils (Knoll, 1985; Golubic & Campbell, 1979). This loss of detail in mineralized microfossils is reflected in the structure of Proterozoic stromatolites which more closely resemble degraded bacteria beneath surface layer biofilms rather than the intact bacteria of the surface biofilm (Knoll, 1985). Whilst loss of cell components reduces the volume of detectable biomarkers available, the permineralization of partially degraded cells would be expected to increase the volume of precipitated silica in a fossil sample, and thus increasing the preservation potential of bacteria within a sample from UV radiation and chemical sources of degradation. However as Knoll notes, mineralization of empty sheathes still allows for analysis of cell division and growth patterns in cyanobacteria with cell walls and/or sheathes that are conducive to mineralization. Less likely to be directly preserved via mineralization are cells with recalcitrant walls or sheathes whose presence can only be inferred and may not be identified at all, resulting in an incomplete picture of the fossilized ecosystem.

The most likely sites for mineralization of bacteria in silica are SiO_2 rich volcanic or hydrothermal sites in aquatic environments. These sites provide a constant resupply of silica brought up from the Earth's crust which will maintain silicification rates of bacteria over long time periods. The high pressures and temperatures of water brought up through the crust will support a higher concentration of silica than water under atmospheric conditions, with a maximum possible solubility of 1660mg/Kg at 340ºC and 890mg/Kg at the critical point (Fournier & Rowe, 1977). The actual concentration of hydrothermal waters will be limited by the supply of silica from the crust, but this represents a maximum possible saturation point of water for the purposes of silicification. The hydrothermal waters at the El Tatio hydrothermal field are discharged from the sub-surface at a temperature of 86ºC, with a pH of 7.2 and an average SiO_2 concentration of 450ppm with a range of 385-750ppm (Jones & Renaut, 1997). Geyser and spring pools have a reduced concentration of 210ppm (Jones & Renaut, 1997).

The adhesion of silica to the surface of bacteria is not caused by direct interaction between the silica and bacterial surface due to a low binding affinity between the two. Studies using acidophilic bacteria to investigate the bonding mechanics in low pH conditions demonstrated that under supersaturated conditions polymerization was slow and the activation energy required to bind to bacterial surfaces were too high to allow for successful nucleation on the cell surface (Fortin & Beveridge, 1997). Yee *et al* demonstrate in their 2003 paper that silica mineralization is most likely to occur when silica is in a supersaturated state (Yee, et al., 2003). When SiO_2 is undersaturated in solution the interaction between cell and silica colloid is weak and minimal mineralization occurs on the surface of cyanobacteria. Barriers to silica nucleation have been shown to be overcome when experiments are performzed on Ferrihydrite-coated bacteria

implying an important role for iron in the mineralization of bacteria (Fein, et al., 2002). It's important to note that the addition of Fe on the surface of the bacterial cell wall/sheath does not change the process from abiotic to biotic, as the cell itself is involved only passively as a site for nucleation to occur. Successive nucleation events occur due to SiO_2-SiO_2 interactions which results in mineralization of the cell surface. Internal mineralization will only occur due to degradation of the cell exterior allowing silica to enter by which point the cell would be dead.

The aim of this study is to assess the capabilities of Raman with regards to its use as an analytical tool to determine the presence of organic material of biological origin in a hydrothermal environment, with particular focus on the impact of silica on the preservation of organic material and their detection via Raman. It will also consider the UV attenuating properties of silica sinter and the potential for degradation of organic signatures in the short term. With the confirmation of silica rich environments on Mars that are likely to have formed in the presence of water in several separate locations on Mars, it is not unlikely that the ExoMars rover could also come across a silica rich area to sample from. As a result it is important to determine the effectiveness of Raman at detecting organics in silica rich substrates.

8.2 Method

8.2.1 Synthetic Sinters

Synthetic silica sinter was created through a neutralization precipitation reaction between sodium metasilicate dissolved in water and hydrochloric acid to create sodium silicate. 80 g/L silica gels were produced, with NaCL salt as a by-product.

Sodium metasilicate was dissolved in deionised water at a concentration of 8g/L and creating an alkaline solution. Mass measurements were made using an A+D 100Z Analytical Balance (accurate to 0.1mg) to obtain 8g of sodium metasilicate and the precise volume of water required was calculated. Sodium metasilicate was dissolved into the prepared water in a 1L beaker and a magnetic stirrer used to aid mixing of the solution. The magnetic stirring rod was washed in decon prior to use and rinsed in deionised water to remove any potential contaminants.

30% hydrochloric acid was used as the neutralizer. Hydrochloric acid was diluted and stored in 50mL Corning Centristar centrifuge tubes. A 1000mL Gilson pipette was used to accurately prepare 30% hydrochloric acid by mixing 15mL of 100% hydrochloric acid with 35mL of deionised water. This solution was then mixed using a KS 501 Digital Orbital Shaker at 60 revolutions per minute for 5 minutes prior to the neutralization procedure. Hydrochloric acid preparation was performed under a fume hood to minimize fume exposure.

Neutralization was performed using 1000mL, 200mL and 20mL Gilson pipettes until the solution reached pH 7. The dissolved sodium metasilicate was kept on the magnetic stirrer and a Fisherbrand pH electrode probe (12mm x 120mm, Product code: 11582533) inserted to monitor changes in pH. The pH probe was calibrated in freshly produced buffer solutions prior to use. To

ensure the accuracy of the pH probe throughout the neutralization process, the probe was periodically removed and washed in deionised water.

30% hydrochloric acid was injected into the sodium metasilicate solution until the solution became fully neutralised. Smaller volumes were injected as pH decreased to ensure that the solution did not become acidic. At pH 7 the silica gel begins to form and the solution becomes more viscous. At this point the pH probe would become unable to monitor pH and the solution would be considered neutralised.

In order to remove the salt byproduct of the reaction, gels were centrifuged in 50mL Corning centrifuge tubes and had the remaining water poured off, before being re-suspended in deionised water and centrifuged again. This was repeated 8 times. Salt removal was confirmed by testing for conductivity in the runoff water. Reduced conductivity after each wash confirmed that salt was being removed from the silica gels.

Following the preparation of synthetic gels, *Phormidium* cyanobacteria suspended in deionised water were mixed in at different concentrations. Concentration of bacteria was determined via optical density. 15 ml of silica gel was used to mix in with 4 ml of cyanobacteria. Prior to mixing the cyanobacteria used were homogenized utilizing a Dounce homogenizer in order to minimize clumping of cells in the mix. Silica gel viscosity was reduced via the addition of deionised water in order to improve mixing. The Gels were then poured into individual trays consisting of glass slides in aluminium foil boats.

After 3 hours of drying, gels were removed and moulded into a more compact shape to improve the size and integrity of the dried sinters produced. An additional glass slide was placed on top of

the silica gels to provide a flat surface on both sides of the sample to aid sample preparation for Raman. Individual blocks were approximately 10mm^2 on the widest side, allowing for 20mm^2 of surface area available to scan per block (Topside and underside). Flat area scans were limited in size by changes in height across the block as loss of focus on the sample surface would impact data collection. Additionally, blocks were 5mm deep, allowing for scans through the block to monitor the effectiveness of Raman through the substrate.

After removal from the oven, individual sinters were separated from the glass slides and bagged prior to Raman. Samples were stuck to microscope stage stubs.

8.2.2 Natural Sinter Samples

Natural silica sinter samples were obtained from the El Tatio hydrothermal field in the Chilean Andes. El Tatio is located at 4320m and is an example of an extreme environment for life. Microbial life needs to contend with higher UV radiation at the surface due to altitude and reduced atmospheric density which results in higher degradation rates. The hydrothermal waters provide an energy and nutrient source for biofilms that cover the silica sinter. Silica sinter precipitation results in bacterial fossilization that can be observed under SEM (Figure 1).

Samples were cut using CS10 Cutoff saw equipped with a diamond blade to expose the inner material. The saw utilises running water to prevent the blade and the sample overheating during the cutting process. This water is recycled throughout the cutting process. As a result the saw was thoroughly washed using a 1:3 decon mix and the saw rinsed in deionised water. The trough used to store water was drained and rinsed to minimize contamination. Samples were cut from the top to the bottom of the sample to expose the interior from the most recently precipitated material to the oldest.

Following the cutting procedure, samples were polished down using new 150, 300, and 600 grade sandpaper and washed once more in deionised water before being left to dry under a fume hood. Samples were then stuck to microscope stage stubs.

8.2.3 UV Degradation

A polychromatic UV source (185nm-2000nm) was utilized to better approximate the UV radiation that would be experienced under Martian conditions. Monochromatic sources such as UV lamps typically used in a laboratory setting would provide an insufficient dose despite their efficacy for laboratory sterilization..

As a substantially weaker source of UV radiation the monochromatic light source was better suited to testing at smaller time periods, allowing for a quantification of time to track signal preservation. Even at shorter time periods it has been previously demonstrated that UV degradation has an observable and significant impact on viability in bacteria from monochromatic light sources after periods as short as 30s (Wadsworth & Cockell, 2017). Tolerance to UV radiation will be higher in cyanobacteria, particularly those common to high-altitude hot-springs however, effects on viability will still be observable on shorter timescales.

Polychromatic solar degradation simulation was performed using a Hamamatsu 150W Xenon lamp [L2273] (185-2000nm) capable of simulating ultraviolet radiation related degradation at the Martian surface. The polychromatic lamp was housed within a secure chamber located inside an extraction hood for safety purposes. The increased intensity of the polychromatic source meant that experiments utilising it were performed on much smaller timescales (10s) than that of the monochromatic light source. The parameters for UV exposure compared to Mars remain the

same as in 7.2.6 with 1s of exposure under experimental conditions translating to 1.39s of exposure under Martian conditions. Thus a 10s exposure equates to 255 J/m^2.

UV irradiance was measured and monitored using a Macam UV203 Ultraviolet Radiometer to allow for an estimation of UV exposure to that at the Martian surface.

A purpose built chamber was used to safely contain and conduct the UV lamp for the experiment. The chamber measures at 46cm x 100cm x 46cm whilst the lamp and lamp housing are suspended 60cm above the bottom of the chamber. Samples could be placed closer to the lamp source for a more intense irradiance if required.

Prior to irradiation the chamber was given a 20 minute warmup period during which the lamp would stabilize its output. Stabilization of lamp output was defined as the output maintaining within 1% variability over a 5 minute period (Hamamatsu Photoniks K.K., 2015). Lamp output was also monitored when swapping between samples for exposure.

To assess the attenuating effects of the synthetic silica sinters, samples underwent Raman spectroscopy prior to UV exposure to establish a baseline spectrum as a control. Raman scans were performed under the same parameters and on the same location on the sample for consistency between scans. Exposure was conducted over a period covering 2 minutes and then a further 8 minutes. Raman scans were conducted after each exposure.

Exposure of laboratory standards to the lamp was performed in increments of 10 minutes. Samples were either exposed to solely UV or were exposed to UV in the presence of perchlorate to assess how perchlorate rich soils on Mars could amplify damage to simple biomarkers. Perchlorate was provided in a powdered form in order to minimize the contamination of samples during the Raman phase of the experiment.

8.2.4 Raman spectroscopy

The Raman spectrometer in use is a Renishaw InVia Raman Microscope, equipped with 532nm and 768nm lasers. The microscope through which samples were viewed and analysed was equipped with 5x, 20x, 50x, 50(L)x (long working distance objective) and 100x objectives. Scans were performed in the band between 500 cm^{-1} and 1800cm^{-1} as this was where the majority of peaks resided. Above 2000cm^{-1} high fluorescence would disrupt the natural sinter samples.

All sample data used was background subtracted unless stated otherwise. Samples that experienced cosmic ray interference during scans (a frequent side effect of Raman scan data) were either rescanned or had the erratic peak removed via algorithmic detection. Every Raman scan was run in triplicate to ensure that peaks were the result of the sample content, rather than as a produced by-product of the interaction between the Raman laser and the sample itself as a result of alterations due to laser burning.

8.2.5 Scanning parameters

A spectra for the *Phormidium* used during artificial silicification was obtained prior to the experiment as a baseline with which to compare the silicified spectra. Additionally the raw *Phormidium* sample was exposed to the same degradation experiment to compare degradation rates between 'protected' and 'unprotected' organic material.

Initial Raman scans were performed at a surface level to observe how the Raman signal changed according to the concentration of *Phormidium* in the sample. Auto-fluorescence is one of the key problems associated with Raman spectroscopy, particularly on organic and biological samples that can contain impurities with a high potential for fluorescence. Scans were performed in triplicate at a minimum to monitor for slight variations in peak data. To minimize signal-to-noise scans were performed with multiple accumulations of scan to form Raman spectra that consisted of the accumulated data of a minimum of ten accumulations.

Following surface level scans the samples were probed vertically to obtain a depth gradient to observe if increased volumes of silica between the sample and the surface would affect the spectrum obtained.

Samples were probed every 1μm from the surface for a total of 3001 scans to reach 3000μm. Scans took place at 50% of laser intensity at 50x magnification with 3 accumulations (repeats) per depth to provide a clearer spectrum. Each scan lasted 0.5 seconds for a total of 1.5 seconds per depth scan. A sample of lower bacterial concentration was used as a more fully saturated

sample with respect to cyanobacteria may have shown a reduction in signal that was limited only by bacterial concentration, rather than due to the influence of the substrate.

8.3 Results

8.3.1 Cyanobacterial Control

Initial scans of the unsilicified cyanobacteria were dominated by peaks associated with B-carotene (957, 1004, 1155, 1192, 1445, 1516 cm^{-1}) (Figure 2). These peaks resonate strongly partially due to the dual beta-rings at the ends of the molecule. Such a strong organic spectra would be unexpected in the context of future Martian exploration due to the intense degradation of matter at the surface as well as the prolonged period of time in which possible sub-surface material would be degrading, however, stronger peaks in this experiment allowed for a more precise qualification of signal obfuscation by the silica-based substrate by the reduction in peak intensity relative to the background.

8.3.2 Raman scans of lab-silicified bacteria

Initial scans of the substrate without bacteria added resulted in either blank or overly-fluoresced scans in which no peak data was visible. Whilst this was notable as it was initially expected that silica peaks would be observed in the substrate, the ability for the substrate to mask organic signatures was not confirmed. Additionally it was observed that clear peak data was often only obtainable utilizing the 514nm Raman laser and not when utilizing the 785nm laser. The synthetic samples were analysed utilizing both laser setups to ensure no data was missed but the

longer wavelength laser often failed to return meaningful data as a result of increased flouresence.

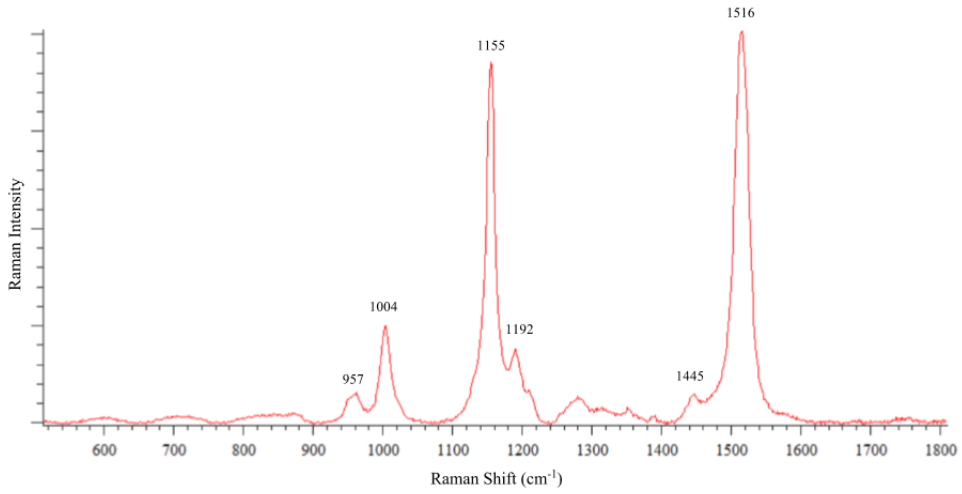

Figure 8.2. Raman spectrum of Phormidium. with β-carotene peaks highlighted (514nm). Scan parameters: 100scan accumulations, 1 second scan time. β-carotene Raman data spectra identified utilising (Tschirner, et al., 2009)

Scans of the synthetically silicified bacteria can be seen in Figure's 4 & 5. Reduction in the concentration of cyanobacteria (and hence Total Organic Carbon) demonstrated that whilst the overall shape of the spectra remains similar to that of the unsilicified cyanobacterium, progressive reductions in concentration are paired with progressive reductions in signal clarity. Smaller peaks are the first to be obfuscated by the fluorescence signal, particularly those at 952, 1192 and 1445 (Tschirner, et al., 2009).

Depth scans were performed from the surface through 3000µm of the silicified cyanobacteria blocks and were capable of obtaining weak spectra reflecting the strongest peaks of the unsilicified bacteria. There is a clear reduction in signal intensity overall with the depth of the sample after the first 500µm, however, the traces of the strongest peaks at 1156cm^{-1} and 1516cm^{-1} were still visible despite the reduction in intensity. The high intensity peaks persist in the top 350µm of the block before a gradual reduction in intensity throughout the rest of the depth gradient (figure 5). Note that the dataset is represented as the raw data obtained as measured by the Raman spectrometer, as any normalization would negate any comparisons with regards to signal intensity.

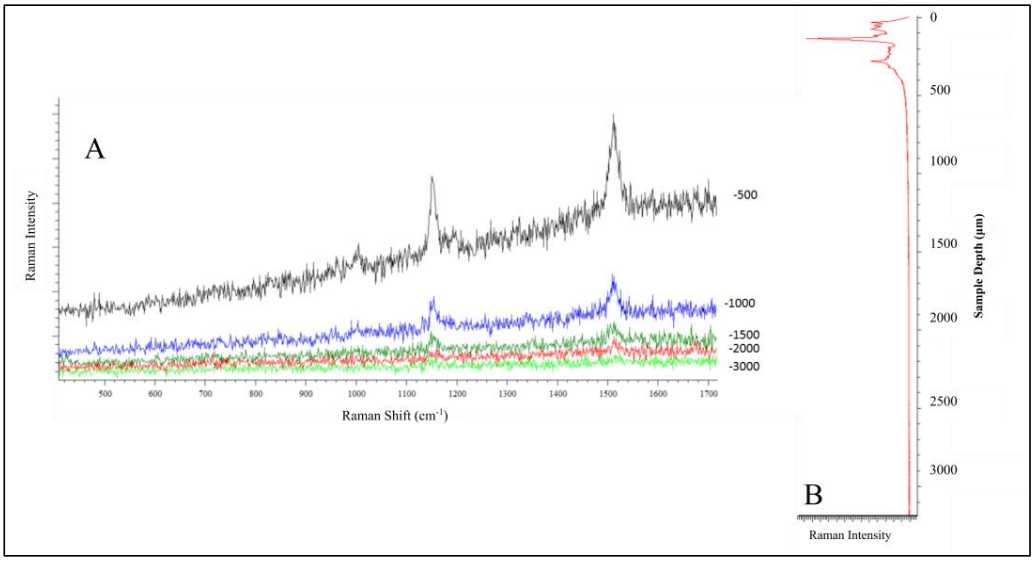

Figure 8.3. A comparison of Raman spectra up to 3000µm into the 0.563 sample. (A) displays the change from 500-3000µm in the sample. (B) Shows the relative intensity of the signal at peak 1516 down the depth gradient.

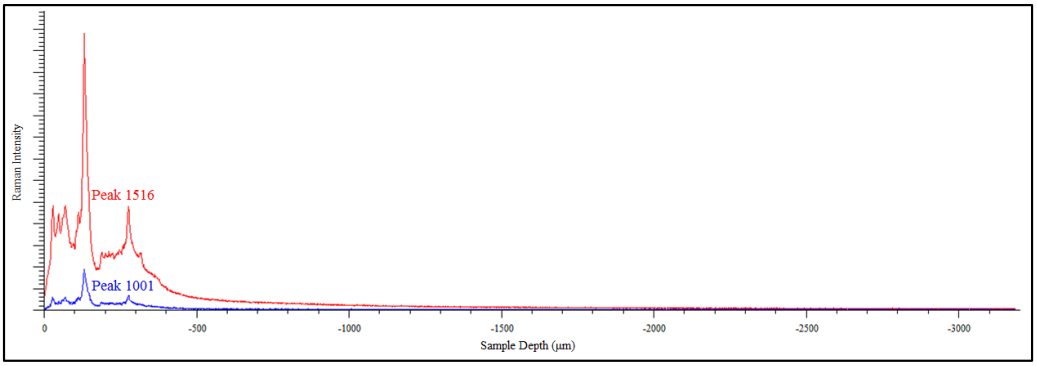

Figure 8.4. Comparison of signal intensity between peaks 1001 (blue) and 1516 (red) during a depth scan. More intense Raman peaks persist over weaker peaks as interference increases. .

A regression analysis of the silicified signals was conducted to compare how the silicified signal changed with respect to the original unsilicified cyanobacterial signal. A direct component least squares (DCLS) analysis is a regression analysis that determines the degree to which the in this case the silicified signal varies compared to the unsilicified signal. Automatic identification of peak data by WiRE is limited as smaller or merged peaks can be missed by the algorithm. Visual identification of low intensity peaks is therefore necessary for identifying differences in observed peak data between sample data and control data. Comparison between sample data and control data via a regression analysis cannot identify individual peaks but it can determine the degree to which sample data matches the control data. This can be observed in Figure 14.

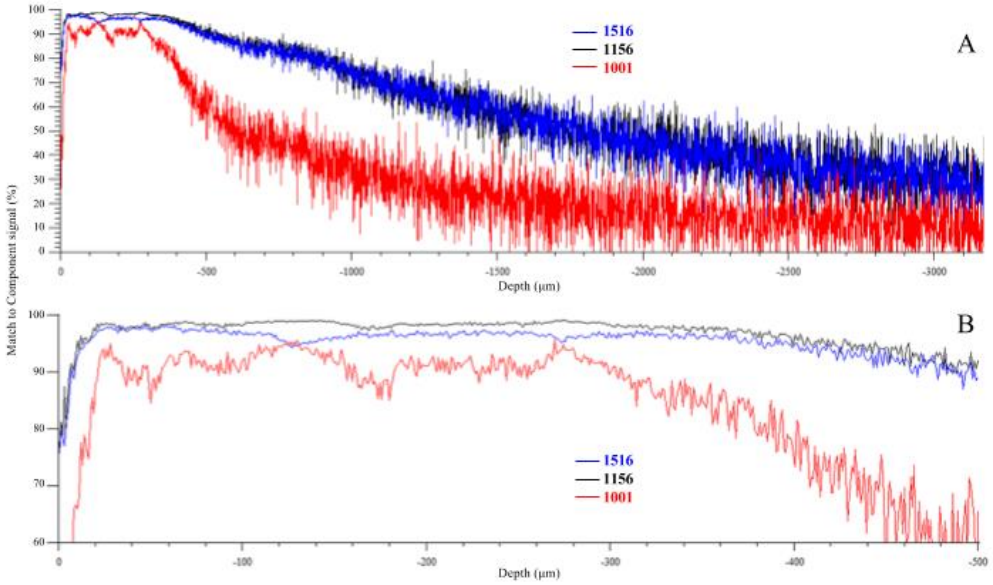

Figure 8.5. Correlation of peak intensity determined through DCLS analysis between the three principal peaks of Phormidium and the silicified sample. (A) Correlation through the full depth sample. (B) Correlation in the top 500µm.

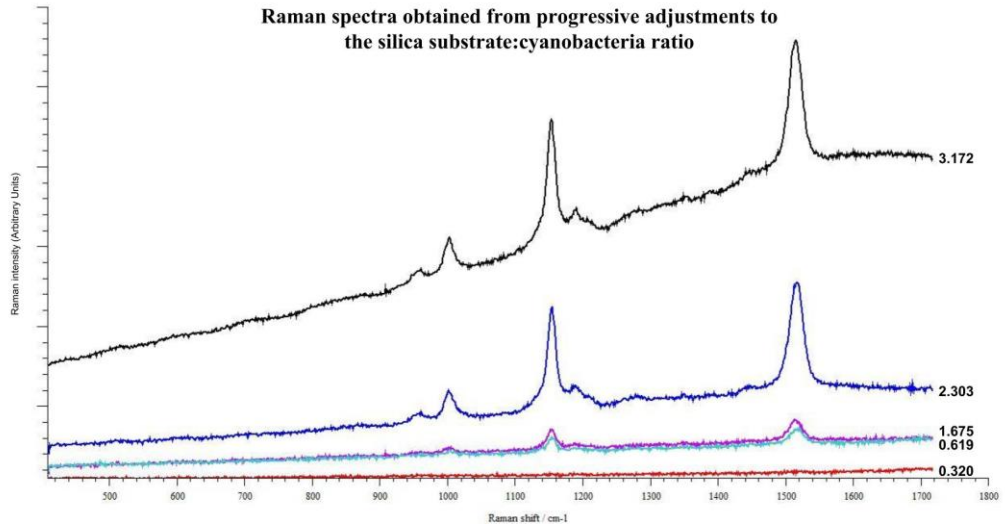

Figure 8.6. Progressive increases in the ratio of silica to cyanobacteria result in reductions in Raman signal strength. Weaker peaks degrade more severely than stronger peaks.

The synthetic samples were also exposed to Mars equivalent UV from a polychromatic UV source to assess how Raman signatures that correspond to organic material are affected by a photolytic degradative process. Samples were exposed to 2 and 10 minutes of UV treatment to assess if and how the signal altered as a result of that treatment. The results can be seen in figure 4. The initial Raman spectra feature much more prominent peaks with respect to the baseline of the data compared to those of the UV-treated samples. The UV-treated samples experience a progressive decline in peak height:background ratio that can be attributed to UV-induced degradation of the β-carotene molecule.

Importantly there is no loss of peak data from the analysed samples. The degradation of height:background ratio is suggestive of an eventual loss of peak data, however, the majority of peaks are still present and maintain their proportional height relative to the most prominent peaks in each sample. There is some loss of minor peaks that appear as shoulders of others although on

repeats of data collection show that this is as much a problem due to fluorescence as it is one of UV degradative damage.

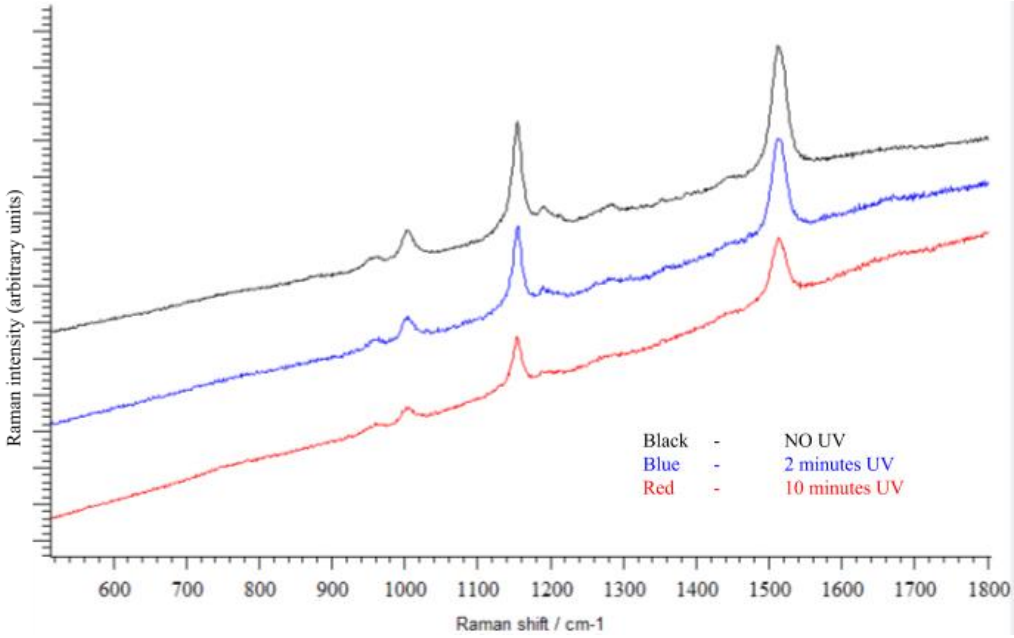

Figure 8.7. Raman spectra of samples exposed to a polychromatic UV radiation source. Scans were run under the same parameters on each occasion, and on the same location on the sample to ensure consistency, however, the scaling of the graph is such that more powerful scans would not affect the interpretation of results. Scans performed utilising 518nm laser for 30x 0.5s accumulations @50% of maximum intensity (Total scan time 15s).

8.3.3 Natural sinters

The majority of spectra obtained from the natural sinters obtained from El Tatio in Chile were obscured by a fluorescence signal. This suggests that the sinter makeup itself and any additionally incorporated minerals could prevent detection of organic matter present. Of the samples that did provide clear peak data, it was clear that fluorescence was still a factor, and that some peaks are likely to have been obscured as a result. Those peaks that are visible are not always prominent on the spectra but their presence is enough to allow some qualitative assessment.

The natural sinter samples were confirmed to contain viable cyanobacteria by grinding the sample into a powder via mortar and pestle that could then be left in nutrient agar until bacterial growth could be observed. The Brown, Mystery and Terrace geyser fragments all produced viable bacteria when left to grow under sunlamps and in a temperature controlled environment.

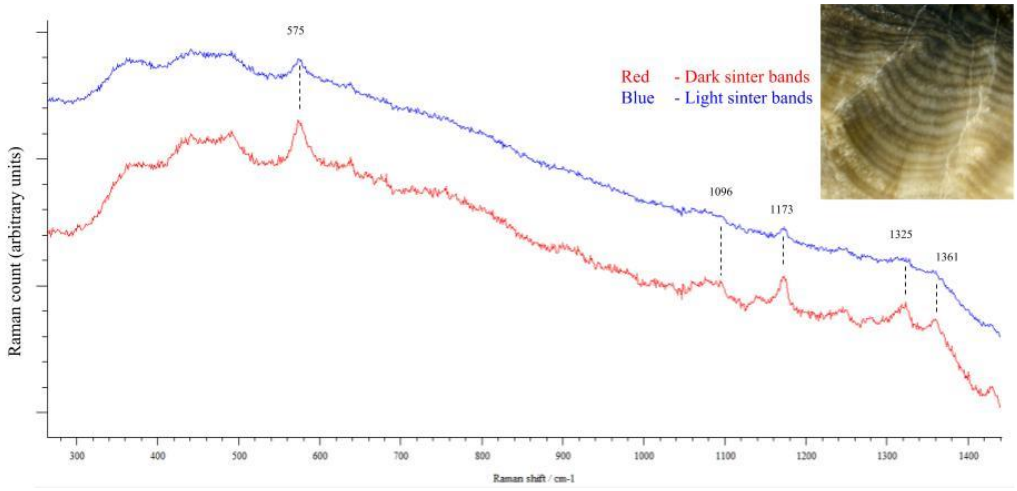

Figure 8.8. Raman spectra showing differences in sinter spectra between light and dark banding in older silica sinter from a cone geyser in El Tatio, Chile. The red spectra corresponds to the dark banding where pore density is highest, whilst the blue spectra corresponds to the lighter bands where porosity is lower and the surface area is predominantly a flat face of sinter. Scans performed utilising 785nm laser for 20x 4.5s accumulations @50% of maximum intensity (Total scan time 90s).

Analysis of most natural sinter samples produced Raman spectra such as those in Figures 4 & 5, and Raman spectra can differ significantly across one sample. The spectra obtained in Figures 4&5 come from the same sample, but from two different areas on the sample. The sample in question comes from a cone geyser in the upper basin in El Tatio and it can be split in two according to its profile. The upper half of the sample consists of newer (younger) sinter growth and obvious elements of large bacterial filaments (As seen in the Sinter Analysis chapter, figures 20-22). Whereas the bottom half of the sample contains no direct visible evidence of bacteria, but consists of pores following a similar pattern of distribution to that of the microbial filaments in the upper half.

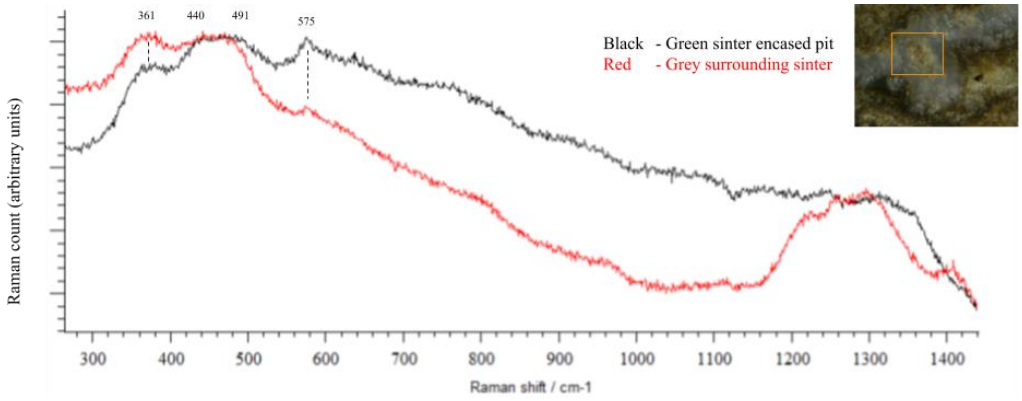

Figure 8.9. Raman spectra of a pit of material (green) presumed to be bacterial in origin and the surrounding sinter (grey) showing different accumulated spectra but similar peak patterns. Scans performed utilising 785nm laser for 10x 5s accumulations @50% of maximum intensity (Total scan time 50s).

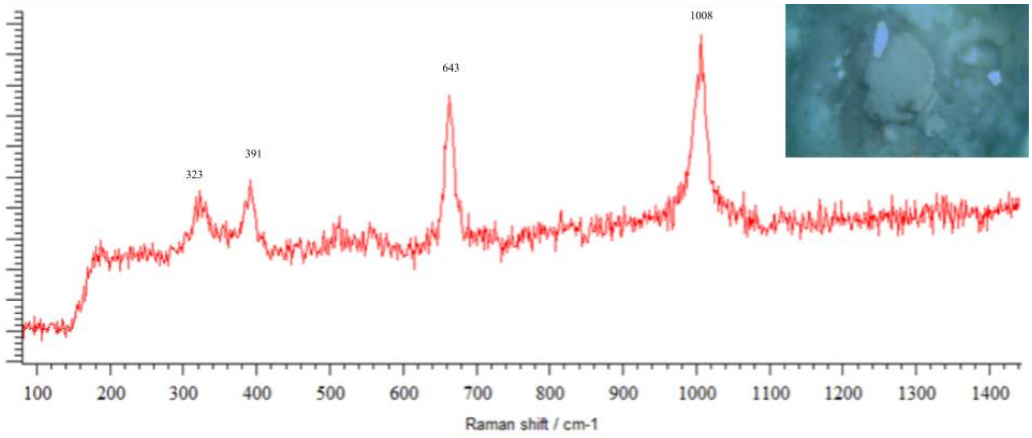

Figure 8.10. Raman data from a sample taken from a fountain geyser in the El Tatio geothermal area. The sample is a laminated/coarse sinter sample taken from the pools that form in the geyser splash zone. Scans performed utilising 518nm laser for 30x 1s accumulations @10% of maximum intensity (Total scan time 30s).

Figures 6 & 7 come from a further two different samples and vary quite significantly from those previously studied in figures 4 & 5. Peak data is clearer in these two samples compared to those in figures 4 & 5, possibly owing to decreased organic content reflected by little evidence of bacteria in SEM imaging.

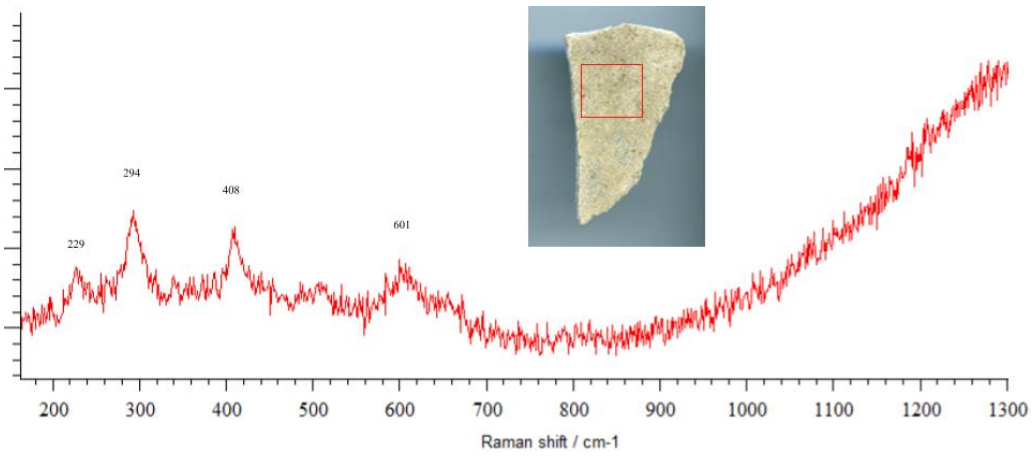

Figure 8.11. Raman spectra of the surface of a fragment of laminated sinter from the Terrace Geyser, Chile. Scans performed utilising 518nm laser for 20x 0.3s accumulations @50% of maximum intensity (Total scan time 6s).

8.3.4 Analysis of extracted TLE of natural samples

In addition to running the standards used for GC-MS calibration, samples of the Total Lipid Extract (TLE) were observed under Raman to obtain the Raman spectra of the organic content of the natural sinter samples when they have been 'de-silicified'. The full process of extracting the TLE can be referred to in the Biomarker analysis chapter. Analysis of the TLE was done via the removal of 1% of the total TLE following re-suspension in 1000µL dichloromethane (DCM) after extractions using the Accelerated Solvent Extractor (ASE). The TLE extract was transferred onto glass slides that had been furnace at 400°C for 8 hours and washed in DCM.

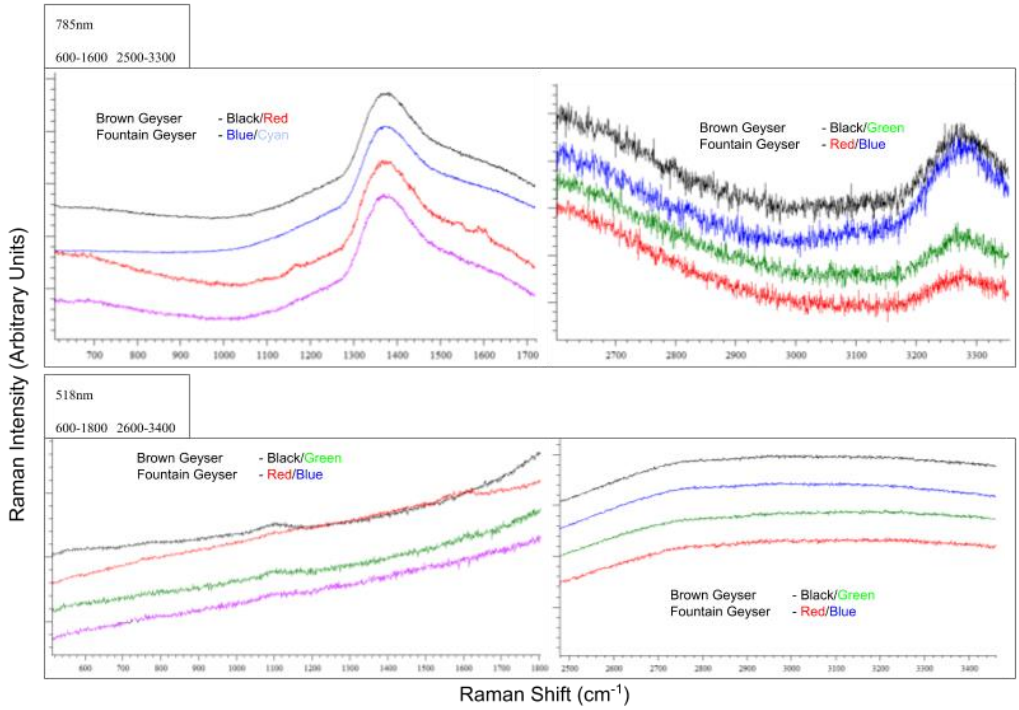

Figure 8.12. Raman spectra obtained from the TLE of two sinter samples at both 785nm & 518nm wavelengths. All four scans were run with the same parameters of 30x 0.5s accumulations at 10% of laser power.

8.3.5 Raman analysis of laboratory standards

Analysis of standards produced varying spectra, some of which experienced minor fluorescence but peak data was visible for most samples. The impact of UV can be seen in figures 10 & 11. Figure 10 shows the impact of UV treatment in the region of 2500cm^{-1} to 3400cm^{-1}. Two notable peaks are observable at 2848 cm^{-1} and 2882 cm^{-1} in the Standards spectra, likely corresponding to C-H bonding from the alkane chain.

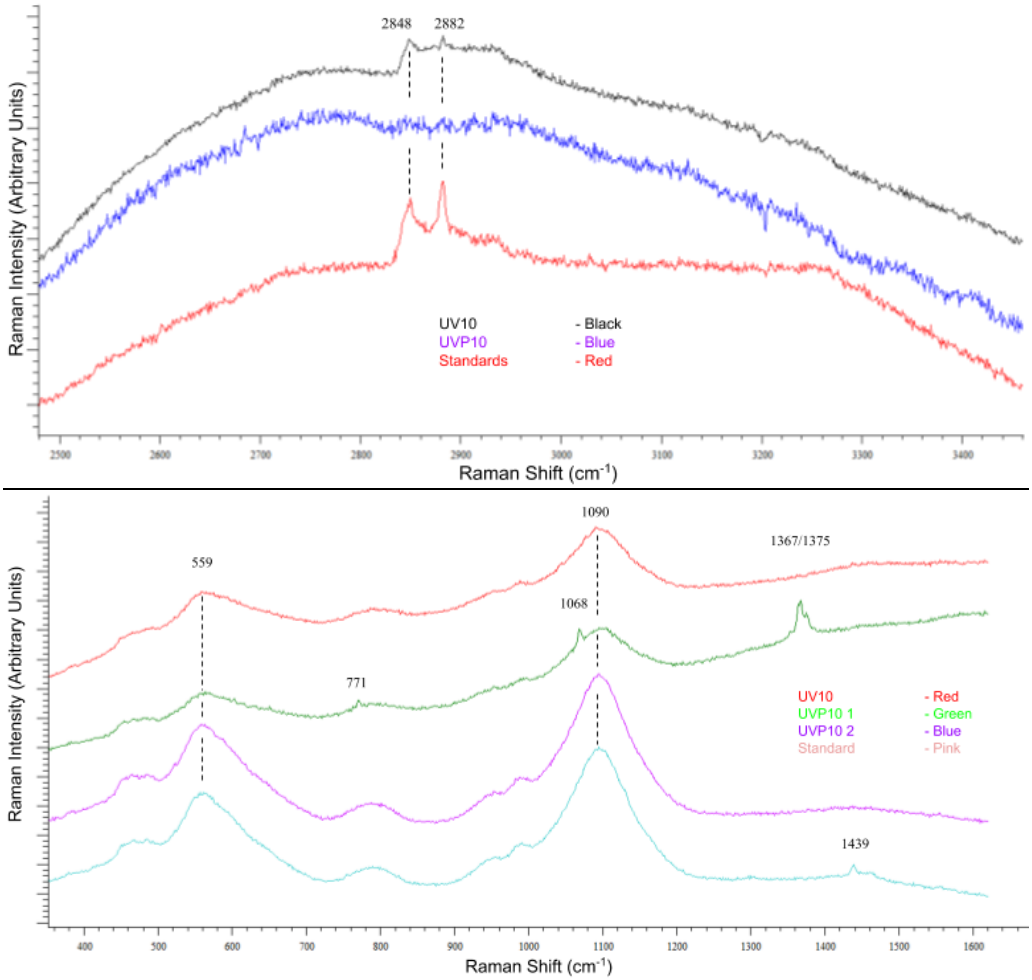

Figure 8.13. Raman spectroscopy of alkane standards before and after UV treatment in the region of 2500cm^{-1} to 3400cm^{-1}. Abbreviations; UV10, 10 minutes of polychromatic UV treatment; UVP10, 10 minutes of polychromatic UV treatment with the addition of the oxidising agent magnesium perchlorate; Standards, the untreated standards sample. Spectra have had a 10% offset applied for clarity.

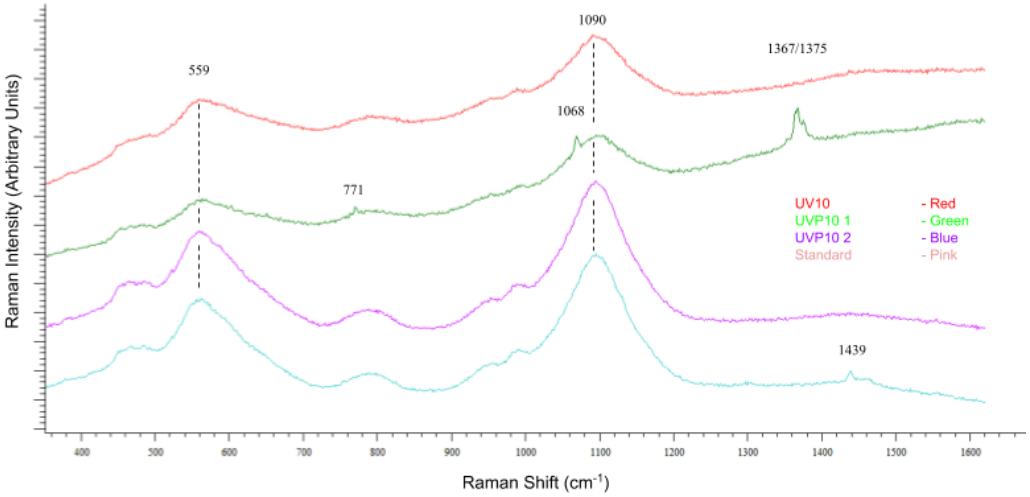

Figure 8.14. Raman spectroscopy of alkane standards before and after UV treatment in the region of 400cm^{-1} to 1800cm^{-1}. Abbreviations; UV10, 10 minutes of polychromatic UV treatment; UVP10, 10 minutes of polychromatic UV treatment with the addition of the oxidising agent magnesium perchlorate; Standards, the untreated standards sample. Spectra have had a 20% offset applied for clarity.

In contrast to Figure 10, Figure 11 shows that UV treatment both in and out of the presence of perchlorate is not necessarily detrimental to all peak data, in fact adding some to the spectra of the standards. The overall shape of the Raman spectra remains constant, with particular focus on the peaks at 559 cm^{-1} and 1090 cm^{-1} but some accessory peaks appear in certain samples. In the standards there is a peak at 1439 cm^{-1} that is confined to this spectra. It appears to have been removed in all UV scenarios. However in the first perchlorate spectra there are three peaks located at 771 cm^{-1} and 1367/1375 cm^{-1} that have been added that do not appear in the UV,

second UVP and the standards spectra. This is presumably a result of the forming of Carbon-to-chlorate species bonds as a result of oxygenation.

8.4 Discussion

8.4.1 Synthetic sinters

Scans of substrates that were mixed with cyanobacteria produced clear spectra matching the unsilicified sample (Figure 4). At higher concentrations of bacteria there was very little loss of peak detail even in the lower-intensity peaks, however, as bacterial concentrations lowered weaker peaks were the first to be obscured by the growing background noise of the samples that was resulting from fluourescence. This is as likely to be the result of a reduction in concentration of organic material as it is to be due to be signal inhibition by the silica substrate. However a similar reduction in signal strength is not seen when using smaller quantities of unsilicified cyanobacteria. The disparity here is most likely due to the homogenisation of bacteria through the silica gel resulting in a much lower ratio of organic matter to substrate than the unsilicified bacteria was capable of achieving.

The percentage correlation to the three principal peaks of the unsilicified β-carotene sample can be seen in Figure 14. When comparing the silicified sample to the full β-carotene spectrum (Figure 14A) the most prominent peaks at 1156nm and 1516nm follow a far more steady decrease in correlation to the *Phormidium* standard than peak 1001nm which falls off sharply

after ~275μm. The decoupling in signal decline suggests that in higher interference samples the weaker the Raman signal of organic content, the less likely that it will be detected as signal degradation is greater. .

The loss of weaker signal resolution as a result of increased interference in the Raman spectra could perhaps be offset through an averaging of multiple accumulations of the Raman spectra. This was tested through attempts to obtain Raman spectra without direct illumination of the sample itself with the Raman laser.

By scanning an area outside the periphery of the sample it was possible to take an obtained dataset of low intensity, low detail signal and normalize the dataset to ignore differences in data intensity followed by creating a composite average of the dataset (creating the composite average of the dataset after normalization results in an average of the spectra shape rather than the spectra intensity) which contained peak data that accurately represented the contents of the silica block. This is likely to be occurring due to scattering of the Raman laser and scattering of the resultant weaker Raman radiation causing a very low intensity signal that appears to be background noise but imperceptible rises in the data allows an average of spectrum shape to reveal peak data. Non-direct sample analysis minimizes the chances of fluorescence events in response to direct illumination; however, this procedure was not effective on all samples.

Figure 4 represents analysis of the distinct thinner bands in the lower half of the sample and it can be seen that there is a distinct difference in Raman spectra obtained from the darker bands (more porous) and the lighter bands (less porous, more sinter). The dark bands which are assumed to be the remnants of the silica that formed around the bacterial filaments return spectra

with more significant peaks than that of the spectra from the lighter bands. If increased porosity is a result of increased filament concentration during sinter precipitation then this could be interpreted as confirmation of organic content.

8.4.2 Long-term preservation of Raman signatures in the Martian UV environment

Determining the signal preservation potential of silica substrates requires an analysis of samples both from short-term degradative external impact factors as well as to take into the account how long-term preservation in silica substrates affects the state of organic molecules.

Synthetic samples exposed to UV radiation experienced varying effects on their Raman spectra as a result of the treatment. Most notably is that the Raman spectra persisted with only the loss of minor peaks which are just as likely to be the result of fluorescence as they are to be a preferential target of UV irradiation. The reduction in peak:background ratio suggests that there will be a timescale on which the degradation of sample is sufficient to obscure the Raman signature. However despite how quickly a polychromatic source of radiation is able to cull the viability of a bacterial sample (Wadsworth & Cockell, 2017) the molecules that make up the contents or structure of a cell appear to be much more resistant to degradation, suggesting that the persistence of biosignatures even in a highly radiative or oxidising environment could still be viable on shorter timescales.

It’s possible that the degradation of organic molecules happens in cycles in the Martian surface due to attenuation of incoming radiation by dust storms, varying solar cycles, etc, (Pavlov, et al.,

2012) where molecules are created and replenished over sufficiently long periods of time that the presence of biomarkers could be synthesised more recently than the Noachian when any possible life could have last existed (Ehresmann, et al., 2011). This however, is dependent on a source for organic compounds that has as of yet not been identified beyond production of simple compounds such as methane (Krasnopolsky, 2006; Oze & Sharma, 2005; Mischna, et al., 2011). Synthesis of complex organic molecules is not an exclusively biogenic process as the prebiotic molecules necessary for the first cellular life would have had to have been produced abiotically. But our understanding of this process is limited to how such compounds formed on an early Earth environment, or an early Mars environment, with little consideration given to how any such molecules could arise on Mars in the present day.

No significant signs of signal degradation were seen in synthetic silica samples that were left untouched for long periods of time (Up to three years) in their respective sample bags in a lab cupboard. The lack of a degradative effect on the encased bacteria confirms that, at least for the short periods of time tested in the lab, situations where external influence is minimized will result in minimal signal degradation/loss.

Analysis of a laboratory n-alkane standard normally used for quantification and qualitative analysis of samples that undergo GC-MS were analysed by Raman spectroscopy both before and after a UV treatment to monitor how the Raman spectra is altered by the degradative effects of UV radiation. In addition to the polychromatic UV source used for this work, the addition of magnesium perchlorate, a powerful oxidiser when exposed to UV light, was used to further induce degradation on the components of the sample by matching one additional component of

the Martian surface (Navarro-Gonzalez, et al., 2003; Millan, et al., 2016; Sephton, et al., 2014). Recent work on establishing the effects of perchlorate on the Martian surface has shown that they further enhance degradation in the Martian soil (Wadsworth & Cockell, 2017).

Raman analysis of the standard resulted in little to no fluorescence of the Raman spectra due to the lack of fluorescent components in the sample. However the spectra of the standards experienced a lot of broader peak data which is being interpreted as interference from hydrogen bonding within the sample, a phenomena already well-studied in Raman and IR spectroscopy (Triggs & Valentini, 1992; Burikov, et al., 2010).

Figure 8 shows two notable peaks at 2848 cm^{-1} and 2882 cm^{-1} in the Standards spectra, which are assume to represent C-H bonding from the alkane chain. There is some obfuscation of these peaks in the UV10 sample but they are still identifiable in the spectra. However in the UV+Perchlorate sample there is no evidence of these peaks. Whilst it would not be expected that there would be a complete loss of C-H bonding in the perchlorate sample, it could be suggestive of a preferential loss of C-H bonds that correspond to the two observable peaks in the standards.

The addition of peaks in some of the UV+perchlorate spectra suggests that two things could be happening. The first is that there is residual perchlorate on the slide that is interfering with the Raman spectra in such a way as to add additional peaks corresponding to Mg-Cl or to Cl-O bonding. The second is that the formation of haloalkanes, specifically chloroalkanes, is reflected on the Raman spectra. In the context of Mars, the presence of haloalkanes could be a possible interpretation of organic content that originated as n-alkanes but has been altered due to Martian geochemistry and UV irradiation. Any confirmation of this would have to be conducted

alongside Mass spectroscopy analysis to determine the full soil content of any Martian samples. Halogenation in the Martian soil is of a high probability due to the high quantities of perchlorate that have already been sampled from various Mars missions (Navarro-González, et al., 2010; Sephton, et al., 2014).

8.5 Conclusion

Continuous Raman spectroscopy has potential as a means of detecting Martian biosignatures, however, the problems associated with fluorescence, as well as the degradation of any organics on Mars means that the technique needs to be accompanied by additional analyses to provide interpretable data.

Complex molecules would be unexpected on Mars both due to the minimized chance of their synthesis but also due to the long-term exposure to highly degradative Martian conditions. Any organics present on Mars would have to be of a sufficient concentration to be detected by Raman, a technique which produces weak signatures in contrast to other similar techniques such as IR spectroscopy. Analysis of Martian samples on Earth either from meteoritic evidence or future sample return missions would be beneficial to further enhancing our understanding of the technique and its viability as a tool for astrobiology. At present it would be expected that the sample will be of significant use to geologic studies on Mars, not least due to it being a non-destructive technique.

9 General Discussion

The work contained within this thesis has focused on two factors crucial for detection of potential biosignatures in an astrobiological context. The first is the establishment of Earth-based analogue sites that match the conditions necessary for astrobiological study. In the case of the site in the Chilean Altiplano at Sairecabur these conditions are to represent Martian soil parameters of atmospheric and soil diurnal temperature cycles, soil humidity cycles, and surface elevated ultraviolet radiation at the soil surface. The second half of this study has focused on the potential for biosignature identification in silica precipitates found on Mars of a possible hydrothermal origin. Like the study on Sairecabur, the hydrothermal study utilised samples taken from a site (El Tatio, Chile) that more closely approximates Martian UV conditions than a site closer to sea level. The hydrothermal study also looked at comparisons biomarker variability between different hydrothermal sites (Chile, NZ, Iceland) and considered the cause of that variability, and the impact of UV on the detection of biomarkers contained within hydrothermal precipitates.

The common thread between each study is the local UV environment and the impact it has on the surrounding environment. In the case of Sairecabur the increasing UV radiation with increasing altitude results in a gradual loss of life on exposed surfaces. At 4269m, the base of the volcano, plant life was present in the form of tall simple grasses sparsely distributed across the ground. Above 4269m this vegetation was no longer present and from and above the second site at 4792m life was limited to the shelter of boulders and rock faces. At the datalogger site at 5056m life was restricted to lichens on the undersides of rocks.

The datalogger site was selected as it was the highest site suitable for inserting dataloggers in the soil. The decision to target the highest site possible was due to increasing altitude providing a better representation of the Martian UV environment. It also would result in a greater discrepancy between the atmospheric temperature and the surface temperature of the soil, also mimicking the conditions on Mars with regards to direct surface heating of the soil. One further site on the volcano was reachable at 5269m but the ground was covered in penitente ice.

Datalogger data showed that the soil conditions at high altitude did match the expected conditions on Mars with regards to direct surface heating of the topsoil driving a diurnal variation in soil temperature and moisture.

The Chilean hydrothermal site at El Tatio is situated at 4320m and is similarly sparse in terms of vegetation, but the geysers on the site support their own ecosystems. Bacterial biofilms coat many of the surfaces around vent exits and their runoffs and one of the consequences of this is the incorporation of these bacteria into the precipitated material. The waters of El Tatio are silica enriched and the silica structures that have formed contain complex webs of bacterial filaments, in addition to the presence of other lifeforms such as diatoms.

One of the aims of this thesis was to establish whether or not silica-rich sites on Mars were an optimal location for future investigations due to the increased potential for biomarker preservation. The contrasting environments between the sparse upper altitudes of Sairecabur and the comparatively richly colonised El Tatio have shown that the silica rich site has been beneficial for biomarker detection.

Biomarkers can take many forms, from organic molecules detectable via mass spectroscopy methods, spectral data from methods such as Raman, and visible identification through microscopic techniques including optical, infrared, and electron microscopy. In the case of the

silica precipitates analysed within this thesis, the visible identification of bacteria within the silica matrix provided a direct indicator of the presence of bacteria. These visual biomarkers also occurred in the form of pores that likely formed as a result of bacterial filaments degrading long after their internment, thus providing a possible biomarker despite the absence of material. Due to the extended timescale for degradation of possible biological material on Mars since it was last theorised to be capable of supporting life it is more likely that these visual indicators of former bacteria are present than the direct evidence of silicified life.

Mass spectroscopy is currently one of the main methods employed by Mars rovers and landers identify material of interest and would continue to be the most powerful of the techniques tested within this thesis. Raman spectroscopy is another tool for precise identification of material but the problems associated with interference and fluorescence of spectra in the natural sinter samples as in 8.3.3 have shown that the uses of Raman are limited by the substrate. The scans of the lab-synthesised samples in 8.3.2 show that Raman is capable of identification of the same cyanobacteria found in the natural samples when the composition of the surrounding material is controlled, but the majority of natural samples provided results that were unable to provide information. Interference resulting from the composition of the Martian surface is an ongoing problem with regards to the use of Raman (Stevens, et al., 2018).

By comparison, no such obfuscation of data occurred via GC-MS and GC-FID but the data requires proper interpretation in order to extract the necessary information that can allow for accurate interpretation.

Material analysed by rovers and landers on Mars is likely to be of very low concentrations of organic material, if any is present at all. The natural sinters analysed are also low in total organic carbon and thus detection of organic molecules requires a larger sample size (>1.0g) than

investigations into other sample types such as lake cores (~0.01-0.3g) used as climate proxies (Denis, et al., 2012). In a Martian context this could require greatly increased sample sizes however spectroscopic instruments for extraterrestrial missions such as Curiosity (Mahaffy, et al., 2012) and the upcoming Europa Clipper (Brockwell, et al., 2016) are of a far greater sensitivity to account for this.

The natural samples analysed via MS also underwent a UV trial to determine how UV radiation affects the potential biosignatures contained within. The study 7.4.3 determined that there is a change in the total alkane mass resulting from organic material that can be explained via alterations to the chemistry of fatty acid compounds within the sample via photo-dissociation of the carboxyl group. Contamination could also account for the increase in organic content but if this were the case it would be expected to see similar increases in all samples as all samples underwent the same procedure for minimizing contamination.

The increases in alkane mass in the UV samples suggest that the degradation of compounds on Mars would have occurred before they would be able to be measured. If lab resources allowed for a further study into investigating the rate at which the natural samples would lose their biosignatures due to UV it would be expected that the increase in alkane weight due to the degradation of fatty acids was confined to the initial stages of degradation and that total alkane weight would reduce with increasing exposure time. As a result, detection of complex organic molecules at the Martian surface is unlikely to be sufficient as the sole source of data for positive confirmations of biosignatures.

The drill that will be equipped on EXOMARS and the Mars 2020 rovers could circumvent this limitation caused by the Martian environment. Deeper soils would provide a UV-safe environment in which organic compounds could resist the majority of the degradation

experienced at the surface and thus represent the best opportunity for the detection of organics. Degradation in deeper soils would be reduced rather than stalled however, and so over longer timescales the potential for detection is still substantially reduced, although the potential for detection is greater than at the surface layer.

10 Conclusions

10.1 Martian Analogues

The diurnal cycle of the soils in the Altiplano has demonstrated a pattern of heating and cooling that resembles similar cycles believed to occur on Mars. The most notable finding from this experiment is that there is a point at which the temperature profile of the subsurface reaches equilibrium. In the case of Sairecabur this equilibrium was fairly shallow at the time of year tested, and wetness sensor data showed that there are only minor fluctuations in water movement at these lower layers, although these measurements were taken in the form of permittivity readings and did not satisfy the sensor's 'wet' threshold. Nonetheless there are alterations to the overall permittivity of the soil even at deeper layers showing that even minor movements of water are sensitive enough to be detected. In a Martian context this aligns with data from the Phoenix lander which found water just beneath the subsurface at the landing site, and of satellite imagery of recurring slope lineae that leak brines onto the Martian surface for brief periods of time.

Longer term analysis of soils in the Altiplano would allow for the knowledge base of the site to be built up to understand how this cycle varies over the course of a year and several seasons. Matching experiments could also be done on sites that are artificially hidden from direct sunlight, to approximate the effects of long-term loss of surface heating that Mars is occasionally subject to due to dust storms. This work would also translate directly to a longer term monitoring station for Martian soils. Burying temperature and soil moisture probes would allow for similar monitoring of the Martian subsurface as has been performed here. The addition of radiation

detection instruments such as that equipped on the Mars Science Laboratory: Curiosity would allow for greater understanding and estimation of the degradation rates of possible biosignatures in the subsurface.

10.2 The preservation potential of silica sinters on Mars.

The precipitation of silica sinters in the presence of bacteria has been shown to encrust and fossilize bacteria in a manner that preserves the bacterium in its form *in situ*. Bacteria that have been silicified have remained viable, even when taken from silica sinters that are not actively being precipitated upon and thus do not have any traces of biofilm growth on their surface.

If viability has been lost the silica sinter can continue to provide two remaining sources of biomarkers. Visual analysis of silica sinters can confirm the presence of bacterial filaments if present, as well as other lifeforms if they appear such as diatoms. The encrustation process will preserve the form in which the silica precipitated although there is some evidence from El Tatio to support the idea that silica sinters will experience further precipitation in deeper layers of sinter after it was first precipitated. The opposite is also true however, with digitate sinters providing pockets of air where no sinter has been precipitated, as well as the very filament rich Brown samples from El Tatio which contained pockets where rich webs of silicified filaments were present across the pocket.

Sinters were also found to contain non-bacterial signatures as a result of plant-wax contamination, particularly noticeable in the samples obtained from New Zealand where

vegetation was much denser and more closely situated to vents than in Chile or Iceland. Whilst the aims of the study were primarily to determine the ability to identify bacterial biosignatures, the incorporation and preservation of fatty acids from plant waxes shows the potential of silica sinters as a biomarker preservation medium. In this instance the 'contamination' of the samples demonstrates their preservation potential. Similar things could be said for the Blue Lagoon sample that's GC-MS results are strongly suggestive of human contamination due to the site's use as a tourist attraction. However in the case of the Blue Lagoon the large volume of human traffic that visits the location means the sample is only demonstrating the ability of GC-MS to detect a wide-array of potential biosignatures, than the sinter's ability to preserve any specific signatures.

Preservation of organic material in the form of n-alkanes and fatty acids (and likely other unanalysed fractions such as GDGTs) shows that even though the sinter samples are comparatively light in total organic content compared to lake and terrestrial soil sediments there is still a signature that can be correlated to the presence of bacterial- or plant-based life.

Further analysis of similar such environments on Mars is dependent on confirming that silica rich environments, which do occur on Mars, are of a precipitated origin typically associated with alkaline waters rather than one of an environment leeched of other material that are typically of an acidic origin.

11 Bibliography

Adams, W. S. &. S. J. C. E., 1926. An attempt to detect Water-Vapor and Oxygen lines in the Spectrum of Mars with the Registering Microphotometer. The Astrophysical Journal, Volume 63, p. 133.

Allen, C. C., 1979. Volcano-ice interactions on Mars. Journal of Geophysical Research, 84(B14), pp. 8048-8059.

Allwood, A. C. et al., 2006. Stromatolite reef from the Early Archaean era of Australia. Nature, Volume 441, pp. 714-718.

Altheide, T., Chevrier, V., Nicholson, C. & Denson, J., 2009. Experimental investigation of the stability and evaporation of sulfate and chloride brines on Mars. Earth and Planetary Science Letters, 282(1), pp. 69-78.

Altwegg, K. et al., 2016. Prebiotic chemicals—amino acid and phosphorus—in the coma of comet 67P/Churyumov-Gerasimenko. Science Advances, 2(5).

Andhika, M., Castaneda, M. H. & Regenspurg, S., 2015. Characterization of silica Precipitation at Geothermal Conditions. Melbourne, Australia, Proceedings World Geothermal Congress.

Arenz, B. E. & Blanchette, R. A., 2011. Distribution and abundance of soil fungi in Antarctica at sites on the Peninsula, Ross Sea Region and McMurdo Dry Valleys. Soil Biology and Biochemistry, 43(2), pp. 308-315.

Australian Government, B. o. M., 2005. El Niño, La Niña and Australia's Climate, Commonwealth of Australia: Australian Government, Bureau of Meteorology.

Bada, J. L. et al., 2007. Urey: Mars Organic and Oxidant Detector. Space Science Reviews, Volume 135, pp. 269-279.

Bar-Nun, A. & Hartman, H., 1978. Synthesis of organic compounds from carbon monoxide and water by UV photolysis. Origins of Life, 9(2), pp. 93-101.

Baross, J. A. & Deming, J. W., 1983. Growth of 'black smoker' bacteria at temperatures of at least 250C. Letters to Nature, Volume 303, pp. 423-426.

Baross, J. A. & Deming, J. W., 1983. Reply from John A. Baross and Jody W. Deming. Letters to Nature, Volume 303, pp. 423-426.

Beatty, T. J. et al., 2005. An obligately photosynthetic bacterial anaerobe from a deep-sea hydrothermal vent. Proceedings of the National Academy of Sciences of the United States of America, 102(26), pp. 9306-9310.

Benning, L. G., Phoenix, V. R. & Mountain, B. W., 2005. Biosilicification: the role of cyanobacteria in silica sinter deposition. In: G. Gadd & K. Semple, eds. Micro-organisms and Earth Systems. Cambridge: Cambridge University Press, pp. 131-150.

Berelson, W. M. et al., 2011. Hot spring siliceous stromatolites from Yellowstone National Park: assessing growth rate and laminae formation. Geobiology, Volume 9, pp. 411-424.

Bibring, J.-P.et al., 2006. Global Mineralogical and Aqueous Mars History Derived from OMEGA/Mars Express Data. Science, 312(5772), pp. 400-404.

Bonner, W. A., 1991. The Origin and Amplification of Biomolecular Chirality. Origins of Life and Evolution of the Biosphere, Volume 21, pp. 59-111.

Boston, P. et al., 2001. Cave biosignature suites: microbes, minerals, and Mars. Astrobiology, 1(1), pp. 25-55.

Boyd, W. L. & Boyd, J. W., 1962. Soil Microorganisms of the McMurdo Sound Area, Antarctica. Applied and Environmental Microbiology, 11(2), pp. 116-121.
Boynton, W. V. et al., 2002. Distribution of Hydrogen in the Near Surface of Mars: Evidence for Subsurface Ice Deposits. Science, 297(5578), pp. 81-85.
Brain, D. A. & Jakowsky, B. M., 1998. Atmospheric loss since the onset of the Martian geologic record: Combined role of impact erosion and sputtering. Journal of Geophysical Research, 103(E10), pp. 22689-22694.
Briggs, R. et al., 1992. Comet Halley as an aggregate of interstellar dust and further evidence for the photochemical formation of organics in the interstellar medium. Origins of life and evolution of the biosphere, 22(5), pp. 287-307.
Brock, T. D., 1994. Life at High Temperatures. [Online]
Available at: https://bioinfo.bact.wisc.edu/themicrobialworld/LAHT/b1.html
[Accessed 21 05 2018].
Bryson, K. L., Chevrier, V., Sears, D. W. & Ulrich, R., 2008. Stability of ice on Mars and the water vapor diurnal cycle: Experimental study of the sublimation of ice through a fine-grained basaltic regolith. Icarus, Volume 196, pp. 446-458.
Bull, C., 1971. Snow Accumulation in Antarctica. In: L. O. Quam & H. D. Porter, eds. Research in the Antarctic: a symposium presented at the Dallas meeting of the American Association for the Advancement of Science, December, 1968. Advancement of Science. s.l.:American Association for the Advancement of Science, pp. 367-421.
Burikov, S. et al., 2010. Raman and IR Spectroscopy research on hydrogen bonding in water-ethanol systems. Molecular Physics, 108(18), pp. 2427-2436.
Burkins, M. B., Virginia, R. A. & Wall, D. A., 2001. Organic carbon cycling in Taylor Valley, Antarctica: quantifying soil reservoirs and soil respiration. Global Change Biology, 7(1), pp. 113-125.
Bush, R. T. & McInerney, F. A., 2013. Leaf wax n-alkane distributons in and across modern plants: Implications for paleoecology and chemotaxonomy. Geochimica et Cosmochimica Acta, Volume 117, pp. 161-179.
Cabrol, N. A. et al., 2014. Record solar UV irradiance in the tropical Andes. Frontiers in Environmental Science, Volume 2.
Cady, S. L. et al., 2003. Morphological Biosignatures and the Search for Life on Mars. Astrobiology, 3(2), pp. 351-368.
Cameron, R. E., King, J. & David, C. N., 1970. Microbiology, Ecology and Microclimatology of Soil Sites in Dry Valleys of Southern Victoria Land, Antarctica. In: M. W. Holdgate, ed. Antarctic Ecology Volume 2. London and New York: Academic Press, pp. 702-716.
Campbell Scientific, 2018. CR1000 Datalogger Operator's Manual. s.l.:Campbell Scientific.
Campbell, K. A. et al., 2015. Geyserite in hot-spring siliceous sinter: Window on Earth's hottest terrestrial (paleo)environment and its extreme life. Earth-Science Reviews, Volume 148, pp. 44-64.
Campbell, K. A., Rodgers, K. A., Brotheridge, J. M. A. & Browne, P. R. L., 2002. An unusual modern silica-carbonate sinter from Pavlova Spring, Ngatamariki, New Zealand. Sedimentology, Volume 49, pp. 835-854.
Campbell, W., 1894. Concerning an Atmosphere on Mars. Publications of the Astronomical Society of the Pacific, 6(38), pp. 273-283.
Capaccioni, F. et al., 2015. The organic-rich surface of comet 67P/Churyumov-Gerasimenko as seen by VIRTIS/Rosetta. Science, 347(6220).

Carrizo, D. et al., 2017. Biomarkers and taphonomic processes in fresh and fossil biosignatures from Hot Spring silica deposits in El Tatio Chile, as a Mars Analogue. Riga, European Planetary Science Congress 2017.
Carrizo, D. et al., 2018. Recent Biomarker Transition in a High Altitude Hydrothermal System (El Tatio, Chile). Houston, 49th Lunar and Planetary Science Conference.
Carr, M. H., 1986. Mars: A Water-Rich Planet. Icarus, Volume 68, pp. 187-216.
Carr, M. H., 1996. Water on early Mars. Ciba Foundation symposium 202, Volume 202, pp. 249-265.
Cary, C. S., McDonald, I. R., Barrett, J. E. & Cowan, D. A., 2010. On the rocks: the microbiology of Antarctic Dry Valley soils. Nature, Volume 8, pp. 129-138.
Cawley, K. M. et al., 2016. Characterization of dissolved organic material in the interstitial brine of Lake Vida, Antarctica. Geochimica et Cosmochimica Acta, Volume 183, pp. 63-78.
Chapman, M. G. & Tanaka, K. L., 2002. Related Magma-Ice Interactions: Possible Origins of Chasmata, Chaos, and Surface Materials in Xanther, Margaritifer, and Meridiani Terrae, Mars. Icarus, 155(2), pp. 324-339.
Chen, Y. et al., 2009. Life without light: microbial diversity and evidence of sulphur- and ammonium-based chemolithoautotrophy in Movile Cave. ISME Journal, 3(9), pp. 1093-1104.
Chicote, E. et al., 2005. Isolation and identification of bacteria from spent nuclear fuel pools. Journal of Industrial Microbiology and Biotechnology, Volume 32, pp. 155-162.
Chollet-Krugler, M., Nguyen, K.-H., Gouault, N. & Tomasi, S., 2013. UV-protectant metabolites from lichens and their symbiotic partners. The Royal Society of Chemistry :Natural Product Reports, Volume 30, pp. 1490-1508.
Clarke, J. D. A., 2006. Antiquity of aridity in the Chilean Atacama Desert. Geomorphology, Volume 73, pp. 101-114.
Clery, D., 2018. Lake spied deep below polar ice cap on Mars. Science, 361(6400), p. 320.
Cockell, C. S. et al., 2000. The Ultraviolet Environment of Mars: Biological Implications Past, Present, and Future. Icarus, Volume 146, pp. 343-359.
Cockell, C. S., McKay, C. P., Warren-Rhodes, K. & Horneck, G., 2008. Ultraviolet radiation-induced limitation to epilithic microbial growth in arid deserts - Dosimetric experiments in the hyperarid core of the Atacama Desert. Journal of Photochemistry and Photobiology B: Biology, 90(2), pp. 79-87.
Cody, A. D. & Lumb, J. T., 1992. Changes in Thermal Activity in the Rotorua Geothermal Field. Geothermics, 21(1), pp. 215-230.
Cody, C. G. et al., 2001. Geochemical roots of autotrophic carbon fixation: hydrothermal experiments in the system citric acid, H2O-(±FeS)−(±NiS). Geochimica et Cosmochimica Acta, 65(20), pp. 3557-3576.
Cody, G. D., 2004. Transition Metal Suldides and the Origins of Metabolism. Annual Review of Earth and Planetary, Volume 32, pp. 569-99.
Cordero, R. R. et al., 2016. The Solar Spectrum in the Atacama Desert. Nature Scientific Reports, Volume 6.
Cortecci, G. et al., 2005. New chemical and original isotopic data on waters from El Tatio geothermal field, northern Chile. Geochemical Journal, Volume 39, pp. 547-571.
Cronin, J. R. & Chang, S., 1993. Organic Matter in Meteorites: Molecular and Isotopic Analyses of the Murchison Meteorite. In: J. M. Greenberg, C. X. Mendoza-Gómez & V. Pirronello, eds. The Chemistry of Life's Origins. Tempe: NATO Science Committee, pp. 209-258.

Dana, G. L., Wharton Jr, R. A. & Dubayah, R. A., 1998. Solar Radiation in the McMurdo Dry Valleys, Antarctica. In: J. C. Priscu, ed. Ecosystem Dynamics in a Polar Desert: the McMurdo Dry Valleys, Antarctica. s.l.:American Geophysical Union, pp. 39-64.
Dartnell, L. R. et al., 2012. Destruction of Raman biosignatures by ionising radiation and the implications for life detection on Mars. Analytical and Bioanalytical Chemistry, 403(1), pp. 131-144.
de Silva, S. L. et al., 2002. The Altilano-Puna Plateau as an analog for Mars. San Francisco, American Geophysical Union, Fall Meeting.
de Silva, S. L. & Francis, P. W., 1991. Volcanoes of the Central Andes. viii ed. Berlin: Springer-Verlag.
del Prado, R. & Sancho, L. G., 2007. Dew as a key factor for the distribution pattern of the lichen species Teloschistes lacunosus in the Tabernas Desert (Spain). Flora - Morphology, Distribution, Functional Ecology of Plants, 202(5), pp. 417-428.
Dello Russo, N., Weaver Jr., H. A., Lisse, C. M. & Vervack Jr., R. J., 2006. Comet Chemistry: Obtaining Clues to the Formation and Evolution of the Solar System with High-Resolution Infrared Spectroscopy. John Hopkins APL Technical Digest, 27(2), pp. 121-132.
Dillion, M. O. & Rundel, P. W., 1990. The Botanical Response of the Atacama and Peruvian Desert Floras to the 1982-83 El Nino Event. In: P. W. Glynn, ed. Global Ecological Consequences of the 1982-83 El Nino-Southern Oscillation. s.l.:Elsevier, pp. 487-504.
Doran, P. T. et al., 2002. Valley floor climate observations from the McMurdo dry valleys, Antarctica, 1986-2000. Journal of Geophysical Research, Volume 107.
Ehlmann, B. L. et al., 2011. Subsurface water and clay mineral formation during the early history of Mars. Nature, Volume 479, pp. 53-60.
Ehresmann, B., Burmeister, S., Wimmer-Schweingruber, R. F. & Reitz, G., 2011. Influence of higher atmospheric pressure on the Martian radiation environment: Implications for possible habitability in the Noachian epoch. Journal of Geophysical Research: Space Physics, 116(A10).
Ellehoj, M. D. et al., 2010. Convective Vortices and dust devils at the Phoenix Mars mission landing site. Journal of Geophysical Research, 115(E4).
Ellis, J. W., 1969. Estimate of Sub-Surface Martian Temperatures. The Journal of The British Astronomical Association, 79(4), pp. 280-285.
Elsila, J. E., Glavin, D. P. & Dworkin, J. P., 2009. Cometary glycine detected in samples returned by Stardust. Meteorics & Planetary Science, 44(9), pp. 1323-1330.
Engel, M. H. & Macko, S. A., 1997. Isotopic evidence for extraterrestrial non-racemic amino acids in the Murchison meteorite. Letters to Nature, Volume 389, pp. 265-268.
Fein, J. B., Scott, S. & Rivera, N., 2002. The effect of Fe on Si adsorption by Bacillus subtilis cell walls: insights into non-metabolic bacterial precipitation of silicate minerals. Chemical Geology, Volume 182, pp. 265-273.
Feldman, W. C. et al., 2004. Global distribution of near-surface hydrogen on Mars. Journal of Geophysical Research, Volume 109.
Fernández-Remolar, D. et al., 2004. The Tinto River, an extreme acidic environment under control of iron, as an analog of the Terra Meridiani hematite site of Mars. Planetary and Space Science, Volume 52, pp. 239-248.
Fernandez-Turiel, J. L. et al., 2005. The hot spring and geyser sinters of El Tatio, Northern Chile. Sedimentary Geology, 180(3-4), pp. 125-147.

Fischer, E., Martínez, G. M. & Rennó, N. O., 2016. Formation and Persistence of Brine on Mars: Experimental Simulations throughout the Diurnal Cycle at the Phoenix Landing Site. Astrobiology, 16(12), pp. 937-948.
Fischer, H. et al., 1999. Ice Core Records of Atmospheric CO2 Around the Last Three Glacial Terminations. Science, 283(5408), pp. 1712-1714.
Fjeldbo, G., Fjeldbo, W. C. & Eshleman, V. R., 1966. Models for the atmosphere of Mars based on the Mariner 4 occulation experiment. Journal of Geophysical research, 71(9), pp. 2307-2316.
Flint, E. A. & Stout, J. D., 1960. Microbiology of Some Soils from Antarctica. Nature, Volume 188, pp. 767-768.
Forte, E., Fratte, M. D., Azzaro, M. & Guglielmin, M., 2016. Pressurized brines in continental Antarctica as a possible analogue of Mars. Nature, Volume 6.
Fortin, D. & Beveridge, T. J., 1997. Role of the bacterium Thiobacillus in the formation of silicates in acidic mine tailings. Chemical Geology, Volume 141, pp. 235-250.
Fortin, D. & Beveridge, T. J., 1997. Role of the bacterium Thiobacillus in the formation of silicates in acidic mine tailings. Chemical Geology, Volume 141, pp. 235-250.
Fountain, A. G. et al., 1999. Physical Controls on the Taylor Valley Ecosystem, Antarctica. American Institute of Biological Sciences, 49(12), pp. 961-971.
Fournier, R. O., 1985. The Behaviour of Silica in Hydrothermal Solutions. In: B. R. Berger, ed. Geology and Geochemistry of Epithermal Systems: Society of Economic Geologists. s.l.:Society of Economic Geology, pp. 45-61.
Fournier, R. O. & Rowe, J. J., 1977. The solubility of amorphous silica in water at high temperatures and high pressures. American Mineralogist, Volume 62, pp. 1052-1056.
Fray, N. et al., 2016. High-molecular-weight organic matter in the particles of comet 67P/Churyumov-Gerasimenko. Nature Letters, Volume 10.
Freckman, D. W. & Virginia, R. A., 1998. Soil Biodiversity and Community Structure in the McMurdo Dry Valleys, Antarctica. In: J. C. Priscu, ed. Ecosystem Dynamics in a Polar Desert: the McMurdo Dry Valleys, Antarctica. s.l.:American Geophysical Union, pp. 323-335.
Freytet, P. & Verrecchia, E. P., 1999. Calcitic radial palisadic fabric in freshwater stromatolites: diagenetic and recrystallized feature or physiochemical sinter crust?. Sedimentary Geology, Volume 126, pp. 97-102.
Friedmann, E. I., Kappen, L., Meyer, M. A. & Nienow, J. A., 1993. Long-Term Productivity in the Cryptoendolithic Microbial Community of the Ross Desert, Antarctica. Microbial Ecology, 25(1), pp. 51-69.
Frydenvang, J. et al., 2017. Diagenetic silica enrichment and late-stage groundwater activity in Gale crater, Mars. Geophysical Research Letters, Volume 44, p. 9.
Gaiero, D. M. et al., 2013. Ground/satellite observations and atmospheric modeling of dust storms originating in the high Puna-Altiplano deserts (South America): Implications for the interpretation of paleo-climatic archives. Journal of Geophysical Research: Atmospheres, 118(9), pp. 3817-3831.
Garreaud, R., Vuille, M. & Clement, A. C., 2003. The climate of the Altiplano: observed current conditions and mechansims of past changes. Palaeogeography, Palaeoclimatology, Palaeoecology, 194(1-3), pp. 5-22.
German, C. R. et al., 1990. Hydrothermal scavenging of rare-earth elements in the ocean. Letters to Nature, Volume 345, pp. 516-518.

Gibson, E. K., Wentworth, S. J. & McKay, D. S., 1983. Chemical Weathering and Diagenesis of a Cold Deseert Soil From Wright Valley, Antarctica: An Analog of Martian Weathering Processes. Journal of Geophysical Research, Volume 88, pp. A912-A928.
Goldspiel, J. M. & Squyres, S. W., 2010. Groundwater discharge and gully formation on martian slopes. Icarus, Volume 211, pp. 238-258.
Golubic, S., 1976. Chapter 4.1 Organisms that Build Stromatolites. In: P. J. Ashworth, J. L. Best & D. R. Parsons, eds. Developments in Sedimentology. s.l.:Elsevier, pp. 113-126.
Golubic, S. & Campbell, S. E., 1979. Analogous microbial forms in recent aubaerial habitats and in precambrian Cherts: Gloethece coerulea Geitler and Eosynechococcus moorei Hofmann. Precambrian Research, Volume 8, pp. 201-217.
Goordial, J. et al., 2016. Nearing the cold-arid limits of microbial life in permafrost of an upper dry vallley, Antarctica. Nature, Volume 10, pp. 1613-1624.
Guidry, S. A. & Chafetz, H. S., 2002. Factors governing subaqueous siliceous sinter precipitation in hot springs: examples from Yellowstone National Park, USA. Sedimentology, Volume 49, pp. 1253-1267.
Harri, A. M. et al., 2014. Mars Science Laboratory relative humidity observations: Initial results. Journal of Geophysical Research: Planets, 119(9), pp. 2132-2147.
Harri, A. -M. et al., 2014. Pressure Observations by the Curiosity rover: Initial results. Journal of Geophysical Research, 119(1), pp. 82-92.
Hassler, D. M. et al., 2014. Mars' Surface Radiation Environment Measured with the Mars Science Laboratory's Curiosity Rover. Science, Volume 343.
Hazen, R. M. & Sverjensky, D. A., 2010. Mineral Surfaces, Geochemical Complexities and the Origins of Life. Cold Spring Harbor Perspectives in Biology, 2(5).
Head III, J. W. & Wilson, L., 2007. Heat transfer in volcano-ice interactions on Mars: synthesis of environments and implications for processes and landforms. Annals of Glaciology, Volume 45.
Head, J. W. et al., 2003. Recent ice ages on Mars. Nature, Volume 426, pp. 797-802.
Hecht, M. H. et al., 2009. Chemistry of Martian Soil at the Phoenix Lander Site. Science, 325(5936), pp. 64-67.
Hendra, P. J. & Stratton, P. M., 1969. Laser-Raman Spectroscopy. Chemical Reviews, 69(3), pp. 325-344.
Herdianita, N. R., Rodgers, K. A. & Brown, P. R. L., 2000. Routine instrumental procedures to characterise the mineralogy of modern and ancient silica sinters. Geothermics, Volume 29, pp. 65-81.
Hinman, N. W. & Lindstrom, R. F., 1996. Seasonal changes in silica deposition in hot spring systems. Chemical Geology, Volume 132, pp. 237-246.
Hock, A. N., 2008. Licancabur Volcano, bolivia and liufe in the Atacama: Environmental physics and analogies to Mars, Los Angeles: Proquest Dissertations And Theses; University of California.
Hock, A. N. et al., 2005. Mars-Relevant Environmental Conditions at the Lakes of Licancabur Volcano, Bolivia, San Francisco: American Geophysical Union, Fall Meeting Abstracts, 2005.
Horowitz, N. H., Cameron, R. E. & Hubbard, J. S., 1972. Microbiology of the Dry Valleys of Antarctica. Science, 176(4032), pp. 242-245.
Houston, J. & Hartley, A. J., 2003. The Central Andean west-slope rainshadow and its potential contribution to the origin of hyper-aridity in the Atacama Desert. International Journal of Climatology, Volume 23, pp. 1453-1464.

Houston, J. & Hartley, A. J., 2003. The Central Andean West-Slope Rainshadow and its Potential Contribution to the Origin of Hyper-Aridity in the Atacama Desert. International Journal of Climatology, Volume 23, pp. 1453-1464.
Huber, C. & Wachtershauser, G., 1997. Activated Acetic Acid by Carbon Fixation on (Fe,Ni)S Under Primordial Conditions. Science, Volume 276, pp. 245-247.
Hutchens, E. et al., 2004. Analysis of methanotrophic bacteria in Movile Cave by stable isotope probing. Environmental Microbiology, 6(2), pp. 111-120.
Hynek, B. M., Beach, M. & Hoke, M. R. T., 2010. Updated global map of Martian valley networks and implications for climate and hydrological processes. Journal of Geophysical Research, Volume 115.
Ichikuni, M., 1970. Incorporation of aluminum and iron into siliceous sinters. Chemical Geology, Volume 6, pp. 273-279.
Iler, R. K., 1979. The Chemistry of Silica: Solubility, Polymerization, Colloid and Surface Properties and Biochemistry of Silica. s.l.:Wiley.
Jacobs, A. F. G., Heusinkveld, B. G. & Berkowicz, S. M., 1999. Dew deposition and drying in a desert system: a simple simulation model. Journal of Arid Environments, Volume 42, pp. 211-222.
Jaggar, T. A., 1898. Some conditions affecting geyser eruption. American Journal of Science, 5(4), pp. 323-333.
Jakosky, B. M. & Farmer, C. B., 1982. The seasonal and global behavior of water vapor in the Mars atmosphere: Complete global results of the Viking Atmospheric Water Detector Experiment. Journal of Geophysical Research: Solid Earth, 87(B4).
Jakosky, B. M. et al., 2003. Subfreezing Activity of Microorganisms and the Potential Habitability of Mars' Polar Regions. Astrobiology, 3(2), pp. 343-350.
Jawhari, T., Hendra, P. J., Willis, H. A. & Judkins, M., 1990. Quantitative analysis using Raman methods. Spectrochimica Acta Part A: Molecular Spectroscopy, 46(2), pp. 161-170.
Jones, B. & Renaut, R. W., 1997. Formation of silica oncoids around geysers and hot springs at El Tatio, northern Chile. Sedimentology, Volume 44, pp. 287-304.
Jones, B. & Renaut, R. W., 1997. Formation of silica oncoids around geysers and hot springs at El Tatio, northern Chile. Sedimentology, Volume 44, pp. 287-304.
Jones, B., Renaut, R. W. & Owen, R. B., 2011. Life cycle of a geyser discharge apron: Evidence from Waikite Geyser, Whakarewarewa geothermal area, North Island, New Zealand. Sedimentary Geology, Volume 236, pp. 77-94.
Jones, B., Renaut, R. W. & Rosen, M. R., 1997. Biogenicity of Silica Precipitation Around Geysers and Hot-Spring Vents, North Island, New Zealand. Journal of Sedimentary Research, 67(1), pp. 88-104.
Jones, B., Renaut, R. W. & Rosen, M. R., 1997. Vertical Zonation of Biota in Microstromatolites Associated with Hot Springs, North Island, New Zealand. PALAIOS, 12(3), pp. 220-236.
Kahn, R., 1985. The evolution of CO2 on Mars. Icarus, 62(2).
Kenig, F. et al., 2016. Perchlorate and volatiles of the brine of Lake Vida (Antarctica): Implication for the in situ analysis of Mars sediments. Journal of Geophysical Research: Planets, 121(7), pp. 1190-1203.
Keys, H. J. R., 1980. Air Tmperature, Wind, Precipitation and Atmospheric Humidity in the McMurdo Region, Antarctica, Wellington: Victoria University of Wellington: Department of Geology.
Kidron, G. J., Herrnstadt, I. & Barzilay, E., 2002. The role of dew as a moisture source for sand microbiotic crusts in the Negev Desert, Israel. Journal of Arid Environments, 52(4), pp. 517-533.
Kieffer, H. H. et al., 1977. Thermal and albedo mapping of Mars during the Viking Primary Mission. Journal of Geophysical Research, Volume 82, pp. 4249-4291.

Kissel, J. & Krueger, F. R., 1987. The organic component in dust from comet Halley as measured by the PUMA mass spectrometer on board Vega 1. Nature, Volume 326, pp. 755-760.
Knoll, A. H., 1985. Exceptional preservation of photosynthetic organisms in silicified carbonates and silicified peats. Philosophical Transactions of the Royal Society of London B: Biological Sciences, Volume 311, pp. 111-122.
Kodama, Y. & Watanabe, K., 2004. Sulfuricurvum kujiense gen. nov., sp. nov., a facultatively anaerobic, chemolithoautotrophic, sulfur-oxidizing bacterium isolated from an underground crude-oil storage cavity. International Journal of Systematic and Evolutionary Microbiology, 54(6), pp. 2297-2300.
Komar, P. D., 1983. Shapes of streamlined islands on Earth and Mars: Experiments and analyses of the minimum-drag form. Geology, Volume 11, pp. 651-654.
Konhauser, K. O., Jones, B., Reysenbach, A.-L. & Renaut, R. W., 2003. Hot spring sinters: keys to understanding Earth's earliest life forms. Canadian Journal of Earth Sciences, Volume 40, pp. 1713-1724.
Konig, B., 2017. Photocatalysis in Organic Synthesis - Past, Present, and Future. European Journal of Organic Chemistry, 2017(15).
Kottek, M. et al., 2006. World Map of the Koppen-Geiger climate classification updated. Meteorologische Zeitschrift, 15(3), pp. 259-263.
Kounaves, S. P. et al., 2010. Discovery of Natural Perchlorate in the Antarctic Dry Valleys and Its Global Implications. Environmental Science & Technology, Volume 44, pp. 2360-2364.
Krasnopolsky, V. A., 2006. Some problems related to the origin of methane on Mars. Icarus, 180(2), pp. 359-367.
Kumaresan, D. et al., 2014. Microbiology of Movile Cave - A chemolithoautotrophic ecosystem. Geomicrobiology Journal, 31(3), pp. 186-193.
Kvenolden, K. A., Lawless, J. G. & Ponnamperuma, C., 1971. Nonprotein Amino Acids in the Murchison Meteorite. Proceedings of the National Academy of Sciences of the United States of America, 68(2), pp. 486-490.
Kvenvolden, K. et al., 1970. Evidence for Extraterrestrial Amino-acids and Hydrocarbons in the Murchison Meteorite. Nature, Volume 228, pp. 923-926.
Labza, N. L. et al., 2010. Evidence for debris flow gully formation initiated by shallow subsurface water on Mars. Icarus, 205(1), pp. 103-112.
Lahav, N., White, D. & Chang, S., 1978. Peptide Formation in the Prebiotic Era: Thermal condensation of Glycine in Fluctuating Clay Environments. Science, 201(4350), pp. 67-69.
Lambert, J.-F., 2008. Adsorption and Polymerization of Amino Acids on Mineral Surfaces: A Review. Origins of Life and Evolution of Biospheres, Volume 38, pp. 211-242.
Le Deit, L. et al., 2012. Extensive surface pedogenic alteration of the Martian Noachian crust suggested by plateau phyllosilicates around Valles Marineris. Journal of Geophysical Research, Volume 117.
Léveillé, R. J. & Datta, S., 2010. Lava tubes and basaltic caves as astrobiological targets on Earth and Mars: A review. Planetary and Space Science, Volume 58, pp. 592-598.
Lincoln, T. A. & Joyce, G. F., 2009. Self-sustained Replication of an RNA Enzyme. Science, 27(323), pp. 1229-1232.
Lipson, D. A. & Schmidt, S. K., 2004. Seasonal Changes in an Alpine Soil Bacterial Community in the Colorado Rocky Mountains. Applied and Environmental Microbiology, 70(5), pp. 2867-2879.
Lloyd, E. F., 1975. Geology of Whakarewarewa hot springs. Wellington: Department of Scientific and Industrial Research (New Zealand).

Mangold, N. et al., 2004. Evidence for Precipitation on Mars from Dendritic Valleys in the Valles Marineris Area. Science, 305(5680), pp. 78-81.
Martins, Z. et al., 2008. Extraterrestrial nucleobases in the Murchison meteorite. Earth and Planetary Science Letters, Volume 270, pp. 130-136.
Martin-Torres, F. J. et al., 2015. Transient liquid water and water activity at Gale crater on Mars. Nature Geoscience, Volume 8, pp. 357-361.
Martone, P. T. et al., 2009. Discovery of Lignin in Seaweed Reveals Convergent Evolution of Cell-Wall Architecture. Current Biology, Volume 19, pp. 169-175.
Matousek, P. et al., 2005. Subsurface Probing in Diffusely Scattering Media Using Spatially Offset Raman Spectroscopy. Applied Spectroscopy, 59(4), pp. 393-400.
Matsumoto, G. I., Hirai, A., Hirota, K. & Watanuki, K., 1990. Organic geocemistry of the McMurdo Dry Valleys soil, Antarctica. Organic Geochemistry, 16(4-6), pp. 781-791.
Matthewman, R. et al., 2016. Organic Matter Responses to Radiation under Lunar Conditions. Astrobiology, 16(11), pp. 900-912.
McEwen, A. S. et al., 2011. Seasonal flows on warm Martian Slopes. Science, 333(6043), pp. 740-743.
McLoughlin, N., Wilson, L. A. & Brasier, M. D., 2008. Growth of synthetic stromatolites and wrinkle sturcures in the absence of microbes - implications for the early fossil record. Geobiology, Volume 6, pp. 95-105.
Meierhenrich, U., 2008. Chirality and Mission ExoMars. In: Amino Acids and the Asymmetry of Life: Caught in the Act of Formation. s.l.:Springer-Verlag Berlin Heidelberg, pp. 180-183.
Mellon, M. T. et al., 2009. Ground ice at the Phoenix Landing Site: Stability state and origin. Journal of Geophysical Research, Volume 114.
Mellon, M. T., Jakosky, B. M. & Kieffer, H. H., 2000. High-resolution thermal inertia mapping from the Mars global surveyor thermal emission spectrometer. Icarus, Volume 148, pp. 437-455.
Mellon, M. T. & Philips, R. J., 2001. Recent Gullies on Mars and the source of liquid water. Journal of Geophysical Research: Planets, 106(E10), pp. 23165-23179.
Millan, M. et al., 2016. Effect on the Presence of Chlorates and Perchlorates on the Pyrolysis of Organic Compounds: Implicatons for Measurements done with the SAM Experiment on bouard the Curiosity Rover. Houston, Universities Space Research Association.
Miller, S. L. & Bada, J. L., 1988. Submarine hot springs and the origin of life. Letters to Nature, Volume 334, pp. 609-611.
Miller, S. L. & Urey, H. C., 1959. Organic Compound Synthesis on the Primitive Earth. Science, Volume 130, pp. 245-251.
Minvielle, M. & Garreaud, R. D., 2011. Projecting Rainfall Changes over the South American Altiplano. American Meteorological Society: Journal of Climate, pp. 4577-4583.
Mischna, M. A. et al., 2011. Atmospheric modeling of Mars methane surface releases. Planetary and Space Science, 59(2-3), pp. 227-237.
Mitrofanov, I. G. et al., 2003. CO2 Snow Depth and Subsuface Water-Ice Abundance in the Northern Hemisphere of Mars. Science, 300(5628), pp. 2081-2084.
Morris, R. V. et al., 2016. Silicic volcanism on Mars evidenced by tridymite in high-SiO2 sedimentary rock at Gale crater. PNAS, 113(26), pp. 7071-7076.
Mountain, B. W., Benning, L. G. & Boerema, J. A., 2003. Experimental studies on New Sealand hot spring sinters: rates of growth and textural development. Canadian Journal of Earth Sciences, Volume 40, pp. 1643-1667.

Mumma, M. J. & Charnley, S. B., 2011. The Chemical Composition of Comets - Emerging Taxonomies and Natal Heritage. Search Annual Review of Astronomy and Astrophysics, Volume 49, pp. 471-524.
Mumma, M. J. & Charnley, S. B., 2011. The Chemical Composition of Comets - Emerging Taxonomies and Natal Heritage. Annual Review of Astronomy and Astrophysics, Volume 49, pp. 471-524.
Mumma, M. J. et al., 2001. A Survey of Organic Volatile Species in Comet C/1999 H1 (Lee) Using NIRSPEC at the Keck Observatory. The Astophysical Journal, 546(2), pp. 1183-1193.
Murray, A. E. et al., 2012. Microbial life at -13C in the brine of an ice-sealed Antarctic lake. Proceedings of the National Academy of Sciences of the United States of America, 109(50), pp. 20626-20631.
Musselwhite, D. S., Swindle, T. D. & Lunine, J. I., 2001. Liquid CO2 breakout and the formation of recent small gullies on Mars. Geophysical Research Letters, 28(7).
Mustard, J. F. et al., 2013. Report of the Mars 2020 Science Definition Team, s.l.: Mars Exploration Program Analysis Group.
Nakajima, T., Yabushita, Y. & Tabushi, I., 1975. Amino acid synthesis through biogenetic-type CO2 fixation. Letters to Nature, Volume 256, pp. 60-61.
Navarro-Gonzalez, R. et al., 2003. Mars-Like Soils in the Atacama Desertm Chile, and the Dry Limit of Microbial Life. Science, 302(5647), pp. 1018-1021.
Navarro-González, R. et al., 2010. Reanalysis of the Viking results suggests perchlorate and organics at midlatitudes on Mars. Journal of Geophyscial Research, Volume 115.
Newsom, H. E., 1980. Hydrothermal Alteration of Impact Melt Sheets with Implications for Mars. Icarus, Volume 40, pp. 207-216.
Nkem, J. N. et al., 2006. Wind disperal of soil invertebrates in the McMurdo Dry Valleys, Antarctica. Polar Biology, Volume 29, pp. 346-352.
Nutman, A. P. et al., 2016. Rapid emergence of life shown by discovery of 3,700-million-year-old microbial structures. Nature, Volume 537, pp. 535-538.
Nylen, T. H. & Fountain, A. G., 2004. Climatology of katabatic winds in the McMurdo dry valleys, southern Victoria Land, Antarctica. Journal of Geophysical Research, Volume 109.
Ojha, L. et al., 2015. Spectral evidence for hydrated salts in recurring slope lineae on Mars. Nature Geoscience, 8(11), pp. 829-832.
Orange, F., Lalonde, S. V. & Konhauser, K. O., 2013. Experimental Simulation of Evaporation-Driven Silica Sinter Formation and Microbial Silicification in Hot Spring Systems. Astrobiology, 13(2), pp. 163-176.
Ordonez, O. F. et al., 2009. Extremophile Culture Collection from Andean Lakes: Extreme Pristine Environments that Host a Wide Diversity of Microorganisms with Tolerance to UV Radiation. Microbial Ecology, Volume 58, pp. 467-473.
Orlando, J. et al., 2010. Bacterial diversity and occurrence of ammonia-oxidizing bacteria in the Atacama Desert soil during a "desrt bloom" event. Soil Biology & Biochemistry, Volume 42, pp. 1183-1188.
Oze, C. & Sharma, M., 2005. Have olivine, will gas: Serpentinization and the abiogenic production of methane on Mars. Geophysical Research Letters, 32(10).
Pacheco, D. J., 2012. Perchlorates on Mars: Implications for the Detection of Organics on Mars. Ogden, Weber State University.
Pancost, R. D. et al., 2005. Lipid biomolecules in silica sinters: indicators of microbial biodiversity. Environmental Microbiology, 7(1), pp. 66-77.
Patel, M. R., Zarnecki, J. C. & Catling, D. C., 2002. Ultraviolet radiation on the surface of Mars and the Beagle 2 UV sensor. Planetary and Space Science, 50(9), pp. 915-927.

Paulino-Lima, I. G. et al., 2013. Isolation of UVC-Tolerant Bacteria from the Hyperarid Atacama Desert, Chile. Microbial Ecology, 65(2), pp. 325-335.
Pavlov, A. et al., 2012. Degradation of the organic molexules in the shallw subsurface of Mars due to irradiation by cosmic rays. Geophysical Research Letters, 39(13).
Pepe-Ranney, C. et al., 2012. Cyanobacterial construction of hot spring siliceous stromatolites in Yellowstone National Park. Environmental Microbiology, 14(5), pp. 1182-1197.
Petterson, I. E. I. et al., 2010. Time-resolved spatially offset Raman spectroscopy for depth analysis of diffusely scattering layers. Analyst, Volume 135, pp. 3255-3259.
Pettit, E. &. S. B. N., 1924. Radiation Measures on the planet Mars. Publications of the Astronomical Society of the Pacific, 36(213), pp. 269-272.
Phoenix , V. R., Konhauser, K. O. & Ferris, G. F., 2003. Experimental study of iron and silica immobilization by bacteria in mixed Fe-Si systems: implications for microbial silicification in hot springs. Canadian Journal of Earth Sciences, Volume 40, pp. 1669-1678.
Phoenix, V. R., Adams, D. G. & Konhauser, K. O., 2000. Cyanobacterial viability during hydrothermal biomineralization. Chemical Geology, Volume 169, pp. 329-338.
Phoenix, V. R. et al., 2006. Chilean high-altitude hot-spring sinters: a model system for UV screening mechanisms by early Precambrian cyanobacteria. Geobiology, Volume 4, pp. 15-28.
Phoenix, V. R. et al., 2006. Chilean high-atitude hot-spring sinters: a model system for UV screening mechanisms by early Precambrian cyanobacteria. Geobiology, Volume 4, pp. 15-28.
Phoenix, V. R., Konhauser, K. O., Adams, D. G. & Bottrell, S. H., 2001. Role of biomineralization as an ultraviolet shield: Implications for Archean life. Geology, 29(9), pp. 823-826.
Piacentini, R. D., Cede, A. & Bárcena, H., 2003. Extreme solar total and UV irradiances due to cloud effect measured near the summer solstice at the high-altitude desertic plateau Puna of Atacama (Argentina). Journal of Atmospheric and Solar-Terrestrial Physics, 65(6), pp. 727-731.
Pizzarello, S. et al., 2001. The Organic Content of the Tagish Lake Meteorite. Science, 293(5538), pp. 2236-2239.
Pollack, J. B. et al., 1979. Properties and Effects of Dust Particles Suspended in the MArtian Atmosphere. Journal of Geophysical Research, 84(B6), pp. 2929-2945.
Pollack, J. B., Ockert-Bell, M. E. & Shepard, M. K., 1995. Viking Lander image analysis of Martian atmospheric dust. Journal of Geophysical Research, Volume 100, pp. 5235-5250.
Portugal, W. et al., 2014. Radiolysis of Amino Acids by Heavy and Energetic Cosmic Ray Analogs in Sumulated Space Environments: □-Glycine Zwitterion Form. Monthly Notices of the Royal Astronomical Society, 441(4), pp. 3209-3225.
Preston, L. J., Benedix, G. K., Genge, M. J. & Sephton, M. A., 2008. A multidisciplinary study of silica sinter deposits with applications to silica identification and detection of fossil life on Mars. Icarus, 198(2), pp. 331-350.
Pulschen, A. A. et al., 2015. UV-resistant yeasts isolated from a high-altitude volcanic area on the Atacama Desert as eukaryotic models for astrobiology. MicrobiologyOpen, 4(4).
Putzig, N. E. & Mellon, M. T., 2007. Apparent thermal inertia and the surface heterogeneity of Mars. Icarus, Volume 191, pp. 68-94.
Raman, C. V., 1928. A new radiation. Bangalore, Indian Journal of Physics.
Raman, C. V. & Krishnan, K. S., 1928. A New Type of Secondary Radiation. Nature, Volume 121, pp. 501-502.

Reid, R. P. et al., 2000. The role of microbes in accretion, lamination and early lithification of modern marine stromatolites. Nature, Volume 406, pp. 989-992.
Rencoret, J., Gutiérrez, A. & del Rio, J. C., 2007. Lipid and lignin composition of woods from different eucalypt species. Holzforschung, Volume 61, pp. 165-174.
Renishaw, 2014. Raman bands explained. [Online]
Available at: http://www.renishaw.com/en/Raman-bands-explained--25808
[Accessed 19 06 2018].
Rodgers, K., Browne, P. & Campbell, K. A., 2011. Silica from Steam Condensate Alteration at Tikitere, New Zealand, Stanford: University of Stanford.
Rohwerder, T., Sand, W. & Lascu, C., 2003. Preliminary Evidence for a Sulphur Cycle in Movile Cave,, Romania. Acta Biotechnologica, 23(1), pp. 101-107.
Rondanelli, R., Molina, A. & Falvey, M., 2015. The Atacama Surface Solar Maximum. Bulletin of the American Meteorological Society, 93(3), pp. 405-418.
Rosenfield, D., Rudich, Y. & Lahav, R., 2001. Desert Dust suppressing precipitation: A possible desertification feedback loop. Proceedings of the National Academy of Sciences, 98(11), pp. 5975-5980.
Ruff, S. W. & Farmer, J. D., 2016. Silica deposits on Mars with features resembling hot spring biosignatures at El Tatio in Chile. Nature Communications.
Rutllant, J. & Ulriksen, P., 1979. Boundary-layer dynamics of the extremely arid northern part of Chile: The Antofagasta Field Experiment. Boundary-Layer Meteorology, 17(1), pp. 41-55.
Sandford, S. A. et al., 2006. Organics Captured from Comet 81P/Wild 2 by the Stardust Spacecraft. Science, 314(5806), pp. 1720-1724.
Sarbu, S., Kane, T., BK & Kinkle, 1996. A Chemoautotrophically Based Cave Ecosystem. Science, 272(5270), pp. 1953-1955.
Schrott, L., 1991. Global Solar Radiation, Soil Temperature and Permafrost in the Central Andes, Argentina: a Progress Report. Permafrost and Periuglacial Processes, Volume 2, pp. 59-66.
Scott, B. J. et al., 2016. The Rotorua Geothermal Field: An experiment in environmental management. Geothermics, Volume 59, pp. 294-310.
Seiff, A. & Kirk, D., 1977. Structure of the Atmosphere of Mars in Summer at Mid-Latitudes. Journal of Geophysical research, 82(28), pp. 4364-4378.
Sellers, W. D., 1965. Heat Transfer in Soil. In: Physical Climatology. s.l.:The University of Chicago Press, Chicago & London; The University of Toronto Press, Toronto 5, Canada, p. 272.
Sephton, M. A. et al., 2014. Perchlorate-induced combustion of organic matter with variable molecular weights: Implications for Mars missions. Geophysical Research Letters, 41(21), pp. 7453-7460.
Serban, M. & Popa, R., 1992. A Unique Chemoautotrophically Based Cave Ecosystem. In: A. I. Camacho, ed. The Natural History of Biospeleology. Madrid: Museo nacional de Ciencias naturales, pp. 637-666.
Shakeel, T., Fatma, Z., Fatma, T. & Yazdani, S. S., 2015. Heterogeneity of alkane chain length in freshwater and marine cyanobacteria. Frontiers in Bioengineering and Biotechnology, Volume 3.
Shaw, N., 1974. Lipid Composition as a Guide to the Classification of Bacteria. Advances in Applied Microbiology, Volume 17, pp. 63-108.
Shock, E. L. & Schulte, M. D., 1990. Amino-acid synthesis in carbonaceous meteorites by aqueous alteration of polycyclic aromatic hydrocarbons. Nature, Volume 343, pp. 728-731.

Siebert, J. & Hirsch, P., 1988. Characterization of 15 Selected Coccal Bacteria Isolated from Antarctic Rock and Soil Samples from the McMurdo-Dry Valleys (South-Victoria Land). Polar Biology, Volume 9, pp. 37-44.
Skok, J. R. et al., 2010. Silica deposits in the Nili Patera caldera on the Syrtis Major volcanic complex on Mars. Nature Geoscience, Volume 3, pp. 838-841.
Smith, J. J. et al., 2006. Bacterial Diversity in Three Different Antarctic Cold Desert Mineral Soils. Microbial Ecology, Volume 5, pp. 413-421.
Sowerby, S. J., Edelwirth, M. & Heckl, W. M., 1998. Self-Assembly at the Prebiotic Solid-Liquid Interface: Structures of Self-Assembled Monolayers of Adenine and Guanine Bases Formed on Inorganic Surfaces. The Journal of Physical Chemistry B, Volume 102, pp. 5914-5922.
Squyres, S. et al., 2008. Detection of Silica-Rich Deposits on Mars. Science, 320(5879), pp. 1063-1067.
Squyres, S. W., Wilhelms, D. E. & Moosman, A. C., 1987. Large-scale volcano-ground ice interactions on Mars. Icarus, 70(3), pp. 385-408.
Stern, C. R., 2004. Active Andean volcanism: its geologic and tectonic setting. Revista Geológica de Chile, 31(2), pp. 161-206.
Sugden, D. E. et al., 1995. Preservation of Miocene glacier ice in East Antarctica. Nature, Volume 376, pp. 412-414.
Tamppari, L. K. et al., 2012. Effects of extreme cold and aridity on soils and habitability: McMurdo Dry Valleys as an analogue for the Mars Phoenix landing site. Antarctic Science, 24(3), pp. 211-228.
Tanaka, K. L. & Chapman, M. G., 1992. Kasei Valles, Mars: Interpretation of Canyon Materials and Flood Sources. Proceedings of Lunar and Planetary Science, Volume 22, pp. 73-83.
Throop, H. & Bally, J., 2009. UV Photolysis and Creatioin of Complex Organic Molexules in the Solar Nebula. Woodlands, Texas, 40th Lunar and Planetary Science Conference.
Tilden, J. E., 1897. On Some Algal Stalactites of the Yellowstone National Park. Botanical Gazette , 24(3), pp. 194-199.
Tobler, D. J., Stefánsson, A. & Benning, L. G., 2008. In-situ grown silica sinters in Icelandic geothermal areas. Geobilogy, Volume 6, pp. 481-502.
Tolles, W. M., Nibler, J. W., McDonald, J. R. & Harvey, A. B., 1977. A Review of the Theory and Application of Coherent Anti-Stokes Raman Spectroscopy (CARS). Applied Spectroscopy, 31(4), pp. 253-271.
Toner, J. D. & Catling, D. C., 2016. The Formation of Liquid Water on Present-Day Mars: Calcium-Magnesium Chloride Brines in the Antarctic Drt Vallets as a Mars Analog. Houston, Universities Space Research Association.
Trent, J. D., Chastain, R. A. & Yayanos, A. A., 1984. Possible artefactual basis for apparent bacterial growth at 250C. Letters to Nature, Volume 307, pp. 737-740.
Triggs, N. E. & Valentini, J. J., 1992. An Investigation of Hydrogen Bonding in Amides Using Raman Spectroscopy. Journal of Physical Chemistry, Volume 96, pp. 6922-6931.
Tschirner, N. et al., 2009. Resonance Raman spectra of B-carotene in solution and in photosystems revisited: an experimental and theoretical study. Physical Chemistry Chemical Physics, Volume 11, pp. 11471-11478.
Vandendriessche, S., Valev, V. K. & Verbiest, T., 2012. Detecting and Analyzing Molecular Chirality on Mars. Concepts and Approaches for Mars Exploration.

Verkaaik, M. F., Hooijschuur, J.-H., Davies, G. R. & Ariese, F., 2015. Raman Spectroscopic Techniques for Planetary Exploration: Detecting Microorganisms through Minerals. Astrobiology, 15(8), pp. 697-707.
Vidiella, P. E., Armesto, J. J. & Gutiérrez, J. R., 1999. Vegetation changes and sequentiaol flowering after rain in the southern Atacama Desert. Journal of Arid environments, Volume 43, pp. 449-458.
Vuille, M., 1999. Atmospheric Circulation over the Bolivian Altiplano During Dry and Wet Periods and Extrene Ogases if the Southern Oscillation. International Journal of Climatology, Volume 19, pp. 1579-1600.
Wadsworth, J. & Cockell, C. S., 2017. Perchlorates on Mars enhance the bacteriocidal effects of UV light. Nature Scientific Reports, 7(4662), p. 8.
Walter, M. R., Buick, R. & Dunlop, J. S. R., 1980. Stromatolites 2,400-3,500 Myr old from the North Pole area, Western Australia. Nature, Volume 284, pp. 443-445.
Wang, J., Bras, R. L., Sivandran, G. & Knox, R. G., 2010. A simple method for the estimation of thermal inertia. Geophysical Research Letters, Volume 37.
Webster, C. R. et al., 2013. Isotope Ratios of H, C, and O in CO2 and H2O of the Martian Atmosphere. Science, 341(6143), pp. 260-263.
Webster, G., Brown, D. C. & Hammond, S., 2008. NASA Phoenix Mars Lander Confirms Frozen Water. [Online]
Available at: https://www.nasa.gov/mission_pages/phoenix/news/phoenix-20080620.html
[Accessed 30 November 2016].
Westall, F. et al., 2013. Habitability on Mars from a Microbial Point of View. Astrobiology, 13(9), pp. 887-897.
Wharon, D. A. & Brown, I. M., 1989. A survey of terrestrial nematodes from the McMurdo Sound region, Antarctica. New Zealand Journal of Zoology, Volume 16, pp. 467-470.
White, D. E., Brannock, W. W. & Murata, K. J., 1956. Silica in hot-spring waters. Geochimica et Cosmochimica Acta, Volume 10, pp. 27-59.
White, R. H., 1984. Hydrolytic stability of biomolecules at high temeratures and its implication for life at 250C. Letters to Nature, Volume 310, pp. 430-432.
Whiteway, J. A. et al., 2009. Mars Water-Ice Clouds and Precipitation. Scoemce, 325(5936), pp. 68-70.
Williams, D. R., 2018. Mars Fact Sheet. [Online]
Available at: https://nssdc.gsfc.nasa.gov/planetary/factsheet/marsfact.html
[Accessed 10 June 2018].
Yee, N. et al., 2003. The effecot of cyanobacteria on silica precipitation at neutral pH: implications for bacterial silicification in geothermal hot springs. Chemical Geology, 199(1-2), pp. 83-90.
Yee, N. et al., 2003. The effect of cyanobacteria on silica precipitation at neutral pH: implications for bacterial silicification in geothermal hot springs. Chemical Geology, 199(1-2), pp. 83-90.
Zakharova, N., 2010. Iceland Field Guide: DEES Graduate Student Field Trip, New York: Department of Earth and Environmental Sciences, Columbia University.
Zangvil, A., 1996. Six years of dew observations in the Negev Desert, Israel. Journal of Arid Environments, Volume 32, pp. 361-370.
Zhang, S. L. et al., 1996. Fourier transform Raman spectroscopy of fuels: curve-fitting of C-H stretching bands. Spectrochimica Acta Part A: Molecular and Biomolecular Spectroscopy, Volume 52, pp. 1529-1540.